

Failure Analysis of Coatings under Thermo-Mechanical Loading

DISSERTATION

zur Erlangung des akademischen Grades

Doktoringenieur
(Dr.-Ing.)

von M.Sc. Joachim Nordmann
geboren am 26.07.1992 in Celle

genehmigt durch die Fakultät für Maschinenbau
der Otto-von-Guericke-Universität Magdeburg

Gutachter:

1. Prof. Dr.-Ing. habil. Dr. h.c. mult. Holm Altenbach
2. Prof. Dr.-Ing. habil. Manja Krüger

Promotionskolloquium am 26.06.2020

Zusammenfassung

Diese Arbeit analysiert das Versagensverhalten eines Eisenaluminium-Aluminium-Verbundes in einem Temperaturbereich von 250°C bis 400°C. Dafür wird zuerst die benötigte Theorie präsentiert und hergeleitet, und daraufhin die Identifizierung aller Materialparameter erklärt, welche entweder direkt aus experimentellen Daten oder durch numerische Optimierung mittels eines neuronalen Netzwerks bestimmt werden. Außerdem wird das, in dieser Arbeit benutzte Modell, mit dem Schädigungsgradienten erweitert und eine Effizienzstudie zwischen unterschiedlichen Berechnungsmethoden durchgeführt.

Abstract

This thesis analyse the failure behaviour of an iron aluminide-aluminium-compound in the temperature range of 250°C to 400°C. The whole theory of the derived model is presented. Further on, the model is extended with the damage gradient and a comparative study is performed to assess which model is computationally more efficient. Next to this, it is explained in detail how all required material parameters are identified from experiments or through numerical optimisation with a neural network.

Contents

List of Figures	vii
List of Tables	ix
Preliminaries and Notation	xi
1 Introduction	1
2 Material Science	3
2.1 Aluminium - Substrate Material	3
2.2 Iron Aluminide - Coating Material	4
2.3 Experiment - Setup and Data Processing	5
3 Basics of the Cohesive Zone Model and the Traction Separation Law	9
3.1 Cohesive Zone Model	9
3.2 Traction Separation Laws	10
3.3 Problems arising through the Use of Cohesive Zone Models	13
4 Continuum Mechanics of an Arbitrary Body with a zero-thickness Interface	15
4.1 Kinematics	15
4.2 Kinetics	18
4.3 Balance Laws & Entropy Inequality	19
4.3.1 Balance of Mass	20
4.3.2 Balance of linear Momentum	20
4.3.3 Balance of angular Momentum	21
4.3.4 Balance of Energy	22
4.3.5 Entropy Inequality	23
4.4 CLAUDIUS-DUHEM- and Dissipation Inequality	23
5 Constitutive Laws	27
5.1 Bulk Constitutive Laws	27
5.2 Interface Constitutive Laws	30
5.2.1 Cohesive Zone Model for Cracking of the Coating	33
5.2.2 Novel Cohesive Zone Model for Delamination of the Coating	34
5.3 Plane-Strain-State	37
6 Finite Element Method	39
6.1 Weak Form of Balance of Linear Momentum	39
6.2 Weak Form of Balance of Energy	40
6.3 Discretisation of the Thermo-Mechanical Problem	41
6.4 Quadratic Plane Strain Element	43
6.5 Linear and Quadratic Plane Cohesive Element	45
6.6 Solution of the Thermo-Mechanical Problem	49
6.6.1 Quasi-Static Analysis	50
6.6.2 Implicit Dynamic Analysis	52

6.7	Viscous Regularisation	53
6.8	Discretisation of Constitutive Laws	55
6.8.1	Coating Constitutive Law	55
6.8.2	Substrate Constitutive Law	56
6.8.3	Cohesive-Zone-Model for Cracking	57
6.8.4	Cohesive-Zone-Model for Delamination	59
6.9	Time Stepping Algorithm	61
7	Damage Gradient Extension of a Cohesive Zone Model	63
7.1	Damage Gradient Extension of the Novel Traction Separation Law	63
7.2	FE Implementation of the Traction Separation Law with Gradient Extension . .	65
8	Verification of User Subroutines and Numerical Models	69
8.1	Test-Setups	69
8.2	Verification of UMAT Subroutines	71
8.2.1	Bulk Constitutive Laws	71
8.2.2	Interface Constitutive Laws	73
8.3	Verification of UEL Subroutines	74
8.3.1	Bulk Constitutive Laws	74
8.3.2	Interface Constitutive Law	75
8.4	Numerical Models	76
8.4.1	Double Cantilever Beam Test	76
8.4.2	Four Point Bend Test	77
9	Identification of Material Parameters	79
9.1	YOUNG's Modulus	79
9.1.1	Substrate	79
9.1.2	Coating	80
9.2	Creep Parameters of the Substrate	82
9.3	Cohesive Parameters	84
9.4	Thermal Parameters of Substrate and Coating	86
10	Simulation Results	89
10.1	Comparison Between Simulation Procedures	89
10.2	Isothermal Simulations	91
10.3	Non-Isothermal Simulation	94
11	Summary, Conclusion and Outlook	99
	References	101
	Appendix A: Continuum Mechanics and Mathematics	A-1
	Appendix B: Experimental Results	B-1

List of Figures

2.1	Phase diagram of aluminium and silicon and YOUNG's modulus of aluminium	3
2.2	Phase diagram of iron and aluminium and YOUNG's modulus of iron aluminide	4
2.3	Sketch of the HVOF process and micrograph of the compound	5
2.4	Experimental setup of the 4PBT and dimensions of the specimen	6
2.5	Calculation of the bending moment from experimental data	7
3.1	Stress distribution at a crack in the sense of DUGDALE and BARENBLATT	9
3.2	Types of TSLs for Mode I opening	11
4.1	Arbitrary body in reference and current configuration	15
4.2	Multiplicative split of the deformation gradient	17
4.3	Arbitrary body with cutting plane with resulting stress and normal vectors	18
4.4	Partitioning of an arbitrary body and interface quantities	19
5.1	Temperature jump across a zero-thickness interface	31
5.2	Plot of heat supply function of the interface	32
5.3	Plot of polynomial TSL from NEEDLEMAN for different values of β	34
5.4	Influence of cohesive parameters on the shape of the novel TSL	36
6.1	Discretisation of an arbitrary body \mathcal{B}	42
6.2	Geometry, nodes and shape functions for a plain element	44
6.3	Transformation between global and local coordinates of an interface element	46
6.4	Geometry, nodes and shape functions for cohesive elements	48
6.5	Influence of viscous regularisation on the FE solution	54
8.1	Test-Setups for UMAT and UEL subroutines of the bulk material	69
8.2	Test-Setups for UMAT and UEL subroutines of the interface material	70
8.3	Results of Test-Setups for elastic UMAT subroutine	71
8.4	Results of Test-Setups for inelastic UMAT subroutine	71
8.5	Creep results of inelastic UMAT subroutine	72
8.6	Results of Test-Setups for the interface for pure Mode I opening	73
8.7	Results of Test-Setups for the interface for Mix Mode opening	73
8.8	Results of Test-Setups for elastic UEL subroutine	74
8.9	Results of Test-Setups for inelastic UEL subroutine	74
8.10	Creep results of inelastic UEL subroutine	75
8.11	Results of Test-Setups for the interface UEL subroutine	76
8.12	FE model of the DCB test	76
8.13	FE model of the 4PBT	77
9.1	M_{exp} vs. Γ_{exp} curves of the substrate for 400°C	79
9.2	Temperature dependence of YOUNG's modulus of the substrate	80
9.3	M_{exp} vs. Γ_{exp} curves of the coating	81
9.4	Temperature dependence of YOUNG's modulus of the coating	81
9.5	M_{exp} and Δu_{exp} vs. t_{exp} curves of the substrate for 400°C	82
9.6	Creep master curve of the substrate	83
9.7	Verification of determined creep parameters for 400°C	84

List of Figures

9.8	Flowchart of the optimisation algorithm	85
9.9	Temperature dependence of heat capacity and conductivity of the substrate . . .	86
9.10	Temperature dependence of heat capacity and conductivity of the coating	87
10.1	Calculation effort for different simulation procedures	89
10.2	Reaction forces calculated at one node for different procedures	90
10.3	Comparison between experiment and simulation at 250°C	92
10.4	Comparison between experiment and simulation at 300°C	92
10.5	Comparison between experiment and simulation at 400°C	93
10.6	Stress distribution in the beam during the simulation at 400°C	94
10.7	Temperature dependence of the minimal time step	95
10.8	Analysed thermo-mechanical problem	96
10.9	Temperature change at two interface points	96
10.10	Temperature distribution in the model during the simulation	97
B.1	M_{exp} vs. Γ_{exp} curves of the substrate for 250°C	B-2
B.2	M_{exp} vs. Γ_{exp} curves of the substrate for 300°C	B-2
B.3	M_{exp} and Δu_{exp} vs. t_{exp} curves of the substrate for 250°C	B-3
B.4	M_{exp} and Δu_{exp} vs. t_{exp} curves of the substrate for 300°C	B-3
B.5	Verification of determined creep parameters for 250°C	B-4
B.6	Verification of determined creep parameters for 300°C	B-4

List of Tables

5.1	Initial values of cohesive parameters for parametric study	36
6.1	Positions and weights of reduced GAUSS integration	45
6.2	Positions and weights of NEWTON-COTES integration	48
8.1	Dummy material parameters for Test-Setups	70
9.1	Determined cohesive zone parameters under isothermal conditions	86
9.2	Density of substrate and coating	88
10.1	Material parameters of substrate and coating	91
10.2	Optimised material parameters under isothermal conditions	91
B.1	Information about all substrate specimens for parameter identification	B-1
B.2	Dimensions of all coating specimens and determined YOUNG's moduli	B-1
B.3	Cross section dimensions of all compound specimens	B-2
B.4	t_{CPU} and N_{Inc} for different procedures with $NE = 200$	B-5
B.5	t_{CPU} and N_{Inc} for different procedures with $NE = 720$	B-5
B.6	t_{CPU} and N_{Inc} for different procedures with $NE = 2720$	B-5
B.7	Temperature dependence of cohesive zone parameters	B-6

Preliminaries and Notation

Throughout the entire text, the direct tensor notation is preferred. Scalars are symbolised by latin italic and greek letters (e.g. a, α), first-order tensors by latin italic lowercase bold letters (e.g. $\mathbf{a} = a_i \mathbf{e}_i$), second-order tensors by latin italic uppercase bold letters (e.g. $\mathbf{A} = A_{ij} \mathbf{e}_i \otimes \mathbf{e}_j$), third-order tensors by latin italic lowercase bold calligraphic letters (e.g. $\mathbf{a} = a_{ijk} \mathbf{e}_i \otimes \mathbf{e}_j \otimes \mathbf{e}_k$) and fourth-order tensors by latin italic uppercase bold calligraphic letters (e.g. $\mathcal{A} = A_{ijkl} \mathbf{e}_i \otimes \mathbf{e}_j \otimes \mathbf{e}_k \otimes \mathbf{e}_l$), where EINSTEIN's summation convention is applied. Considering a CARTESIAN coordinate system with an orthonormal basis, e.g. \mathbf{e}_i with $i \in \{1, 2, 3\}$, basic operations for tensors used in this treatise are the scalar product of two first-order tensors

$$\mathbf{a} \cdot \mathbf{b} = a_i b_j \mathbf{e}_i \cdot \mathbf{e}_j = a_i b_i = c \quad c \in \mathbb{R},$$

the dyadic product

$$\mathbf{a} \otimes \mathbf{b} = a_i b_j \mathbf{e}_i \otimes \mathbf{e}_j = \mathbf{C},$$

the composition of a second- and a first-order tensor

$$\mathbf{A} \cdot \mathbf{a} = A_{ij} a_k \mathbf{e}_i \otimes \mathbf{e}_j \cdot \mathbf{e}_k = A_{ik} a_k \mathbf{e}_i = b_i \mathbf{e}_i = \mathbf{b},$$

the composition of two second-order tensors

$$\mathbf{A} \cdot \mathbf{B} = A_{ij} B_{kl} \mathbf{e}_i \otimes \mathbf{e}_j \cdot \mathbf{e}_k \otimes \mathbf{e}_l = A_{ij} B_{jl} \mathbf{e}_i \otimes \mathbf{e}_l = C_{il} \mathbf{e}_i \otimes \mathbf{e}_l = \mathbf{C},$$

the double scalar product between two second-order tensors

$$\mathbf{A} : \mathbf{B} = A_{ij} B_{kl} \mathbf{e}_i \otimes \mathbf{e}_j : \mathbf{e}_k \otimes \mathbf{e}_l = A_{ij} B_{ij} = b \quad b \in \mathbb{R},$$

and the double scalar product between a fourth- and a second-order tensor

$$\mathcal{A} : \mathbf{B} = A_{ijkl} B_{mn} \mathbf{e}_i \otimes \mathbf{e}_j \otimes \mathbf{e}_k \otimes \mathbf{e}_l : \mathbf{e}_m \otimes \mathbf{e}_n = A_{ijkl} B_{kl} \mathbf{e}_i \otimes \mathbf{e}_j = C_{ij} \mathbf{e}_i \otimes \mathbf{e}_j = \mathbf{C}$$

Up next, we introduce different transpositions of tensors which depend on the order of the tensor. The transposed of second-order tensors is

$$\mathbf{A}^\top = A_{ji} \mathbf{e}_i \otimes \mathbf{e}_j = A_{ij} \mathbf{e}_j \otimes \mathbf{e}_i.$$

The left or right transposition of third-order tensors are

$$\mathbf{a}^L = a_{ijk} \mathbf{e}_j \otimes \mathbf{e}_i \otimes \mathbf{e}_k = a_{jik} \mathbf{e}_i \otimes \mathbf{e}_j \otimes \mathbf{e}_k,$$

$$\mathbf{a}^R = a_{ijk} \mathbf{e}_i \otimes \mathbf{e}_k \otimes \mathbf{e}_j = a_{ikj} \mathbf{e}_i \otimes \mathbf{e}_j \otimes \mathbf{e}_k$$

and the transpositions of fourth-order tensors are

$$\mathcal{A}^L = A_{ijkl} \mathbf{e}_j \otimes \mathbf{e}_i \otimes \mathbf{e}_k \otimes \mathbf{e}_l = A_{jikl} \mathbf{e}_i \otimes \mathbf{e}_j \otimes \mathbf{e}_k \otimes \mathbf{e}_l,$$

$$\mathcal{A}^R = A_{ijkl} \mathbf{e}_i \otimes \mathbf{e}_j \otimes \mathbf{e}_l \otimes \mathbf{e}_k = A_{ijlk} \mathbf{e}_i \otimes \mathbf{e}_j \otimes \mathbf{e}_k \otimes \mathbf{e}_l,$$

$$\mathcal{A}^\top = A_{ijkl} \mathbf{e}_l \otimes \mathbf{e}_k \otimes \mathbf{e}_i \otimes \mathbf{e}_j = A_{klij} \mathbf{e}_i \otimes \mathbf{e}_j \otimes \mathbf{e}_k \otimes \mathbf{e}_l.$$

In the following equation, the KRONECKER delta δ_{ij} is used to represent the second-order identity tensor

$$\mathbf{1} = \delta_{ij} \mathbf{e}_i \otimes \mathbf{e}_j = \mathbf{e}_i \otimes \mathbf{e}_i \quad \text{with} \quad \delta_{ij} = \begin{cases} 1 & \text{if } i = j \\ 0 & \text{if } i \neq j \end{cases}$$

and the identity tensor of fourth-order

$$\mathcal{G} = \delta_{ik} \delta_{jl} \mathbf{e}_i \otimes \mathbf{e}_j \otimes \mathbf{e}_k \otimes \mathbf{e}_l = \mathbf{e}_i \otimes \mathbf{e}_j \otimes \mathbf{e}_i \otimes \mathbf{e}_j$$

and the transposer of fourth-order

$$\mathcal{J} = \delta_{il} \delta_{jk} \mathbf{e}_i \otimes \mathbf{e}_j \otimes \mathbf{e}_k \otimes \mathbf{e}_l = \mathbf{e}_j \otimes \mathbf{e}_i \otimes \mathbf{e}_i \otimes \mathbf{e}_j.$$

The identity tensor of fourth-order maps every second-order tensor into itself

$$\mathbf{A} = \mathcal{G} : \mathbf{A}$$

and the transposer into the transposed second-order tensor

$$\mathbf{A}^\top = \mathcal{J} : \mathbf{A}.$$

The relation between the fourth-order identity tensor and the transposer is

$$\mathcal{J} = \mathcal{G}^\text{L}.$$

The zero first-order tensor is represented as

$$\mathbf{o} = o \mathbf{e}_i$$

and the zero second-order tensor as

$$\mathbf{0} = 0 \mathbf{e}_i \otimes \mathbf{e}_j.$$

The norm of a first-order tensor is defined as

$$|\mathbf{a}| = \sqrt{\mathbf{a} \cdot \mathbf{a}} = \sqrt{a_i a_j \mathbf{e}_i \cdot \mathbf{e}_j} = \sqrt{a_1^2 + a_2^2 + a_3^2}$$

and the norm of a second-order tensor as

$$\|\mathbf{A}\| = \sqrt{\mathbf{A} : \mathbf{A}} = \sqrt{A_{ij} A_{kl} \mathbf{e}_i \otimes \mathbf{e}_j : \mathbf{e}_k \otimes \mathbf{e}_l} = \sqrt{A_{11}^2 + A_{12}^2 + A_{13}^2 + A_{21}^2 + \dots + A_{33}^2}.$$

Using the tensor notation, latin indices run through the values 1, 2, and 3, while greek indices represent the two tangential and the normal directions of a local coordinate system $\{\mathbf{t}_1, \mathbf{t}_2, \mathbf{n}\}$. The vector valued nabla operator is defined as $\nabla = \mathbf{e}_i \partial / \partial x_i$ at three dimensions. $\square \cdot \nabla$ is the divergence, $\square \times \nabla$ is the rotation and $\square \otimes \nabla$ is the gradient of a tensor where \square holds for all first and second order tensors. An extended overview of tensor algebra and analysis is given in basic textbooks on continuum mechanics featuring mathematical propaedeutics, e.g. in AL-TENBACH [1], LAI, RUBIN & KREML [2], BERTRAM [3, 4], LEBEDEV, CLOUD & EREMEYEV [5] or ITSKOV [6].

In some chapters it is necessary to use an alternative representation of the base of a second- or fourth-order tensor to keep the notation short and compact. Therefore, we introduce following representation for a second-order tensor

$$A_{ij} \mathbf{e}_i \otimes \mathbf{e}_j = A_{ij}|_{ij} ,$$

and a fourth-order tensor

$$A_{ijkl} \mathbf{e}_i \otimes \mathbf{e}_j \otimes \mathbf{e}_k \otimes \mathbf{e}_l = A_{ijkl}|_{ijkl} .$$

Also, this representation is used for writing down time integration algorithm.

$$\square_{\square_{j+1}} = \square_{\square_j} + \Delta \square_{\square_{j+1}} \iff \square_{\square}|_{j+1} = \square_{\square}|_j + \Delta \square_{\square}|_{j+1}$$

\square_{\square} stands for a variable with an index. For the numerical implementation of the model the vector-matrix notation is used. Vectors are denoted as latin upright lowercase sans serif bold letters (e.g. displacement vector $\mathbf{u} = [u_1 \ u_2 \ u_3]^T$), matrices as latin upright uppercase sans serif bold letters (e.g. stiffness matrix \mathbf{K}), third-order matrices as latin lowercase bold fraktur letters (e.g. \mathfrak{a}) and fourth-order matrices as latin uppercase bold fraktur letters (e.g. \mathfrak{A}).

In the following almost all letters, operators, symbols, indexes and abbreviations are presented which are used in this treatise.

Latin Letters

a	creep multiplier	\mathbf{f}_{vis}	artificial force vector
a_d	factor for heat production	F	force
A	area	F_{ij}	deformation gradient component
\mathbf{A}	interface material tangent matrix	\mathbf{F}	deformation gradient
\mathfrak{A}	bulk material tangent matrix	g	separation
b	width	g_{cr}	length scale for cracking
\mathbf{b}	\mathbf{B} -operator matrix for displacements	g_{del}	length scale for delamination
B	arbitrary body	\mathbf{g}	separation vector
\mathbf{B}	left CAUCHY-GREEN tensor	G_c	fracture energy
\mathbf{B}	\mathbf{B} -operator matrix for temperature	G_s	energy conductivity
c	heat capacity	h	height of specimen
c_{vis}	damping factor	\mathbf{h}^{ext}	external heat vector
C	arbitrary constant	\mathbf{h}^{int}	internal heat vector
C_p	penalty stiffness for contact	H	heat
\mathbf{C}	elasticity matrix	H^{ext}	external heat
\mathbf{C}^{cap}	heat capacity matrix	H^{int}	internal heat
\mathbf{C}^{con}	heat conductivity matrix	\mathbf{H}	displacement gradient
C	right CAUCHY-GREEN tensor	\mathcal{I}	interface surface
d	damage	J	determinant of deformation gradient
\mathbf{D}	damping matrix	\mathbf{J}	JACOBIAN matrix
e	specific internal energy	k_d	exponent for heat production
e_i	global base vector	K	creep constant
e_α	local base vector	\mathbf{K}	stiffness matrix
E	YOUNG'S modulus	\mathbf{K}^{dyn}	dynamic stiffness matrix
E_{int}	internal energy	l_1	first length of specimen
E_{kin}	kinetic energy	l_2	second length of specimen
\mathbb{E}^3	EUCLIDIAN space	l_{crack}	length of crack
f	arbitrary function	l_{ele}	length of element
\mathbf{f}	force vector	l_{tip}	length of crack tip
\mathbf{f}^{ext}	external force vector	\mathbf{L}	velocity gradient
\mathbf{f}^{int}	internal force vector	\mathbf{L}_u	relation matrix for displacements

\mathbf{L}_θ	relation matrix for temperature	t	time
m	mass	t_{CPU}	computational time
M	bending moment	\mathbf{t}	stress or traction vector
M_{st}	steady-state bending moment	\mathbf{t}_1	first tangential vector
\mathbf{M}	mass matrix	\mathbf{t}_2	second tangential vector
\mathbf{M}_{vis}	artificial mass matrix	T	temperature (CELSIUS)
\mathbf{M}_d	relation matrix for damage	T_{b0}	normalisation for stress in bulk
\mathbf{M}_u	relation matrix for displacements	T_{i0}	normalisation for traction in interface
\mathbf{M}_θ	relation matrix for temperature	T_{ij}	stress tensor component
\mathbf{n}	normal vector	T_{vM}	VON MISES equivalent stress
N	creep exponent	T_α	traction vector component
N_{inc}	number of increments	\mathbf{T}	CAUCHY stress tensor
\mathbf{N}_d	damage shape function matrix	\mathbf{T}_d	dissipative stress tensor
\mathbf{N}_u	displacement shape function matrix	$\overset{\text{K}}{\mathbf{T}}$	KIRCHOFF stress tensor
\mathbf{N}_θ	temperature shape function matrix	$\overset{\text{PK}}{\mathbf{T}}$	first PIOLA-KIRCHOFF stress tensor
p	damage exponent	u	displacement
\mathbf{p}	total <i>DOF</i> vector	\mathbf{u}	displacement vector
P	arbitrary material point	\mathbf{v}_i	eigenvector
P_{mech}	mechanical power	V	volume
P_{non}	non-mechanical power	w	weight of integration point
q_η	entropy flux	W	work
q	heat flux	W^{dyn}	dynamical work
\mathbf{q}	heat flux vector	W^{ext}	external work
Q	arbitrary reference point	W^{int}	internal work
Q	activation energy	x	coordinate of material point
\mathbf{Q}	rotation matrix of an element	\mathbf{x}	position vector
r	specific heat source	\mathbf{y}	local <i>DOF</i> vector
\mathbf{r}	residual vector	Y_E	energy release rate
\mathbf{r}^u	displacement residual vector	Y_{E0}	critical energy release rate
\mathbf{r}^θ	temperature residual vector	\mathbf{Y}	exponential map
R	universal gas constant	\mathbf{z}_α	vector of local coordinate system
\mathbf{R}	rotation matrix of one node	\mathbf{Z}_d	damage \mathbf{B} -operator of interface
\mathbf{R}_{in}	inelastic residual matrix	\mathbf{Z}_u	displacement \mathbf{B} -operator of interface
s	length scale parameter	\mathbf{Z}_θ	temperature \mathbf{B} -operator of interface
S_{i0}	normalisation for energy release rate		
\mathbf{S}	material tangent matrix		

Greek Letters

α_i	eigenvalue	κ	heat conduction coefficient
β	shear stiffness factor	λ	first LAME constant
γ	radius	μ	second LAME constant
Γ	curvature	ν	POISSON'S ratio
Γ_{norm}	normalised curvature	ξ	natural element coordinate
Γ_{st}	steady-state curvature	ξ	vector of natural element coordinates
δ	KRONECKER delta	ρ	density
η	specific entropy	χ	ratio of s and l_{ele}
H_η	entropy	Φ	motion
θ	absolute temperature (KELVIN)	ψ	HELMHOLTZ free energy
Θ	temperature vector		
Θ	temperature jump		

Operators & Indexes

$\square \cdot \square$	scalar product	\square_{in}	inelastic contribution
$\square \times \square$	cross product	\square_{el}	elastic contribution
\square_0	quantity in the ref. configuration	\square_{mech}	mechanical part
\square^T	transposition	\square_{therm}	thermal part
\square^R	right transposition	\square_{exp}	experimental quantity
\square^L	left transposition	\square_{max}	maximum value of quantity
\square^{-1}	inverse	\square_{lin}	linear part of quantity
$\partial \square$	boundary	\square_{nl}	non-linear part of quantity
$d\square$	differential quantity	$\dot{\square}$	first time derivative
\otimes	dyadic product	$\ddot{\square}$	second time derivative
∇	nabla operator	\square_n	quantity in normal direction
$\Delta \square$	difference	\square_t	quantity in tangential direction
$\delta \square$	variation	\square_e	quantity refers to one element
\square_N	quantity of the nodes	\square_N	nodal quantity
\square_b	bulk	\square_+	plus side of interface
\square_i	interface	\square_-	minus side of interface
\square_s	substrate		
\square_c	coating		

Logical Operators

\in	element of	\neq	unequal
\forall	for all	\wedge	and
$=$	equal	\vee	or
\approx	approximately	\cup	allocation
\leq	less equal		
\geq	greater equal		

Abbreviations

exp	exponential function	TSL	Traction Separation Law
lim	limit	PFM	Phase Field Method
ln	natural logarithm	CDM	Continuum Damage Mechanics
log	logarithm with respect to base 10	PDE	Partial Differential Equation
det	determinant of a matrix	HVOF	High Velocity Oxygen Fuel spraying
tr	trace operation	Fe	iron
NE	number of elements	Al	aluminium
DOF	degree of freedom	Nb	niobium
4PBT	Four Point Bend Test	UMAT	user defined material
DCB	Double Cantilever Beam	UEL	user defined element
FEM	Finite Element Method	wt.-%	weight percentage
FE	Finite Element	at.-%	atom percentage
IP	Integration Point		
CZM	Cohesive Zone Model		

1 Introduction

Since the very beginning of mankind it is the desire of humans to understand all aspects of nature. This is transferable into engineering as well. An engineer tries to understand the created part in all aspects too, thus, the created part fulfils all requirements to perfection, in the end. Nowadays, this creation process is supported by a whole bunch of simulations to get a deeper insight in the function and mechanisms of the part. This gets more important in the 21st century, because it is state of the art to call for a more sustainable and responsible usage of resources and this call is getting louder every year. Due to this call the requirements onto used materials increases, since the manufactured parts made of these materials get subjected to higher loads - which can be of mechanical, thermal and/or chemical type - and at the same time weight of the parts is reduced [7–9]. In the context of sustainability and responsibility to save resources and money, as well as materials and CO₂ and to follow the mentioned call in the end [8]. A direct result is that traditional materials (e.g. concrete, steel, wood, etc.) reach their limits, and new techniques as well as materials have to be developed. One technique could be to combine two materials and create a composite, which combines the benefits of the base materials (e.g. steel-enhanced concrete) or to coat a material with a thin ceramic to protect the material against heat (thermal-barrier-coating, oxidation resistance) [10–12]. Another way is to create a single-crystal-alloy, which has a higher strength compared to the same alloy with many crystals [13]. Other examples are fibre-enhanced composites or high temperature materials based on refractory metals [14]. Further on, money- and time-savings can be achieved by reducing the number of experiments (e.g. tensile or fatigue test) and replace them by simulations. Whereby, these experiments are usually performed until total failure of the specimen, hence simulations have to be able to predict total failure of the specimen too. But this is not straight forward as someone could expect.

The arising field is called fracture mechanics which is of enormous interest for the scientific community. This field was founded by GRIFFITH in 1921 [15]. However, only simple models can be analysed with GRIFFITH's theory. To overcome this drawback, different models (Cohesive Zone Model - CZM [16, 17], Continuum Damage Mechanics - CDM [18, 19], Phase Field Method - PFM [20]) were introduced next to a complete new theory called "Peridynamics" [21]. Anyway, the simulation of failure is still very difficult and time-consuming. For this reasons fracture mechanical problems are topics of many treatises [20, 22, 23], books [18, 19] and papers [24–28], as well as for this PhD thesis.

The foundations for this PhD thesis are the master thesis [29] and the article [30] by the author in which a metal compound made of aluminium (substrate) and iron aluminide (coating) is analysed under isothermal conditions at 400°C in a Four Point Bend Test (4PBT) with the linear beam theory of BERNOULLI & EULER, without usage of the Finite Element Method (FEM). Further on, in these works methods are presented to identify all required material parameters from 4PBT measurements, thus, no further experiments are required. The motivation for this analysis was, as mentioned above, that increase and combination of loads and weight reduction are contrary for durability and wear of engineering applications. Therefore, important parts get coated, e.g. the combustion chamber in combustion engines or steam and gas turbines. However, the coating makes the designing process more difficult, thus, the aim of the works by the author is to derive a simple model, which is able to describe the compound at complex loadings.

In this thesis we extend the model of [29, 30] to large deformations and non-isothermal conditions, as well as to fracture mechanics and simulate failure of the mentioned compound. The fracture mechanical model, that is used in this thesis, is the CZM. This model was developed around 1960 through BARENBLATT [16] and DUGDALE [17]. Due to the fact that the compound shows a strong inelastic material behaviour and the simulated time is long (ca. $t = 2000$ s) for fracture mechanical analysis, the small time-step, that is required for such an analysis, is the major drawback and produces in the end high calculation times, which are not desired. Therefore, we investigate the size of the time-step in comparison to different simulation procedures (quasi-static, dynamic) and extend the CZM with the damage gradient.

The structure of this thesis differs slightly from the structure of a common thesis. For the reason of shortness of this thesis it is only referred to the literature when it is necessary to present basic principles, that are required for this work. Therefore, this thesis is addressed to advanced readers, which have a basic knowledge of continuum mechanics. At first, we present the used materials, explain their specific properties and the experimental setup. This is done because this knowledge is necessary to understand the assumptions, which are used later on to formulate the model. In the next chapter the theory of the CZM is explained, as well as the main part of every CZM the Traction Separation Law (TSL). Next to this, problems of the CZM are explained, that arise due to the use of this model. These problems are present in the numerical application, especially. We go on with presenting equations of balance for a body with a zero-thickness interface, because equations of balance are not continuous, due to the interface any more, thus, a jump in these equations arises. Up next the basic principles of thermodynamics are applied to derive relations for constitutive models and upon these relations constitutive models are formulated. To solve the arising system of Partial Differential Equations (PDEs) the FEM is used. Therefore, derived models are discretised and Finite Element (FE) formulations are derived in the next chapter. These formulations are implemented in the FE software ABAQUS by using the UEL and UMAT subroutines, which one is used depends on the performed analyses for this thesis and is later on explained in more detail. Last step before using the derived models is to perform patch tests with the UEL and tests with the UMAT subroutines. This is presented in the ongoing chapter. Then the determination of all material parameters is explained, and an optimisation procedure is presented, which is used to determine the interface parameters from 4PBT measurements as well. For this optimisation procedure the FE software ABAQUS is connected with the software package MATLAB by using the tool ABAQUS2MATLAB [31]. In the ongoing chapter simulation results are presented and interpreted. Further on, a comparison between all used simulation procedures and techniques is made. The quasi-static simulations with viscous regularisation are compared to implicit dynamic simulations and the model with damage gradient extension is compared to a quasi-static simulation with viscous regularisation as well. Although, a thermal model is derived, whereby most presented simulations are isothermal. The last chapter summarises this thesis and presents a conclusion and an outlook for future works.

2 Material Science

This chapter presents the materials, which are used in this work and their specific properties. This knowledge is necessary to understand some assumptions, that are made in this work, as it is mentioned in Chapter 1. Further on, the 4PBT is presented and explained and how the measured data are processed. However, we keep the explanations short and only give the most important information. For more information we refer to [29, 30].

2.1 Aluminium - Substrate Material

The substrate material of the specimen, which is presented in the last section of this chapter is the specific aluminium alloy AlSi10MgT6. This alloy consists of an amount of 9 wt.-% – 11 wt.-% of silicon and an amount of 0.20 wt.-% – 0.45 wt.-% of magnesium. The silicon is added to improve the casting properties and wear resistance (cf. [32]). Due to this high amount of silicon, this alloy is eutectic, which results in a low melting point (ca. 585°C), as can be seen in Fig. 2.1, left-hand side. The addition of magnesium improves the strength of the alloy. However, this addition is limited to 1% because brittleness increases [7]. The last step is to perform a T6 heat treatment with this alloy, to derive the final properties. For reasons of simplicity we do not go into more detail and refer to the specific literature.

Usually, an aluminium crystal is anisotropic, which leads to a direction dependent YOUNG's modulus, that is presented in Fig. 2.1 on the right-hand side. Nevertheless, this dependence is not high, and because an aluminium piece consists of many crystals the macroscopic behaviour is approximately isotropic. Therefore, the anisotropic behaviour of the YOUNG's modulus is not taken into account and it is also assumed that the alloy is homogeneous. This is valid as can

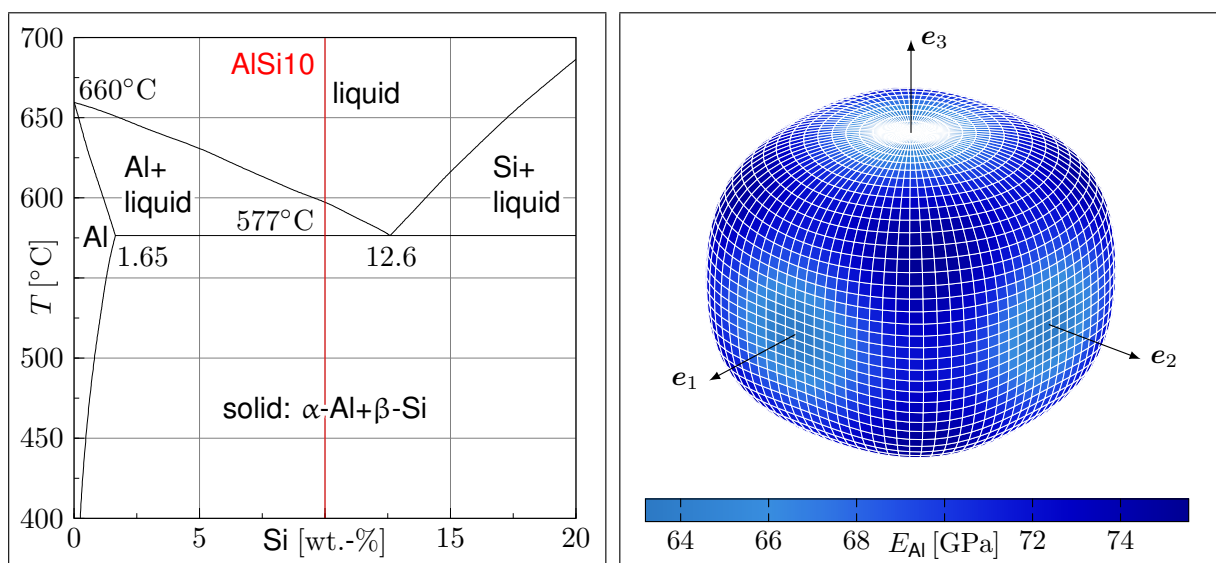


Figure 2.1: Section of the phase diagram of aluminium and silicon after [7] (left-hand side) and anisotropic YOUNG's modulus of aluminium (right-hand side) - values are taken from [4] and the visualisation is done with the tool of [33]

be seen on the micrograph in Fig. 2.3 on the right-hand side. Next to this fact the temperature range considered in this work needs to be discussed. The application temperature in this treatise ranges from 250°C – 400°C, which corresponds to a homologous temperature of ca. 43 % – 68 %. In this temperature regime metals show a strong creep behaviour, which is usually divided into three parts; the primary, secondary and tertiary part. The first part is characterised by a reduction of the creep rate, the second part by a constant (or minimum) creep rate and the third part by an increase of the creep rate. In this work only the second part is considered, since this part is of most concern in technical application, and to keep the model as simple as possible, because the main concern of this thesis is the simulation of the fracture behaviour. Hence, isotropy is assumed the creep deformations is isotropic as well. More informations about the creep behaviour of metals can be found for example in [34, 35].

2.2 Iron Aluminide - Coating Material

The iron aluminides Fe_3Al and FeAl are among the most widely studied intermetallics because of their low cost, low density, good wear resistance, ease of fabrication and resistance to oxidation and corrosion [38]. For technical applications the Al content is limited to ca. 50 at.-%. In this work the used alloy $\text{Fe}_{24}\text{Al}_{10.6}\text{Nb}$ consists of 40 at.-% of Al with a B2 crystal structure, as can be seen in the phase diagram in Fig. 2.2 on the left-hand side. Nb is added to improve the creep resistance of this alloy [38]. Commonly, an iron aluminide crystal is homogeneous and only shows a strong anisotropic behaviour. This can be visualised by plotting the direction dependent YOUNG's modulus which ranges from 60 GPa – 300 GPa ,cf. Fig. 2.2 on the right-hand side. Next to the anisotropic character of iron aluminide another problem is the manufacturing process, which is High Velocity Oxygen Fuel (HVOF) spraying here. In this process the iron aluminide is used as a particle, which is molten in a combustion chamber by using gas, accelerated in a nozzle and then sprayed onto the substrate material [39]. This is presented schematically in Fig. 2.3 on the left-hand side. However, this process is used since it allows the production of relatively thick coatings (here ca. 1 mm) economically and fast. Due to the HVOF spraying technique, the coating consists in the end of oxides, pores and unmelted particles. This can be seen in the micrograph in Fig. 2.3 on the right-hand side, as well as in the sketch of Fig. 2.3 on

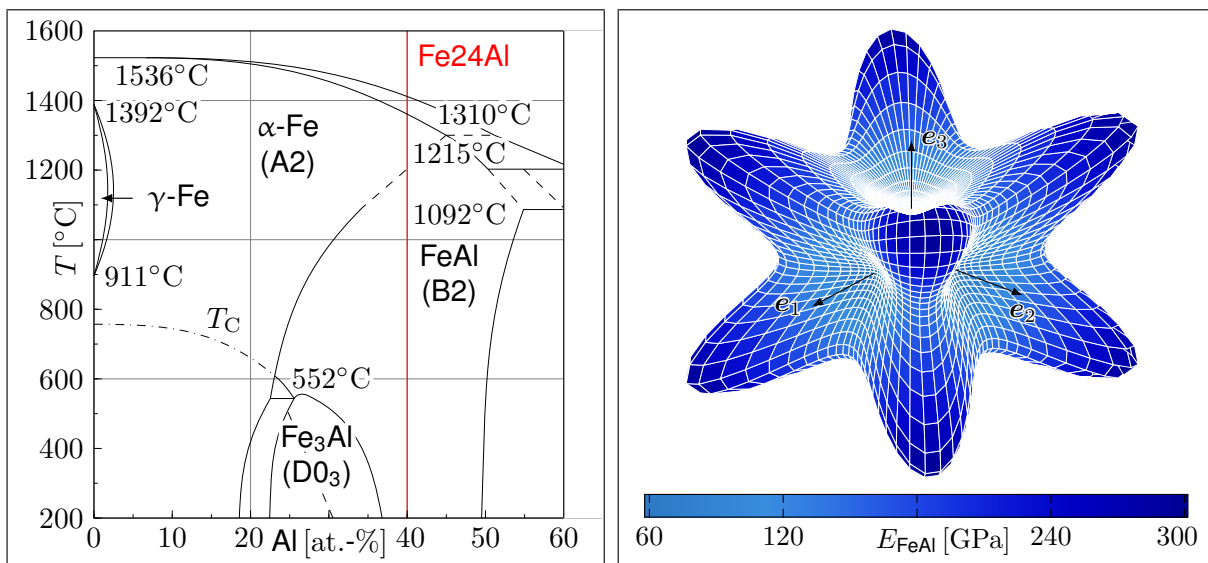


Figure 2.2: Section of the phase diagram of iron and aluminium after [36] (left-hand side) and anisotropic YOUNG's modulus of iron aluminide (right-hand side) - values are taken from [37] and the visualisation is done with the tool of [33]

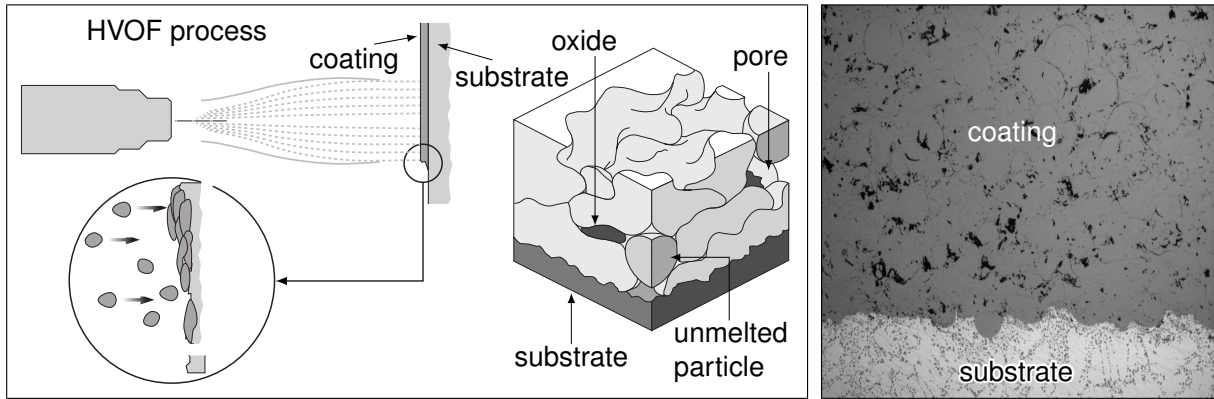


Figure 2.3: Sketch of the HVOF process and the resulting coating after [40, 41] (left-hand side) and micrograph of the real compound (right-hand side)

the left-hand side. Further on, the solidified iron aluminide drops can be seen. The amount of porosity is ca. 7%. Consequently, it is very rigorous and questionable to assume the coating as homogeneous and isotropic. Nevertheless, it is done to keep the model as simple as possible, because the main concern is the simulation of the failure behaviour. Relevant creep deformation of the used iron aluminide alloy is not occurring in the temperature range of 250°C – 400°C, which is investigated in this work.

2.3 Experiment - Setup and Data Processing

The 4PBT is a standard material test, similar to the tensile test. But in contrast to the tensile test in the 4PBT, the stress state is not uniaxial, which makes the processing of the measured data more complicated. However, for the determination of material parameters it is a benefit. This test is often applied to brittle materials, who would fail in a tensile test too soon (e.g. ceramics). The testing machine can be seen in Fig. 2.4 in the top, left-hand side picture. It consists of two lower supports on which the specimen is placed and can move without friction. On the upper two supports a load, or more precisely a displacement is applied. The distance between the two lower supports is $l_2 = 40$ mm, and the distance between the upper supports is $l_1 = 20$ mm. Between the lower supports three sensors are placed on equal distances from each other. The two outer sensors are directly placed below the upper supports, and the third one is placed in the middle of both of them. During the 4PBT four quantities are measured. These are

- the test force F_{exp} ,
- the test time t_{exp} ,
- the displacement of the upper supports u_{exp}
- and the difference displacement measured between the three sensors Δu_{exp} .

All this informations are visualised in the sketch presented in Fig. 2.4 on the top, right-hand side picture next to the dimensions of the specimen. Further on, it can be seen that the specimen is only coated on one side, and the specimen is always placed in a 4PBT in the way that the coating lies on the lower supports and is loaded with a tensile stress, consequently. Every specimen is ca. 50 mm long, has a width b of ca. 3 mm and a total height $h = h_s + h_c$ of ca. 4 mm. Whereby, the index \square_s stands for "substrate" and the index \square_c for "coating". The bottom, left-hand side diagram of Fig. 2.4 presents one coated specimen, who was not tested until failure of the coating occurred. Later on, the most important curve, resulting from the 4PBT, is the F_{exp} vs. t_{exp} curve (cf. Fig. 2.5, left-hand side). However, for the determination of material parameters (cf. Chap. 9) the M_{exp} vs. t_{exp} (cf. Fig. 2.5, right-hand side) and the M_{exp} vs. Γ_{exp}

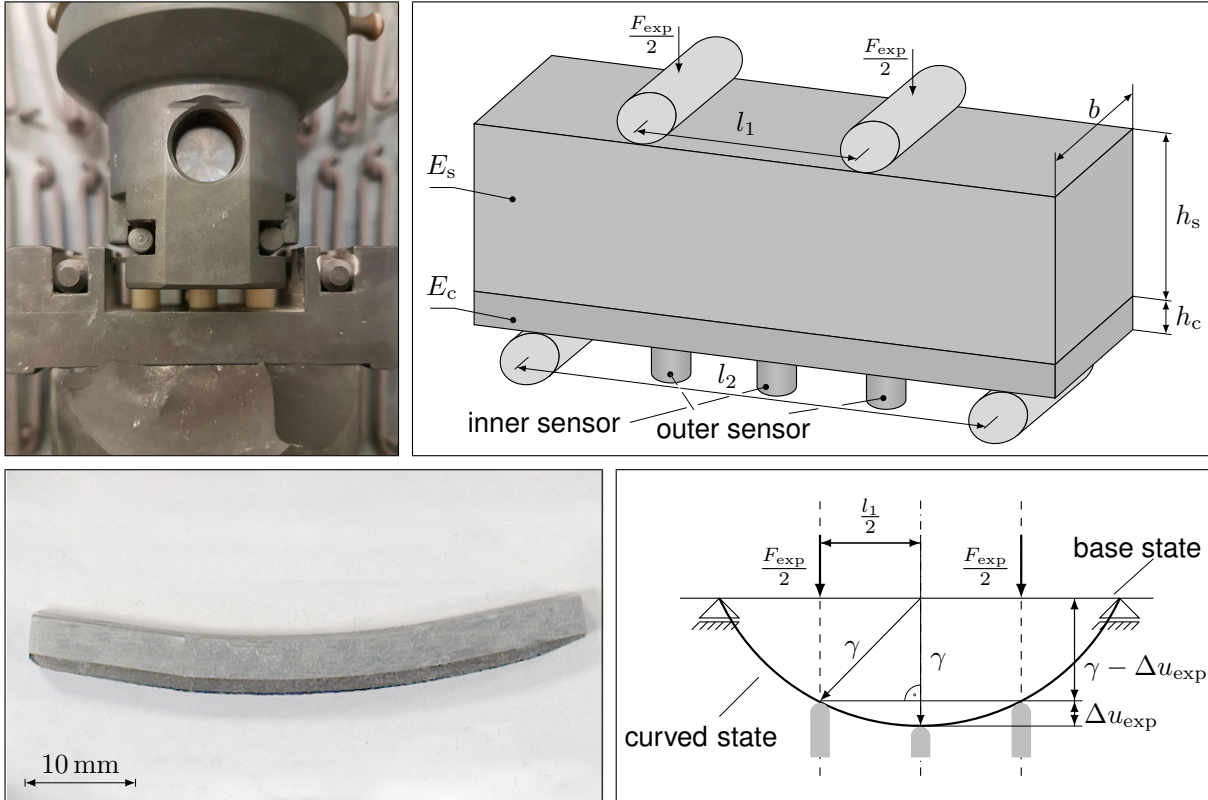


Figure 2.4: Experimental setup of the 4PBT (top, left-hand side), dimensions of the specimen (top, right-hand side), deformed specimen (bottom, left-hand side) and curvature calculation (bottom, right-hand side)

curve are required, respectively. These curves are derived from the measured data by applying the linear beam theory of BERNOULLI & EULER. In this work we only give a brief overview. More details on this procedure can be found in [29, 30]. The complete procedure is based on the constant bending moment, which is present between the upper supports. It is determined with the formula

$$M_{\text{exp}} = \frac{F_{\text{exp}}}{4} (l_2 - l_1). \quad (2.1)$$

Much more, it is possible to determine the radius γ_{exp} of the beam (cf. Fig 2.4 bottom, right-hand side) from the difference displacement Δu_{exp} , at first. In the following, the curvature Γ_{exp} is assumed to be constant along the cross section height. Since the difference displacement is measured at the bottom of the specimen and whole beam theory is related to the neutral axis of the beam, the radius is corrected with the distance from the bottom to the neutral axis. The resulting expression for the curvature is

$$\Gamma_{\text{exp}} = \frac{2}{2\gamma_{\text{exp}} + 2h_c + h_s} \quad \text{with} \quad \gamma_{\text{exp}} = \frac{l_1^2 + \Delta u_{\text{exp}}^2}{2\Delta u_{\text{exp}}^2}. \quad (2.2)$$

All the presented assumptions and equations are only valid for small deformations, which is a very strong assumption. At first, it is necessary to check if the beam is lean. This is the case, when the cross section dimensions are much smaller compared to the length of the beam. Here, this is not exactly the case. The height $h \approx 4 \text{ mm} < 50 \text{ mm}$ but it is not much smaller and the ratio is only 12.5. The situation is similar by comparing the width and the length, $b \approx 3 \text{ mm} < 50 \text{ mm}$. This is smaller and the ratio is 16.6, but not much smaller. Further on, the applied final displacement, which is $u_{\text{exp}} \approx 1.5 \text{ mm}$, is approximately half of the height of the beam (cf.

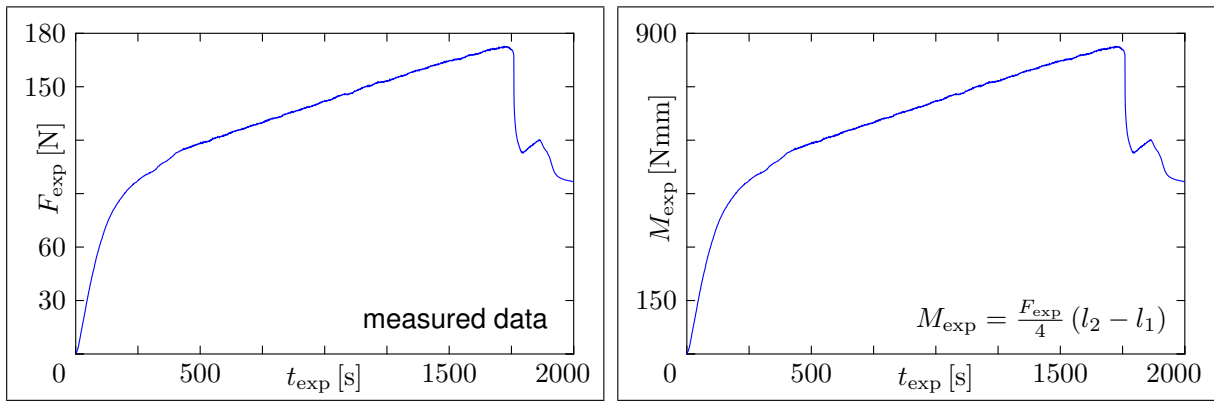


Figure 2.5: Calculation of the bending moment from experimental data - experimental data (left) and calculated bending moment (right)

Fig. 2.4 bottom, right-hand side). Therefore, the assumption of small deformations is only valid for the first 500 s, approximately. Then it is necessary to consider large deformations. Therefore, the material parameters are determined from the measured data as soon as possible. An interesting point is, although that material parameters are determined in the framework of small deformations, it is possible to use them in a model, which considers large deformations. This can be concluded by looking at the final results (cf. Fig. 10.4).

3 Basics of the Cohesive Zone Model and the Traction Separation Law

This section is divided into three subsections. In the first one we give a brief overview over CZMs, mention important works in this field and present the main assumptions of these models. The second subsection is dedicated to the different types of TSLs, who can be used in a CZM, and in which situation a specific law is applied. In the third subsection numerical problems are explained, which arise when CZMs are used.

3.1 Cohesive Zone Model

The theory of cohesive zones was initiated by BARENBLATT [16, 43] and DUGDALE [17] in order to overcome limitations of the concept of linear elastic fracture mechanics, established by GRIFFITH [15, 22]. Namely, the infinite stress at the crack tip and the existence of a pre-crack. It is a phenomenological framework to model crack evolution and crack nucleation in solid bodies. The crack is divided into two regions (inner and terminal region); *"In the inner region the opposite sides of the cracks are at a significant spacing so that interaction between these sides does not occur."* [16]. Further on, they are stress-free. *"In the terminal region the opposite sides of the crack come close to each other so that there are very large interaction forces attracting one side of the crack to the other."* [16]. These are the cohesive forces. The three main assumptions of BARENBLATT are:

- the dimensions of the terminal region are small compared to the size of the crack ($l_{tip} \ll l_{crack}$),
- the behaviour of the terminal region depends only on local quantities and not on the applied load,
- and both sides of the crack are smoothly joined at the end.

The last assumption leads to a finite stress at the end of a crack. Figure 3.1 presents the two surfaces (\mathcal{I}_+ and \mathcal{I}_-), which are created due to cracking and schematic stress distributions in

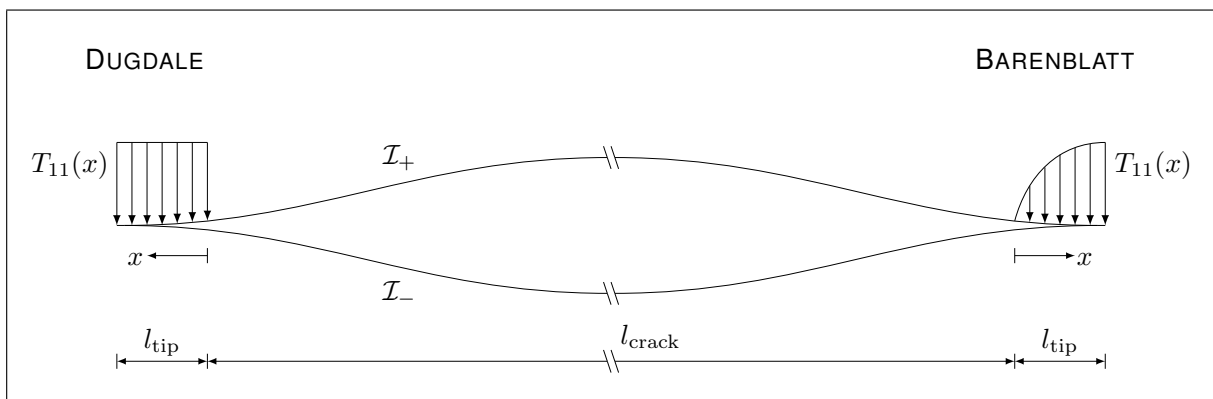


Figure 3.1: Stress distribution at a crack in the sense of DUGDALE (left-hand side) and BARENBLATT (right-hand side) after [42]

the terminal region (crack tip) in the sense of DUGDALE (Fig. 3.1, left-hand side) and BARENBLATT (Fig. 3.1, right-hand side). DUGDALE assumed that the stress at the crack tip is the yield strength ($T_{11}(x) = T_y$) and that this stress is constant to analyse the yielding of a steel sheet containing slits. In contrast to that, BARENBLATT analysed crack evolution in a perfect brittle solid. In general, prescription of stress is done with a TSL. This law defines the stress or traction in the terminal region as a function of the distance between the surfaces \mathcal{I}_+ and \mathcal{I}_- (separation), which is state of the art. This has the benefit, that no pre-crack has to exist. However, BARENBLATT formulated his TSL as a function of the distance x from the end of the crack to the end of the cohesive zone.

After introducing this theory to the scientific community nearly two decades no big interest arose in this field, since the effort to solve the arising problem was too high. However, with the advance of the numerical solution techniques, especially the FEM, it got possible to solve the arising systems of PDEs. This led to a big interest in CZMs to describe cracking and crack evolution in a solid. From our knowledge, one of the first users of this theory was HILLERBORG [44] in 1976 to describe failure of concrete. The CZM is added to a FE mesh by introducing cohesive or interface elements. After this, the cohesive zone framework attracted a lot of attention due to contributions of NEEDLEMAN [45, 46], TVERGAARD & HUTCHINSON [47], ORTIZ & PANDOLFI [48], XU & NEEDLEMAN [49], RICE & WANG [50], CAMACHO ET AL. [51] among others. *"In all the CZMs (except BARENBLATTs model, DUGDALES model and CAMACHOs model), the traction separation relations for the interfaces are such that with increasing interfacial separation, the traction across the interface reaches a maximum, then decreases and eventually vanishes permitting a complete decohesion."* [28]. The traction separation relation or TSL is the most important part of every CZM, therefore, we dedicate the whole next section to this topic and do not go into more detail.

In general, the CZM can be applied to every interface in a continuum. Whereby, it should be clear, that this model is rather suitable when the geometry of the interface is known a priori and not unknown. For this reason, it is very common to use CZMs to analyse e.g. failure of fibre-matrix-composites [52], delamination of plies [53, 54] or coatings (this is the case in this work), peeling tests [55] or indentation tests [56] (In all these simulations the interface is known.). Examples for the usage of CZMs with an unknown interface are hard to find and difficult to analyse, therefore, we exclude this topic in this work. Also, the need to know the geometry of the interface (crack path) to apply CZMs to a problem can be interpreted as a disadvantage. However, every model has advantages and disadvantages and this is not the biggest disadvantage of this model. Further disadvantages are that stresses start to oscillate, that a length scale is added to the model [57] and that the NEWTON-RAPHSON procedure is destabilised due to a strong softening behaviour. However, the latter two disadvantages are a result of every model considering fracture mechanical processes or an inelastic material behaviour. This will be discussed in Section 3.3. Advantages of CZMs are, that they are easily applied to an existing model and no pre-crack is necessary. Especially, the latter reason is important.

3.2 Traction Separation Laws

As mentioned in the foregoing section, the TSL is the key part of every CZM and it has a strong influence on how the crack will open and propagate. Commonly, the TSL is formulated as a phenomenological law without any thermodynamic background. However, influences like the failure mechanism (e.g. brittle or ductile), the opening mode (Mode I, II, III), the material of the solid and to which problem the TSL is applied, are always included in the TSL. Further on, the TSL could depend on the separation velocity $\dot{t}_i = f(\dot{g})$ [61, 62] instead of the separation $t_i =$

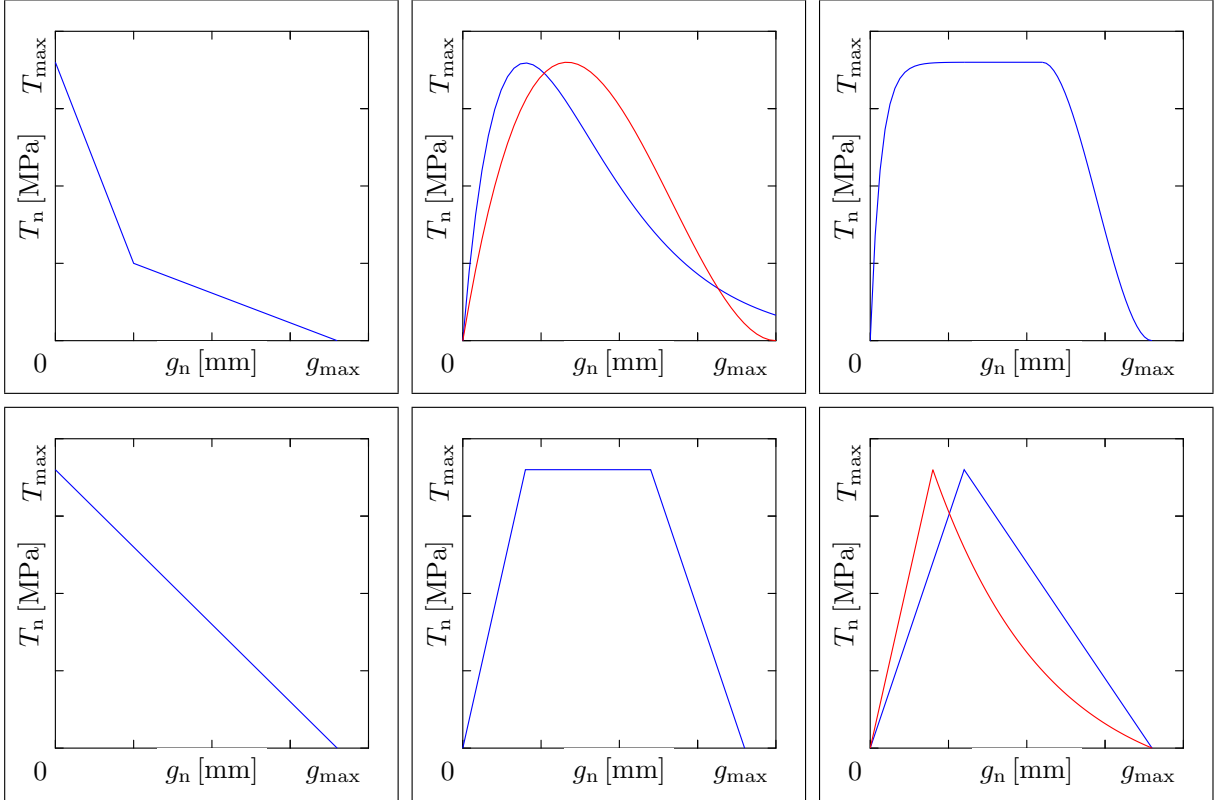


Figure 3.2: Types of TSLs for Mode I opening after: BAŽANT [58] (top, left-hand side); NEEDLEMAN [45, 46] blue - exponential TSL, red - polynomial TSL (top, centre); SCHEIDER [59] (top, right-hand side); HILLERBORG [44] (bottom, left-hand side); TVEERGARD & HUTCHINSON [47] (bottom, centre); ABAQUS [60] blue - linear softening, red - exponential softening (bottom, right-hand side)

$f(g)$, or it could exist a coupling between the different opening modes (mix mode behaviour). All this information can have an influence on the crack and the crack propagation, therefore it has to be considered when the TSL is formulated. For this reason a lot of different TSLs are formulated by researchers to analyse their specific problems. Here, we can only present an overview of frequently used TSLs. They are shown in Fig. 3.2 for pure Mode I opening. All standard TSLs, next to the presented ones, have in common that they are characterised by two independent parameters; the maximum traction and the maximum separation. The other parameters which are used in the TSL usually depend or are formulated with a dependence on these two parameters. Sometimes, the maximum traction is replaced by the fracture energy G_c , which is the area under the TSL and it is calculated through integration.

$$G_c = \int_0^{g_{\max}} T_n \, dg_n \quad (3.1)$$

Brittle cracking can be modelled with simple linear TSLs, which were presented and used by HILLERBORG or BAŽANT for example to model the cracking of concrete (Fig. 3.2 top, left and bottom, left). Since it can be assumed for brittle failure that any inelastic deformation is material separation, these TSLs have no elastic range [42]. However, the introduction of a small elastic zone is useful for the numerical treatment. In contrast, smooth TSLs with an elastic range, a long range on the level of maximum traction and a slow degradation are used to describe ductile failure mechanisms. Some examples for these TSLs are presented in the diagrams in Fig. 3.2 top, centre and right position, and in Fig. 3.2 bottom, centre position. The bottom, right diagram

in Fig. 3.2 presents schematic the two possible shapes of TSLs, which are implemented in the commercial software tool ABAQUS. Both TSLs can be adjusted in order that it gets possible to model brittle or ductile failure. However, application of these TSLs is limited due to their simplicity. The foundations of both TSLs can be found in [63–65].

In the early stages of the TSLs these laws were formulated very simple, with no thermodynamic background (as mentioned earlier) and for every direction separately (cf. HILLERBORG [44]). Hence, someone can write traction and separation vector as follows.

$$\mathbf{t}_i = T_n \mathbf{e}_n + T_{t1} \mathbf{e}_{t1} + T_{t2} \mathbf{e}_{t2} = T_\alpha \mathbf{e}_\alpha \quad \forall \alpha \in \{1, 2, 3\} \quad (3.2)$$

$$\mathbf{g} = g_n \mathbf{e}_n + g_{t1} \mathbf{e}_{t1} + g_{t2} \mathbf{e}_{t2} = g_\alpha \mathbf{e}_\alpha \quad \forall \alpha \in \{1, 2, 3\} \quad (3.3)$$

However, usually one fracture mode does not arise without another one and in general the modes influence each other. Therefore, it is necessary to introduce a coupling between the different modes, which leads to mix mode TSLs. Further on, it is required that the TSL fulfils thermodynamic restrictions, similar to constitutive laws in standard continuum mechanics. This demand leads to the procedure to derive the TSL from an energy potential, which depends on the separation in some way (cf. GURTIN [66]). The most often used possibilities are to formulate the potential as a function of the separate components

$$\psi_i = f(g_n, g_{t1}, g_{t2}, \beta) \quad (3.4)$$

or to introduce an effective separation (in-plane isotropy) and formulate the potential depending on this scalar quantity.

$$\psi_i = f(g_{\text{eff}}, \beta) \quad \text{with } g_{\text{eff}} = \sqrt{g_n^2 + \beta (g_{t1}^2 + g_{t2}^2)} \quad (3.5)$$

The factor β describes the ratio between normal and tangential opening in Eqs. (3.4) and (3.5) and is called shear stiffness factor [56, 67]. However, as will be illustrated subsequently, the simulations are not very sensitive to the choice of β [67]. The required separation components are determined with the scalar product between separation (Eq. (3.3)) and base vector $g_\alpha = \mathbf{g} \cdot \mathbf{e}_\alpha \quad \forall \alpha \in \{1, 2, 3\}$. In this work we use Eq. (3.4) for one TSL (cf. Sect. 5.2.1) and formulate another potential, which depends on the separation vector.

$$\psi_i = f(\mathbf{g}) \quad (3.6)$$

In Eq. (3.6) the mix mode behaviour is introduced due to the introduction of an inelastic separation portion (cf. Sect. 5.2.2). Finally, the traction components are derived through partial derivatives of the potential.

$$T_\alpha = \frac{\partial \psi_i}{\partial g_\alpha} \quad \forall \alpha \in \{1, 2, 3\} \quad (3.7)$$

With this procedure it is possible to derive TSLs, who are physically motivated as done in this work or presented in [27, 62] or phenomenological laws [50, 67]. The whole time a local coordinate system is used for the TSL formulations which has the basis $\{\mathbf{e}_n, \mathbf{e}_{t1}, \mathbf{e}_{t2}\}$ and not $\{\mathbf{e}_1, \mathbf{e}_2, \mathbf{e}_3\}$. The determination of the local coordinate system is done through directional derivatives in the tangential directions of the interface, and performing the cross product between these vectors to determine the normal vector of the interface surface. Further information can be found in the specific literature, we refer to [22, 23, 68].

Commonly, the TSL is prescribed (e.g. [27, 44, 47, 50, 62, 67]) and then the global behaviour is analysed. The high number of authors mentioned makes clear, that this is the common pro-

cedure. Of course the inverse way is possible (e.g. NASE [69]), but then it is difficult to fulfil thermodynamics, therefore, it is uncommon. Up to now, we explained the TSL and presented some formulated TSLs. However, these models can only be used to model failure when loading occurs. They are not able to model unloading, since some of them are reversible TSLs (e.g. [46, 47, 67]) without a damage variable. Hence, if someone wants to model fracture under cyclic loading, an irreversible TSL (e.g. [27, 56]) and a contact condition must be applied to the TSL, and maybe a friction formulation for the tangential direction, when required [70, 71].

For more detailed explanations concerning TSLs, for what problems they are used, and what different TSLs exist, we refer to the book of SCHWALBE [42] or the reviews of CHANDRA [28] and NEEDLEMAN [57].

3.3 Problems arising through the Use of Cohesive Zone Models

This section summarises important problems, which occur by applying CZMs to model fracture and failure of a continuum with one or more zero-thickness interfaces. We begin with physical and mathematical problems, who arise through the usage of CZMs and then go on with numerical problems which are present when this model is used in a FE simulation. We begin with the physical problem:

The physical problem is that a length scale is added to the model. *"Because the material constitutive relation is between stress and strain while the cohesive constitutive relation is between force and displacement, the overall response is size dependent."* [57]. This length scale can be addressed to the number of elements (NE) which are used to discretise the model when a FE analysis is performed and a traction-separation relation is used. The other possibility is to use a TSL with a fracture energy-separation relation, then the NE is replaced by the geometric dimensions of the problem. In [57, 72] this is pointed out by analysing a one-dimensional bar problem under small deformations, with HOOKE's law and a bilinear TSL. Up to now, no solution for this problem is known.

The mathematical problem is that the balance of linear momentum changes its properties in the static and the dynamic case. *"In the static case the elliptic character of the set of partial differential equations is lost, while, on the other hand, in the dynamic case we typically observe a change of a hyperbolic set into an elliptic set. In either case the rate boundary value problem becomes ill-posed and numerical solutions suffer from spurious mesh sensitivity."* [72]. This can be addressed back to the fact that stress-strain relations are used, whereby, force-displacement relations would be more suitable. This violates the stability criterion of the material [73, 74]. To solve this problem higher order terms in the continuum description are necessary [72] or one must take into account the viscosity of the material [72, 75]. This leads directly to one numerical problem, which arises through the simulation of cracking and crack propagation along a predefined path by using cohesive elements. Due to the fact that the problem becomes ill-posed through the strong softening behaviour [75, 76], the numerical solution scheme, usually a NEWTON-RAPHSON procedure, is destabilised. One solution to solve this is to consider higher order terms in the continuum description, as it is mentioned earlier, but this has some disadvantages (e.g. increase of $DOFs$, unexplainable material parameters, needs C_1 -continuity, etc.). The other and more simple possibility is to add a damping term to the constitutive law or to the global residual vector. This additional term consumes the redundant energy due to cracking and crack propagation. This principle is called viscous regularisation and is common for many unstable analyses [76, 77]. The problem with viscous regularisation is, that the user has to make an initial guess for the damping factor, since, if the damping factor is too high no deformation will take place because all energy is consumed. In contrast to that, if the damping

factor is too low the procedure will converge, but requires very small time steps what can lead to convergence problems of the global solution scheme (e.g. NEWTON-RAPHSON). Hence, to find a proper damping factor is a trial and error procedure.

Another possibility is to use other solution schemes like the RIKS method which is more adequate for an ill-posed problem. But this scheme suffers from the problem, that it does not converge quadratically and is more complex as the NEWTON-RAPHSON procedure, which leads in the end to higher calculation times. The user has to decide, if it is worth it to use this scheme, or to start a trial and error procedure to find a suitable damping factor. By studying the literature most researchers prefer the NEWTON-RAPHSON procedure to obtain the solution.

A further, main problem for numerical solution schemes is that a CZM requires a high initial stiffness to avoid an elastic opening of the interface before cracking occurs. Besides, this leads to spurious traction oscillations near the crack [78–81]. The optimum would be to set the initial stiffness to infinity. However, because of this spurious traction oscillations this is not possible. Commonly, the initial stiffness is ten up to one hundred times higher than the stiffness of the surrounding material. On the contrary, higher values can be achieved with stabilised CZMs, as shown in [82]. Another possibility to reduce the occurrence of these oscillations is to use non-standard integration schemes to calculate the cohesive element stiffness matrix. Usually, full GAUSS integration is used to evaluate the stiffness matrix which results in a stiffness matrix with the following structure in the local coordinate system for a four node plane element with two displacement *DOF*. \mathbf{C}_i represents the elasticity matrix of the TSL.

$$\mathbf{K}_{i,uu}^e = \frac{1}{3} \begin{bmatrix} 2\mathbf{C}_i & \mathbf{C}_i & -\mathbf{C}_i & -2\mathbf{C}_i \\ \mathbf{C}_i & 2\mathbf{C}_i & -2\mathbf{C}_i & -\mathbf{C}_i \\ -\mathbf{C}_i & -2\mathbf{C}_i & 2\mathbf{C}_i & \mathbf{C}_i \\ -2\mathbf{C}_i & -\mathbf{C}_i & \mathbf{C}_i & 2\mathbf{C}_i \end{bmatrix}$$

Hence, this matrix is fully coupled. In contrast, it results the following stiffness matrix by using NEWTON-COTES integration.

$$\mathbf{K}_{i,uu}^e = \begin{bmatrix} \mathbf{C}_i & \mathbf{0} & \mathbf{0} & -\mathbf{C}_i \\ \mathbf{0} & \mathbf{C}_i & -\mathbf{C}_i & \mathbf{0} \\ \mathbf{0} & -\mathbf{C}_i & \mathbf{C}_i & \mathbf{0} \\ -\mathbf{C}_i & \mathbf{0} & \mathbf{0} & \mathbf{C}_i \end{bmatrix}$$

The difference in these two schemes is that, through the use of NEWTON-COTES integration for the element, only nodes placed at opposite sides influences each other, and hence, the oscillations are reduced. By using GAUSS integration all nodes of the element influences each other. Therefore, it is recommended to use NEWTON-COTES integration for cohesive elements.

4 Continuum Mechanics of an Arbitrary Body with a zero-thickness Interface

In this chapter the basic equations of continuum mechanics for an arbitrary body \mathcal{B} with a zero-thickness interface \mathcal{I} in the EUCLIDEAN space \mathbb{E}^3 are derived (cf. Fig. 4.1), which serves as the foundation for the following chapters. Due to the fact that it is not the aim of this treatise to give a full introduction to continuum mechanics and to keep this chapter short, only the necessary aspects and concepts are introduced. For further information the interested reader is referred to the specific literature, e.g. ALTENBACH [1], BERTRAM [3, 4], NAUMENKO & ALTENBACH [35], HOLZAPFEL [83] or FAGERSTRÖM & LARSSON [84] and others, respectively. The explanations given here are based on these books, as well. It is started with the introduction of the kinematic relation, followed by the kinetic relation, then the equations of balance followed by the entropy inequality and then the CLAUSIUS [85]-DUHEM [86]- and the dissipation inequality are presented. In this chapter no comment is given on constitutive laws, since this is done in Chapter 5.

4.1 Kinematics

The first step in continuum mechanics is to describe the motion of an arbitrary body \mathcal{B} with the boundary $\partial\mathcal{B}$ in the EUCLIDEAN space \mathbb{E}^3 . Thereby, the body consists of a continuous set of material points P . For the spatial description of the motion of the body a cartesian coordinate system $x_i e_i$ is employed. Furthermore, it is distinguished between two configurations. The reference and the current configuration. The reference configuration describes the body in the base state at time $t = t_0$ with subsection of the body to thermal q_{b0} and mechanical t_{b0} loadings, boundary and initial conditions. Every quantity of this configuration is marked with the index \square_0 . In contrast, the current configuration describes the body at time $t > t_0$ in which the body is moved due to thermal and mechanical loadings.

Between these configurations a motion $\Phi(x_0, t)$ can be introduced, which maps every position vector x_0 of a material point P_0 of the reference configuration into the position vector x of

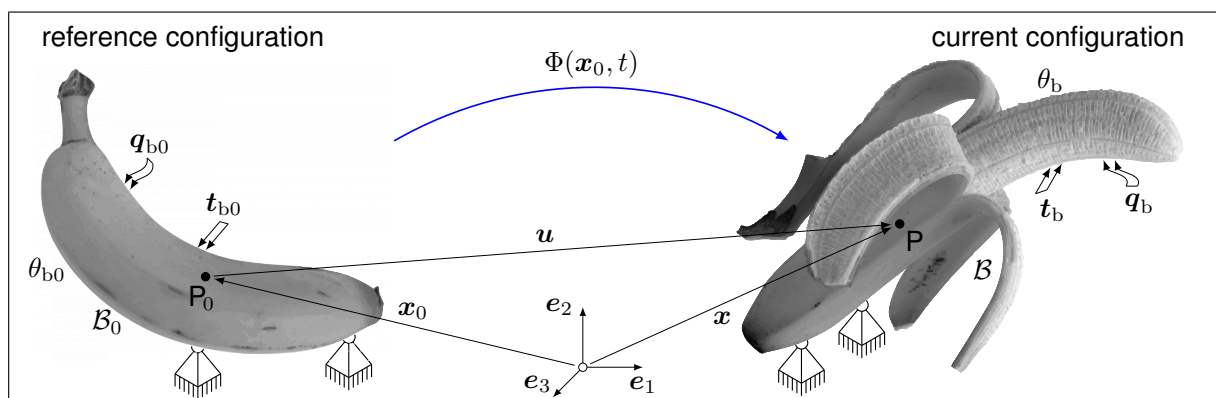


Figure 4.1: Arbitrary Body in EUCLIDEAN space \mathbb{E}^3 with a zero-thickness interface in reference and current configuration subjected to mechanical and thermal loadings

the material point P in the current configuration.

$$\mathbf{x} = \Phi(\mathbf{x}_0, t) \quad \text{with} \quad \mathbf{x}_0 = \Phi(\mathbf{x}, t_0) \quad (4.1)$$

With position vectors at hand the displacement vector is defined as

$$\mathbf{u} = \mathbf{x} - \mathbf{x}_0. \quad (4.2)$$

Figure 4.1 presents both configurations. Additionally, two different descriptions of the motion are possible in continuum mechanics. The first possibility is to describe the motion with respect to the reference configuration which is called material or LAGRANGEan description and the second possibility is to describe the motion with respect to the current configuration. This is called spatial or EULERian description. In this treatise the LAGRANGEan description is used, which is the common description in solid mechanics. Whereas, the EULERian description is preferred in fluid mechanics. Equation (4.1) represents the LAGRANGEan description of the motion. The EULERian description is achieved with the inverse motion Φ^{-1} .

$$\mathbf{x}_0 = \Phi^{-1}(\mathbf{x}, t) \quad (4.3)$$

"As an alternative, the motion can be interpreted as a time-dependent change of coordinates." [3]. Therefore, a LAGRANGEan coordinate system $x_0_i e_i$ and an EULERian coordinate system $x_i e_i$ is introduced.

Next to the description of the motion it is necessary to describe the deformation of the body \mathcal{B} . Hence, the change of an infinitesimal line element $d\mathbf{x}_0$ at the point P_0 from reference in current configuration must be described. This change is given by

$$d\mathbf{x} = \Phi(\mathbf{x}_0 + d\mathbf{x}_0, t) - \Phi(\mathbf{x}_0, t) \quad (4.4)$$

in the LAGRANGEan description. Expanding the first term of Eq. (4.4) in a TAYLOR series (cf. [87]) and assume that quadratic- and higher-order terms are negligible yields the common expression for the deformation gradient

$$\mathbf{F} = \frac{\partial \mathbf{x}}{\partial \mathbf{x}_0} = \mathbf{1} + \frac{\partial \mathbf{u}}{\partial \mathbf{x}_0} \quad (4.5)$$

which can be expressed with the LAGRANGEan nabla operator and the displacement gradient \mathbf{H}_0 , as well.

$$\mathbf{F} = \mathbf{1} + \mathbf{H}_0 = \mathbf{1} + \mathbf{u} \otimes \nabla_0 \quad (4.6)$$

Consideration of higher-order terms in the TAYLOR series expansion would lead to strain gradient theories e.g. [88]. This tensor transforms a line element from the reference into the current configuration. The deformation gradient \mathbf{F} is a two-field-tensor, since the right index refers to the reference and the left index to the current configuration. Further on, the determinant of this tensor is positive definite ($J = \det(\mathbf{F}) > 0$), thus, the deformation gradient is invertible. Yet this tensor is not symmetric and contains rigid body motions what leads to some problems, which are explained later in this chapter. The velocity of the deformation in a LAGRANGEan description is

$$\mathbf{L} = \dot{\mathbf{F}} \cdot \mathbf{F}^{-1}. \quad (4.7)$$

Due to the fact that the materials considered in this work, show an inelastic material behaviour and large deformations occur, it is necessary to perform the multiplicative split of the deforma-

tion gradient into an elastic and an inelastic part (cf. LEE [89]).

$$\mathbf{F} = \mathbf{F}_{\text{el}} \cdot \mathbf{F}_{\text{in}} \quad (4.8)$$

The interpretation of the multiplicative split is presented in Figure 4.2. The inelastic deformation gradient \mathbf{F}_{in} can be interpreted as a transformation of the body \mathcal{B} in an intermediate configuration which lies between reference and current configuration and is stress-free. To determine the inelastic deformation gradient it is necessary to formulate an evolution equation. This is described in Chapter 5. For the formulation of constitutive laws (cf. Chap. 5) the elastic deformation gradient \mathbf{F}_{el} is required which transforms the body from the intermediate into the current configuration.

$$\mathbf{F}_{\text{el}} = \mathbf{F} \cdot \mathbf{F}_{\text{in}}^{-1} \quad (4.9)$$

Due the fact that the deformation gradient is not symmetric and contains rigid body motions (translations and rotations) it is not possible to formulate constitutive laws with this tensor because the constitutive law would be not invariant (cf. [3]). To overcome this the right

$$\mathbf{C} = \mathbf{F}^\top \cdot \mathbf{F} \quad \mathbf{C}_{\text{el}} = \mathbf{F}_{\text{el}}^\top \cdot \mathbf{F}_{\text{el}} \quad \mathbf{C}_{\text{in}} = \mathbf{F}_{\text{in}}^\top \cdot \mathbf{F}_{\text{in}} \quad (4.10)$$

and the left

$$\mathbf{B} = \mathbf{F} \cdot \mathbf{F}^\top \quad \mathbf{B}_{\text{el}} = \mathbf{F}_{\text{el}} \cdot \mathbf{F}_{\text{el}}^\top \quad \mathbf{B}_{\text{in}} = \mathbf{F}_{\text{in}} \cdot \mathbf{F}_{\text{in}}^\top \quad (4.11)$$

CAUCHY-GREEN tensors are introduced. These tensors are positive definite, symmetric and contain no rotations, any more. This can be seen by performing the spectral decomposition of the deformation gradient, but this is out of the scope of this treatise and the reader is referred to the specific literature. Further on, these tensors are called stretch tensors. By subtracting

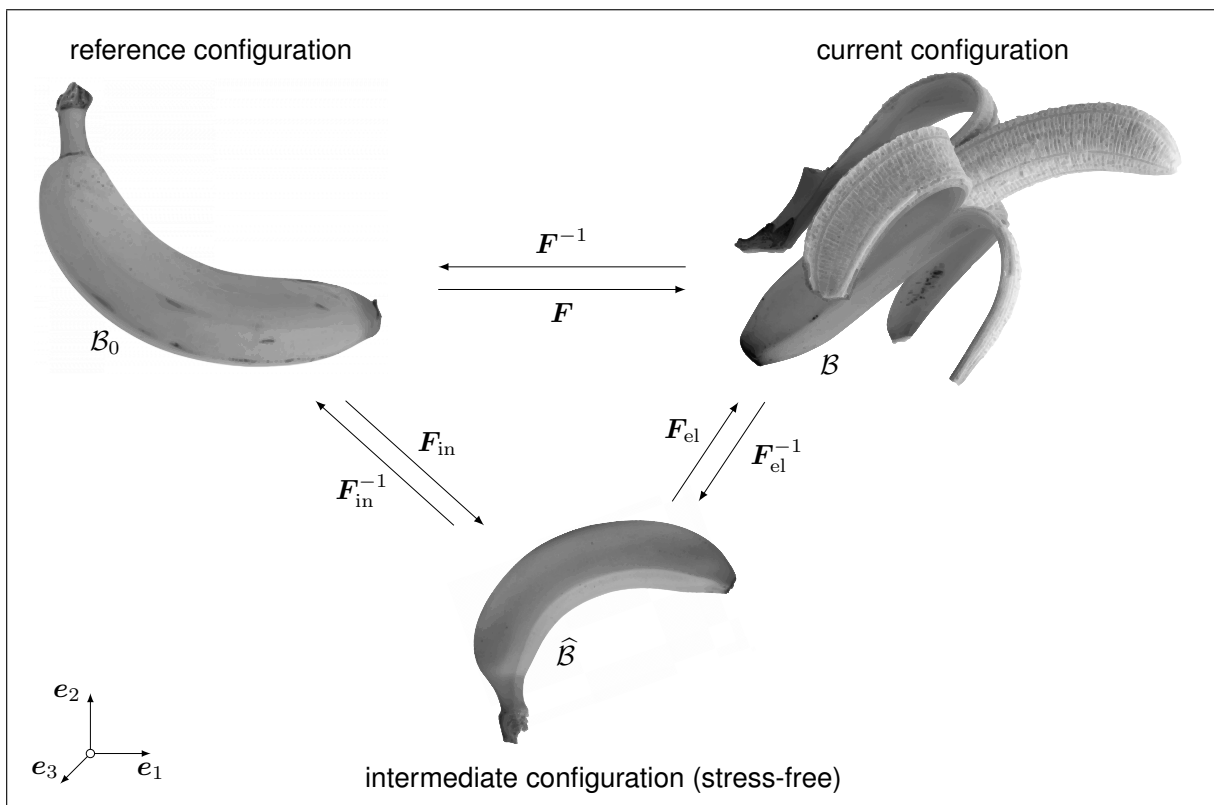


Figure 4.2: Multiplicative split of the deformation gradient

the identity tensor $\mathbf{1}$ from the left or right CAUCHY-GREEN tensor, respectively, stretch tensors these tensors are transformed to strain tensors. However, this is not a strain tensor like the e.g. GREEN-LAGRANGE strain tensor. No common strain tensors are introduced in this work since they are not suitable for fracture mechanical analyses, as stated earlier. For this reason the right and left CAUCHY-GREEN tensors are used to formulate the constitutive laws.

At last, the transformation of an infinitesimal volume or area element between reference and current configuration is required. This is also done through the deformation gradient. The infinitesimal volume is transformed with

$$dV = J dV_0 \quad (4.12)$$

and the infinitesimal area with

$$\mathbf{n}_{\partial\mathcal{B}} dA = J \mathbf{F}^{-\top} \cdot \mathbf{n}_{\partial\mathcal{B}_0} dA_0. \quad (4.13)$$

4.2 Kinetics

The analysis of a body in continuum mechanics is usually done in the current configuration by applying the cut principle. "*The material body is separated from its environment, while the ambient influences are represented by forces and moments.*" [90]. Figure 4.3 illustrates this principle. Due to the cutting the body is separated into two parts, \mathcal{B}_+ and \mathcal{B}_- . For the interaction of these two parts a surface force vector $\Delta \mathbf{f}$ has to be introduced on each surface. Relating this surface force vector to the surface area yields in the limiting case the stress vector, which acts on the surface.

$$\mathbf{t} = \lim_{\Delta A \rightarrow 0} \frac{\Delta \mathbf{f}}{\Delta A} \quad (4.14)$$

The stress vectors acting on the body parts \mathcal{B}_+ and \mathcal{B}_- have the same magnitude but a reverse orientation (actio = reactio), hence,

$$\mathbf{t}_+ + \mathbf{t}_- = \mathbf{o} \quad (4.15)$$

holds true. Further on, it is assumed that $\Delta \mathbf{f}$ is a smooth function. Up next, a relation between the stress vector and the surface orientation, characterised by the surface normal vector, is required. CAUCHY proves (for some assumptions) a linear relationship between these two quantities.

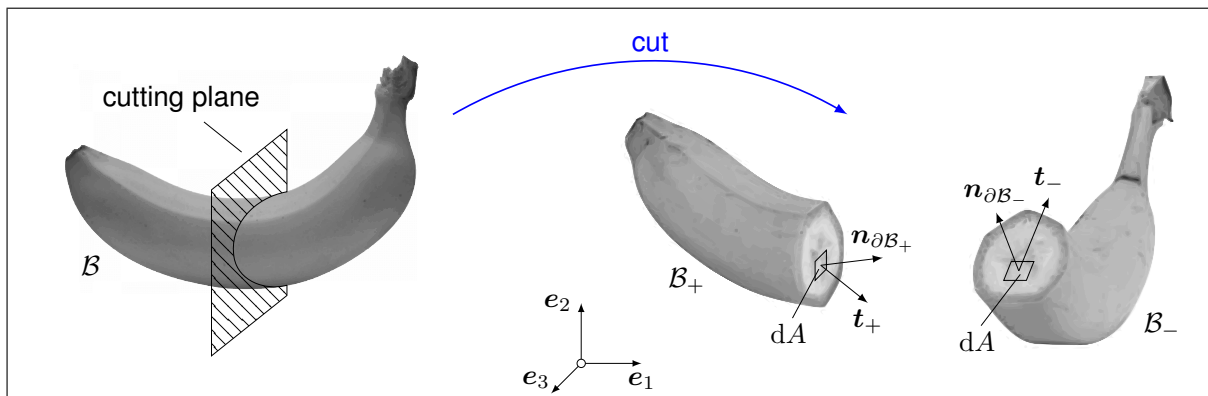


Figure 4.3: Arbitrary body with cutting plane with resulting stress and normal vectors

$$\mathbf{t} = \mathbf{n}_{\partial\mathcal{B}} \cdot \mathbf{T} = \mathbf{T} \cdot \mathbf{n}_{\partial\mathcal{B}} \quad \Longleftrightarrow \quad \mathbf{t}_{+/-} = \mathbf{n}_{\partial\mathcal{B}_{+/-}} \cdot \mathbf{T} = \mathbf{T} \cdot \mathbf{n}_{\partial\mathcal{B}_{+/-}} \quad (4.16)$$

In Eq. (4.16) \mathbf{T} is the CAUCHY stress tensor which is a two-field-tensor with both indexes in the current configuration, also, this stress tensor is sometimes called "true stress". From the balance of angular momentum results that this stress tensor is symmetric (cf. Chap. 4.3.3). Since it is difficult to measure the actual area in an experiment another stress tensor is introduced which relates the actual force to the reference area ΔA_0 .

$$\mathbf{t} = \lim_{\Delta A_0 \rightarrow 0} \frac{\Delta \mathbf{f}}{\Delta A_0} \quad (4.17)$$

Referring to Eq. (4.16) it is possible to formulate a similar equation with the normal vector of the reference configuration $\mathbf{n}_{\partial\mathcal{B}_0}$ and the first PIOLA-KIRCHHOFF stress tensor.

$$\mathbf{t} = \overset{\text{PK}}{\mathbf{T}} \cdot \mathbf{n}_{\partial\mathcal{B}_0} \quad (4.18)$$

The first PIOLA-KIRCHHOFF stress tensor is a two-field-tensor like the deformation gradient. One index refers to the current and the other to the reference configuration. This stress tensor is called "engineering" or "nominal" stress tensor, as well. With Eq. (4.13) and the symmetry of the CAUCHY stress tensor it is possible to derive a relation between the CAUCHY and the first PIOLA-KIRCHHOFF stress tensor. This relation is

$$\overset{\text{PK}}{\mathbf{T}} = J \mathbf{T} \cdot \mathbf{F}^{-\top}. \quad (4.19)$$

Last required stress measure for this work is the KIRCHHOFF stress which is the product of J and the CAUCHY stress

$$\overset{\text{K}}{\mathbf{T}} = J \mathbf{T}. \quad (4.20)$$

These measures are used independently for different FE equations.

4.3 Balance Laws & Entropy Inequality

In the foregoing sections the kinematic and kinetic relations are derived. These relations are used in this section to formulate the equations of balance and the entropy inequality, which provide the basic equations, relations and restrictions of a model of continuum mechanics. All equations are formulated in the current configuration and for the whole body, whereby, it is pos-

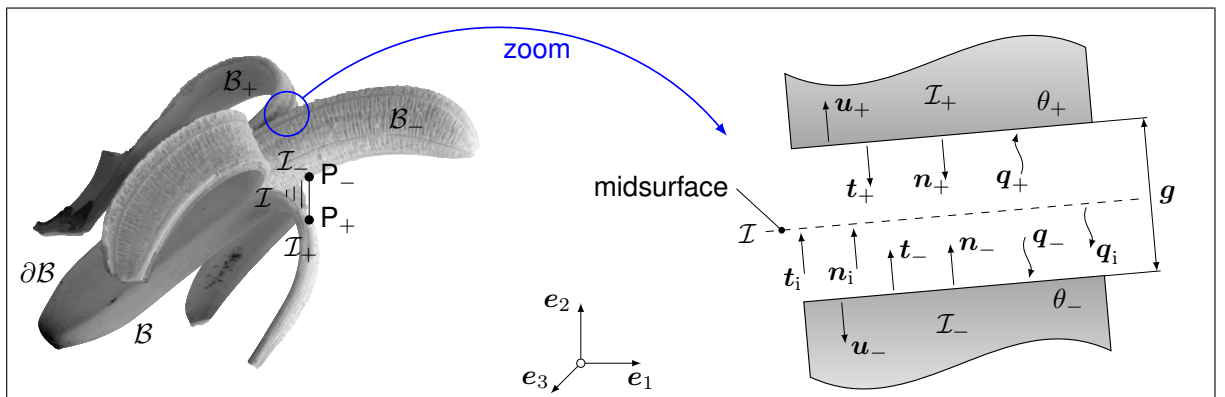


Figure 4.4: Partitioning of an arbitrary body with a zero-thickness interface and introduction of the quantities acting on the interface

sible to localise them under the assumption that each material point shows the same behaviour as the neighbouring points. This assumption is very crucial and questionable in the sense of fracture mechanics (CZMs in this treatise), however, it is a common procedure in many fields, e.g. CZM, PFM or CDM ([18, 20, 23]). Besides, a new theory was developed in the 1990th from SILLING ([21]) to overcome this assumption, therefore, this will be discussed later. The body \mathcal{B} with a zero-thickness interface \mathcal{I} , which is subjected to thermal q_b and mechanical t_b loadings, is presented in Fig. 4.1, already. Now, the current configuration of the body is analysed in detail for the formulation of the equations of balance. This is presented in Figure 4.4. Due to the failure of the interface the body is separated in the parts \mathcal{B}_+ and \mathcal{B}_- , as well as the boundary of the body ($\partial\mathcal{B}_+$ and $\partial\mathcal{B}_-$) and the interface (\mathcal{I}_+ and \mathcal{I}_-). Further on, Fig. 4.4 presents a detailed view on the interface, how the quantities act on the interface surfaces and how they are oriented. For simplifications in the theory, a midsurface is introduced to which all quantities are referred. Last assumption is that the body and the interface are homogeneous and isotropic.

At the beginning of separation the surfaces \mathcal{I}_+ and \mathcal{I}_- are in contact. However, evolving separation leads to failure of this connection and as result a crack starts to propagate along the interface \mathcal{I} . The connection between the interface surfaces \mathcal{I}_+ and \mathcal{I}_- is described by a TSL. Feasible shapes of TSLs are presented in Fig. 3.2 for pure Mode I opening. This TSL is applied to every point P which is placed on the interface to describe crack propagation.

4.3.1 Balance of Mass

It is assumed that the mass of the body \mathcal{B} does not change during loading, thus, it holds true

$$m_0 = m. \quad (4.21)$$

Due to the fact that the interface is of zero-thickness, it has no density, which leads to the conclusion that the interface has no mass and thus, it does not contribute to the overall mass of the complete body. Equation (4.21) is rewritten with the density. It follows

$$\int_{\mathcal{B}_0} \rho_0 \, dV_0 = \int_{\mathcal{B}} \rho \, dV. \quad (4.22)$$

Localisation of Eq. (4.22) and usage of Eq. (4.12) leads to

$$\frac{\rho_0}{\rho} = J. \quad (4.23)$$

Hence, the change of density can be expressed through the determinant of the deformation gradient.

4.3.2 Balance of linear Momentum

"The balance of linear momentum states that the rate of linear momentum of the body equals the resulting force acting on the body." [4]. In integral form it is

$$\underbrace{\int_{\mathcal{B}} \rho \ddot{\mathbf{u}} \, dV}_{\text{bulk}} = \underbrace{\int_{\partial\mathcal{B}} \mathbf{t}_{\partial\mathcal{B}} \, dA + \int_{\mathcal{I}_+} \mathbf{t}_+ \, dA + \int_{\mathcal{I}_-} \mathbf{t}_- \, dA}_{\text{interface}}. \quad (4.24)$$

Body forces are neglected and the last two terms of Eq. (4.24) represent the contributions coming from the interface. With CAUCHY's relation (Eq. (4.16)) and GAUSS divergence theorem

it results

$$\int_{\mathcal{B}} \rho \ddot{\mathbf{u}} \, dV = \int_{\mathcal{B}} \mathbf{T} \cdot \nabla \, dV + \int_{\mathcal{I}_+} \mathbf{t}_+ \, dA + \int_{\mathcal{I}_-} \mathbf{t}_- \, dA, \quad (4.25)$$

and from the force equilibrium of the interface (cf. Fig. 4.4) follows

$$\int_{\mathcal{I}_+} \mathbf{t}_+ \, dA + \int_{\mathcal{I}_-} \mathbf{t}_- \, dA = \mathbf{o}. \quad (4.26)$$

With Eq. (4.26) and localisation of Eq. (4.25) the final form of balance of linear momentum is

$$\rho \ddot{\mathbf{u}} = \mathbf{T} \cdot \nabla. \quad (4.27)$$

Hence, a zero-thickness interface does not influence the balance of linear momentum, since it vanishes for the whole body. This is axiomatic assumed through Eq. (4.26). However, to derive FE equations it is preferable to use Equation (4.25), since this equation is already split up into the different parts of the continuum.

4.3.3 Balance of angular Momentum

The balance of angular momentum states that the rate of angular momentum of the body, with respect to a fixed point Q with the position vector \mathbf{x}_Q , equals the resulting moment of all forces acting on the body [4].

$$\underbrace{\int_{\mathcal{B}} \rho \mathbf{x}_Q \times \ddot{\mathbf{u}} \, dV}_{\text{bulk}} = \underbrace{\int_{\partial \mathcal{B}} \mathbf{x}_Q \times \mathbf{t}_{\partial \mathcal{B}} \, dA + \int_{\mathcal{I}_+} \mathbf{x}_Q \times \mathbf{t}_+ \, dA + \int_{\mathcal{I}_-} \mathbf{x}_Q \times \mathbf{t}_- \, dA}_{\text{interface}} \quad (4.28)$$

Usage of Eq. (4.26) simplifies Eq. (4.28) to

$$\int_{\mathcal{B}} \rho \mathbf{x}_Q \times \ddot{\mathbf{u}} \, dV = \int_{\partial \mathcal{B}} \mathbf{x}_Q \times \mathbf{t}_{\partial \mathcal{B}} \, dA. \quad (4.29)$$

In the next step Eq. (4.27) is multiplied (cross product) with the position vector \mathbf{x}_Q and then subtracted from Equation (4.28). It follows

$$\int_{\mathcal{B}} (\mathbf{x}_Q \times \mathbf{T}) \cdot \nabla - \mathbf{x}_Q \times (\mathbf{T} \cdot \nabla) \, dV = \mathbf{o}. \quad (4.30)$$

This must hold for all bodies, therefore the integrand must be zero [4]. From the product rule follows

$$\mathbf{x}_Q \times \mathbf{T} \cdot \nabla = \mathbf{o}. \quad (4.31)$$

This holds true when the CAUCHY stress tensor \mathbf{T} is symmetric.

$$\mathbf{T} = \mathbf{T}^\top \quad (4.32)$$

More details can be found e.g. in BERTRAM [4]. For polar media a non-symmetric CAUCHY stress tensor results from the balance of angular momentum. Falsely, sometimes this result is called BOLTZMANN axiom. However, this is not correct because the symmetry of the CAUCHY

stress tensor is proven through Eq. (4.31) and not provided axiomatically.

4.3.4 Balance of Energy

The balance of energy or first law of thermodynamics is the fourth equation which is necessary for the formulation of a model in continuum mechanics. It states that the rate of kinetic \dot{E}_{kin} and internal energy \dot{E}_{int} is equal to the mechanical P_{mech} and non-mechanical power P_{non} supplied to a body

$$\dot{E}_{\text{kin}} + \dot{E}_{\text{int}} = P_{\text{mech}} + P_{\text{non}}. \quad (4.33)$$

Whereby, kinetic energy results only from the body because the interface is of zero-thickness.

$$E_{\text{kin}} = \int_{\mathcal{B}} \frac{1}{2} \rho \dot{\mathbf{u}} \cdot \dot{\mathbf{u}} \, dV \quad (4.34)$$

The internal energy is assumed to be the sum of a bulk (index "b") and an interface part (index "i") with the specific internal energy e , cf. [84].

$$E_{\text{int}} = \int_{\mathcal{B}} \rho e_b \, dV + \int_{\mathcal{I}} e_i \, dA \quad (4.35)$$

Additionally, the split into a bulk and an interface part is used for the mechanical and non-mechanical power.

$$P_{\text{mech}} = \int_{\mathcal{B}} \mathbf{T} : \mathbf{L} \, dV + \int_{\mathcal{I}} \mathbf{t}_i \cdot \dot{\mathbf{g}} \, dA \quad (4.36)$$

$$P_{\text{non}} = \int_{\mathcal{B}} \rho r_b - \nabla \cdot \mathbf{q}_b \, dV + \int_{\mathcal{I}} r_i + q_i \, dA, \quad q_i = q_- = -q_+ = -\mathbf{n}_i \cdot \mathbf{q}_i \quad (4.37)$$

In these equations \mathbf{t}_i , \mathbf{q}_i and \mathbf{n}_i are the traction, heat flux and normal vector of the interface which act on the midsurface (cf. Fig. 4.4) and r is a scalar heat supply which is split up, as well. Further on, the heat resulting from each interface surface is defined as:

$$q_+ = -\mathbf{n}_+ \cdot \mathbf{q}_+$$

$$q_- = -\mathbf{n}_- \cdot \mathbf{q}_-$$

Hence, a heat flux pointing from the interface into the bulk increases the energy of the bulk. The separation and the temperature jump of the interface are defined as:

$$\mathbf{g} = \mathbf{u}_+ - \mathbf{u}_- \quad (4.38)$$

$$\Theta = \theta_+ - \theta_- \quad (4.39)$$

Inserting Eqs. (4.34)–(4.37) into Eq. (4.33) and rearrange the terms, final form is derived with one contribution for the bulk material and another one for the interface.

$$\underbrace{\int_{\mathcal{B}} \rho \dot{\mathbf{u}} \cdot \dot{\mathbf{u}} + \rho \dot{e}_b - \mathbf{T} : \mathbf{L} - \rho r_b + \nabla \cdot \mathbf{q}_b \, dV}_{\text{bulk}} + \underbrace{\int_{\mathcal{I}} \dot{e}_i - \mathbf{t}_i \cdot \dot{\mathbf{g}} - r_i - q_i \, dA}_{\text{interface}} = 0 \quad (4.40)$$

Equation (4.40) is the basis to simulate heat conduction (e.g. ABAQUS [60]). Here, it is assumed that the mechanical response will not influence the thermal response and that the bulk

has no internal heat production $r_b = 0$. Heat is only produced due to cracking of the interface which is taken into account by the internal heat production of the interface r_i . For this reasons Eq. (4.40) simplifies to

$$\int_{\mathcal{B}} \rho \dot{e}_b + \nabla \cdot \mathbf{q}_b \, dV + \int_{\mathcal{I}} \dot{e}_i - r_i - q_i \, dA = 0. \quad (4.41)$$

Equation (4.41) is split up into a bulk and an interface portion and then localisation is performed.

$$\begin{aligned} \rho \dot{e}_b + \nabla \cdot \mathbf{q}_b &= 0 \\ \dot{e}_i - r_i - q_i &= 0 \end{aligned} \quad (4.42)$$

4.3.5 Entropy Inequality

In this section the entropy inequality or second law of thermodynamics is derived. This inequality states that entropy production of a process is non-negative. This statement leads to

$$\begin{aligned} 0 &\leq \dot{H}_\eta - \frac{q_\eta}{\theta} \quad \text{with} \\ \frac{q_\eta}{\theta} &= \int_{\mathcal{B}} \rho \frac{r_b}{\theta} \, dV - \int_{\partial \mathcal{B}} \mathbf{n}_{\partial \mathcal{B}} \cdot \left(\frac{\mathbf{q}_b}{\theta} \right) \, dA + \int_{\mathcal{I}} \frac{r_i}{\theta} \, dA + \int_{\mathcal{I}} \frac{q_i}{\theta} \, dA. \end{aligned} \quad (4.43)$$

In this equation H_η is the entropy and $\frac{q_\eta}{\theta}$ is the entropy flux. The entropy is divided into a bulk and an interface part, similar as it is done for the internal energy, with η as the specific entropy

$$H_\eta = \int_{\mathcal{B}} \rho \eta_b \, dV + \int_{\mathcal{I}} \eta_i \, dA. \quad (4.44)$$

By using GAUSS' divergence theorem, the final form is obtained, which is divided into a bulk and an interface part as well.

$$\underbrace{\int_{\mathcal{B}} \rho \dot{\eta}_b - \rho \frac{r_b}{\theta} + \nabla \cdot \left(\frac{\mathbf{q}_b}{\theta} \right) \, dV}_{\text{bulk}} + \underbrace{\int_{\mathcal{I}} \dot{\eta}_i - \frac{r_i}{\theta} - \frac{q_i}{\theta} \, dA}_{\text{interface}} \geq 0 \quad (4.45)$$

Both integrals can be considered independently and then localisation is performed. It follows

$$\begin{aligned} \rho \dot{\eta}_b - \rho \frac{r_b}{\theta} + \nabla \cdot \left(\frac{\mathbf{q}_b}{\theta} \right) &\geq 0, \\ \dot{\eta}_i - \frac{r_i}{\theta} - \frac{q_i}{\theta} &\geq 0. \end{aligned} \quad (4.46)$$

4.4 CLAUSIUS-DUHEM- and Dissipation Inequality

In Sects. 4.3.4 and 4.3.5 the balance of energy and the entropy inequality are derived. Now, these equations are used to derive the CLAUSIUS-DUHEM- and the dissipation inequality. From these the basic relations and restrictions for the constitutive laws for the bulk and the interface material are distilled. Further details of deriving these equations are presented in Appendix A. As a first step, HELMHOLTZ free energy [91] for the bulk and the interface is introduced.

$$\psi_{b/i} = e_{b/i} - \theta \eta_{b/i} \quad (4.47)$$

The time derivative of this variable yields

$$\dot{\psi}_{b/i} = \dot{e}_{b/i} - \dot{\theta} \eta_{b/i} - \theta \dot{\eta}_{b/i}. \quad (4.48)$$

Combining Eqs. (4.40) and (4.45), as well as replacing specific internal energy by HELMHOLTZ free energy and use of the product rule yields the global form of CLAUDIUS-DUHEM inequality

$$\underbrace{\int_{\mathcal{B}} \mathbf{T} : \mathbf{L} - \rho \dot{\psi}_b - \rho \eta_b \dot{\theta} - \frac{1}{\theta} \mathbf{q}_b \cdot (\nabla \theta) \, dV}_{\text{bulk}} + \underbrace{\int_{\mathcal{I}} \mathbf{t}_i \cdot \dot{\mathbf{g}} - \dot{\psi}_i - \eta_i \dot{\theta} \, dA}_{\text{interface}} \geq 0 \quad (4.49)$$

for the bulk and the interface. However, acceleration effects are not considered. The name of Eq. (4.49) was introduced by TRUESDELL [92, 93]. Also, this equation can be localised, and is then split up into the bulk and the interface portion to derive the basic relations for the constitutive laws.

$$0 \leq \mathbf{T} : \mathbf{L} - \rho \dot{\psi}_b - \rho \eta_b \dot{\theta} - \frac{1}{\theta} \mathbf{q}_b \cdot (\nabla \theta) \quad (4.50)$$

$$0 \leq \mathbf{t}_i \cdot \dot{\mathbf{g}} - \dot{\psi}_i - \eta_i \dot{\theta} \quad (4.51)$$

The CLAUDIUS-DUHEM inequality must be fulfilled for any arbitrary process, hence, this equation is the origin of a thermodynamic consistent constitutive model. The next step requires to formulate the dependencies of the HELMHOLTZ free energy. In this work the bulk material depends on the elastic deformation gradient and the temperature

$$\psi_b = f(\mathbf{F}_{el}, \theta), \quad (4.52)$$

and the interface on an elastic separation, a scalar damage variable and the temperature

$$\psi_i = f_{\text{new}}(\mathbf{g}_{el}, d, \theta) \quad (4.53)$$

on the one hand and separation and temperature

$$\psi_i = f_{\text{NEEDLE}}(\mathbf{g}, \theta) \quad (4.54)$$

on the other hand. The elastic separation in Eq. (4.53) is determined through the additive split of the separation vector \mathbf{g} .

$$\mathbf{g} = \mathbf{g}_{el} + \mathbf{g}_{in} \quad (4.55)$$

This accounts for a viscous behaviour of the interface, because the bulk material shows a strong creep behaviour which influences the cohesive zone too. *"In general, the overall rate dependence can arise as a consequence of rate dependence of the bulk material's behaviour, of the interface response itself, or of both."* [94]. Next to that the experiment shows a relaxation behaviour during the delamination process (cf. Chap. 6), which is captured by the inelastic part. Further more, the additive decomposition is valid, although large deformations are considered because metals are investigated. Hence, the deformations at the crack tip and the crack itself keep small. Moreover, the split of separation into elastic and inelastic part acts like a viscous regularisation (cf. [76, 95]) for the numerical solution scheme, later on. Depending on the requirements, it is common to assume that the HELMHOLTZ free energy depends on more quantities, what leads to the concept of internal state variables (cf. COLEMAN & GURTIN [96]). The time derivatives of Eqs. (4.52)–(4.54) are

$$\dot{\psi}_b = \frac{\partial \psi_b}{\partial \mathbf{F}_{el}} : \dot{\mathbf{F}}_{el} + \frac{\partial \psi_b}{\partial \theta} \dot{\theta}, \quad (4.56)$$

$$\dot{\psi}_i = \frac{\partial \psi_i}{\partial \mathbf{g}_{el}} \cdot \dot{\mathbf{g}}_{el} + \frac{\partial \psi_i}{\partial d} \dot{d} + \frac{\partial \psi_i}{\partial \theta} \dot{\theta}, \quad (4.57)$$

$$\dot{\psi}_i = \frac{\partial \psi_i}{\partial \mathbf{g}} \cdot \dot{\mathbf{g}} + \frac{\partial \psi_i}{\partial \theta} \dot{\theta}. \quad (4.58)$$

Equation (4.56) is inserted in Eq. (4.50) and Eqs. (4.57) and (4.58) in Equation (4.51). After some manipulations and rearranging of terms following forms are derived.

$$0 \leq \left[\mathbf{T} \cdot \mathbf{F}_{el}^{-\top} - \rho \frac{\partial \psi_b}{\partial \mathbf{F}_{el}} \right] : \dot{\mathbf{F}}_{el} - \rho \left[\eta_b + \frac{\partial \psi_b}{\partial \theta} \right] \dot{\theta} + \mathbf{T}_d : \mathbf{L}_{in} - \frac{1}{\theta} \mathbf{q}_b \cdot (\nabla \theta) \quad (4.59)$$

$$0 \leq \left[\mathbf{t}_i - \frac{\partial \psi_i}{\partial \mathbf{g}_{el}} \right] \cdot \dot{\mathbf{g}}_{el} - \left[\eta_i + \frac{\partial \psi_i}{\partial \theta} \right] \dot{\theta} + \mathbf{t}_i \cdot \dot{\mathbf{g}}_{in} - \frac{\partial \psi_i}{\partial d} \dot{d} \quad (4.60)$$

$$0 \leq \left[\mathbf{t}_i - \frac{\partial \psi_i}{\partial \mathbf{g}} \right] \cdot \dot{\mathbf{g}} - \left[\eta_i + \frac{\partial \psi_i}{\partial \theta} \right] \dot{\theta} \quad (4.61)$$

Equations (4.59)–(4.61) are the final forms with the dissipative stress tensor \mathbf{T}_d and the inelastic velocity gradient \mathbf{L}_{in} defined as:

$$\mathbf{T}_d = \mathbf{F}_{el}^{\top} \cdot \mathbf{T} \cdot \mathbf{F}_{el}^{-\top} \quad (4.62)$$

$$\mathbf{L}_{in} = \dot{\mathbf{F}}_{in} \cdot \mathbf{F}_{in}^{-1} \quad (4.63)$$

Equations (4.59)–(4.61) must be fulfilled for any arbitrary process, thus, it follows directly the relation for the stress tensor and the traction vector (Eq. (4.65) for the novel TSL of Sect. 5.2.2 and Eq. (4.66) for the TSL of Sect. 5.2.1)

$$\mathbf{T} = \rho \frac{\partial \psi_b}{\partial \mathbf{F}_{el}} \cdot \mathbf{F}_{el}^{\top}, \quad (4.64)$$

$$\mathbf{t}_i = \frac{\partial \psi_i}{\partial \mathbf{g}_{el}}, \quad (4.65)$$

$$\mathbf{t}_i = \frac{\partial \psi_i}{\partial \mathbf{g}} \quad (4.66)$$

plus the relations for the specific entropies

$$\eta_b = - \frac{\partial \psi_b}{\partial \theta}, \quad (4.67)$$

$$\eta_i = - \frac{\partial \psi_i}{\partial \theta} \quad (4.68)$$

of the bulk and the interface portion. Further on, these results are a consequence of the rate independence of Eqs. (4.52)–(4.54). For further informations it is referred to [35]. What remains is the dissipation inequality of the bulk

$$0 \leq \mathbf{T}_d : \mathbf{L}_{in} - \frac{1}{\theta} \mathbf{q}_b \cdot (\nabla \theta), \quad (4.69)$$

and the interface portion

$$0 \leq \mathbf{t}_i \cdot \dot{\mathbf{g}}_{in} - \frac{\partial \psi_i}{\partial d} \dot{d}. \quad (4.70)$$

Equations (4.64)–(4.70) are the basis to formulate constitutive laws and evolution equations for all variables. This is explained in the following chapter.

5 Constitutive Laws

This chapter presents the basics how constitutive laws are derived and what constitutive laws are used in this work, as it is mentioned in Chapter 3. The starting points are Eqs. (4.64)–(4.70). At first, derivation of constitutive laws of the bulk material is explained and then the derivation of the interface constitutive laws.

5.1 Bulk Constitutive Laws

In this work the bulk material consists of two different materials. This is explained in detail in Chapter 2. However, one of these materials behaves purely elastic and the other one shows an inelastic behaviour. Further on, both materials are compressible, assumed to be homogeneous and isotropic, and the material properties differ only slight. Therefore, the same constitutive law is applied, once without and once with an inelastic portion. To consider large deformations it is directly worked with the deformation gradient (Eq. (4.5)) and the multiplicative split of this one (Eq. (4.8)). The explanation for consideration of large deformations is given in Chap. 2 as well. It is begun with Eq. (4.52) which is additively split up into a mechanical and a thermal part,

$$\psi_b = \psi_b^{\text{mech}}(\mathbf{F}_{\text{el}}) + \psi_b^{\text{therm}}(\theta) \quad (5.1)$$

whereby the mechanical part still depends on the temperature, because of the elastic properties. However, this will not influence the thermal response (as it is assumed in the balance of energy (cf. Sect. 4.3.4) and vice versa). Inserting Eq. (5.1) into Eq. (4.64) leads to

$$\mathbf{T} = \rho \frac{\partial \psi_b^{\text{mech}}}{\partial \mathbf{F}_{\text{el}}} \cdot \mathbf{F}_{\text{el}}^{\top} \quad (5.2)$$

for the stress and insertion into Eq. (4.67) to

$$\eta_b = - \frac{\partial \psi_b^{\text{therm}}}{\partial \theta} \quad (5.3)$$

for the entropy. At first, the mechanical part of HELMHOLTZ free energy is defined and later on the thermal part. For the formulation of a constitutive law it is necessary to satisfy four principles according to BERTRAM [3] or TRUESDELL & NOLL [97]. These are:

1. Principle of determinism for thermo-mechanical materials
"The state of a material point is determined from the present and the past but not from the future."
2. Principle of local action for simple thermo-mechanical materials
"The state of a material point depends only on the infinitesimal neighbourhood."
3. Principle of material objectivity for thermo-mechanical materials
"The total dissipation of all materials is invariant under EUKLIDIAN transformations."
4. Principle of invariance under superimposed rigid body motions for thermo-mechanical simple materials
"The state of a material is not changing under rigid body transformations."

Since the elastic deformation gradient contains rigid body rotations, it is necessary to reformulate Eq. (5.2) to fulfil the fourth principle. With the use of Eq. (4.23) it follows

$$\mathbf{T} = \frac{2}{J} \frac{\partial \rho_0 \psi_b}{\partial \mathbf{B}_{el}} \cdot \mathbf{B}_{el}. \quad (5.4)$$

The transformation of the density with the determinant of the deformation gradient is possible because the inelastic deformation should be isochoric ($J_{in} = 1$). This leads to

$$J = J_{el}. \quad (5.5)$$

A detailed explanation how Eq. (5.4) is derived is given in Appendix A. As a consequence of these four principles and the aforementioned assumptions the CIARLET-GEYMONAT [98] strain energy potential is chosen which is based on the left CAUCHY-GREEN tensor. Another reason is the unbounded poly-convexity of this potential, as long as POISSON'S ratio $\nu > 0$ holds true [99]. The potential is formulated with respect to the first and third invariant of the left CAUCHY-GREEN tensor, and with LAMÉ'S constants λ and μ . Due to the usage of the left CAUCHY-GREEN tensor the second invariant vanishes in the potential. The LAMÉ'S constants are defined as

$$\lambda = \frac{E\nu}{(1-2\nu)(1+\nu)} \quad \text{and} \quad \mu = \frac{E}{2(1+\nu)} \quad (5.6)$$

wherein, E represents the YOUNG'S modulus. Moreover, the potential is transformed to the elastic part of the left CAUCHY-GREEN tensor \mathbf{B}_{el} . It is

$$\rho_0 \psi_b^{\text{mech}} = \frac{\lambda}{4} [III_{\mathbf{B}_{el}} - \ln(III_{\mathbf{B}_{el}}) - 1] + \frac{\mu}{2} [I_{\mathbf{B}_{el}} - \ln(III_{\mathbf{B}_{el}}) - 3]. \quad (5.7)$$

Hence, it results the formulation for the CAUCHY stress tensor from Eq. (5.4)

$$\mathbf{T} = \frac{1}{J} \left[\frac{\lambda}{2} (J^2 - 1) \mathbf{1} + \mu (\mathbf{B}_{el} - \mathbf{1}) \right], \quad (5.8)$$

the dissipative stress tensor from Eq. (4.62)

$$\mathbf{T}_d = \frac{1}{J} \left[\frac{\lambda}{2} (J^2 - 1) \mathbf{1} + \mu (\mathbf{C}_{el} - \mathbf{1}) \right], \quad (5.9)$$

the first PIOLA-KIRCHHOFF stress tensor from Eq. (4.19)

$$\mathbf{T}^{\text{PK}} = \frac{\lambda}{2} (J^2 - 1) \mathbf{F}^{-\top} + \mu (\mathbf{F} \cdot \mathbf{C}_{in}^{-1} - \mathbf{F}^{-\top}), \quad (5.10)$$

and the KIRCHHOFF stress tensor from Eq. (4.20)

$$\mathbf{T}^{\text{K}} = \frac{\lambda}{2} (J^2 - 1) \mathbf{1} + \mu (\mathbf{F} \cdot \mathbf{C}_{in}^{-1} \cdot \mathbf{F}^{\top} - \mathbf{1}). \quad (5.11)$$

The constitutive law for a pure elastic material can be derived from Eqs. (5.10) and (5.11) with the assumption that no inelastic deformation occurs $\mathbf{F}_{in} = \mathbf{1}$. Up next, Eq. (4.69) (dissipation inequality) is used to derive an evolution equation for the inelastic deformation gradient and an equation for the heat flux vector. At first, the inelastic evolution equation is derived. One assumption is that the evolution equation can be multiplicative split up into one part depending on the stress tensor and another part accounting for the temperature dependence. Further on, the inelastic deformation should be isochoric ($J_{in} = 1$), which is a common assumption for creep deformations of metals (cf. ODQVIST [34]). The time derivative of the determinant of the inelastic deformation gradient yields

$$\frac{\partial J_{\text{in}}}{\partial t} = \text{tr}(\mathbf{L}_{\text{in}}) = 0. \quad (5.12)$$

Hence, the inelastic velocity gradient should be a tensor of deviatoric type. However, a dependence onto the hydrostatic part of the stress tensor is still possible and not omitted through Eq. (5.12). An example for a theory, that uses an inelastic deformation based on the hydrostatic part of the stress tensor is non-associated plastic flow based on MOHR-COULOMB yielding. Due to the fact that metals are investigated this is not required, thus, the inelastic velocity gradient depends only on the deviatoric part of the dissipative stress tensor. Much more, we perform the multiplicative split of the inelastic velocity gradient into a stress and a temperature dependent function (cf. [35]). It results

$$\mathbf{L}_{\text{in}} = f_{\text{T}}(\overline{\mathbf{T}}_{\text{d}}) f_{\theta}(\theta). \quad (5.13)$$

Further more, the first function should be of power-law type and the second is the ARRHENIUS function with the activation energy Q and the universal gas constant R , which was redefined in 2019 and has the value $R = 8.31446261815324 \text{ J/K mol}$ [100]. Other dependencies are possible as well (cf. [101]), but this assumption is sufficient to model the inelastic behaviour of the material, which is used in this work (cf. Chap. 9). It results

$$\mathbf{L}_{\text{in}} = a_{\text{b}} \left[\frac{T_{\text{vM}}}{T_{\text{b0}}} \right]^{N_{\text{b}}} \frac{\overline{\mathbf{T}}_{\text{d}}}{T_{\text{vM}}} \exp\left(-\frac{Q}{R\theta}\right). \quad (5.14)$$

Also, this equation implies that the exponent N_{b} does not depend on the temperature. This is a suitable assumption for metals (cf. [34]). Keep in mind that this evolution equation is not valid when an extreme BAUSCHINGER effect occurs which leads to a flow against the stress [102]. The plastic dissipation gets negative in this case. From Eq. (4.63) the final form is obtained.

$$\dot{\mathbf{F}}_{\text{in}} = \mathbf{L}_{\text{in}} \cdot \mathbf{F}_{\text{in}} \quad (5.15)$$

In contrast to other authors, e.g. [18, 35], no dissipative potential is defined and used to derive the evolution equation. This often applied procedure is omitted because we simply adopt NORTON's law (cf. ODQVIST [34]) and extend it only to large deformations. The deviatoric part of the dissipative stress tensor follows from the additive split

$$\mathbf{T}_{\text{d}} = \check{\mathbf{T}}_{\text{d}} + \overline{\mathbf{T}}_{\text{d}}, \quad (5.16)$$

wherein, volumetric and deviatoric part are defined as

$$\check{\mathbf{T}}_{\text{d}} = \frac{\text{tr}(\mathbf{T}_{\text{d}})}{3} \mathbf{1} \quad \text{and} \quad \overline{\mathbf{T}}_{\text{d}} = \mathbf{T}_{\text{d}} - \frac{\text{tr}(\mathbf{T}_{\text{d}})}{3} \mathbf{1}, \quad (5.17)$$

and the equivalent stress in Eq. (5.14) is the VON MISES stress, which is defined as

$$T_{\text{vM}} = \sqrt{\frac{3}{2} \overline{\mathbf{T}}_{\text{d}} : \overline{\mathbf{T}}_{\text{d}}}. \quad (5.18)$$

The symmetric dissipative stress tensor leads to a symmetric inelastic velocity gradient. With this at hand, the mechanical part is completely determined and the first term of Eq. (4.69) is fulfilled. Up next the second term of Eq. (4.69) has to be fulfilled too. This is possible by using FOURIER's law ([103]).

$$\mathbf{q}_{\text{b}} = -\kappa_{\text{b}} (\nabla \theta) \quad (5.19)$$

Hence, the dissipation inequality is fulfilled and the thermal part can be specified. In this work

the thermal part is chosen in that way, that heat capacity c_b is a linear function of temperature ($c_b = C_{b1}\theta + C_{b2}$). This is done due to the fact that for metals thermal material parameters (heat capacity, thermal expansion, density, etc.) depend linear on the temperature in the range from room to near melting temperature, approximately [104, 105]. By integrating this function with the relation

$$c_b = -\theta \frac{\partial^2 \psi_b^{\text{therm}}}{\partial \theta^2} \quad (5.20)$$

one gets following thermal part of HELMHOLTZ free energy

$$\psi_b^{\text{therm}} = C_{b2}(\theta - \theta_0) - \frac{C_{b1}}{2}(\theta^2 + \theta_0^2) + C_{b1}\theta\theta_0 - C_{b2}\theta \ln\left(\frac{\theta}{\theta_0}\right). \quad (5.21)$$

Herein, θ_0 is the reference temperature. Equation (5.20) can be derived when the internal energy in Eq. (4.42) is replaced by Equation (4.48). This is not presented here, because the balance of energy is used in the form of Equation (4.42). The entropy follows from Eq. (5.3) and with Eq. (5.21) to

$$\eta_b = C_{b1}(\theta - \theta_0) + C_{b2} \ln\left(\frac{\theta}{\theta_0}\right). \quad (5.22)$$

The internal energy results from Eq. (4.47) as

$$e_b = \frac{C_{b1}}{2}(\theta^2 - \theta_0^2) + C_{b2}(\theta - \theta_0), \quad (5.23)$$

and this leads to the linear dependence of heat capacity with the relation

$$c_b = \frac{\partial e_b}{\partial \theta}, \quad (5.24)$$

also.

5.2 Interface Constitutive Laws

The interface constitutive laws are derived differently. For the cracking of the coating a common TSL is used without the additive split of the separation vector (Eq. (4.55)). In contrast, the TSL to describe the delamination of the coating from the substrate is derived according to the procedure of the foregoing section. However, in both cases the HELMHOLTZ free energy is additive split up into a mechanical and a thermal part.

$$\psi_i = \psi_i^{\text{mech}}(\mathbf{g}_{\text{el}}, d) + \psi_i^{\text{therm}}(\theta) \quad \vee \quad \psi_i = \psi_i^{\text{mech}}(\mathbf{g}) + \psi_i^{\text{therm}}(\theta) \quad (5.25)$$

Inserting Eq. (5.25) into Eq. (4.65) or Eq. (4.66) leads to

$$\mathbf{t}_i = \frac{\partial \psi_i^{\text{mech}}}{\partial \mathbf{g}_{\text{el}}} \quad \vee \quad \mathbf{t}_i = \frac{\partial \psi_i^{\text{mech}}}{\partial \mathbf{g}} \quad (5.26)$$

for the traction. The derivation for the thermal quantities differs slightly from the procedure for the bulk part. First of all, the thermal quantities entropy, internal energy and heat capacity depend on the temperature jump (cf. Eq. (4.39)) and second, the parameters of the interface (maximum separation, maximum traction, etc.) do not depend on the temperature directly. They depend on the interface temperature which is determined as the mean value of the tempera-

tures of the interface surfaces.

$$\theta_i = \frac{1}{2}(\theta_+ + \theta_-). \quad (5.27)$$

Due to the heat supply and the change of heat conductivity in the interface caused by cracking, the temperature on the interface surfaces changes. This is shown in Figure 5.1. The thermal potential is defined in that fashion, that the heat conduction of the body is not influenced or disturbed by the interface, as long as, the interface is not damaged or no temperature jump exists. However, heat capacity of the interface should be a constant function ($c_i = C_{i1}$). This is assumed, because it is not possible to split up the interface contribution of the balance of energy into two parts when the weak form of this equation is derived, otherwise. More details are given in Section 6.2. Therefore, the following potential is chosen.

$$\psi_i^{\text{therm}} = (C_{i1} - C_{i2})\Theta - C_{i1}\Theta \ln(\Theta) \quad (5.28)$$

Further on, the derived relations for the thermal properties are all transformed to the temperature jump. From Eq. (4.68) results

$$\eta_i = -\frac{\partial \psi_i^{\text{therm}}}{\partial \theta} = -\frac{\partial \psi_i^{\text{therm}}}{\partial \Theta} \quad (5.29)$$

for the entropy and

$$c_i = -\theta \frac{\partial^2 \psi_i^{\text{therm}}}{\partial \theta^2} = -\Theta \frac{\partial^2 \psi_i^{\text{therm}}}{\partial \Theta^2} \quad (5.30)$$

for the heat capacity. As well, heat capacity can be determined from the internal energy with

$$c_i = \frac{\partial e_i}{\partial \theta} = \frac{\partial e_i}{\partial \Theta}. \quad (5.31)$$

Using Eq. (5.28) and Eq. (5.29) leads to

$$\eta_i = C_{i1} \ln(\Theta) + C_{i2} \quad (5.32)$$

for the entropy and from Eq. (4.47) results the function for the internal energy.

$$e_i = C_{i1} \Theta \quad (5.33)$$

By utilising Eq. (5.30) or Eq. (5.31) it can be proven that a constant heat capacity is achieved from the thermal potential, defined in Equation (5.28). For heat conduction through the inter-

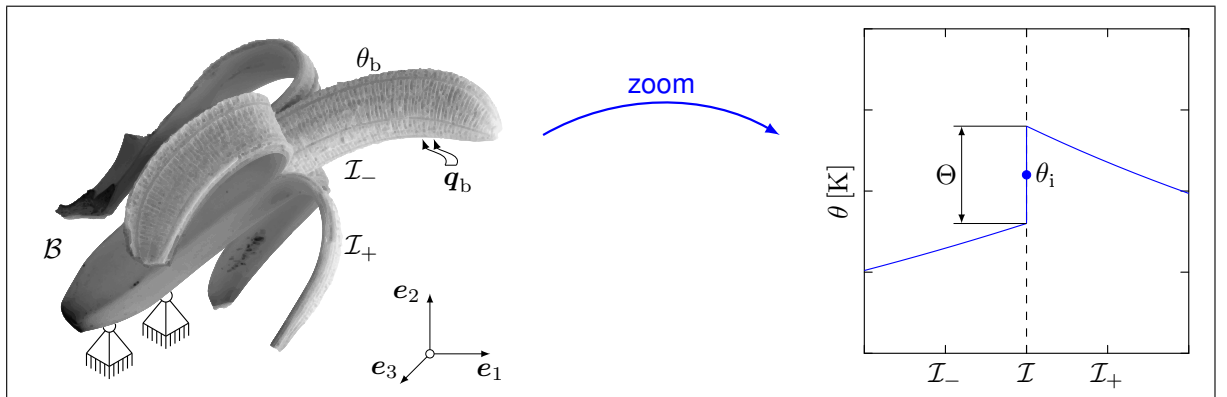


Figure 5.1: Temperature jump across a zero-thickness interface

face a simple model is defined, which is similar to the model used in [84]. The heat, conducted through the interface surfaces q_i , is based on a scalar thermal conductivity (isotropy is assumed) and the temperature jump. Moreover, heat conduction in the normal direction dominates the conduction process through the interface, compared to the tangential direction (cf. [106]). With these assumptions following scalar equation for heat conduction through the interface is defined.

$$q_i = \frac{\kappa_i}{g_{\text{con}}} (\theta_+ - \theta_-) = \frac{\kappa_i}{g_{\text{con}}} \Theta \quad (5.34)$$

The length scale g_{con} in Eq. (5.34) is set to the value of g_{cr} or g_{del} . The choice depends on the TSL. This formulation guarantees that heat conduction through the body is not influenced by the interface without a temperature jump. The same assumption as for the thermal potential. Further on, the interface conductivity is based on the scalar damage variable of the interface.

$$\kappa_i = d\kappa_{\text{air}} + (1 - d)\kappa_b \quad (5.35)$$

As long as the interface is undamaged, the interface behaves like the bulk to conduct heat. However, up to the onset of failure of the interface the heat conductivity starts to change from the value of the bulk to the value of the surrounding medium (which is air in this work). Although, the conductivity of air compared to that one of metals is negligibly $\kappa_{\text{air}} = 0$. The length scale g_{con} is introduced for dimension purposes, because without this factor q_i would be of dimension W/mm , however, the dimension of q_i is W/mm^2 . A similar correction has to be applied to heat capacity for dimension purposes, as well.

The heat supply (of the interface) in the balance of energy results from the failure of the interface. For this reason it is assumed that the heat supply r_i depends on the damage variable, only. As long as, the damage growth the heat supply increases exponentially, however, for total failure of the interface ($d = 1$) the heat supply is zero. This correlation is expressed through the function

$$r_i = a_d (1 - d)^2 [\exp(k_d d) - 1] \quad (5.36)$$

with the two parameters a_d and k_d . The function is based on the measurements of [107]. In this work the heat production around a crack tip is measured. Parameter a_d influences only the maximum of the function and is therefore of no concern, for now. In contrast, parameter k_d influences the shape of the function. Figure 5.2 on the left-hand-side presents the shape of the heat supply function r_i for different values of k_d and $a_d = 1 \text{ W}/\text{mm}^2$. To compare the introduced

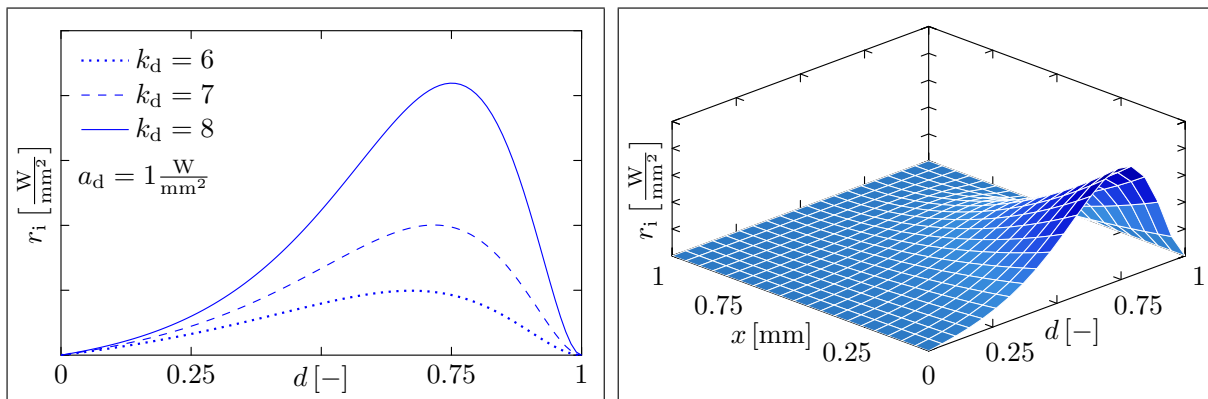


Figure 5.2: Plot of heat supply function of the interface for different values of k_d (left-hand-side) and evolution of heat supply at a crack tip (right-hand-side)

function to the work of [107] we perform a theoretical experiment. Think of an undamaged material in which a crack starts to evolve and consequently, propagates through the material. The crack is described by a coordinate x , which starts at the crack tip ($x = 0\text{mm}$). Now, damage evolves and the crack propagates. The resulting distribution of the heat supply around the crack tip is visualised in Fig. 5.2 on the right-hand-side. To conclude, the defined function gives a suitable approximation of the heat supply in the vicinity of a crack tip.

5.2.1 Cohesive Zone Model for Cracking of the Coating

The first interface constitutive law or TSL which is used is the polynomial TSL of NEEDLEMAN [67], but it is used in the form of SCHEIDER [108], because the orientation of the traction vector in this work is vice versa to the orientation defined in [67]. Originally, this law is defined to describe the failure of plastically deforming solids, including structural metals and composites through void nucleation [67]. Here, this potential is used because it allows to simulate the increasing of the test force after the coating of the specimen has failed (cf. Fig. 2.5). Further details concerning this topic can be found in [109]. The potential from which the traction relations are derived takes the form

$$\begin{aligned} \psi_i^{\text{mech}} = \frac{27}{4} T_{\text{max}} g_{\text{cr}} \left[\right. & \frac{1}{2} \left(\frac{g_{\text{n}}}{g_{\text{cr}}} \right)^2 \left(1 - \frac{4}{3} \frac{g_{\text{n}}}{g_{\text{cr}}} + \frac{1}{2} \left(\frac{g_{\text{n}}}{g_{\text{cr}}} \right)^2 \right) \\ & + \frac{\beta}{2} \left(\frac{g_{\text{t1}}}{g_{\text{cr}}} \right)^2 \left(1 - 2 \frac{g_{\text{n}}}{g_{\text{cr}}} + \left(\frac{g_{\text{n}}}{g_{\text{cr}}} \right)^2 \right) \\ & \left. + \frac{\beta}{2} \left(\frac{g_{\text{t2}}}{g_{\text{cr}}} \right)^2 \left(1 - 2 \frac{g_{\text{n}}}{g_{\text{cr}}} + \left(\frac{g_{\text{n}}}{g_{\text{cr}}} \right)^2 \right) \right] \end{aligned} \quad (5.37)$$

with g_{n} as the normal, g_{t1} as the first and g_{t2} as the second tangential separation. g_{cr} is the maximum separation and the parameter β is the shear stiffness, although, the influence of this parameter onto the shape of the TSL is only slight and can be chosen arbitrary. However, it has to be greater than zero, otherwise, the material tangent matrix for the FE implementation is singular. Figure 5.3 presents the TSL for different values of β and maximum separation g_{cr} for the two dimensional case ($g_{\text{t2}} = 0$). From Fig. 5.3 can be clearly seen that the chosen potential has a very dominant tangential (shear) behaviour, which is necessary for the correct simulation of the fracture process. The normal and tangential directions are determined as follows

$$\begin{aligned} g_{\text{n}} &= \mathbf{g} \cdot \mathbf{n}_i, \\ g_{\text{t1}} &= \mathbf{g} \cdot \mathbf{t}_1, \\ g_{\text{t2}} &= \mathbf{g} \cdot \mathbf{t}_2. \end{aligned} \quad (5.38)$$

Equation (5.37) is valid for arbitrary values of g_{n} . Nevertheless, we restrict the usage of Equation (5.37) to cases where $g_{\text{n}} > 0$ holds, hence, no contact occurs. The tractions follow as the derivatives of Eq. (5.37) with respect to normal and tangential separations.

$$T_{\text{n}} = \frac{27}{4} T_{\text{max}} \left[\frac{g_{\text{n}}}{g_{\text{cr}}} \left(1 - 2 \frac{g_{\text{n}}}{g_{\text{cr}}} + \left(\frac{g_{\text{n}}}{g_{\text{cr}}} \right)^2 \right) + \beta \left(\frac{g_{\text{n}}}{g_{\text{cr}}} - 1 \right) \left(\left(\frac{g_{\text{t1}}}{g_{\text{cr}}} \right)^2 + \left(\frac{g_{\text{t2}}}{g_{\text{cr}}} \right)^2 \right) \right] \quad (5.39)$$

$$T_{\text{t1}} = \frac{27}{4} T_{\text{max}} \beta \frac{g_{\text{t1}}}{g_{\text{cr}}} \left(1 - 2 \frac{g_{\text{n}}}{g_{\text{cr}}} + \left(\frac{g_{\text{n}}}{g_{\text{cr}}} \right)^2 \right) \quad (5.40)$$

$$T_{\text{t2}} = \frac{27}{4} T_{\text{max}} \beta \frac{g_{\text{t2}}}{g_{\text{cr}}} \left(1 - 2 \frac{g_{\text{n}}}{g_{\text{cr}}} + \left(\frac{g_{\text{n}}}{g_{\text{cr}}} \right)^2 \right) \quad (5.41)$$

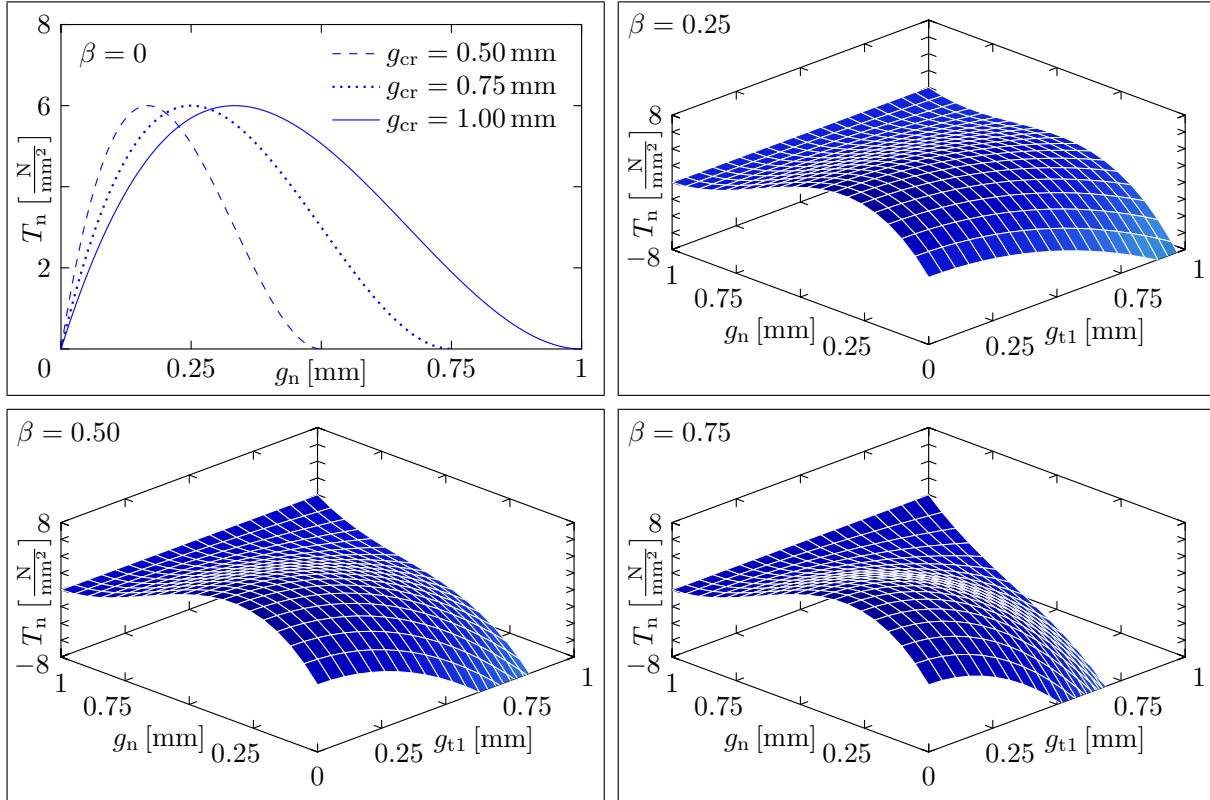


Figure 5.3: Plot of polynomial TSL from NEEDLEMAN for different values of β : pure normal separation with $\beta = 0$ for different values of maximum separation (top, left-hand side), shape of TSL for $g_{cr} = 1$ mm and $\beta = 0.25$ (top, right-hand side), $\beta = 0.50$ (bottom, left-hand side) and $\beta = 0.75$ (bottom, right-hand side)

Under the condition $g_n \leq 0$ contact occurs, which is captured through a linear dependence with a penalised contact stiffness.

$$t_i = C_p g \tag{5.42}$$

The big disadvantage of this model is that it is not able to model unloading of the interface, because it exists no damage variable, which could save the actual damage state before unloading occurs. However, this model is chosen because it has other advantages (e.g. material tangent matrix is smooth, increase in the test force can be simulated, etc.) as figured out in [109] and a damage variable is introduced for the thermal model through the comparison of actual traction value and maximum traction in the softening regime.

5.2.2 Novel Cohesive Zone Model for Delamination of the Coating

As stated in Sect. 4.4 the rate dependent behaviour of the substrate material will influence the fracture process. For this reason the delamination process in this work is not simulated with a common CZM as presented in Fig. 3.2 of Section 3.2. A novel CZM is formulated which is based on the deformation mechanisms of the substrate (creep deformation) and according to the basic principles of continuum mechanics (concept of internal state variables). Besides, this choice is influenced by the works of SONG [61] and MUSTO [94], which had great success by formulating rate dependent CZMs suitable for their specific problems. Further on, only two new parameters are introduced compared to a rate independent CZM, which have to be identified through experiments. Since, all other parameters are set equal one or can be identified from the material parameters of the substrate or of the coating. The mechanical part of HELMHOLTZ free

energy is specified first. This part is formulated as a quadratic function of elastic separation in combination with a degradation function f_d , which is introduced with the effective stress concept (cf. LEMAITRE [19] or KACHANOV [110]).

$$\psi_1^{\text{mech}} = \frac{1}{2} \frac{f_d(d)}{g_{\text{del}}} \mathbf{g}_{\text{el}} \cdot \mathbf{C}_i \cdot \mathbf{g}_{\text{el}} \quad \text{with} \quad f_d(d) = (1 - d)^p \quad (5.43)$$

Dependence of degradation function f_d to parameter p leads to a finite value for the thermodynamic driving Y_E force, when $p > 1$ and $d = 1$ [26]. In this work the parameter is chosen as $p = 2$, thus, the thermodynamic driving force is defined as

$$Y_E = -\frac{\partial \psi_1}{\partial d} = \frac{(1 - d)}{g_{\text{del}}} \mathbf{g}_{\text{el}} \cdot \mathbf{C}_i \cdot \mathbf{g}_{\text{el}}, \quad (5.44)$$

and the traction relation follows from Eq. (5.26) and Eq. (5.43) to

$$\mathbf{t}_i = \frac{(1 - d)^2}{g_{\text{del}}} \mathbf{C}_i \cdot \mathbf{g}_{\text{el}}. \quad (5.45)$$

Therein, the parameter g_{del} is used to normalise the separation, thus, the cohesive zone elasticity \mathbf{C}_i is of dimension MPa (cf. ABAQUS [60]). Last part of the interface model are the evolution equations for the inelastic separation and the damage. To derive these equations Eq. (4.70), the dissipation inequality,

$$0 \leq \mathbf{t}_i \cdot \dot{\mathbf{g}}_{\text{in}} + Y_E \dot{d} \quad (5.46)$$

is used, since this equation must be fulfilled at every time. For inelastic separation a power-law type is defined with extension to damage [111, 112], hence, secondary and tertiary stages of inelastic separation can be described.

$$\dot{\mathbf{g}}_{\text{in}} = \frac{a_i g_{\text{del}}}{(1 - d)} \left[\frac{|\mathbf{t}_i|}{T_{i0}} \right]^{N_i} \frac{\mathbf{t}_i}{|\mathbf{t}_i|} \quad \text{if} \quad |\mathbf{t}_i| > 0 \quad (5.47)$$

Therein, evolution of inelastic separation starts when the EUCLIDIAN norm of the traction vector \mathbf{t}_i is bigger as zero. This equation fulfils Eq. (5.47) because the term $\mathbf{t}_i \cdot \dot{\mathbf{g}}_{\text{in}}$ is always positive or zero.

Damage evolution equation follows from dissipation inequality with the assumption that the damage rate is always positive ($\dot{d} \geq 0$), hence, healing effects of the material are excluded. Next to that damage can only evolve from zero to one. A suitable damage evolution equation which fulfils these criteria and the inequality is

$$\dot{d} = (1 - d) \left(\frac{Y_E - Y_{E0}}{S_{i0}} \right) \frac{|\dot{\mathbf{g}}_{\text{in}}|}{g_{\text{del}}}. \quad (5.48)$$

This form is similar to an evolution equation used by BOUVARD [27]. Damage evolves when the normal separation is positive (no contact), material is under loading, elastic energy release rate is bigger as the threshold Y_{E0} , and an inelastic evolution takes place.

$$g_n > 0, \quad Y_E > Y_{E0}, \quad \dot{Y}_E \geq 0, \quad \dot{\mathbf{g}}_{\text{in}} \neq 0$$

With Eq. (5.47) and Eq. (5.48) each term of the dissipation inequality is fulfilled at every time and consequently the complete dissipation inequality is fulfilled. Under contact ($g_n \leq 0$) Eq. (5.42) is applied as well. Figure 5.4 presents the influence of the most important parameters on the shape of the novel TSL. These parameters are a_i , N_i , S_{i0} and Y_{E0} . For these investigations the

Table 5.1: Initial values of cohesive parameters for parametric study

parameter	g_{del} [mm]	C_p [MPa]	a_i [s ⁻¹]	N_i [-]	T_{i0} [MPa]	S_{i0} [$\frac{N}{mm}$]	Y_{E0} [$\frac{N}{mm}$]
value	1.0	1.0	1.0	2.0	1.0	$1 \cdot 10^{-3}$	0

initial values of the parameters are chosen arbitrary and they are summarised in Table 5.1. Then they are varied one by one under pure Mode I opening. The top, left-hand side diagram of Fig. 5.4 shows the change of shape of the TSL under a variation of the creep factor a_i . An increase of this factor leads to a reduction of the maximum traction of the TSL and a further onset of the damage evolution. However, the influence of a_i is less compared to the influence of N_i , which reduces the maximum traction more drastically if it is increased. This can be seen by comparing range of the axis of top, left-hand side and bottom, right-hand side diagram of Figure 5.4. If the creep parameters are constant and the damage parameter S_{i0} is reduced, the whole TSL reduces, because the damage evolves much faster. But the slope of the TSL is not changed, see Fig. 5.4 the bottom, left-hand side diagram. Due to an increase of the energy release rate threshold, the complete shape of the TSL is changed, as can be seen in Fig. 5.4 on the top, right-hand side diagram.

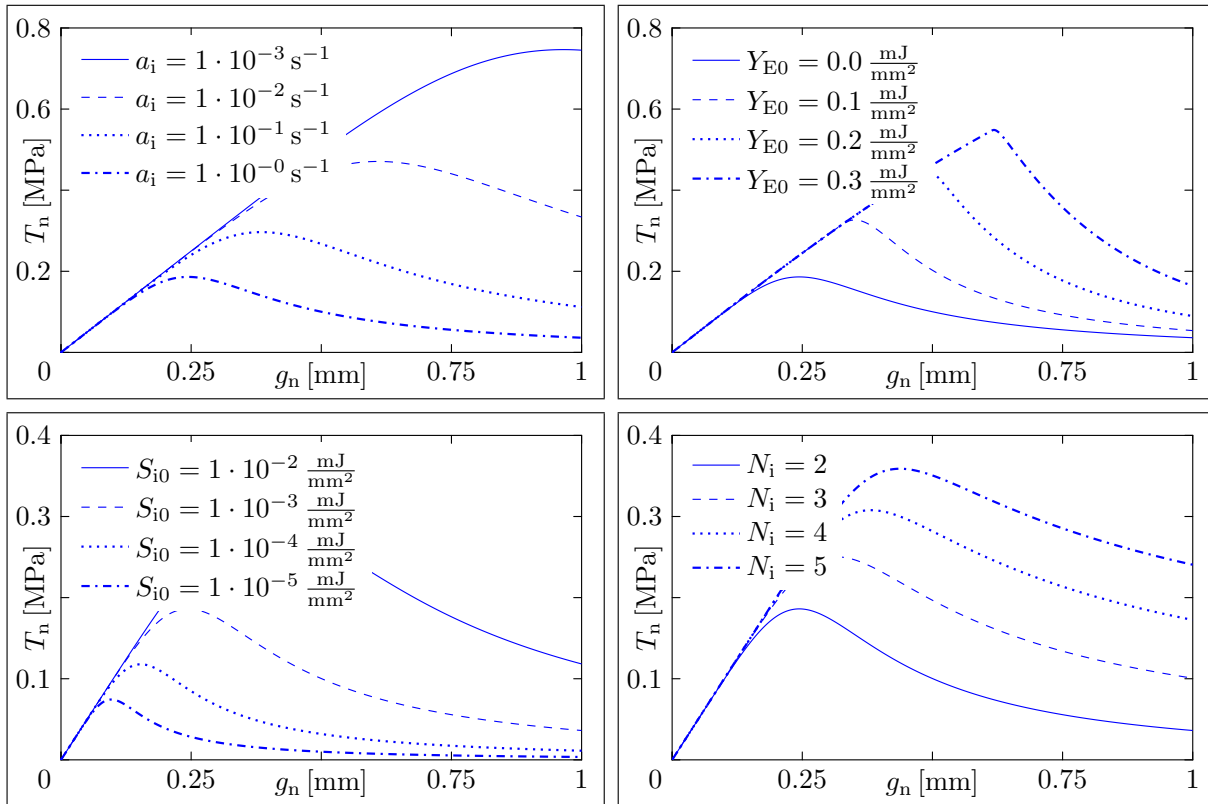


Figure 5.4: Influence of cohesive parameters on the shape of the novel TSL: variation of creep factor (top, left-hand side), variation of elastic energy release rate threshold (top, right-hand side), variation of damage divisor (bottom, left-hand side) and variation of creep exponent (bottom, right-hand side)

5.3 Plane-Strain-State

Commonly, the aim of continuum mechanics is to describe the motion and deformation of an arbitrary body \mathcal{B} in the three-dimensional EUCLIDEAN space \mathbb{E}^3 under given loading and temperature (cf. Chap. 4). However, in general it is not possible to solve the arising system of PDEs without the help of numerical solution schemes like the FEM. But it is more important, that it is not always necessary to solve the full system of PDEs. Often, it is possible to reduce the problem size, because in one or two directions no gradients occur, for example due to the specific boundary conditions or when the extension in this direction is small compared to the other two directions. Examples for such simplifications are the plain-stress-state (PT) and the plain-strain-state (PE). "*Since the "plane case" brings great simplifications of calculation as compared to the general three-dimensional problem and since the plane problems are of a particular interest from the practical and technical standpoints, AIRY's [113] initial results were followed in the last hundred years by extremely numerous works in which a great variety of mathematical methods were used.*" [114]. Here, we restrict ourselves to the PE which yields the deformation gradient

$$\mathbf{F} = F_{ij} \mathbf{e}_i \otimes \mathbf{e}_j + e_3 \otimes e_3 \quad \forall i, j \in \{1, 2\} \quad \iff \quad [F_{ij}] = \begin{bmatrix} F_{11} & F_{12} & 0 \\ F_{21} & F_{22} & 0 \\ 0 & 0 & 1 \end{bmatrix},$$

and the CAUCHY stress tensor

$$\mathbf{T} = T_{ij} \mathbf{e}_i \otimes \mathbf{e}_j + T_{33} \mathbf{e}_3 \otimes \mathbf{e}_3 \quad \forall i, j \in \{1, 2\} \quad \iff \quad [T_{ij}] = \begin{bmatrix} T_{11} & T_{12} & 0 \\ T_{21} & T_{22} & 0 \\ 0 & 0 & T_{33} \end{bmatrix}.$$

in case of isotropy. In this state it is assumed that in the third direction (e_3) no deformation occurs and a stress remains, only. For a PT it is vice versa. The stress T_{33} or deformation F_{33} is calculated afterwards from the constitutive law and not from the balance of linear momentum. Further on, from these results follows that the direction vector of the third direction is the normal vector of the remaining plane problem ($\mathbf{n} = e_3$). Due to the fact that both states are used in continuum mechanics, frequently, and it is not referred to the scientist who introduced these states first, we want to mention some of them to honour their research. The assumptions can be addressed to the works of AIRY [113], MAXWELL [115], LÉVY [116], FLAMANT [117] and GOLOVIN [118] among others (e.g. MICHELL [119], CAROTHERS [120], LOVE [121]). For a deeper insight in the history of the PT and PE the interested reader is referred to the review of P. P. TEODORESCU [114] from 1964.

In this work it is possible to assume a PE, because a 4PBT is analysed. The setup of this experiment is presented in Chapter 2. Since the stress state in the middle of the specimen is analysed, no loading in the direction of e_3 occurs, nor a boundary in this direction exists and the specimen is symmetric with respect to the e_1 – e_2 plane, which leads to a symmetric deformation in e_3 and consequently, no deformation in the middle of the specimen. Therefore, a PE is assumed for the analyses in this work.

Next to these assumptions a PE has one advantage compared to the PT which is explained in detail in [122]. Due to the change from the EUCLIDEAN space \mathbb{E}^3 to a reduced EUCLIDEAN space \mathbb{E}^2 , when using a PT or PE, it is necessary to determine the reduced elasticity tetrad. However, in numerics constitutive laws are used in the displacement controlled form, which requires the correction of the elasticity tetrad in a PT, but not in a PE. To conclude, under a PE Eqs. (5.10) and (5.11) can be used without any correction.

6 Finite Element Method

In general, the solution of Eq. (4.25) and Eq. (4.41) is determined through the use of numerical solution schemes because an exact solution is determinable only for special geometries or loadings. Especially, when the mechanical and the thermal problem are coupled. Commonly, in continuum mechanics the FEM is used to solve the arising system of PDEs. In this chapter the basic FE equations, that have to be solved, are derived, the used element types are explained and features, which are necessary for the solution of the FE equations, in the framework of interface or cohesive elements are explained. For more informations about the presented statements it is referred to ALLIX & CORIGLIANO [63], PARK [68], HOLZAPFEL [83], SCHEIDER [108], WRIGGERS [123] and DHONDT [124]. In this work a thermo-mechanical problem is solved, therefore, two independent variables exist: the displacement \mathbf{u} and the absolute temperature θ . At first, the weak forms of balance of linear momentum and energy are derived and the solution scheme is presented. Then it is necessary to discretise the solution domain. In this section the tensor notation is abandoned and the vector-matrix notation is introduced, as it is common for the FEM. However, it must be remarked that the vector-matrix notation is used without the transformation of second- and fourth-order tensors into six dimensional vectors and matrices, respectively. For example, a fourth-order tensors is transformed into a fourth-order matrix.

6.1 Weak Form of Balance of Linear Momentum

The starting point to derive the weak form of balance of linear momentum is to multiply Eq. (4.25) with the test function $\delta \mathbf{u}$, which is arbitrary, but zero on an area where DIRICHLET boundary conditions are prescribed. In this work the test function is a virtual displacement, another test function would be a virtual velocity $\delta \dot{\mathbf{u}}$. The former test function leads to the principle of virtual work and latter test function to the principle of virtual power in the sense of [4]. Any way, in the literature the principle of virtual power is labelled as principle of virtual work, also (cf. WRIGGERS [123]). Although, in a physical sense the product between force and velocity is power and not work. It follows

$$\int_{\mathcal{B}} \rho \delta \mathbf{u} \cdot \ddot{\mathbf{u}} \, dV = \int_{\mathcal{B}} \delta \mathbf{u} \cdot (\mathbf{T} \cdot \nabla) \, dV + \int_{\mathcal{I}_+} \delta \mathbf{u}_+ \cdot \mathbf{t}_+ \, dA + \int_{\mathcal{I}_-} \delta \mathbf{u}_- \cdot \mathbf{t}_- \, dA. \quad (6.1)$$

Wherein, the test function must be split up on the interface. The product rule of the divergence yields

$$(\delta \mathbf{u} \cdot \mathbf{T}) \cdot \nabla = \mathbf{T} : (\delta \mathbf{u} \otimes \nabla) + \delta \mathbf{u} \cdot (\mathbf{T} \cdot \nabla)$$

and with Eq. (4.26) it is possible to rearrange Eq. (6.1) as follows

$$\int_{\mathcal{B}} \rho \delta \mathbf{u} \cdot \ddot{\mathbf{u}} \, dV + \int_{\mathcal{B}} \mathbf{T} : (\delta \mathbf{u} \otimes \nabla) \, dV + \int_{\mathcal{I}} (\delta \mathbf{u}_- - \delta \mathbf{u}_+) \cdot \mathbf{t}_+ \, dA = \int_{\mathcal{B}} (\delta \mathbf{u} \cdot \mathbf{T}) \cdot \nabla \, dV. \quad (6.2)$$

The right-hand side of Eq. (6.2) can be transformed with GAUSS divergence theorem, the interface traction vector \mathbf{t}_i is introduced (cf. Fig. 4.4) and the symmetry of the CAUCHY stress tensor

is used. It results

$$\int_{\mathcal{B}} \rho \delta \mathbf{u} \cdot \ddot{\mathbf{u}} \, dV + \int_{\mathcal{B}} (\delta \mathbf{u} \otimes \nabla) : \mathbf{T} \, dV + \int_{\mathcal{I}} (\delta \mathbf{u}_+ - \delta \mathbf{u}_-) \cdot \mathbf{t}_i \, dA = \int_{\partial \mathcal{B}} \delta \mathbf{u} \cdot \mathbf{t}_b \, dA. \quad (6.3)$$

Introducing the separation vector \mathbf{g} and perform the pull-back of the two volume integrals with the determinant of the deformation gradient J leads to the formulation of ABAQUS [60].

$$\int_{\mathcal{B}_0} \rho_0 \delta \mathbf{u} \cdot \ddot{\mathbf{u}} \, dV_0 + \int_{\mathcal{B}_0} J (\delta \mathbf{u} \otimes \nabla) : \mathbf{T} \, dV_0 + \int_{\mathcal{I}} \delta \mathbf{g} \cdot \mathbf{t}_i \, dA = \int_{\partial \mathcal{B}_0} \delta \mathbf{u} \cdot \mathbf{t}_{b0} \, dA_0 \quad (6.4)$$

In this work two different formulations of Eq. (6.4) are used. For the UMAT subroutine of ABAQUS Eq. (6.4) is formulated with the KIRCHHOFF stress tensor

$$\int_{\mathcal{B}_0} \rho_0 \delta \mathbf{u} \cdot \ddot{\mathbf{u}} \, dV_0 + \int_{\mathcal{B}_0} (\delta \mathbf{u} \otimes \nabla) : \overset{\text{K}}{\mathbf{T}} \, dV_0 + \int_{\mathcal{I}} \delta \mathbf{g} \cdot \mathbf{t}_i \, dA = \int_{\partial \mathcal{B}_0} \delta \mathbf{u} \cdot \mathbf{t}_{b0} \, dA_0 \quad (6.5)$$

and for the UEL subroutine Eq. (6.4) is formulated with the first PIOLA-KIRCHHOFF stress tensor.

$$\int_{\mathcal{B}_0} \rho_0 \delta \mathbf{u} \cdot \ddot{\mathbf{u}} \, dV_0 + \int_{\mathcal{B}_0} (\delta \mathbf{u} \otimes \nabla_0) : \overset{\text{PK}}{\mathbf{T}} \, dV_0 + \int_{\mathcal{I}} \delta \mathbf{g} \cdot \mathbf{t}_i \, dA = \int_{\partial \mathcal{B}_0} \delta \mathbf{u} \cdot \mathbf{t}_{b0} \, dA_0 \quad (6.6)$$

The required manipulations for the second integrand of Eq. (6.6) can be seen only in index notation and are presented in App. A, therefore. Further on, the relation between the nabla operators $\nabla_0 = \nabla \cdot \mathbf{F}$ is required. A general expression of Eqs. (6.4)–(6.6), which is more clear and precise, can be achieved by rewriting the integrands of these equations as virtual works. This leads to

$$\delta W^{\text{dyn}} + \delta W^{\text{int}} = \delta W^{\text{ext}} \quad \text{with} \quad \delta W^{\text{int}} = \delta W_b^{\text{int}} + \delta W_i^{\text{int}}. \quad (6.7)$$

Wherein, it is not distinguished between different stress measures for reason of simplicity.

6.2 Weak Form of Balance of Energy

The weak form of the balance of energy is achieved through multiplication of Eq. (4.41) with a virtual temperature $\delta \theta$ as the test function and split up the interface contribution into two parts.

$$\int_{\mathcal{B}} \delta \theta (\rho \dot{e}_b + \nabla \cdot \mathbf{q}_b) \, dV + \int_{\mathcal{I}_+} \delta \theta_+ (\dot{e}_+ - r_+ - q_+) \, dA + \int_{\mathcal{I}_-} \delta \theta_- (\dot{e}_- - r_- - q_-) \, dA = 0 \quad (6.8)$$

Again, the product rule of the divergence is used to reformulate the second term of the first integrand.

$$\nabla \cdot (\mathbf{q}_b \delta \theta) = \mathbf{q}_b \cdot (\nabla \delta \theta) + \delta \theta (\nabla \cdot \mathbf{q}_b)$$

With the heat of the midsurface q_i , GAUSS divergence theorem and assuming that internal energy and heat supply of the two interface parts depend on each other, as stated, (this is based on the balance of interface forces and guarantees that the interface does not exist for the global problem).

$$\begin{aligned} \dot{e}_i &= \dot{e}_- = -\dot{e}_+ \\ r_i &= r_- = -r_+ \end{aligned}$$

Eq. (6.8) leads to

$$\int_{\mathcal{B}} \rho \delta \theta \dot{e}_b - \mathbf{q}_b \cdot (\nabla \delta \theta) dV + \int_{\mathcal{I}} (\delta \theta_+ - \delta \theta_-) (r_i + q_i - \dot{e}_i) dA = - \int_{\partial \mathcal{B}} \delta \theta \mathbf{n}_{\partial \mathcal{B}} \cdot \mathbf{q}_b dA. \quad (6.9)$$

Interestingly, the internal energy rate of the interface is negative, which seems realistic because due to failure of the interface the internal energy will reduce until total failure of the interface occurs. Vice versa, an increasing of the internal energy of the interface during failure is unrealistic. And with Eqs. (5.19), (5.24) and (5.33), the chain rule for the internal energies and the heat relation $q_b = -\mathbf{n}_{\partial \mathcal{B}} \cdot \mathbf{q}_b$ Eq. (6.9) yields

$$\int_{\mathcal{B}} \rho c_b \delta \theta \dot{\theta} + \kappa_b (\nabla \delta \theta) \cdot (\nabla \theta) dV + \int_{\mathcal{I}} \delta \Theta r_i + \delta \Theta q_i - c_i \delta \Theta \dot{\Theta} dA = \int_{\partial \mathcal{B}} \delta \theta q_b dA. \quad (6.10)$$

Wherein, $\delta \Theta$ is the virtual temperature jump. Since it is assumed that heat conduction is decoupled from the mechanical problem (cf. Sect. 4.3.4) the integrals in Eq. (6.10) refer to the reference configuration and no pull-back is required. It results

$$\int_{\mathcal{B}_0} \rho_0 c_b \delta \theta \dot{\theta} + \kappa_b (\nabla \delta \theta) \cdot (\nabla \theta) dV_0 + \int_{\mathcal{I}} \delta \Theta r_i + \delta \Theta q_i - c_i \delta \Theta \dot{\Theta} dA = \int_{\partial \mathcal{B}_0} \delta \theta q_{b0} dA_0 \quad (6.11)$$

which is equal to the formulation of ABAQUS [60], if no interface would be considered. For later use it is more convenient to rewrite Eq. (6.11) as

$$\delta H^{\text{int}} = \delta H^{\text{ext}} \quad \text{with} \quad \delta H^{\text{int}} = \delta H_b^{\text{int}} + \delta H_i^{\text{int}}. \quad (6.12)$$

6.3 Discretisation of the Thermo-Mechanical Problem

This section explains shortly how the two systems of PDEs (Eq. (6.7) and Eq. (6.12)) are discretised to solve them in space and time with the FEM. The given statements are addressed to the advanced reader, for basic informations it is referred to the textbooks presented at the beginning of this chapter and it is limited to the plane case. Equation (6.7) and Eq. (6.12) cannot be solved on the complete body \mathcal{B} at a specific time point due to the arbitrary shape of the body, in general. To overcome this deficiency the body \mathcal{B} is separated into a finite number of elements (NE) (cf. Fig. 6.1) and then all elements are assembled to approximate the complete body. However, it remains only an approximation of the body $\tilde{\mathcal{B}}$ and not the exact body \mathcal{B} .

$$\mathcal{B} \approx \tilde{\mathcal{B}} = \bigcup_{i=1}^{NE} \mathcal{B}_{e_i} \quad (6.13)$$

Generally, it is not possible to approximate the behaviour the body exactly. Equation (6.7) and Eq. (6.12) are discretised, as well.

$$\begin{aligned} \delta W_e^{\text{ext}} &= \delta W_e^{\text{int}} + \delta W_e^{\text{dyn}} \\ \delta H_e^{\text{ext}} &= \delta H_e^{\text{int}} \end{aligned} \quad (6.14)$$

Summation of all element contributions gives the comparative weak forms

$$\sum_{i=1}^{NE} \delta W_i^{\text{ext}} = \sum_{i=1}^{NE} \delta W_i^{\text{int}} + \sum_{i=1}^{NE} \delta W_i^{\text{dyn}},$$

$$\sum_{i=1}^{NE} \delta H_i^{\text{ext}} = \sum_{i=1}^{NE} \delta H_i^{\text{int}} .$$

Within the finite element methodology, interpolation functions have to be chosen in order to approximate the primary field variables [123]. In this work this primary variables are the displacements \mathbf{u} and the temperature θ (Remark: Later on, the damage variable d is used as a primary variable, also. But this is then explained). Henceforth, the tensor notation is replaced by the vector-matrix notation, as it is common in computational mechanics. The displacement vector and temperature of an element are approximated by shape functions \mathbf{N} and a discrete degree of freedom (*DOF*) vector \mathbf{u}_N and θ_N of the element.

$$\mathbf{u}_e = \mathbf{N}_u \cdot \mathbf{u}_N \tag{6.15}$$

$$\theta_e = \mathbf{N}_\theta \cdot \theta_N \tag{6.16}$$

This can be expressed through the introduction of a total *DOF* vector of the element \mathbf{p}_e , as well.

$$\mathbf{p}_e = [\mathbf{u}_e^\top \quad \theta_e]^\top \tag{6.17}$$

Every node has two displacement *DOFs* (u_1, u_2) and one temperature *DOF* (θ), cf. Fig. 6.2 or Fig. 6.4. In this work the standard isoparametric concept is used, hence, the geometry is approximated by the same shape functions. On the one hand the geometry is approximated in the reference (Eq. (6.18)) and on the other hand in the current configuration (Eq. (6.19)).

$$\mathbf{x}_{0_e} = \mathbf{N}_u \cdot \mathbf{x}_{0_N} \tag{6.18}$$

$$\mathbf{x}_e = \mathbf{N}_u \cdot \mathbf{x}_N \tag{6.19}$$

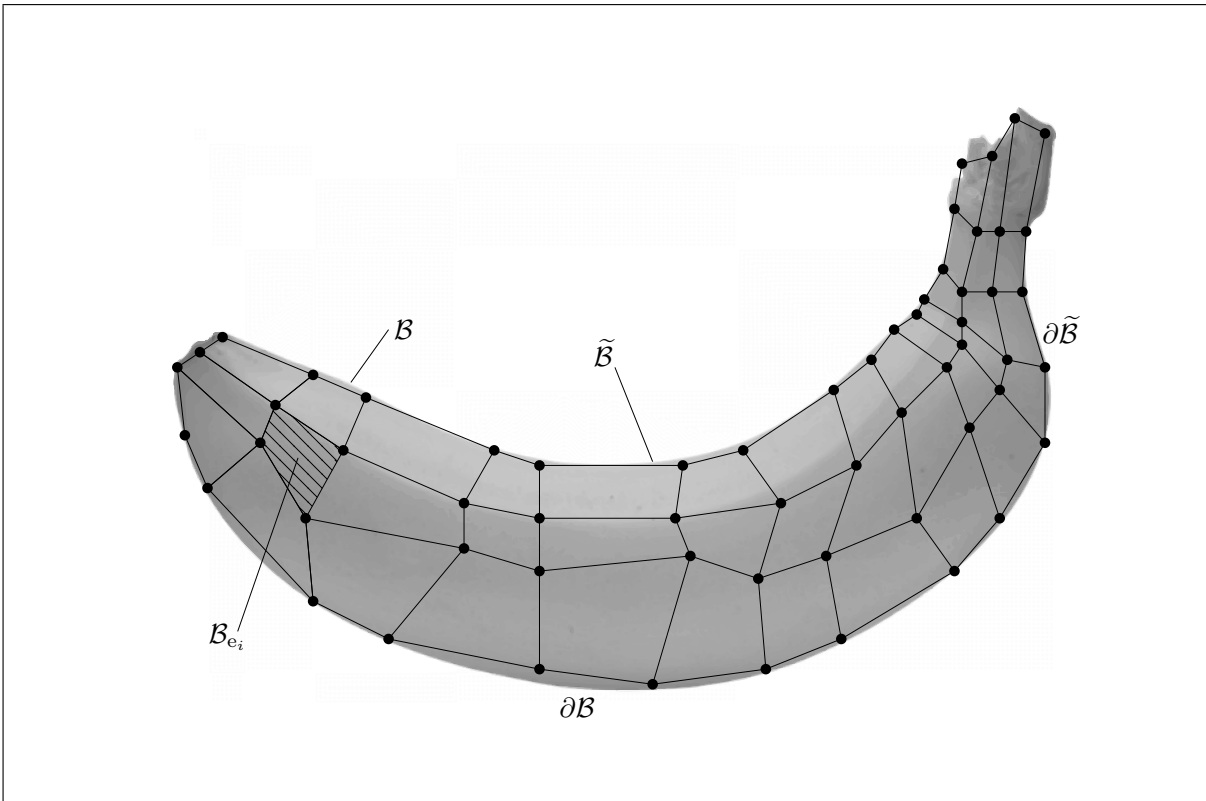


Figure 6.1: Discretisation of an arbitrary body B with FEs, as well as, the boundary ∂B based on [123]

Therein, \mathbf{x}_e denotes the element position and \mathbf{u}_e the element displacement vector and θ_e the element temperature. Whereas, the vectors \mathbf{x}_N , \mathbf{u}_N and θ_N are comprised of all nodal coordinates, displacements and temperatures for one element.

$$\mathbf{x}_N = [\mathbf{x}_N^1 \quad \mathbf{x}_N^2 \quad \dots \quad \mathbf{x}_N^{NN}]^T, \quad \mathbf{x}_N^i = [x_1^i \quad x_2^i]^T \quad \forall i \in \{1, 2, \dots, NN\} \quad (6.20)$$

$$\mathbf{u}_N = [\mathbf{u}_N^1 \quad \mathbf{u}_N^2 \quad \dots \quad \mathbf{u}_N^{NN}]^T, \quad \mathbf{u}_N^i = [u_1^i \quad u_2^i]^T \quad \forall i \in \{1, 2, \dots, NN\} \quad (6.21)$$

$$\theta_N = [\theta_N^1 \quad \theta_N^2 \quad \dots \quad \theta_N^{NN}]^T \quad (6.22)$$

In Eqs. (6.20)–(6.22) \square^i is the node index, and NN denotes the number of nodes per element. Both fields are represented by the same shape functions. The matrix $\mathbf{N}_{u/\theta}$ includes all shape functions:

$$\mathbf{N}_{u/\theta} = [\mathbf{N}_{u/\theta}^1 \quad \mathbf{N}_{u/\theta}^2 \quad \dots \quad \mathbf{N}_{u/\theta}^{NN}] \quad (6.23)$$

where $\mathbf{N}_{u/\theta}^i$ stands for the matrix of the shape functions with respect to the i th node [90]:

$$\mathbf{N}_u^i = N_b^i \mathbf{1}^i \quad \forall i \in \{1, 2, \dots, NN\} \quad (6.24)$$

$$\mathbf{N}_\theta^i = N_b^i \quad \forall i \in \{1, 2, \dots, NN\} \quad (6.25)$$

Due to the formulation of shape functions with so-called natural coordinates ξ (cf. Figs. 6.2 and 6.4), a transformation between physical and natural coordinates is required. This transformation is performed with the JACOBIAN matrix \mathbf{J} .

$$\frac{\partial}{\partial \xi} = \frac{\partial \mathbf{x}_e}{\partial \xi} \cdot \frac{\partial}{\partial \mathbf{x}_e} = \mathbf{J} \cdot \frac{\partial}{\partial \mathbf{x}_e} \quad \Longleftrightarrow \quad \frac{\partial}{\partial \mathbf{x}_e} = \mathbf{J}^{-1} \cdot \frac{\partial}{\partial \xi} \quad (6.26)$$

At last, the determinant of the JACOBIAN $\det(\mathbf{J})$ is introduced to relate the infinitesimal volume in physical coordinates into natural coordinates (In this work the plane case is analysed, hence, the direction e_3 is replaced by a constant width b).

$$dV = b dx_1 dx_2 = b \det(\mathbf{J}) d\xi_1 d\xi_2 \quad (6.27)$$

For sure, the transformations of Eqs. (6.26) and (6.27) can be done with respect to the reference configuration by using the position vector of the reference configuration \mathbf{x}_{0_e} . For further discretisation of the problem it is necessary to introduce FEs. In this work the bulk part is discretised with an 8-node, quadratic plain strain SERENDIPITY element (cf. Fig. 6.2) and the interface part is discretised with a 4-node, linear and a 6-node, quadratic cohesive element (cf. Fig. 6.4), respectively. These elements are presented in the following two sections. Thereby, only the contributions resulting from one element are analysed.

6.4 Quadratic Plane Strain Element

Figure 6.2 presents the SERENDIPITY element, that is used to discretise the bulk part of Eqs. (6.7) and (6.12). The node ordering is according to ABAQUS [60] and every node has three *DOFs*. A displacement in the direction of e_1 and e_2 plus a scalar temperature. Through the inversion of the JACOBIAN matrix the displacement gradient of Eq. (6.5) or Eq. (6.6) (The displacement gradient is rewritten in vector-matrix notation.), and the temperature gradient of Eq. (6.11) are approximated as follows:

$$\mathbf{H}_e = \mathbf{u}_e \cdot \nabla^T = \frac{\partial \mathbf{N}_u}{\partial \xi} \cdot \mathbf{u}_N \cdot \mathbf{J}^{-1} = \frac{\partial N_{u,ik}}{\partial \xi_l} u_k \frac{\partial \xi_l}{\partial x_{e,j}}, \quad (6.28)$$

$$\Gamma_e = \nabla \theta_e = \frac{\partial \mathbf{N}_\theta}{\partial \xi} \cdot \boldsymbol{\theta}_N \cdot \mathbf{J}^{-1} = \frac{\partial N_{\theta,k}}{\partial \xi_j} \theta_k \frac{\partial \xi_j}{\partial x_{e,i}}. \quad (6.29)$$

Nevertheless, in contrast to the standard procedure in computational mechanics no VOIGT or MANDEL notation is introduced to rewrite the stress and displacement gradient matrix. Due to this circumstance a third-order \mathbf{b} -operator and a second-order \mathbf{B} -operator matrix are introduced to derive an alternative expression for the displacement and temperature gradient.

$$\mathbf{H}_e = \mathbf{b}_e^R \cdot \mathbf{u}_N = b_{ijk} u_k \quad \text{with} \quad b_{ikj} = \frac{\partial N_{u,ik}}{\partial \xi_l} \frac{\partial \xi_l}{\partial x_{e,j}} \quad (6.30)$$

$$\Gamma_e = \mathbf{B}_e^\top \cdot \boldsymbol{\theta}_N = B_{ik} \theta_k \quad \text{with} \quad B_{ki} = \frac{\partial N_{\theta,k}}{\partial \xi_j} \frac{\partial \xi_j}{\partial x_{e,i}} \quad (6.31)$$

In Eq. (6.28) and (6.30) the indices $i, j, l \in \{1, 2\}$ and the index $k \in \{1, 2, \dots, 2NN\}$. For Eq. (6.29) and (6.31) the indices $i, j \in \{1, 2\}$ and the index $k \in \{1, 2, \dots, NN\}$. With this at hand all bulk parts of Eqs. (6.7) and (6.12) are discretised. The weak form of balance of linear momentum yields

$$\delta W_e^{\text{dyn}} = b \int_{-1}^1 \int_{-1}^1 \rho_0 \delta \mathbf{u}_N^\top \cdot \mathbf{N}_u^\top \cdot \mathbf{N}_u \cdot \ddot{\mathbf{u}}_N \det(\mathbf{J}_0) \, d\xi_1 d\xi_2 = \delta \mathbf{u}_N^\top \cdot \mathbf{M}_e \cdot \ddot{\mathbf{u}}_N, \quad (6.32)$$

$$\delta W_{b,e}^{\text{int}} = b \int_{-1}^1 \int_{-1}^1 \delta \mathbf{u}_N^\top \cdot \mathbf{b}_e^L : \overset{\text{K}}{\mathbf{T}}_e \det(\mathbf{J}_0) \, d\xi_1 d\xi_2 = \delta \mathbf{u}_N^\top \cdot \mathbf{f}_{b,e}^{\text{int}}, \quad (6.33)$$

$$\delta W_{b,e}^{\text{int}} = b \int_{-1}^1 \int_{-1}^1 \delta \mathbf{u}_N^\top \cdot \mathbf{b}_{0e}^L : \overset{\text{PK}}{\mathbf{T}}_e \det(\mathbf{J}_0) \, d\xi_1 d\xi_2 = \delta \mathbf{u}_N^\top \cdot \mathbf{f}_{b,e}^{\text{int}}, \quad (6.34)$$

$$\delta W_e^{\text{ext}} = \int_{-1}^1 \int_{-1}^1 \delta \mathbf{u}_N^\top \cdot \mathbf{N}_u^\top \cdot \mathbf{t}_{b0,e} \det(\mathbf{J}_0) \, d\xi_1 d\xi_2 = \delta \mathbf{u}_N^\top \cdot \mathbf{f}_e^{\text{ext}}. \quad (6.35)$$

Again, it is not distinguished between different stress measures in the internal force vector for reason of simplicity. Eq. (6.33) is used for the UMAT subroutine and Eq. (6.34) for the UEL subroutine.

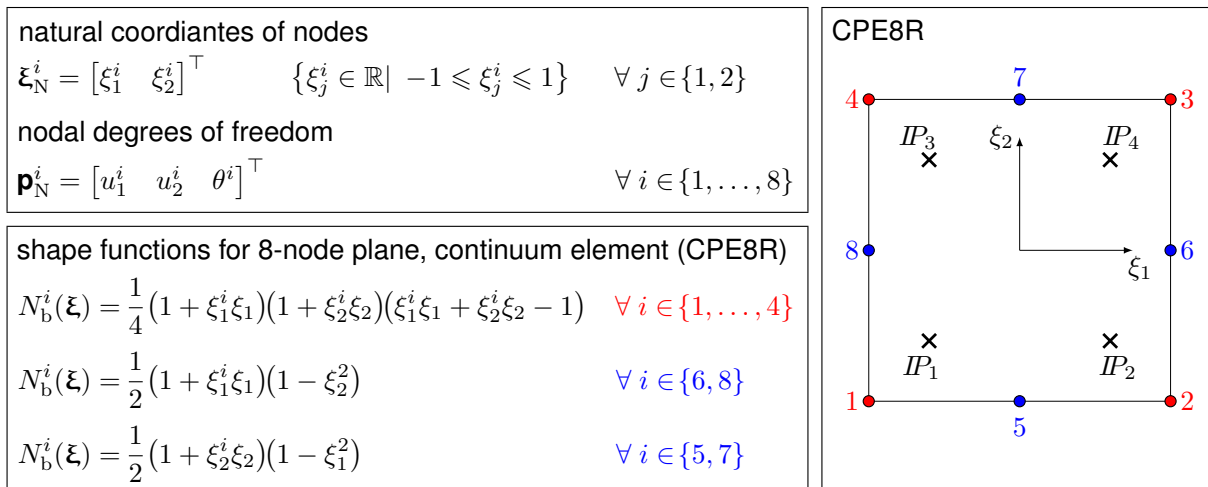


Figure 6.2: Geometry, nodes and shape functions (after [125]) for a 8-node, quadratic plain strain element; figure is based on [90]

Table 6.1: Positions and weights of reduced GAUSS integration for a plane element with quadratic shape functions

integration point	IP_1	IP_2	IP_3	IP_4
positions (ξ_1^i, ξ_2^j)	$(-\frac{1}{\sqrt{3}}, -\frac{1}{\sqrt{3}})$	$(\frac{1}{\sqrt{3}}, -\frac{1}{\sqrt{3}})$	$(-\frac{1}{\sqrt{3}}, \frac{1}{\sqrt{3}})$	$(\frac{1}{\sqrt{3}}, \frac{1}{\sqrt{3}})$
weights (w_i, w_j)	(1, 1)	(1, 1)	(1, 1)	(1, 1)

From the weak form of balance of energy follows

$$\begin{aligned}
 \delta H_{b,e}^{\text{int}} &= b \int_{-1}^1 \int_{-1}^1 \delta \boldsymbol{\theta}_N^\top \cdot \left[\rho_0 c_b \mathbf{N}_\theta^\top \cdot \mathbf{N}_\theta \cdot \dot{\boldsymbol{\theta}}_N + \kappa_b \mathbf{B}_e \cdot \mathbf{B}_e^\top \cdot \boldsymbol{\theta}_N \right] \det(\mathbf{J}_0) \, d\xi_1 d\xi_2 \\
 &= b \int_{-1}^1 \int_{-1}^1 \delta \boldsymbol{\theta}_N^\top \cdot \left[\mathbf{C}_{b,e}^{\text{cap}} \cdot \dot{\boldsymbol{\theta}}_N + \mathbf{C}_{b,e}^{\text{con}} \cdot \boldsymbol{\theta}_N \right] \det(\mathbf{J}_0) \, d\xi_1 d\xi_2 = \delta \boldsymbol{\theta}_N^\top \cdot \mathbf{h}_{b,e}^{\text{int}}, \quad (6.36)
 \end{aligned}$$

$$\delta H_e^{\text{ext}} = \int_{-1}^1 \int_{-1}^1 \delta \boldsymbol{\theta}_N^\top \cdot \mathbf{N}_\theta^\top q_{b0} \det(\mathbf{J}_0) \, d\xi_1 d\xi_2 = \delta \boldsymbol{\theta}_N^\top \cdot \mathbf{h}_e^{\text{ext}}. \quad (6.37)$$

The heat capacity and heat conductivity matrix of Eq. (6.36) are defined as follows.

$$\begin{aligned}
 \mathbf{C}_{b,e}^{\text{cap}} &= \rho_0 c_b \mathbf{N}_\theta^\top \cdot \mathbf{N}_\theta \\
 \mathbf{C}_{b,e}^{\text{con}} &= \kappa_b \mathbf{B}_e \cdot \mathbf{B}_e^\top
 \end{aligned}$$

In the last step the integrals of Eqs. (6.32)–(6.37) have to be solved. In this work the integration is performed with the standard reduced GAUSS integration to avoid *locking* of the element. The drawback of reduced integration is, that zero-energy modes (deformations) can occur. This is called *hour-glassing*. For a quadratic plane strain element with reduced integration only one zero-energy mode remains, however, this mode is never calculated [126–128]. Further on, this integration scheme suits well to the chosen, polynomial shape functions [129]. The integration points can be seen in Fig. 6.2, as well. All integrals of Eqs. (6.32)–(6.37) are functions of the natural coordinates of the element and can also be written as a function of these coordinates $f_e(\xi_1, \xi_2)$. The integrals are approximated through a sum over integration points.

$$\int_{-1}^1 \int_{-1}^1 f_e(\xi_1, \xi_2) \, d\xi_1 d\xi_2 \approx \sum_{i=1}^2 \sum_{j=1}^2 w_i w_j f_e(\xi_1^i, \xi_2^j) \quad (6.38)$$

For the presented plane element with reduced integration and quadratic shape functions, the positions and weights of the four integration points are given in Table 6.1.

6.5 Linear and Quadratic Plane Cohesive Element

In this section the formulation of a linear and a quadratic plane cohesive element is explained. This formulation differs slightly from the procedure of defining continuum elements because all quantities refer to a midsurface (cf. Fig. 4.4). Therefore, the position of this midsurface is

required, first. This is determined as the mean position of the interface surfaces \mathcal{I}_+ and \mathcal{I}_- .

$$\bar{\mathbf{x}}_e = \frac{1}{2}(\mathbf{x}_+ + \mathbf{x}_-) \quad (6.39)$$

Further on, the local coordinate system is required. In this work the plane case is analysed, only. Because of this it exists just one tangential and one normal direction. The second tangential direction is the base vector e_3 , which is required to determine the normal vector. The tangential direction is determined through derivative with respect to the curvilinear coordinate in this direction, because the element is small, the natural element coordinate ξ_1 coincides with the curvilinear coordinate (cf. GOYAL [23]). It results

$$\mathbf{z}_{1e} = \frac{\partial \bar{\mathbf{x}}_e}{\partial \xi_1} \quad (6.40)$$

With the cross product between this vector and the base vector \mathbf{e}_3 it results the normal direction

$$\mathbf{z}_{2e} = \mathbf{e}_3 \times \mathbf{z}_{1e} \quad (6.41)$$

Finally, this set of vectors is normalised to form the base of the local coordinate system. Remember, that the index " α " stands for the different directions of the local coordinate system.

$$\mathbf{e}_{\alpha e} = \frac{\mathbf{z}_{\alpha e}}{|\mathbf{z}_{\alpha e}|} \quad \forall \alpha \in \{1, 2\} \quad (6.42)$$

In contrast to continuum elements the transformation between physical and natural coordinates is not done with a common JACOBIAN matrix. For this kind of elements the JACOBIAN matrix is represented by the length of the normal vector in the current configuration. Hence, for a plane cohesive element this leads to

$$dA = b |\mathbf{z}_{2e}| d\xi_1 \quad (6.43)$$

TSLs for a cohesive element are formulated in the local coordinate system. Due to this fact, it is necessary to transform all global quantities of the problem into the local coordinate system. This transformation is done by an orthogonal rotation matrix, defined as

$$\mathbf{R}_e = \begin{bmatrix} \mathbf{e}_{1e}^\top \\ \mathbf{e}_{2e}^\top \end{bmatrix} \iff \mathbf{R}_e = \frac{1}{|\mathbf{z}_{2e}|} \begin{bmatrix} \mathbf{z}_{1e}^\top \\ \mathbf{z}_{2e}^\top \end{bmatrix} \quad (6.44)$$

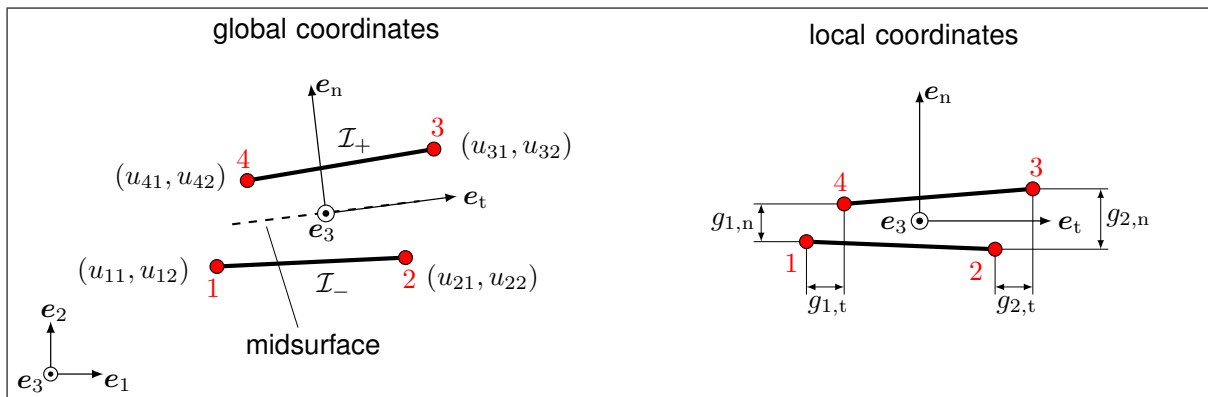


Figure 6.3: Transformation between global and local coordinates for a linear, plane interface element through rotation matrix \mathbf{Q} based on [68]

for one node. Hence, a cohesive element uses three coordinate systems. The global reference system, a local system for the TSL, and a natural one for the element formulation and integration. The usage of the right formulation of Eq. (6.44) has the advantage that the transformation between physical and natural coordinates reduces to

$$dA = b d\xi_1 .$$

Up next, the continuous variables displacement, node coordinates and temperature are approximated by discrete nodal values through the use of shape functions. However, this is not straightforward for this type of element. It is started with the separation vector \mathbf{g} . To determine this quantity the nodal displacement *DOF*s have to be rotated into the local coordinate system with a rotation matrix \mathbf{Q}_e , that is based on rotation matrix \mathbf{R}_e . The matrix \mathbf{R}_e rotates only the quantities of one node and \mathbf{Q}_e rotates the quantities of all nodes.

$$\mathbf{Q}_e = \begin{bmatrix} \mathbf{R}_e & \dots & \mathbf{0} \\ \vdots & \ddots & \vdots \\ \mathbf{0} & \dots & \mathbf{R}_e \end{bmatrix} \quad (6.45)$$

Further on, a separation-displacement-relation matrix \mathbf{L}_u is introduced. This matrix subtracts the displacement values of nodes, which are placed on opposite surfaces from each other, and therefore calculates the separation between both surfaces. It follows the approximated separation vector of the element as

$$\mathbf{g}_e = \mathbf{N}_u \cdot \mathbf{L}_u \cdot \mathbf{Q}_e \cdot \mathbf{u}_N = \mathbf{Z}_{u,e}^{\text{lin}} \cdot \mathbf{u}_N \quad \text{with} \quad \mathbf{Z}_{u,e}^{\text{lin}} = \mathbf{N}_u \cdot \mathbf{L}_u \cdot \mathbf{Q}_e . \quad (6.46)$$

This is presented in Figure 6.3. Similar, the temperature jump is calculated

$$\Theta_e = \mathbf{N}_\theta \cdot \mathbf{L}_\theta \cdot \theta_N = \mathbf{Z}_{\theta,e} \cdot \theta_N \quad \text{with} \quad \mathbf{Z}_{\theta,e} = \mathbf{N}_\theta \cdot \mathbf{L}_\theta . \quad (6.47)$$

In contrast to Eq. (6.46) no rotation matrix is required, because the temperature is a scalar quantity and cannot be rotated. The approximated midsurface is determined through the introduction of a second relation matrix \mathbf{M}_u , which relates the current position vectors of the interface surface to each other, according to Equation (6.39). It results

$$\bar{\mathbf{x}}_e = \frac{1}{2} \mathbf{N}_u \cdot \mathbf{M}_u \cdot \mathbf{x}_N \quad (6.48)$$

and the derivative of this equation yields the approximated tangential vector of the local coordinate system.

$$\mathbf{z}_{1,e} = \frac{1}{2} \frac{\partial \mathbf{N}_u}{\partial \xi_1} \cdot \mathbf{M}_u \cdot \mathbf{x}_N \quad (6.49)$$

All required relation matrices are presented in App. A, their size and structure depends on the *NN* of the element and the ordering of the *DOF* vector. Here, they are presented for a 4-node and a 6-node plane cohesive element, according to Figure 6.4. In contrast to Sect. 6.4 the shape function matrices $\mathbf{N}_{u/\theta}$ include only the shape functions of one interface surface

$$\mathbf{N}_{u/\theta} = \left[\mathbf{N}_{u/\theta}^1 \quad \dots \quad \mathbf{N}_{u/\theta}^{NN/2} \right] , \quad (6.50)$$

where $\mathbf{N}_{u/\theta}^i$ stands for the matrix of the shape functions with respect to the *i*th node of one surface.

$$\mathbf{N}_u^i = N_i^i \mathbf{1} \quad \forall i \in \{1, \dots, NN/2\} \quad (6.51)$$

Table 6.2: Positions and weights of NEWTON-COTES integration for a plane cohesive element with linear and quadratic shape functions

integration point	linear		quadratic		
	IP_1	IP_2	IP_1	IP_2	IP_3
positions (ξ_1^i)	(-1)	(1)	(-1)	(0)	(1)
weights (w_i)	(1)	(1)	($\frac{1}{3}$)	($\frac{4}{3}$)	($\frac{1}{3}$)

$$\mathbf{N}_\theta^i = N_1^i \quad \forall i \in \{1, \dots, NN/2\} \quad (6.52)$$

The shape functions and further informations for the element are presented in Figure 6.4. With this at hand we can analyse the variation of separation and temperature jump.

$$\delta \mathbf{g}_e = \frac{\partial \mathbf{g}_e}{\partial \mathbf{u}_N} \cdot \delta \mathbf{u}_N \quad (6.53)$$

$$\delta \Theta_e = \frac{\partial \Theta_e}{\partial \theta_N} \cdot \delta \theta_N \quad (6.54)$$

Inserting Eqs. (6.46) and (6.47) into Eqs. (6.53) and (6.54) leads to

$$\delta \mathbf{g}_e = \left(\mathbf{Z}_{u,e}^{\text{lin}} + \mathbf{Z}_{u,e}^{\text{nl}} \cdot \mathbf{u}_N \right) \cdot \delta \mathbf{u}_N \quad \text{with} \quad \mathbf{Z}_{u,e}^{\text{nl}} = \mathbf{N}_u \cdot \mathbf{L}_u \cdot \frac{\partial \mathbf{Q}_e}{\partial \mathbf{u}_N}, \quad (6.55)$$

$$\delta \Theta_e = \mathbf{Z}_{\theta,e} \cdot \delta \theta_N. \quad (6.56)$$

For a shorter notation of the separation another \mathbf{Z} matrix is introduced.

$$\mathbf{Z}_{u,e} = \mathbf{Z}_{u,e}^{\text{lin}} + \mathbf{Z}_{u,e}^{\text{nl}} \cdot \mathbf{u}_N \quad (6.57)$$

The dependence of the rotation matrix \mathbf{Q}_e onto the nodal displacements is usually benign [23, 130]. However, we want to present the full formulation of the principle of virtual work for a cohesive element. Although, we neglect the mentioned dependence as well ($\mathbf{Z}_{u,e}^{\text{nl}} = \mathbf{0}$). Hence,

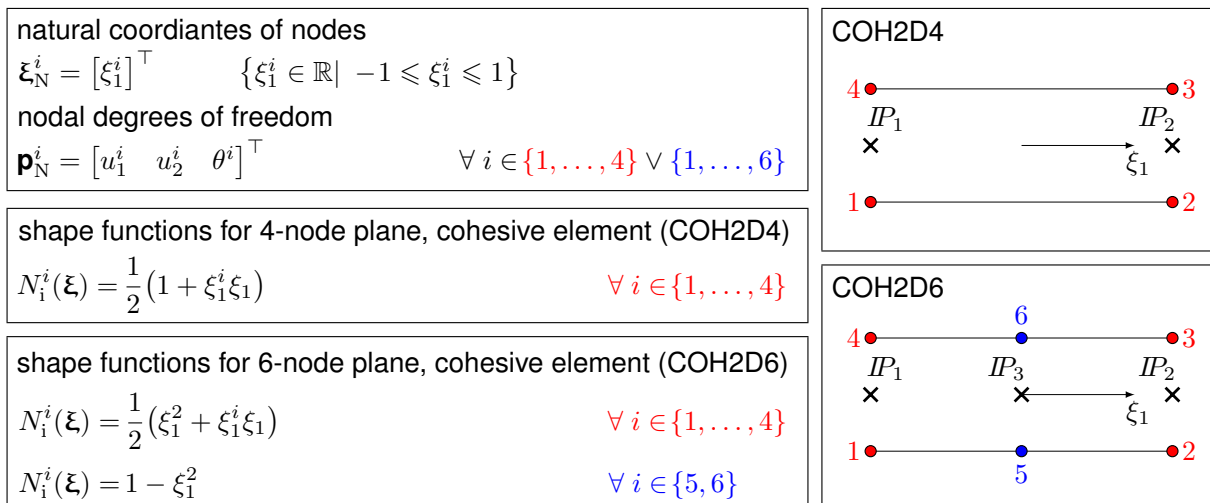


Figure 6.4: Geometry, nodes and shape functions for a 4-node linear, and a 6-node quadratic plane cohesive element; figure is based on [90]

the separation is approximated as

$$\mathbf{g}_e = \mathbf{Z}_{u,e} \cdot \mathbf{u}_N \quad \text{with } \mathbf{Z}_{u,e} = \mathbf{Z}_{u,e}^{\text{lin}}, \quad (6.58)$$

and the variation of the separation as

$$\delta \mathbf{g}_e = \mathbf{Z}_{u,e} \cdot \delta \mathbf{u}_N \quad \text{with } \mathbf{Z}_{u,e} = \mathbf{Z}_{u,e}^{\text{lin}}. \quad (6.59)$$

The interface quantity of balance of linear momentum (Eq. (6.5) or (6.6)) leads with Eq. (6.59) to

$$\delta W_{i,e}^{\text{int}} = b \int_{-1}^1 \delta \mathbf{u}_N^{\top} \cdot \mathbf{Z}_{u,e}^{\top} \cdot \mathbf{t}_{i,e} |z_{2e}| d\xi_1 = \delta \mathbf{u}_N^{\top} \cdot \mathbf{f}_{i,e}^{\text{int}}, \quad (6.60)$$

and for the interface portion of the balance of energy (Eq. (6.11)) results

$$\begin{aligned} \delta H_{i,e}^{\text{int}} &= b \int_{-1}^1 \delta \theta_N^{\top} \cdot \left[\mathbf{z}_{\theta,e}^{\top} r_i + \kappa_i \mathbf{z}_{\theta,e}^{\top} \cdot \mathbf{z}_{\theta,e} \cdot \theta_N - c_i \mathbf{z}_{\theta,e}^{\top} \cdot \mathbf{z}_{\theta,e} \cdot \dot{\theta}_N \right] |z_{2e}| d\xi_1 \\ &= b \int_{-1}^1 \delta \theta_N^{\top} \cdot \left[\mathbf{z}_{\theta,e}^{\top} r_i + \mathbf{C}_{i,e}^{\text{con}} \cdot \theta_N - \mathbf{C}_{i,e}^{\text{cap}} \cdot \dot{\theta}_N \right] |z_{2e}| d\xi_1 = \delta \theta_N^{\top} \cdot \mathbf{h}_{i,e}^{\text{int}}. \end{aligned} \quad (6.61)$$

with Eqs. (6.47) and (6.56). The heat capacity and heat conductivity of Eq. (6.61) are defined similar as for the bulk material.

$$\begin{aligned} \mathbf{C}_{i,e}^{\text{cap}} &= c_i \mathbf{z}_{\theta,e}^{\top} \cdot \mathbf{z}_{\theta,e} \\ \mathbf{C}_{i,e}^{\text{con}} &= \kappa_i \mathbf{z}_{\theta,e}^{\top} \cdot \mathbf{z}_{\theta,e} \end{aligned}$$

Finally, an integration scheme is required for Eqs. (6.60) and (6.61). In this work the NEWTON-COTES integration scheme is used. The reason to use this integration scheme is already discussed in Chap. 2 and therefore, not mentioned again. For both cohesive elements the full NEWTON-COTES integration is used. For the 4-node element two integration points are required and for the 6-node element three integration points, cf. Figure. 6.4. Again, the integrals can be written as a function of the natural coordinate $f_e(\xi_1)$ and then the integral is approximated by the summation over a defined number of integration points at which the integral is evaluated.

$$\int_{-1}^1 f_e(\xi_1) d\xi_1 \approx \begin{cases} \sum_{i=1}^2 w_i f_e(\xi_1^i) & \text{linear} \\ \sum_{i=1}^3 w_i f_e(\xi_1^i) & \text{quadratic} \end{cases} \quad (6.62)$$

The position of the integration points and their weights are summed up in Table 6.2.

6.6 Solution of the Thermo-Mechanical Problem

Sections 6.4 and 6.5 present the discretisation of Eqs. (6.7) and (6.12) for one element. To get to the discretised form of the whole problem the element contributions need to be assembled. This is written with the operator \cup . It results:

$$\begin{aligned}
 \delta W^{\text{dyn}} &= \bigcup_1^{NE} \delta W_e^{\text{dyn}} & \delta W_b^{\text{int}} &= \bigcup_1^{NE} \delta W_{b,e}^{\text{int}} & \delta W_i^{\text{int}} &= \bigcup_1^{NE} \delta W_{i,e}^{\text{int}} \\
 \delta W^{\text{ext}} &= \bigcup_1^{NE} \delta W_e^{\text{ext}} & & & & \\
 \delta H_b^{\text{int}} &= \bigcup_1^{NE} \delta H_{b,e}^{\text{int}} & \delta H_i^{\text{int}} &= \bigcup_1^{NE} \delta H_{i,e}^{\text{int}} & \delta H^{\text{ext}} &= \bigcup_1^{NE} \delta H_e^{\text{ext}}
 \end{aligned} \tag{6.63}$$

Arranging the global quantities in residual form gives

$$\begin{aligned}
 \delta \mathbf{u}^\top \cdot \mathbf{r}^u &= \delta \mathbf{u}^\top \cdot [\mathbf{M} \cdot \ddot{\mathbf{u}} + \mathbf{f}_b^{\text{int}} + \mathbf{f}_i^{\text{int}} - \mathbf{f}^{\text{ext}}] = 0, \\
 \delta \theta^\top \cdot \mathbf{r}^\theta &= \delta \theta^\top \cdot [\mathbf{h}_b^{\text{int}} + \mathbf{h}_i^{\text{int}} - \mathbf{h}^{\text{ext}}] = 0.
 \end{aligned}$$

Wherein, all quantities have no index \square_N or \square_e , any more. This states that these are the global quantities which are used to solve the problem. With the introduction of a total internal force vector, that is defined as $\mathbf{f}^{\text{int}} = \mathbf{f}_b^{\text{int}} + \mathbf{f}_i^{\text{int}}$, and a total internal heat vector defined as $\mathbf{h}^{\text{int}} = \mathbf{h}_b^{\text{int}} + \mathbf{h}_i^{\text{int}}$, and the statement that the virtual displacement and temperature are arbitrary the final equations, which have to be solved, are derived.

$$\mathbf{r}^u = \mathbf{M} \cdot \ddot{\mathbf{u}} + \mathbf{f}^{\text{int}} - \mathbf{f}^{\text{ext}} = \mathbf{o} \tag{6.64}$$

$$\mathbf{r}^\theta = \mathbf{h}^{\text{int}} - \mathbf{h}^{\text{ext}} = \mathbf{o} \tag{6.65}$$

The solution in time and space is obtained from Eqs. (6.64) and (6.65) through an implicit solution scheme with the standard backward EULER operator which is defined as

$$\square_{j+1} = \square_j + \Delta t \dot{\square}_{j+1} \quad \text{with } \square \in \{ \mathbf{u}, \dot{\mathbf{u}}, \theta \}. \tag{6.66}$$

The backward EULER operator is used, because of its absolute stability and simplicity. Higher order integration schemes lead to more complex equations, and more quantities must be saved in every time step. An explicit integration scheme is not used, because the definition of a criterion for the stable time increment is very difficult. Usually, for a dynamic analysis the NEWMARK or HILBER-HUGHES-TAYLOR procedure is used [131]. In this work, the backward EULER operator is used because of his high numerical damping [60]. The reason for this is that the fracture process is actually a quasi-static process. However, in the case of crack onset and crack propagation an acceleration occurs, which leads to problems in a common quasi-static analysis (This is discussed in Sect. 6.7 in more detail). Therefore, dynamic and quasi-static analyses are carried out and compared to each other. The weakly coupled problem of Eqs. (6.64) and (6.65) is solved for the quasi-static case. The dynamic analysis is done for the isothermal case. Thus, it remains Equation (6.64).

6.6.1 Quasi-Static Analysis

In the quasi-static case no acceleration effects are considered, hence, the system of equations which needs to be solved is

$$\mathbf{r}^u = \mathbf{f}^{\text{int}} - \mathbf{f}^{\text{ext}} = \mathbf{o}, \tag{6.67}$$

$$\mathbf{r}^\theta = \mathbf{h}^{\text{int}} - \mathbf{h}^{\text{ext}} = \mathbf{o}. \tag{6.68}$$

The Eqs. (6.67) and (6.68) have to be solved for the unknown displacements \mathbf{u}_{j+1} and temperatures θ_{j+1} at the next time step. Therefore, the residual vectors and the unknown vectors are aligned in new vectors

$$\mathbf{r}_{j+1} = [\mathbf{r}_{j+1}^u \quad \mathbf{r}_{j+1}^\theta]^\top, \quad \mathbf{p}_{j+1} = [\mathbf{u}_{j+1} \quad \theta_{j+1}]^\top$$

and then is the residual vector extended in a TAYLOR series, which is aborted after the linear term. Therein, the index "j" is the index of the actual time increment and the index "k" is the counter for the necessary iterations in one time increment.

$$\mathbf{r}(\mathbf{p}_{j+1}^{k+1}) = \mathbf{r}(\mathbf{p}_{j+1}^k) + \frac{\partial \mathbf{r}(\mathbf{p}_{j+1}^k)}{\partial \mathbf{p}_{j+1}^k} \cdot \Delta \mathbf{p}_{j+1}^{k+1} \quad \text{with} \quad \Delta \mathbf{p}_{j+1}^{k+1} = \mathbf{p}_{j+1}^{k+1} - \mathbf{p}_{j+1}^k \quad (6.69)$$

This procedure leads to the common NEWTON-RAPHSON procedure, that was published by CAUCHY [132] in 1847, first. The iteration is performed for every time increment until the residual vector is approximately zero. The standard ABAQUS tolerances and criteria are used. For further informations it is referred to [60, 133]. The derivative $\partial \mathbf{r} / \partial \mathbf{p}$ is called stiffness matrix \mathbf{K} in the sense of the FEM. Because of displacement and temperature *DOF*'s, the stiffness matrix can be divided into four sub-matrices, and every sub-matrix can be divided into a bulk and an interface contribution. Hence, eight sub-matrices can be identified. Further on, the external force and heat vector do not depend on the unknown vector [123, 133]. From now on, the indices "j+1", "k" and "k+1" are omitted for reasons of clarity. The eight contributions are:

$$\begin{aligned} \mathbf{K}_b^{uu} &= \frac{\partial \mathbf{f}_b^{\text{int}}}{\partial \mathbf{u}} & \mathbf{K}_b^{u\theta} &= \frac{\partial \mathbf{f}_b^{\text{int}}}{\partial \theta} & \mathbf{K}_b^{\theta u} &= \frac{\partial \mathbf{h}_b^{\text{int}}}{\partial \mathbf{u}} & \mathbf{K}_b^{\theta\theta} &= \frac{\partial \mathbf{h}_b^{\text{int}}}{\partial \theta} \\ \mathbf{K}_i^{uu} &= \frac{\partial \mathbf{f}_i^{\text{int}}}{\partial \mathbf{u}} & \mathbf{K}_i^{u\theta} &= \frac{\partial \mathbf{f}_i^{\text{int}}}{\partial \theta} & \mathbf{K}_i^{\theta u} &= \frac{\partial \mathbf{h}_i^{\text{int}}}{\partial \mathbf{u}} & \mathbf{K}_i^{\theta\theta} &= \frac{\partial \mathbf{h}_i^{\text{int}}}{\partial \theta} \end{aligned}$$

The contributions \mathbf{K}_b^{uu} and \mathbf{K}_i^{uu} represent the pure mechanical problem, and $\mathbf{K}_b^{\theta\theta}$ and $\mathbf{K}_i^{\theta\theta}$ represent the pure thermal problem. The other contributions are the coupling matrices between both problems (fields). They are arranged in the stiffness matrix as

$$\mathbf{K} = \begin{bmatrix} \mathbf{K}_b^{uu} & \mathbf{K}_b^{u\theta} \\ \mathbf{K}_b^{\theta u} & \mathbf{K}_b^{\theta\theta} \end{bmatrix} + \begin{bmatrix} \mathbf{K}_i^{uu} & \mathbf{K}_i^{u\theta} \\ \mathbf{K}_i^{\theta u} & \mathbf{K}_i^{\theta\theta} \end{bmatrix}$$

In Chapt. 3 we assumed that the mechanical and thermal problem are not coupled. Hence, all coupling matrices are zero

$$\mathbf{K}_b^{u\theta} = \mathbf{K}_b^{\theta u} = \mathbf{K}_i^{u\theta} = \mathbf{K}_i^{\theta u} = \mathbf{0},$$

and it remains

$$\mathbf{K} = \begin{bmatrix} \mathbf{K}_b^{uu} & \mathbf{0} \\ \mathbf{0} & \mathbf{K}_b^{\theta\theta} \end{bmatrix} + \begin{bmatrix} \mathbf{K}_i^{uu} & \mathbf{0} \\ \mathbf{0} & \mathbf{K}_i^{\theta\theta} \end{bmatrix} \quad (6.70)$$

for the stiffness matrix. Usually, the problems are not coupled. This is not the case here, because the damage evolution has a slight influence on the temperature distribution around the interface, and the material parameters depend on the temperature. Indeed, it is possible to decouple the problems. But the solution has to be obtained simultaneously, and it is not possible to perform the thermal simulation first and the mechanical simulation afterwards. The four remaining contributions of the stiffness matrix are derived through the assembly of all element stiffness matrices of the problem.

$$\mathbf{K}_b^{uu} = \bigcup_{i=1}^{NE} \mathbf{K}_{b,e_i}^{uu} \quad \mathbf{K}_b^{\theta\theta} = \bigcup_{i=1}^{NE} \mathbf{K}_{b,e_i}^{\theta\theta} \quad \mathbf{K}_i^{uu} = \bigcup_{i=1}^{NE} \mathbf{K}_{i,e_i}^{uu} \quad \mathbf{K}_i^{\theta\theta} = \bigcup_{i=1}^{NE} \mathbf{K}_{i,e_i}^{\theta\theta}$$

Wherein the element contributions are derived from Eqs. (6.33) or (6.34), (6.36), (6.60) and (6.61). The temperature rate is approximated by the backward EULER operator, the derivative of the rotation matrix of the interface with respect to the displacement vector is neglected (because it is neglected for the internal virtual work too), and the influence of the temperature derivatives of heat capacity and heat conduction matrix are usually benign, and are neglected due to this fact [124]. With these assumptions it results:

$$\begin{aligned}
 \mathbf{K}_{b,e}^{uu} &= b \int_{-1}^1 \int_{-1}^1 \mathbf{b}_e^L : \mathfrak{A}_e^K : \mathbf{b}_e^R \det(\mathbf{J}_0) \, d\xi_1 d\xi_2 \vee b \int_{-1}^1 \int_{-1}^1 \mathbf{b}_{0e}^L : \mathfrak{A}_e^{IK} : \mathbf{b}_{0e}^R \det(\mathbf{J}_0) \, d\xi_1 d\xi_2 \\
 \mathbf{K}_{b,e}^{\theta\theta} &= b \int_{-1}^1 \int_{-1}^1 \left[\mathbf{C}_{b,e}^{\text{con}} + \frac{1}{\Delta t} \mathbf{C}_{b,e}^{\text{cap}} \right] \det(\mathbf{J}_0) \, d\xi_1 d\xi_2 \\
 \mathbf{K}_{i,e}^{uu} &= b \int_{-1}^1 \mathbf{z}_{u,e}^\top \cdot \mathbf{A}_{i,e} \cdot \mathbf{z}_{u,e} |\mathbf{z}_{2e}| \, d\xi_1 \\
 \mathbf{K}_{i,e}^{\theta\theta} &= b \int_{-1}^1 \left[\mathbf{C}_{i,e}^{\text{con}} - \frac{1}{\Delta t} \mathbf{C}_{i,e}^{\text{cap}} \right] |\mathbf{z}_{2e}| \, d\xi_1
 \end{aligned} \tag{6.71}$$

In the displacement part of the bulk and interface contribution for one element, a derivative of the stress matrix with respect to the deformation gradient, and a derivative of the traction vector with respect to the separation vector is required. These are the material tangent matrix of the bulk and interface contribution, respectively. They are determined in Section 6.8. Through inversion of the stiffness matrix the solution for one step in a time increment is obtained

$$\Delta \mathbf{p} = -\mathbf{K}^{-1} \cdot \mathbf{r} \tag{6.72}$$

which is followed by the update of the unknown vector

$$\mathbf{p}_{j+1}^{k+1} = \mathbf{p}_{j+1}^k + \Delta \mathbf{p}_{j+1}^{k+1} \tag{6.73}$$

for the next iteration. This is repeated until a defined user tolerance is reached. Again, the standard tolerances and criteria of ABAQUS are used.

6.6.2 Implicit Dynamic Analysis

The variable time increment for the dynamic analysis between two time steps is defined as

$$\Delta t = t_{j+1} - t_j \tag{6.74}$$

With the backward EULER operator (Eq. (6.66)) and Eq. (6.74) the acceleration and velocity are approximated.

$$\dot{\mathbf{u}}_{j+1} = \frac{1}{\Delta t} (\mathbf{u}_{j+1} - \mathbf{u}_j) \tag{6.75}$$

$$\ddot{\mathbf{u}}_{j+1} = \frac{1}{(\Delta t)^2} (\mathbf{u}_{j+1} - \mathbf{u}_j) - \frac{1}{\Delta t} \dot{\mathbf{u}}_j \tag{6.76}$$

The velocity of the actual time step $\dot{\mathbf{u}}_j$ is known, hence, replacing the acceleration in Eq. (6.64) with Eq. (6.76) leads to an equation, that depends on the unknown displacement for the new

time step \mathbf{u}_{j+1} , only. Linearisation of this residual (cf. Sect. 6.6.1)

$$\mathbf{r}^u(\mathbf{u}_{j+1}^{k+1}) = \mathbf{r}^u(\mathbf{u}_{j+1}^k) + \frac{\partial \mathbf{r}^u(\mathbf{u}_{j+1}^k)}{\partial \mathbf{u}_{j+1}^k} \cdot \Delta \mathbf{u}_{j+1}^{k+1} \quad \text{with} \quad \Delta \mathbf{u}_{j+1}^{k+1} = \mathbf{u}_{j+1}^{k+1} - \mathbf{u}_{j+1}^k \quad (6.77)$$

and using Eqs. (6.75) and (6.76) yields the stiffness matrix for an implicit dynamic procedure.

$$\mathbf{K}^{\text{dyn}} = \frac{1}{(\Delta t)^2} \mathbf{M} + \frac{1}{\Delta t} \mathbf{D} + \mathbf{K} \quad \text{with} \quad \mathbf{D} = \frac{\partial \mathbf{f}^{\text{int}}}{\partial \dot{\mathbf{u}}} \quad \text{and} \quad \mathbf{K} = \frac{\partial \mathbf{f}^{\text{int}}}{\partial \mathbf{u}} \quad (6.78)$$

Therein, \mathbf{D} represents the damping matrix of the problem, which has to be introduced afterwards and \mathbf{K} is the stiffness matrix of the quasi-static problem (cf. Sect. 6.6.1). As well, both matrices can be divided into a bulk and an interface contribution. (However, this is not presented.) The damping matrix could be introduced through RAYLEIGH damping [134, 135], as it is common in dynamics or through other viscous effects, that exist in the model and have to be considered. Again, through inversion the displacement increment is determined

$$\Delta \mathbf{u}_{j+1}^{k+1} = - \left[\mathbf{K}_{j+1}^{\text{dyn},k} \right]^{-1} \cdot \mathbf{r}_{j+1}^{u,k}, \quad (6.79)$$

and in the following the update of the displacement is performed.

$$\mathbf{u}_{j+1}^{k+1} = \mathbf{u}_{j+1}^k + \Delta \mathbf{u}_{j+1}^{k+1} \quad (6.80)$$

Finally, with the updated displacement and Eqs. (6.75) and (6.76) the velocity and acceleration can be updated and then the next time step can be evaluated.

6.7 Viscous Regularisation

In Sects. 6.6.1 and 6.6.2 the main equations which have to be solved are derived. Any way, due to the fracture process the stiffness matrix loses its positiv-definiteness and consequently leads to a destabilisation of the NEWTON-RAPHSON procedure (cf. e.g. YU ET AL. [77] or HAMITOCHE ET AL. [136]), which is a consequence of the negative material tangent matrix of the interface due to onset of damage. A further problem which arises due to the fracture process, and which is very important is that the solution of the initial boundary value problem is not unique, any more [75]. To overcome these problems we use the viscous regularisation technique, that leads to a positiv-definit stiffness matrix for sufficient small time-steps. Therein, we use the technique of ABAQUS [60]. An alternative would be to use the scheme of e.g. GAO & BOWER [76] or NEEDLEMAN [95]. In contrast to ABAQUS these schemes act on the material tangent matrix and not the stiffness matrix of the problem. The choice of the viscous regularisation scheme depends on the physical problem. In case that the deformation rate of a process is too fast, damping should be considered through a regularisation of the constitutive law. However, when the process is not really quasi-static then a regularisation on the stiffness matrix is necessary. This is the case here, due to the onset of cracking.

We begin with a simple experiment to explain the problem in more detail. Whereby, this experiment has no background and is only for illustrative purposes. Think of a body with a zero-thickness interface which is subjected to a mechanical load and boundary conditions. The body is fixed in e_1 direction and at the bottom in e_2 direction at the edges, and a load is applied at the top in e_2 direction. As it can be seen in Fig. 6.5 in the top, left-hand side picture. The top, right-hand side diagram of Fig. 6.5 presents the corresponding TSL, which is calculated in the point P_1 . Applying the NEWTON-RAPHSON procedure to solve the problem under quasi-static

(Eq. (6.67)) or dynamical (Eq. (6.79)) assumptions leads to a displacement history in the point P_2 , as it can be seen in Fig. 6.5 in the bottom, left-hand side diagram (solid blue line). The corresponding velocity history is presented in Fig. 6.5 in the bottom, right-hand side diagram (solid line). Due to the jump in the displacement and velocity history, the NEWTON-RAPHSON procedure fails to converge, usually and the simulation is aborted. This result occurs only, since the change in the displacement increment is too large. To overcome this problem a dissipative part in Eq. (6.67) or Eq. (6.79) is necessary. In ABAQUS this is done by adding a viscous force \mathbf{f}_{vis} to the residual vector \mathbf{r}^u . This viscous force is defined as

$$\mathbf{f}_{\text{vis},e} = c_{\text{vis}} \mathbf{M}_{\text{vis},e} \cdot \dot{\mathbf{u}}_e \quad (6.81)$$

for one element with c_{vis} as a solution dependent damping parameter which must be greater as zero. The artificial mass matrix is defined as

$$\mathbf{M}_{\text{vis},e} = b \int_{-1}^1 \int_{-1}^1 \mathbf{N}_u^T \cdot \mathbf{N}_u \det(\mathbf{J}_0) d\xi_1 d\xi_2 \quad (6.82)$$

and the velocity vector results from the backward EULER scheme (cf. Eq. (6.75)). Assembling element quantities leads the global ones, again. This step is omitted since it is presented, already. The linearisation of the global residual vector yields a viscous part of the stiffness matrix which is

$$\frac{\partial \mathbf{f}_{\text{vis}}}{\partial \mathbf{u}} = \frac{\partial \mathbf{f}_{\text{vis}}}{\partial \dot{\mathbf{u}}} \cdot \frac{\partial \dot{\mathbf{u}}}{\partial \mathbf{u}} = \frac{c_{\text{vis}}}{\Delta t} \mathbf{M}_{\text{vis}} \quad (6.83)$$

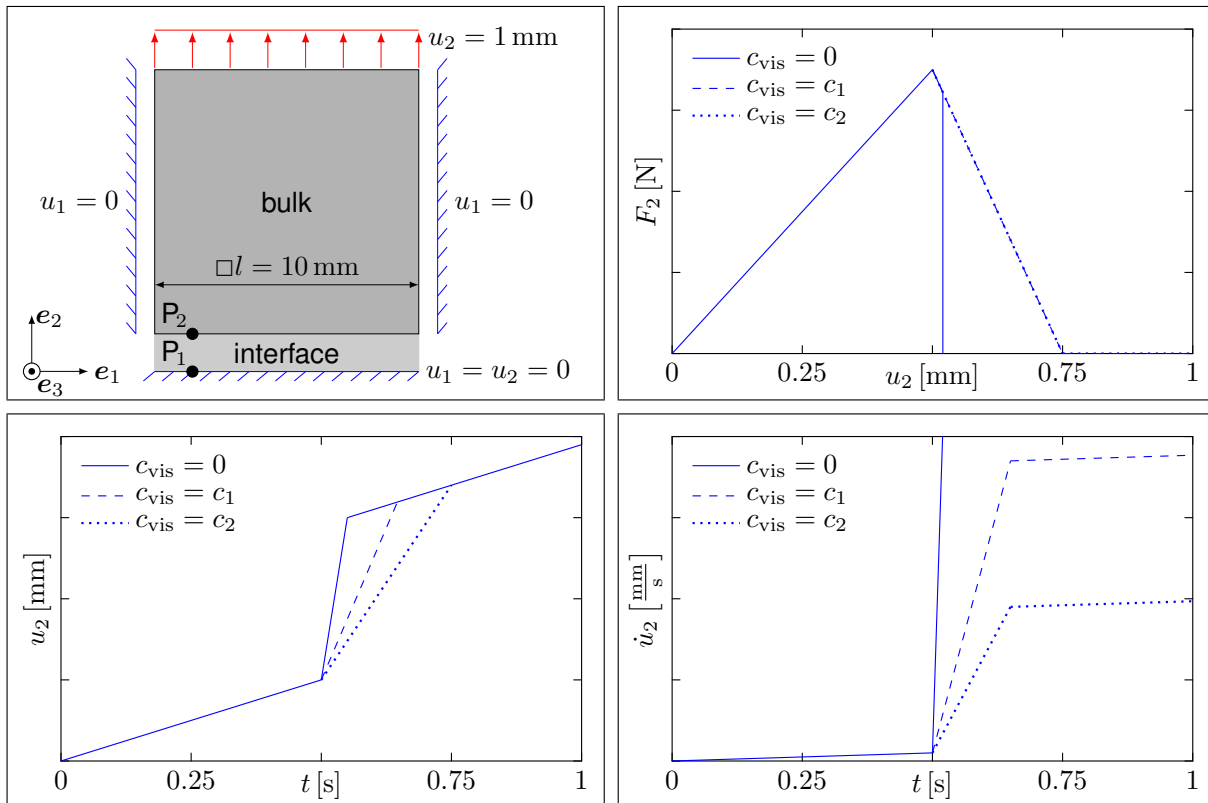


Figure 6.5: Experimental setup (top, left-hand side), TSL in point P_1 (right, left-hand side), displacement history (bottom, left-hand side) and velocity history (bottom, right-hand side) of point P_2 for different values of the damping parameter

and because of the dependence of Eq. (6.83) on the time step this term gets large when the time increment reduces during the fracture process which leads to a positive-definit stiffness matrix in the end. The change of the displacement and velocity history is presented in Fig. 6.5 in the bottom, left- and right-hand side diagram with $c_2 > c_1$. A damping parameter greater than zero yields a finite velocity and a lesser displacement jump and the NEWTON-RAPHSON scheme converges. However, the damping parameter c_{vis} must be chosen wisely, since the solution is influenced. Consequently, a too high value for the damping parameter will lead to no deformation at all because all energy is dissipated through the viscous term. Therefore, a control algorithm is necessary which adjusts the damping parameter according to the solution history. The control algorithm is based on the viscous and total energy of the problem. In all time steps the viscous energy should be a small fraction of the total energy. This guarantees, that the solution is not strongly influenced by the viscous regularisation scheme. If this holds not true, and the viscous energy is of the same magnitude as the total energy, this solution must be abandoned. The maximum allowed fraction in ABAQUS is 5%, whereby, the user can adjust this tolerance. To calculate the damping parameter in the first increment a second parameter is defined. ABAQUS calls this parameter dissipated energy fraction. By default this parameter is of value $2 \cdot 10^{-4}$ and can be adjusted by the user, as well. Further informations concerning this topic can be found in [60].

6.8 Discretisation of Constitutive Laws

This section presents the systematic derivation of discretised formulations of the constitutive laws which are presented in Section 5. It is started with the bulk materials and then the CZMs are discretised. In all cases the backward EULER operator is used because of absolute stability of the implicit integration scheme.

6.8.1 Coating Constitutive Law

The coating material behaves linear elastic, therefore, the inelastic deformation gradient is

$$\mathbf{F}_{\text{in}} = \mathbf{1},$$

then the multiplicative split reduces to

$$\mathbf{F} = \mathbf{F}_{\text{el}},$$

and Eq. (4.10)₃ yields the inelastic right CAUCHY-GREEN tensor with

$$\mathbf{C}_{\text{in}} = \mathbf{1}.$$

With this at hand from Eqs. (5.10) and (5.11) follows the formulation for the first PIOLA-KIRCHHOFF and the KIRCHHOFF stress tensor, respectively

$$\begin{aligned} \overset{\text{PK}}{\mathbf{T}}_{\text{c}} &= \frac{\lambda_{\text{c}}}{2} (J^2 - 1) \mathbf{F}^{-\top} + \mu_{\text{c}} (\mathbf{F} - \mathbf{F}^{-\top}), \\ \overset{\text{K}}{\mathbf{T}}_{\text{c}} &= \frac{\lambda_{\text{c}}}{2} (J^2 - 1) \mathbf{1} + \mu_{\text{c}} (\mathbf{F} \cdot \mathbf{F}^{\top} - \mathbf{1}) \end{aligned} \quad (6.84)$$

with the LAMÉ constants λ_{c} and μ_{c} of the coating material. For the numerical implementation of this constitutive law in Chap. 5 the material tangent matrix is required. This derivative is very

complex and can only be written down in index notation, wherein the element index is omitted.

$$\begin{aligned} \overset{\text{IFK}}{\mathcal{A}} = \frac{\partial \overset{\text{IFK}}{\mathbf{T}}_c}{\partial \mathbf{F}} = \overset{\text{IFK}}{A}_{c,ijmn} = \lambda_c J^2 F_{ji}^{-1} F_{nm}^{-1} \Big|_{ijmn} \\ - \left[\frac{\lambda_c}{2} (J^2 - 1) - \mu_c \right] F_{ni}^{-1} F_{jm}^{-1} \Big|_{ijmn} + \mu_c \delta_{im} \delta_{nj} \Big|_{ijmn} \end{aligned} \quad (6.85)$$

$$\overset{\text{K}}{\mathcal{A}} = \frac{\partial \overset{\text{K}}{\mathbf{T}}_c}{\partial \mathbf{F}} = \overset{\text{K}}{A}_{c,ijmn} = \lambda_c J^2 \delta_{ij}^{-1} F_{nm}^{-1} \Big|_{ijmn} + \mu_c [\delta_{im} F_{jn} + \delta_{jm} F_{in}] \Big|_{ijmn}$$

A detailed explanation is presented in the Appendix A. In the last step Eqs. (6.84) and (6.85) have to be transformed in vector-matrix notation and the backward EULER scheme is applied. Since in this work third- and fourth-order operator matrices are used no MANDEL [137] notation is introduced. Further on, this would be not necessary and not efficient because the deformation gradient is not symmetric. It results

$$\begin{aligned} \overset{\text{IFK}}{\mathbf{T}}_c \Big|_{j+1} &= \frac{\lambda_c}{2} (J^2 - 1) \mathbf{F}^{-\top} \Big|_{j+1} + \mu_c (\mathbf{F} - \mathbf{F}^{-\top}) \Big|_{j+1} \\ \overset{\text{K}}{\mathbf{T}}_c \Big|_{j+1} &= \frac{\lambda_c}{2} (J^2 - 1) \mathbf{1} \Big|_{j+1} + \mu_c (\mathbf{F} \cdot \mathbf{F}^{\top} - \mathbf{1}) \Big|_{j+1} \end{aligned} \quad (6.86)$$

for the stresses and

$$\begin{aligned} \overset{\text{IFK}}{A}_{c,iomn} \Big|_{j+1} &= \lambda_c J^2 F_{oi}^{-1} F_{nm}^{-1} \Big|_{j+1} - \left[\frac{\lambda_c}{2} (J^2 - 1) - \mu_c \right] F_{ni}^{-1} F_{om}^{-1} \Big|_{j+1} + \mu_c \delta_{im} \delta_{no} \\ \overset{\text{K}}{A}_{c,iomn} \Big|_{j+1} &= \lambda_c J^2 \delta_{io}^{-1} F_{nm}^{-1} \Big|_{j+1} + \mu_c [\delta_{im} F_{on} + \delta_{om} F_{in}] \Big|_{j+1} \end{aligned} \quad (6.87)$$

for the material tangent matrices. In these equations an alternative notation for the time step index $j+1$ is used to keep the equations short and clear.

6.8.2 Substrate Constitutive Law

The substrate material shows the presented inelastic material behaviour of Section 5.1. Hence, Eq. (5.10), Eq. (5.11) and Eqs. (5.14)–(5.18) are used. At first, Eqs. (5.10) and (5.11) are reformulated with the vector-matrix notation and ongoing both equations are discretised by applying the backward EULER scheme.

$$\begin{aligned} \overset{\text{IFK}}{\mathbf{T}}_s \Big|_{j+1} &= \frac{\lambda_s}{2} (J^2 - 1) \mathbf{F}^{-\top} \Big|_{j+1} + \mu_s (\mathbf{F} \cdot \mathbf{C}_{\text{in}}^{-1} - \mathbf{F}^{-\top}) \Big|_{j+1} \\ \overset{\text{K}}{\mathbf{T}}_s \Big|_{j+1} &= \frac{\lambda_s}{2} (J^2 - 1) \mathbf{1} \Big|_{j+1} + \mu_s (\mathbf{F} \cdot \mathbf{C}_{\text{in}}^{-1} \cdot \mathbf{F}^{\top} - \mathbf{1}) \Big|_{j+1} \end{aligned} \quad (6.88)$$

Like before, the next step is to derive the material tangent matrices.

$$\begin{aligned} \overset{\text{IFK}}{A}_{s,iomn} \Big|_{j+1} &= \lambda_s J^2 F_{oi}^{-1} F_{nm}^{-1} \Big|_{j+1} - \left[\frac{\lambda_s}{2} (J^2 - 1) - \mu_s \right] F_{ni}^{-1} F_{om}^{-1} \Big|_{j+1} \\ &+ \mu_s \left[\delta_{im} C_{\text{in},no}^{-1} + F_{ik} \frac{\partial C_{\text{in},ko}^{-1}}{\partial F_{mn}} \right] \Big|_{j+1} \end{aligned} \quad (6.89)$$

$$\begin{aligned} \left. A_{s,iomn}^k \right|_{j+1} &= \left. \lambda_s J^2 \delta_{io}^{-1} F_{nm}^{-1} \right|_{j+1} \\ &+ \mu_s \left[\delta_{im} C_{in,nl}^{-1} F_{ol} + F_{ik} \frac{\partial C_{in,kl}^{-1}}{\partial F_{mn}} F_{ol} + \delta_{om} F_{ik} C_{in,kn}^{-1} \right] \Big|_{j+1} \end{aligned} \quad (6.90)$$

The derivative of the inelastic right CAUCHY-GREEN matrix is derived through numerical derivation with the forward difference quotient. This is done since it is only required to use informations from the past and the presented time step. In index notation this derivative is written as

$$\left. \frac{\partial C_{in,kl}^{-1}}{\partial F_{mn}} \right|_{j+1} = \left. \frac{C_{in,kl}^{-1}(F_{mn} + \Delta F) - C_{in,kl}^{-1}(F_{mn})}{\Delta F} \right|_{j+1}. \quad (6.91)$$

Wherein, the increment of the deformation gradient ΔF is chosen to be of magnitude, thus, the floating point precision is not reduced. This leads to a value of $\Delta F = 7.5 \cdot 10^{-7}$. Another possibility is to determine this derivative from the total differential. However, this is too costly for the slight influence of this term. Finally, the time integration of Eq. (5.15) is required. Applying the backward EULER operator and reformulate the discretised equation in residual form yields

$$\mathbf{R}_{in} \Big|_{j+1} = [\mathbf{1} - \Delta t \mathbf{L}_{in}] \cdot \mathbf{F}_{in} \Big|_{j+1} - \mathbf{F}_{in} \Big|_j = \mathbf{0}. \quad (6.92)$$

This equation is governed by the dissipative stress

$$\mathbf{T}_d \Big|_{j+1} = \frac{1}{J} \left[\frac{\lambda_s}{2} (J^2 - 1) \mathbf{1} + \mu_s (\mathbf{C}_{el} - \mathbf{1}) \right] \Big|_{j+1}$$

which results from the elastic deformation gradient

$$\mathbf{F}_{el} \Big|_{j+1} = \mathbf{F} \cdot \mathbf{F}_{in}^{-1} \Big|_{j+1}$$

and the linearisation leads to

$$\mathbf{R}_{in} \Big|_{j+1} \approx \mathbf{R}_{in} \Big|_{j+1} + \frac{\partial \mathbf{R}_{in}}{\partial \mathbf{F}_{in}} : \Delta \mathbf{F}_{in} \Big|_{j+1} = \mathbf{0}. \quad (6.93)$$

The fourth-order tangent matrix is determined with the forward difference scheme. This is done in almost the same manner as in Eq. (6.91). A slight difference occurs due to the symmetry of the inelastic deformation gradient. Therefore, we apply the MANDEL scheme [137] to transform the residual matrix and the fourth-order tangent matrix into a vector and a matrix. After this the NEWTON-RAPHSON procedure is used to solve the problem. Due to the integration scheme (backward EULER) the assumed property that the inelastic deformation is isochoric gets lost. To overcome this problem the exponential mapping technique is used [138, 139] which is the basis for a time stepping algorithm, as well. This is explained in Section 6.9. After the exponential mapping Eq. (6.92) is reformulated.

$$\mathbf{R}_{in} \Big|_{j+1} = \mathbf{Y} \cdot \mathbf{F}_{in} \Big|_{j+1} - \mathbf{F}_{in} \Big|_j = \mathbf{0} \quad \text{with } \mathbf{Y} \Big|_{j+1} = \exp(-\Delta t \mathbf{L}_{in}) \Big|_{j+1} \quad (6.94)$$

6.8.3 Cohesive-Zone-Model for Cracking

The discretisation of Eqs. (5.39) and (5.40) is simple. At the beginning of each time step the separation vector for one element \mathbf{g} (element index is omitted) is determined with Eq. (6.46) for the next time step $j+1$. When this is done Eqs. (5.39) and (5.40) can be evaluated to get the

tractions for the next time step. These are

$$T_n|_{j+1} = \frac{27}{4} T_{\max} \left[\frac{g_n}{g_{cr}} \left(1 - 2 \frac{g_n}{g_{cr}} + \left(\frac{g_n}{g_{cr}} \right)^2 \right) + \beta \left(\frac{g_{t1}}{g_{cr}} \right)^2 \left(\frac{g_n}{g_{cr}} - 1 \right) \right] \Big|_{j+1} \quad (6.95)$$

$$T_{t1}|_{j+1} = \frac{27}{4} T_{\max} \beta \frac{g_{t1}}{g_{cr}} \left(1 - 2 \frac{g_n}{g_{cr}} + \left(\frac{g_n}{g_{cr}} \right)^2 \right) \Big|_{j+1} \quad (6.96)$$

in the case that $g_n > 0$. In the contact case $g_n \leq 0$ Eq. (5.42) is evaluated to determine the tractions.

$$T_n|_{j+1} = C_p g_n|_{j+1} \quad (6.97)$$

$$T_{t1}|_{j+1} = C_p g_{t1}|_{j+1} \quad (6.98)$$

The contact stiffness is ten times higher than the stiffness for the case of a positive normal separation. Such a simple contact relation is chosen to reduce the numerical problems resulting from a contact formulation. For example, when a LAGRANGE multiplier is used it could happen, that the separation gets positive and then the TSL is used instead of the contact formulation. Hence, the required number of iterations in one time step will drastically increase, and finally the algorithm fails to converge. The material tangent matrix contains four components with the following arrangement.

$$\mathbf{A}_{cr}|_{j+1} = \begin{bmatrix} \frac{\partial T_n}{\partial g_n} & \frac{\partial T_n}{\partial g_{t1}} \\ \frac{\partial T_{t1}}{\partial g_n} & \frac{\partial T_{t1}}{\partial g_{t1}} \end{bmatrix} \Big|_{j+1} \quad (6.99)$$

These components are derived from Eqs. (6.95) and (6.96) and Eqs. (6.97) and (6.98), respectively. For no contact ($g_n > 0$) results

$$\frac{\partial T_n}{\partial g_n} \Big|_{j+1} = \frac{27}{4} T_{\max} \frac{(g_{cr}^2 - 4g_{cr}g_n + 3g_n^2 + \beta g_{t1}^2)}{g_{cr}^3} \Big|_{j+1}, \quad (6.100)$$

$$\frac{\partial T_n}{\partial g_{t1}} \Big|_{j+1} = -\frac{27}{2} T_{\max} \beta g_{t1} \frac{(g_{cr} - g_n)}{g_{cr}^3} \Big|_{j+1}, \quad (6.101)$$

$$\frac{\partial T_{t1}}{\partial g_n} \Big|_{j+1} = -\frac{27}{2} T_{\max} \beta g_{t1} \frac{(g_{cr} - g_n)}{g_{cr}^3} \Big|_{j+1}, \quad (6.102)$$

$$\frac{\partial T_{t1}}{\partial g_{t1}} \Big|_{j+1} = \frac{27}{4} T_{\max} \beta \frac{(g_{cr} - g_n)^2}{g_{cr}^3} \Big|_{j+1}, \quad (6.103)$$

and for the case of contact ($g_n \leq 0$)

$$\frac{\partial T_n}{\partial g_n} \Big|_{j+1} = C_p, \quad (6.104)$$

$$\frac{\partial T_n}{\partial g_{t1}} \Big|_{j+1} = 0, \quad (6.105)$$

$$\frac{\partial T_{t1}}{\partial g_n} \Big|_{j+1} = 0, \quad (6.106)$$

$$\left. \frac{\partial T_{t1}}{\partial g_{t1}} \right|_{j+1} = C_p. \quad (6.107)$$

6.8.4 Cohesive-Zone-Model for Delamination

The solution of the TSL is obtained by applying the backward EULER scheme to the equations and obtain the solution through a NEWTON-RAPHSON procedure. At first, it is assumed that the influence of the derivatives with respect to the temperature is slight and can be neglected. With this the equations simplify to

$$\mathbf{t}_i = \frac{(1-d)^2}{g_{del}} \mathbf{C}_i \cdot \mathbf{g}_{el} \quad (6.108)$$

$$\mathbf{g}_{el} = \mathbf{g} - \mathbf{g}_{in} \quad (6.109)$$

$$\dot{\mathbf{g}}_{in} = \frac{a_i g_{del}}{(1-d)} \left[\frac{|\mathbf{t}_i|}{T_{i0}} \right]^{N_i} \frac{\mathbf{t}_i}{|\mathbf{t}_i|} \quad (6.110)$$

$$Y_E = \frac{(1-d)}{g_{del}} \mathbf{g}_{el}^\top \cdot \mathbf{C}_i \cdot \mathbf{g}_{el}, \quad (6.111)$$

$$\dot{d} = \frac{(1-d)}{g_{del}} \left(\frac{Y_E - Y_{E0}}{S_{i0}} \right) |\dot{\mathbf{g}}_{in}| \quad (6.112)$$

in vector-matrix form. Up next, the backward EULER scheme is applied to discretise the equations and then we arrange these equations in a residual vector. For a more compact notation we introduce the following abbreviations and normalise the separation \mathbf{g} with the parameter $g_{del} = 1 \text{ mm}$ and get a strain which has the magnitude of the separation (cf. [60]).

$$c_1 \Big|_{j+1} = a_i \left[\frac{|\mathbf{t}_i|}{T_{i0}} \right]^{N_i} \Big|_{j+1}$$

$$c_2 \Big|_{j+1} = \frac{Y_E - Y_{E0}}{S_{i0}} \Big|_{j+1}$$

$$\mathbf{c}_1 \Big|_{j+1} = 2 \mathbf{g}_{in} \Big|_{j+1} - \mathbf{g}_{in} \Big|_j - \mathbf{g} \Big|_{j+1}$$

$$\mathbf{C}_1 \Big|_{j+1} = \frac{g_{del}}{(1-d)^2} \mathbf{C}_i^{-1} \Big|_{j+1}$$

$$\mathbf{C}_2 \Big|_{j+1} = \mathbf{1} + \frac{(N_i - 1)}{|\mathbf{t}_i|^2} \mathbf{t}_i \cdot \mathbf{t}_i^\top \Big|_{j+1}$$

Notice that through the matrix \mathbf{C}_2 a coupling between normal and tangential separation occurs, hence, mix-mode occurs when $N_i > 1$. It is a result of the creep behaviour. This coupling can be avoided by assuming that the interface has a linear dependence between inelastic separation and traction ($N_i = 1$), see [62]. Consequently, the constitutive matrix of the cohesive zone \mathbf{C}_i (cf. App. A) has a diagonal structure only for the beginning, as long as no inelastic separation occurs. The traction part of the residual vector is

$$\mathbf{r}_t \Big|_{j+1} = \mathbf{C}_1 \cdot \mathbf{t}_i \Big|_{j+1} - \mathbf{g} \Big|_{j+1} + \mathbf{g}_{in} \Big|_j + \Delta t \frac{g_{del}}{(1-d)} c_1 \frac{\mathbf{t}_i}{|\mathbf{t}_i|} \Big|_{j+1} = \mathbf{o}, \quad (6.113)$$

and the damage part yields

$$r_d \Big|_{j+1} = d \Big|_{j+1} - d \Big|_j - \Delta t c_1 c_2 \Big|_{j+1} = 0. \quad (6.114)$$

These parts form the residual vector $\mathbf{r}_{\text{del}} = [\mathbf{r}_t^T \quad r_d]^T$ which is linearised

$$\mathbf{r}_{\text{del}} \approx \mathbf{r}_{\text{del}}^k + \frac{\partial \mathbf{r}_{\text{del}}^k}{\partial \mathbf{y}_{j+1}^k} \cdot \Delta \mathbf{y}_{j+1}^k = \mathbf{r}_{\text{del}}^k + \mathbf{S}_{j+1}^k \cdot \Delta \mathbf{y}_{j+1}^k = \mathbf{o}, \quad (6.115)$$

and the resulting system of equations is solved by applying the common NEWTON-RAPHSON procedure with iteration index k

$$\Delta \mathbf{y}_{j+1}^k = - [\mathbf{S}_{j+1}^k]^{-1} \cdot \mathbf{r}_{\text{del}}^k. \quad (6.116)$$

This is followed by the update of the unknown vector \mathbf{y} for the next iteration until the residual reaches a user specified tolerance ($1 \cdot 10^{-5}$).

$$\mathbf{y}_{j+1}^{k+1} = \mathbf{y}_{j+1}^k + \Delta \mathbf{y}_{j+1}^k \quad (6.117)$$

The tangent matrix consists of four sub-matrices:

$$\begin{aligned} \mathbf{S}_{11} &= \frac{\partial \mathbf{r}_t}{\partial \mathbf{t}_i} \Big|_{j+1} = \mathbf{C}_1 \Big|_{j+1} + \frac{c_1 g_{\text{del}}}{(1-d) |\mathbf{t}_i|} \mathbf{C}_2 \Big|_{j+1} \\ \mathbf{S}_{12} &= \frac{\partial \mathbf{r}_t}{\partial d} \Big|_{j+1} = \frac{2}{(1-d)} \mathbf{C}_1 \cdot \mathbf{t}_i \Big|_{j+1} + \Delta t \frac{c_1 g_{\text{del}}}{(1-d)^2 |\mathbf{t}_i|} \mathbf{t}_i \Big|_{j+1} \\ \mathbf{S}_{21} &= \frac{\partial r_d}{\partial \mathbf{t}_i^T} \Big|_{j+1} = \Delta t c_1 \left[\frac{1}{(1-d) S_{i0}} \mathbf{C}_1^T - \frac{N_i c_2}{|\mathbf{t}_i|^2} \mathbf{t}_i^T \right] \Big|_{j+1} \\ \mathbf{S}_{22} &= \frac{\partial r_d}{\partial d} \Big|_{j+1} = 1 + \frac{c_1}{(1-d)^2 S_{i0}} \mathbf{C}_1 \cdot \mathbf{t}_i \Big|_{j+1} \end{aligned}$$

They are arranged in the tangent matrix in the following fashion.

$$\mathbf{S}_{j+1}^k = \begin{bmatrix} \mathbf{S}_{11} & \mathbf{S}_{12} \\ \mathbf{S}_{21} & \mathbf{S}_{22} \end{bmatrix}$$

After the successful solution inelastic separation and elastic energy release rate for the next time increment are recalculated.

$$\mathbf{g}_{\text{in}} \Big|_{j+1} = \mathbf{g}_{\text{in}} \Big|_j + \Delta t \frac{c_1 g_{\text{del}}}{(1-d) |\mathbf{t}_i|} \mathbf{t}_i \Big|_{j+1} \quad (6.118)$$

$$Y_E \Big|_{j+1} = \frac{(1-d)}{g_{\text{del}}} \mathbf{g}_{\text{el}}^T \cdot \mathbf{C}_i \cdot \mathbf{g}_{\text{el}} \Big|_{j+1} \quad (6.119)$$

Since of this implementation of the TSL the material tangent matrix for the element stiffness matrix follows from the inversion of \mathbf{S}_{11} in every time step (cf. WRIGGERS [123] for more details).

$$\mathbf{A}_{\text{del}} = \mathbf{S}_{11}^{-1} \quad (6.120)$$

This has the benefit that it is not necessary to calculate the material tangent matrix after the solution of the constitutive law in a time step.

6.9 Time Stepping Algorithm

As it is mentioned in Sect. 6.8.2, the integration algorithm is not able to ensure that the inelastic deformation keeps isochoric for arbitrary time increments. This requirement founds the basis for a time stepping algorithm and this algorithm ensures that the inelastic deformation keeps isochoric for a sufficient small time step. Therefore, the exponential mapping is performed, and for a more comprehensive formulation we skip the index $j+1$. The TAYLOR series expansion of \mathbf{Y} yields

$$\mathbf{Y} = \sum_{k=0}^{\infty} \frac{(-\Delta t \mathbf{L}_{\text{in}})^k}{k!} = \mathbf{1} - \Delta t \mathbf{L}_{\text{in}} + \frac{1}{2} (\Delta t \mathbf{L}_{\text{in}})^2 - \frac{1}{6} (\Delta t \mathbf{L}_{\text{in}})^3 + \dots$$

and for sufficient small time steps Δt the quadratic, cubic and all higher terms can be neglected in the TAYLOR series expansion. Under this condition only the constant and the linear term remain, which yields the same expression as through the application of the backward EULER scheme (cf. Eq. (6.92)). Therefore, we can abort the series expansion in an analytical consideration after the linear term, and use the quadratic term to control the time increment. Since it holds true, if the time step is sufficient small, that

$$\frac{1}{2} (\Delta t \mathbf{L}_{\text{in}})^2 = \mathbf{0}. \quad (6.121)$$

In a numerical sense this is not possible. To overcome this we define a tolerance and take the norm of the inelastic velocity gradient. It follows

$$\frac{\Delta t^2}{2} \|\mathbf{L}_{\text{in}}^2\| \leq \text{tol}. \quad (6.122)$$

If this holds true, the time step is increased for the next increment, and if this is not true, the actual time increment is aborted, the time step is reduced and the calculation of the increment starts again. The quadrature of the inelastic velocity matrix is performed through the spectral decomposition of this one. Otherwise, the quadrature is not possible. The spectral decomposition for the inelastic velocity matrix leads to

$$\mathbf{L}_{\text{in}} = \sum_{i=1}^3 \frac{\alpha_i}{|\mathbf{v}_i|^2} \mathbf{v}_i \cdot \mathbf{v}_i^{\top} \iff \mathbf{L}_{\text{in}}^2 = \sum_{i=1}^3 \frac{\alpha_i^2}{|\mathbf{v}_i|^2} \mathbf{v}_i \cdot \mathbf{v}_i^{\top} \quad (6.123)$$

with the eigenvalues α_i and corresponding eigenvectors \mathbf{v}_i . The formulas for determination of eigenvalues and eigenvectors are summarised in Appendix A. This section is closed with the words of SIMO: "... , the exponential mapping is the crucial tool in formulating time stepping algorithms." [139].

7 Damage Gradient Extension of a Cohesive Zone Model

In contrast to their efficient application and implementation, CZMs cause some numerical problems. When the peak traction of TSL is reached, the numerical solution scheme gets unstable due to e.g. snap-back effects, which occur because of the softening behaviour [76, 140] and the solution starts to oscillate (depending on the discretisation) [75]. Usually, the solution scheme is a NEWTON-RAPHSON procedure as in this work. Further on, the shape of TSL is dependent on the mesh-size (spatial discretisation of the problem) because the continuum constitutive relation is between stress and strain, while the cohesive constitutive relation is between force and displacement, respectively traction and separation [57]. All this is mentioned in Chap. 3 in more detail and is only mentioned again to found the basis for this chapter.

Nowadays, the Phase-Field-Method (PFM) is very popular for the simulation of problems in fracture mechanics. In contrast to common continuum mechanics in which the balance laws are the main equations that have to be solved, in the PFM the damage evolution equation is added to the equations of balance of the problem through micro mechanical investigations. Hence, the damage variable is treated as a DOF of the problem like displacements or the temperature and is no longer an internal variable, any more. Further on, the gradient of the damage is added to the problem, which accounts for non-local phenomena at the crack tip, like the growth of cavities or coalescence of micro voids or cracks. Another reason is that this should produce a smooth transition between the separated crack surfaces (smears the displacement jump in case of cracking).

In this work we apply the principles of the PFM to the TSL of Sect. 5.2.2 to investigate the influences and solve the size dependence of a CZMs through this extension, maybe. However, for this investigation we neglect the inelastic component in the separation vector for reasons of simplicity.

7.1 Damage Gradient Extension of the Novel Traction Separation Law

The equations of balance which are presented in Chap. 4 are still valid as well as the CLAUSIUS-DUHEM-inequality. However, Eq. (4.53) loses validity. For the damage gradient extension of the TSL the free energy depends on the damage gradient next to separation, damage and temperature.

$$\psi_i = f(\mathbf{g}, d, \nabla d, \theta) \quad (7.1)$$

This can be split up into a mechanical and a thermal part, for sure. From Eq. (7.1) the common expressions for the traction (Eq. (4.65)) without inelastic separation and the entropy (Eq. (4.68)) are derived. Up to this point no equation changed due to the damage gradient. Since the dissipation inequality is the only equation, which is influenced by this extension. It changes to

$$-\frac{\partial \psi_i}{\partial d} \dot{d} - \frac{\partial \psi_i}{\partial (\nabla d)} \cdot (\nabla \dot{d}) \geq 0 \quad (7.2)$$

by negligence of the temperature. These results follow from the rate independence of the CLAUSIUS-DUHEM-inequality, again. Up next, the mechanical part of the free energy potential is defined. It is additively decomposed into a local and a non-local part.

$$\psi_i^{\text{mech}} = \underbrace{\frac{1}{2} \frac{(1-d)^2}{g_{\text{del}}} \mathbf{g} \cdot \mathbf{C}_i \cdot \mathbf{g}}_{\text{local}} + \underbrace{\frac{G_s}{2s} [d^2 + s^2 |\nabla d|^2]}_{\text{non-local}} \quad (7.3)$$

From this potential results the traction relation

$$\mathbf{t} = \frac{(1-d)^2}{g_{\text{del}}} \mathbf{C}_i \cdot \mathbf{g}, \quad (7.4)$$

thermal part is neglected and the local term is known from Section 5.2. The non-local part is formulated as a quadratic function too, with the energy conductivity G_s and length scale parameter s , similar, as in phase field modelling [141]. Contrary, in phase field modelling the parameter G_s is the fracture energy of the surface G_c . Here, this interpretation is not possible because a CZM is formulated on a surface, already. Hence, the dimension of G_s is N or $\frac{\text{mJ}}{\text{mm}}$ and not $\frac{\text{N}}{\text{mm}}$ or $\frac{\text{mJ}}{\text{mm}^2}$. Therefore, we interpret the material parameter G_s as an energy conductivity in the direction of the damage gradient.

Up next, we have to define an evolution equation. Therefore, it is necessary to integrate Eq. (7.2) again which leads to

$$\int_{\mathcal{I}} -\frac{\partial \psi_i}{\partial d} \dot{d} - \frac{\partial \psi_i}{\partial (\nabla d)} \cdot (\nabla \dot{d}) \, dA \geq 0. \quad (7.5)$$

The terms with the damage variable can be transformed by considering product rule, GAUSS' divergence theorem and the requirement that scalar product between normal vector of the interface and damage gradient is zero on the boundaries. The applied procedure is the same as the one used in phase field modelling [25]. It results

$$\int_{\mathcal{I}} \underbrace{-\left[\frac{\partial \psi_i}{\partial d} - \nabla \cdot \frac{\partial \psi_i}{\partial (\nabla d)} \right]}_{Y_E} \dot{d} \, dA \geq 0, \quad (7.6)$$

which can be localised after the introduction of thermodynamic driving force or elastic energy release rate Y_E . The final form reads

$$Y_E \dot{d} \geq 0 \quad \text{with} \quad Y_E = -\left[\frac{\partial \psi_i}{\partial d} - \nabla \cdot \frac{\partial \psi_i}{\partial (\nabla d)} \right]. \quad (7.7)$$

This looks familiar, however, because of the damage gradient extension the relation for elastic energy release rate has changed compared to Equation (5.44). To guarantee that the second term of Eq. (7.7) is always positive, Eq. (5.48) is applied with negligence of the inelastic separation velocity.

$$\dot{d} = (1-d) \left(\frac{Y_E - Y_{E0}}{S_{i0}} \right) \quad (7.8)$$

Further on, same restrictions hold for damage evolution as in the case of no gradient extension.

$$\mathbf{g} \cdot \mathbf{n}_i \geq 0, \quad Y_E > Y_{E0}, \quad \dot{Y}_E \geq 0$$

Finally, from Eq. (7.7) the formulation of energy release rate is derived.

$$Y_E = \frac{(1-d)}{g_{del}} \mathbf{g} \cdot \mathbf{C}_i \cdot \mathbf{g} - \frac{G_s}{s} \left[d - s^2 (\nabla \cdot \nabla d) \right] \quad (7.9)$$

7.2 Finite Element Implementation of the Traction Separation Law with Damage Gradient Extension

FE implementation of the damage gradient extended TSL differs slightly from the implementation presented in Chapter 6. Further on, the implementation is only presented for the isothermal case but the extension of the procedure to the non-isothermal case is straight forward. It is only necessary to add the balance of energy to the system of PDEs, which needs to be solved through the FEM. At first, we analyse the balance of linear momentum. It results the same virtual work contribution for the interface which is already presented in Section 6.5. It is

$$\delta W_{i,e}^{int} = b \int_{-1}^1 \delta \mathbf{u}_N^T \cdot \mathbf{Z}_{u,e}^T \cdot \mathbf{t}_{i,e} |z_{2e}| d\xi_1 = \delta \mathbf{u}_N^T \cdot \mathbf{f}_{i,e}^{int} \quad (7.10)$$

for one element and the separation for one element is determined after Equation (6.58). Now, we begin with the discretisation of the damage evolution equation for one element. Since the second derivative of the damage variable is required for the elastic energy release rate, it is necessary to use quadratic shape functions to approximate the element quantities, at least. This leads to a constant gradient of the damage gradient. For shape functions of lower order the damage gradient vanishes from the discretised FE equations and an extension of the TSL with damage gradient would not be necessary. The plane quadratic cohesive element, which is used in this work and implemented into the commercial FE code ABAQUS using the UEL subroutine is presented in Fig. 6.4. We begin with introducing the damage variable vector, that contains the scalar damage variable of every node for one element.

$$\mathbf{d}_N = [d_N^1 \quad d_N^2 \quad \dots \quad d_N^{NN}]^T \quad (7.11)$$

This vector is used to approximate the damage variable and the variation of the damage variable for one element through the multiplication of this one with the damage shape function matrix \mathbf{N}_d and a relation matrix \mathbf{M}_d .

$$\begin{aligned} d_e &= \frac{1}{2} \mathbf{N}_d \cdot \mathbf{M}_d \cdot \mathbf{d}_N = \mathbf{Z}_{d,e} \cdot \mathbf{d}_N & \text{with } \mathbf{Z}_{d,e} &= \frac{1}{2} \mathbf{N}_d \cdot \mathbf{M}_d \\ \delta d_e &= \frac{1}{2} \mathbf{N}_d \cdot \mathbf{M}_d \cdot \delta \mathbf{d}_N = \mathbf{Z}_{d,e} \cdot \delta \mathbf{d}_N \end{aligned} \quad (7.12)$$

The presented determination is similar to the determination of the interface temperature θ_i . A mean value is determined in Eq. (7.12) because a cohesive element has no integration points in the normal direction, hence, damage cannot vary in the normal direction, which leads to the problem that the maximum damage value is 2 in the case of total failure. To overcome this the mean value is determined. Up next, Eq. (7.8) is discretised with the backward EULER operator and the variation is performed. This leads to

$$\delta D_{i,e} = \int_{\mathcal{I}} \delta d_e \left[\dot{d}_e - (1-d_e) \left(\frac{Y_E - Y_{E0}}{S_{i0}} \right) \right] dA = 0, \quad (7.13)$$

wherein the time step indices " $j+1$ " and " j " are omitted for reasons of clarity, again. Inserting Eq. (7.12) into Eq. (7.13) yields the approximated damage evolution equation for one element.

$$\delta D_{i,e} = b \int_{-1}^1 \delta \mathbf{d}_N^\top \cdot \mathbf{z}_{d,e}^\top \cdot \left[\mathbf{z}_{d,e} \cdot \mathbf{d}_N - (1 - \mathbf{z}_{d,e} \cdot \mathbf{d}_N) \left(\frac{Y_E - Y_{E0}}{S_{i0}} \right) \right] |\mathbf{z}_{2e}| d\xi_1 = 0 \quad (7.14)$$

A more practical formulation of Eq. (7.14) is

$$\delta D_{i,e} = \delta \mathbf{d}_N^\top \cdot \mathbf{r}_{i,e}^d. \quad (7.15)$$

The allocation of all element quantities resulting from Eq. (7.14) or Eq. (7.15) yields the complete approximation of the damage evolution equation.

$$\delta D_i = \bigcup_{i=1}^{NE} \delta D_{i,e_i} \quad (7.16)$$

The solution of the system of PDEs resulting from Eqs. (6.67) and (7.16) is obtained only for the quasi-static case through linearisation of the residual vectors and applying the NEWTON-RAPHSON procedure. The required stiffness matrix can be divided into eight different contributions

$$\begin{aligned} \mathbf{K}_b^{uu} &= \frac{\partial \mathbf{f}_b^{\text{int}}}{\partial \mathbf{u}} & \mathbf{K}_b^{\text{ud}} &= \frac{\partial \mathbf{f}_b^{\text{int}}}{\partial \mathbf{d}} & \mathbf{K}_b^{\text{du}} &= \frac{\partial \mathbf{r}_b^d}{\partial \mathbf{u}} & \mathbf{K}_b^{\text{dd}} &= \frac{\partial \mathbf{r}_b^d}{\partial \mathbf{d}} \\ \mathbf{K}_i^{uu} &= \frac{\partial \mathbf{f}_i^{\text{int}}}{\partial \mathbf{u}} & \mathbf{K}_i^{\text{ud}} &= \frac{\partial \mathbf{f}_i^{\text{int}}}{\partial \mathbf{d}} & \mathbf{K}_i^{\text{du}} &= \frac{\partial \mathbf{r}_i^d}{\partial \mathbf{u}} & \mathbf{K}_i^{\text{dd}} &= \frac{\partial \mathbf{r}_i^d}{\partial \mathbf{d}} \end{aligned}$$

which are arranged as follows

$$\mathbf{K} = \begin{bmatrix} \mathbf{K}_b^{uu} & \mathbf{K}_b^{\text{ud}} \\ \mathbf{K}_b^{\text{du}} & \mathbf{K}_b^{\text{dd}} \end{bmatrix} + \begin{bmatrix} \mathbf{K}_i^{uu} & \mathbf{K}_i^{\text{ud}} \\ \mathbf{K}_i^{\text{du}} & \mathbf{K}_i^{\text{dd}} \end{bmatrix}.$$

The first index refers to the corresponding residual vector (\mathbf{r}^u or \mathbf{r}^d) and the second index refers to the corresponding *DOF* vector (\mathbf{u} or \mathbf{d}). Before we go on and derive the explicit expression for every component, it is necessary to approximate Equation (7.9). The first term of Eq. (7.9) is approximated easily but the damage gradient term is difficult because it is necessary to determine the second derivatives in the normal and tangential direction. For the reason that it exists no element coordinate in the normal direction, it only remains the derivative in tangential direction (z_1). It follows with the chain rule:

$$\frac{\partial d_e}{\partial z_{1e}} = \frac{1}{2} \frac{\partial \mathbf{N}_d}{\partial \xi_1} \frac{\partial \xi_1}{\partial z_{1e}} \cdot \mathbf{M}_d \cdot \mathbf{d}_N = \frac{1}{2 |\mathbf{z}_{2e}|} \frac{\partial \mathbf{N}_d}{\partial \xi_1} \cdot \mathbf{M}_d \cdot \mathbf{d}_N. \quad (7.17)$$

Equation (7.17) is the approximation of the damage gradient, which is a linear function of the natural element coordinate ξ_1 because quadratic shape functions are used. Hence, the second derivative exists and is constant. The expression is

$$\frac{\partial^2 d_e}{\partial z_{1e}^2} = \frac{1}{2 |\mathbf{z}_{2e}|^2} \frac{\partial^2 \mathbf{N}_d}{\partial \xi_1^2} \cdot \mathbf{M}_d \cdot \mathbf{d}_N. \quad (7.18)$$

Wherein, we neglected the derivative of the normal vector with respect to the element coordinate, with the assumption that the influence is only slight, as it is done for the internal virtual work of the interface. Further on, this leads to great simplification. Insertion of Eq. (7.18) into

Eq. (7.9) yields the approximation of the elastic energy release rate.

$$Y_{E,e} = \frac{(1 - \mathbf{z}_{d,e} \cdot \mathbf{d}_N)}{g_{del}} \mathbf{g}^\top \cdot \mathbf{C}_i \cdot \mathbf{g} - \frac{G_s}{s} \left[\mathbf{z}_{d,e} \cdot \mathbf{d}_N - s^2 \frac{\partial^2 d_e}{\partial z_{1e}^2} \right] \quad (7.19)$$

Next to that, a dimensionless parameter χ is introduced, that describes the ratio of the length scale parameter s and the element length l_{ele} . This parameter is defined as

$$\chi = \frac{s}{l_{ele}} > 0 \quad (7.20)$$

and must be larger than zero to guarantee convergence of the model ($\chi=0$ results in a singular JACOBIAN). However, a value of χ in the range of zero to one results in a very coarse approximation with unfeasible results. MIEHE [142] recommend choosing χ larger than two.

Now, all required quantities are known and the contributions of the stiffness matrix can be determined. First, we analyse briefly the bulk part in which no damage evolves, hence, from the statement $\dot{d} = 0$ results the following stiffness matrix $\mathbf{K}_{b,e}^{dd}$ for one element:

$$\mathbf{K}_{b,e}^{dd} = b \int_{-1}^1 \int_{-1}^1 \frac{1}{\Delta t} \mathbf{N}_d^\top \cdot \mathbf{N}_d \det(\mathbf{J}_0) d\xi_1 d\xi_2, \quad (7.21)$$

which yields after allocation \mathbf{K}_b^{dd} . The mixed contributions $\mathbf{K}_b^{ud} = \mathbf{K}_b^{du} = \mathbf{0}$ and the contribution \mathbf{K}_b^{uu} is determined from the allocation of Eq. (6.71)₁. For the interface contributions Eqs. (6.60) and (7.14) are used, and as usual, at first the equations are derived for one element and then the global equations follow from the allocation of the element parts. The pure displacement part $\mathbf{K}_{i,e}^{uu}$ is known from Sect. 6.5 and is not presented (cf. Eq. (6.71)₃). The derivative of Eq. (6.60) with respect to the damage vector yields

$$\mathbf{K}_{i,e}^{ud} = b \int_{-1}^1 \mathbf{z}_{u,e}^\top \cdot \frac{\partial \mathbf{t}_{i,e}}{\partial \mathbf{d}_N^\top} |\mathbf{z}_{2e}| d\xi_1 \quad (7.22)$$

for one element and through derivation of Eq. (7.14) with respect to the displacement vector results

$$\mathbf{K}_{i,e}^{du} = -b \int_{-1}^1 \frac{(1 - \mathbf{z}_{d,e} \cdot \mathbf{d}_N)}{S_{i0}} \mathbf{z}_{d,e}^\top \cdot \frac{\partial Y_{E,e}}{\partial \mathbf{g}_e^\top} \cdot \mathbf{z}_{u,e} |\mathbf{z}_{2e}| d\xi_1 \quad (7.23)$$

and through derivation of Eq. (7.14) with respect to the damage vector results

$$\mathbf{K}_{i,e}^{dd} = b \int_{-1}^1 \left[\left(\frac{1}{\Delta t} + \frac{(Y_{E,e} - Y_{E0})}{S_{i0}} \right) \mathbf{z}_{d,e}^\top \cdot \mathbf{z}_{d,e} - \frac{(1 - \mathbf{z}_{d,e} \cdot \mathbf{d}_N)}{S_{i0}} \mathbf{z}_{d,e}^\top \cdot \frac{\partial Y_{E,e}}{\partial \mathbf{d}_N^\top} \right] |\mathbf{z}_{2e}| d\xi_1 \quad (7.24)$$

for one element, as well. Allocation of the element contributions leads to the four interface parts for the global stiffness matrix \mathbf{K} . The required derivatives in Eqs. (7.22)–(7.24) are

$$\frac{\partial \mathbf{t}_{i,e}}{\partial \mathbf{d}_N^\top} = - \frac{2(1 - \mathbf{z}_{d,e} \cdot \mathbf{d}_N)}{g_{del}} \mathbf{C}_i \cdot \mathbf{g} \cdot \mathbf{z}_{d,e}, \quad (7.25)$$

$$\frac{\partial Y_{E,e}}{\partial \mathbf{g}_e^\top} = \frac{2(1 - \mathbf{Z}_{d,e} \cdot \mathbf{d}_N)}{g_{del}} \mathbf{g}^\top \cdot \mathbf{C}_i, \quad (7.26)$$

$$\frac{\partial Y_{E,e}}{\partial \mathbf{d}_N^\top} = - \left[\frac{1}{g_{del}} \mathbf{g}^\top \cdot \mathbf{C}_i \cdot \mathbf{g} + \frac{G_s}{s} \right] \mathbf{Z}_{d,e}, \quad (7.27)$$

wherein all quantities are evaluated at the new time step " $j+1$ ".

Note that in the stiffness parts $\mathbf{K}_{b,e}^{dd}$ and $\mathbf{K}_{i,e}^{dd}$ a term $\frac{1}{\Delta t}$ arises. This term gets large for sufficient small time increments and causes the stiffness matrix to be positive definite in the case of cracking and crack propagation. This is similar to viscous regularisation, whereby the gradient extension is physically motivated, which is an advantage. However, the gradient extension leads to more *DOFs*, which is a big disadvantage next to other problems (e.g. new material parameters which are not interpretable). The latter presented simulations will allow a more reasonable discussion of the gradient extension.

8 Verification of User Subroutines and Numerical Models

Before we use the models of Chaps. 5 and 7, it is necessary to verify their correct implementation in the FEM. This is done with special Test-Setups, that produce predictable results. For e.g. a user defined FE (UEL) has to pass the Patch-Test, hence, convergence of a simulation, performed with this FE, is achieved. These tests lead to homogeneous stress states in the investigated FE. More details concerning this topic can be found in BATHE [143]. Similar investigations are necessary for user defined materials (UMAT). The structure of this chapter is as follows. At first, the four performed Test-Setups are presented and explained. Then we go on and present the results of the tests for the four UMAT subroutines, which is followed by the results of the Patch-Tests for the UEL subroutines with the damage gradient extension. However, to keep this chapter short, only the results for one tensile direction (e_2) are presented. The other tensile direction and the two shear tests are not presented, but they are passed as well. Finally, the FE model of the DCB (Double Cantilever Beam) and the 4PBT are presented in this chapter.

8.1 Test-Setups

The first Test-Setups are shown in Fig. 8.1 on the left-hand side with one FE and on the right-hand side for four arbitrary FEs. These are the setups for the tests of the bulk constitutive laws, as well as the UEL subroutines. The boundary conditions are applied in that way, that only a deformation in e_2 -direction results. The dimensions of the square are $10\text{mm} \times 10\text{mm}$, which leads with the applied displacement of 1mm to a strain of 10% in the end. Hence, these tests are performed under large deformations. Contrary to the Test-Setups for the bulk material Fig. 8.2 presents the two settings for the interface constitutive laws. On the left-hand side the setting for pure Mode I opening is presented, whereas, on the right-hand side the setting for Mix Mode

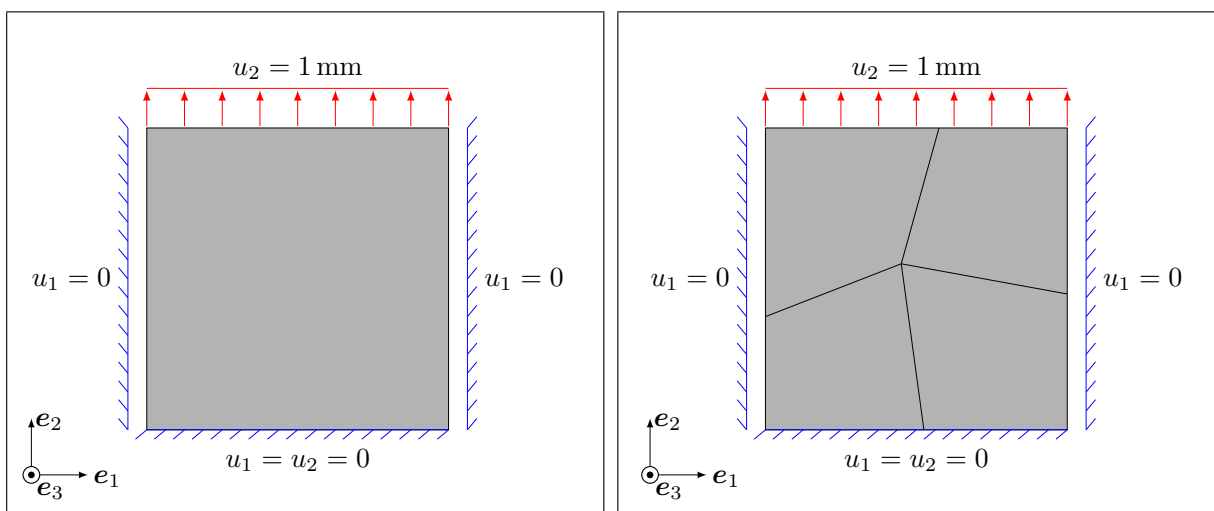


Figure 8.1: Test-Setups for UMAT and UEL subroutines of the bulk material with one FE (left-hand side) and four arbitrary elements (right-hand side) in e_2 -direction

Table 8.1: Dummy material parameters for Test-Setups with $i \in \{b, i\}$

		material		
		bulk	interface	
parameter	E_i	[GPa]	100.0	1.0
	ν	[-]	0.25	—
	a_i	[s ⁻¹]	$1 \cdot 10^{-10}$	$1 \cdot 10^{-10}$
	N_i	[-]	3.0	3.0
	T_{i0}	[MPa]	1.0	1.0
	T_{\max}	[MPa]	—	100.0
	g_{cr}	[mm]	—	0.55
	β	[-]	—	1.0
	g_{del}	[mm]	—	0.55
	S_{i0}	[$\frac{\text{mJ}}{\text{mm}^2}$]	—	$5 \cdot 10^{-3}$
	Y_{E0}	[$\frac{\text{mJ}}{\text{mm}^2}$]	—	$1 \cdot 10^{-4} / 200.0$
	G_s	[$\frac{\text{mJ}}{\text{mm}}$]	—	$1 \cdot 10^{-3}$
	s	[mm]	—	25.0

opening is presented. This is done to test the damage evolution through the damage gradient along non loaded areas of the interface. All tests are performed with a dummy material for the

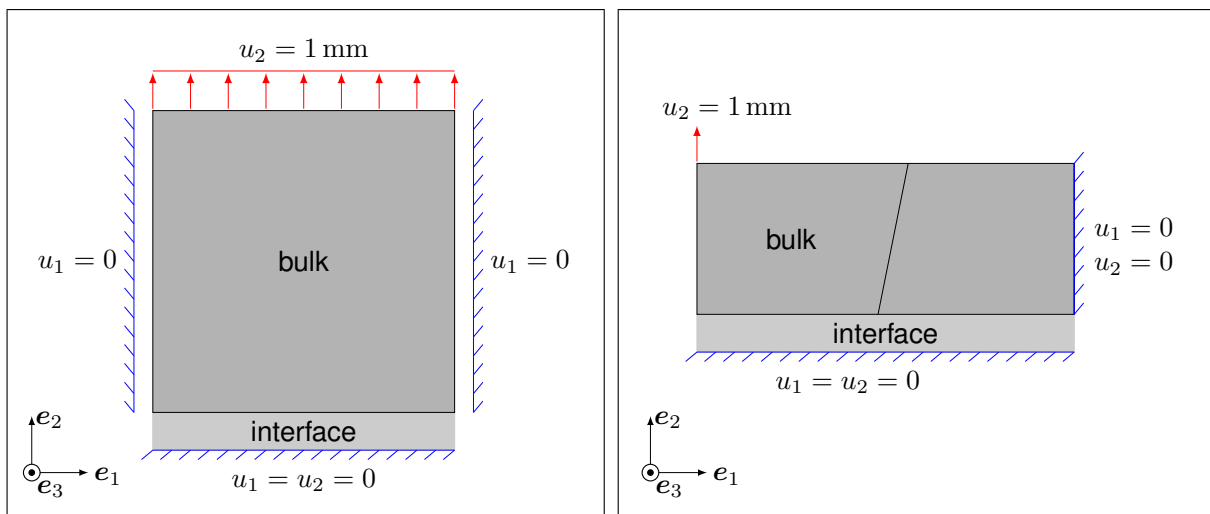


Figure 8.2: Test-Setups for UMAT and UEL subroutines of the interface material with one rigid bulk element and one (quadratic) or two (linear) interface elements (left-hand side) and two rigid arbitrary bulk elements and two (quadratic) or four (linear) interface elements (right-hand side)

bulk and the interface. The used material parameters are summed up in Table 8.1.

8.2 Verification of UMAT Subroutines

8.2.1 Bulk Constitutive Laws

At first, we verify the correct implementation of the bulk material with a pure elastic behaviour and perform all tests. Figure 8.3 presents the results for the e_2 -direction with a constant displacement load: on the left-hand side for one FE and on the right-hand side for four FEs. In both cases a homogeneous stress state results for all stresses and it is always the same value

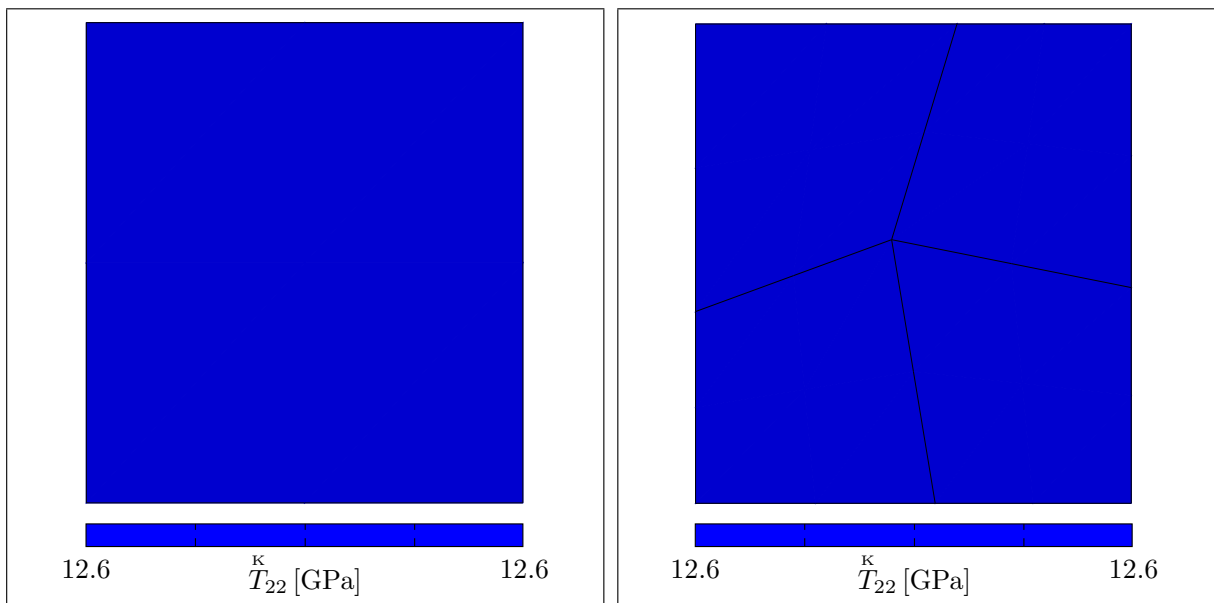


Figure 8.3: Results of Test-Setups for elastic UMAT subroutine for the bulk material in e_2 -direction with one FE (left-hand side) and with four FEs (right-hand side)

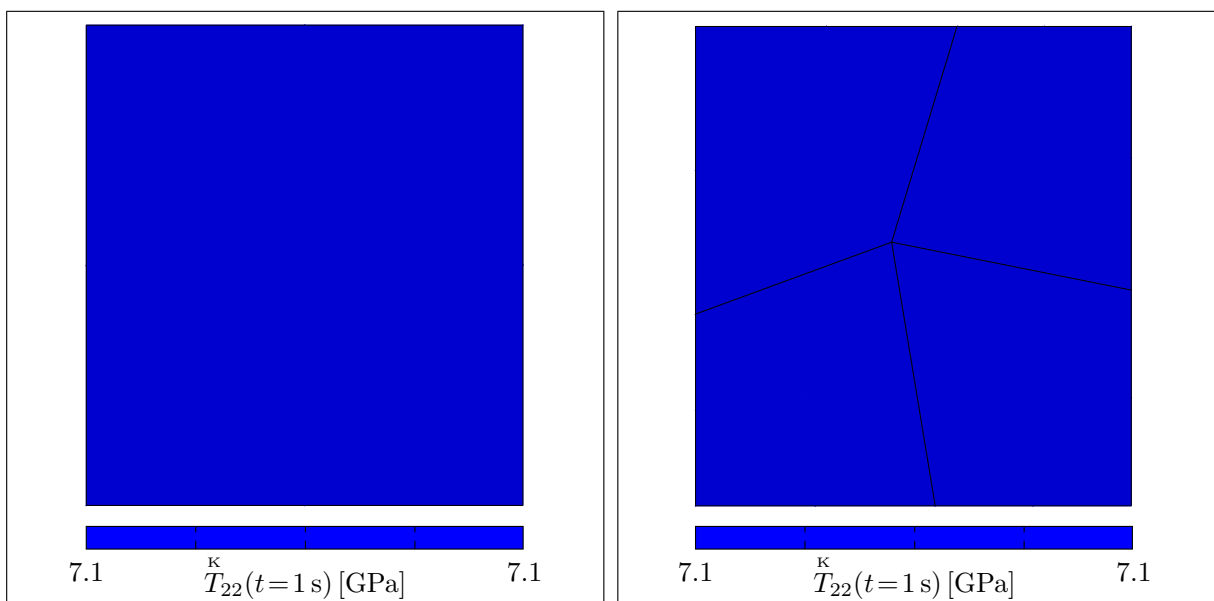


Figure 8.4: Results of Test-Setups for inelastic UMAT subroutine for the bulk material in e_2 -direction for one FE (left-hand side) and four FEs (right-hand side)

calculated. Additionally, this test is performed with a prescribed stress instead a displacement. This test is passed for both settings, as well as the shear tests. Further on, the solution is always obtained in one step and no further iterations are required. Hence, we can conclude that the elastic material behaviour for the bulk material of Chap. 5 is correct implemented through the UMAT subroutine.

Up next, we verify the implementation of the inelastic material behaviour of the bulk material in the UMAT subroutine. Figure 8.4 presents the homogeneous stress states in e_2 -direction of the final time step ($t = 1$ s): on the left-hand side for one element and on the right-hand side for four elements. To verify the correct implementation of the inelastic evolution equation we extract the stress and the displacement for one node on top, where the load is applied. The results are presented in Figure 8.5, on the left-hand side the results are presented by using one FE and on the right-hand side by using four FEs. The diagrams placed on top show the stress relaxation under a constant displacement and the diagrams placed on bottom show linear increase of the displacement under a constant stress. In both cases the tests are passed without any problems. Further on, the defined tolerance of $7.5 \cdot 10^{-7}$ for the time stepping algorithm (cf. Sec. 6.9) is chosen correct because it results a homogeneous stress state in every iteration of the step, which is not disturbed through a non-isochoric evolution of the inelastic deformation gradient.

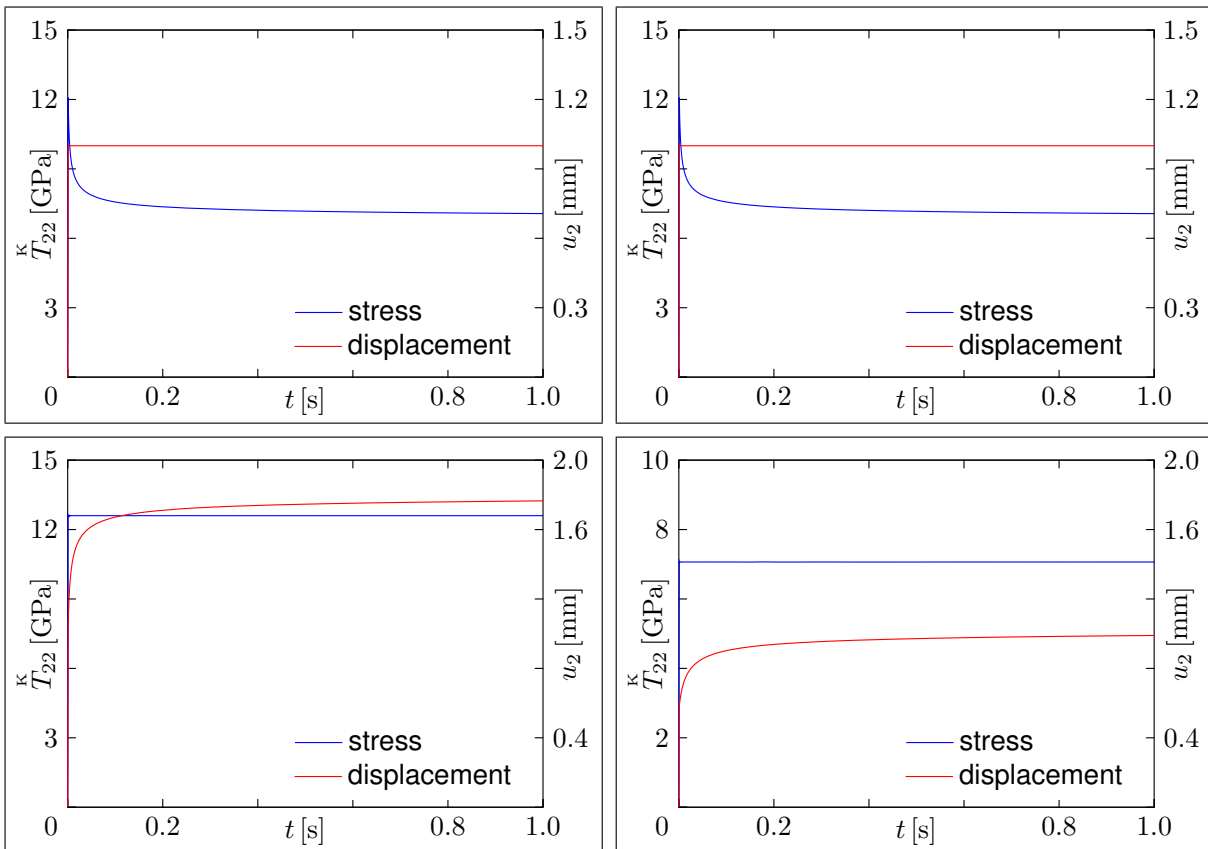


Figure 8.5: Creep results of inelastic UMAT subroutine in e_2 -direction for one FE (left-hand side) and four FEs (right-hand side); on top placed diagrams show the stress relaxation under constant displacement and bottom placed diagrams show the linear increase of the displacement under constant stress

8.2.2 Interface Constitutive Laws

The verification of the two implemented TSLs is done by analysis of the TSLs, which results at one node after finishing the FE simulation. For Mode I opening Fig. 8.6 presents these results. The TSL is presented (T_n vs. g_n) and the reaction force is plotted versus the normal separation. In both cases no oscillations or other problems are found, hence, it can be concluded that the implementation is correct, up to now. The left-hand side of Fig. 8.6 presents these relations for the polynomial TSL of NEEDLEMAN (cf. Sect. 5.2.1) and the right-hand side for the developed novel TSL (cf. Sect. 5.2.2). In the next step we investigate the behaviour of the two TSLs under Mix Mode conditions, which are simulated with the DCB experiment of Fig. 8.2: on the right-hand side. The results are presented in Fig. 8.7 on the left-hand side for the normal direction and on the right-hand side for the tangential direction. Again, the TSLs are smooth and no oscillations occur. The only problem is that even for this small Mix Mode experiment usage of a viscous regularisation scheme is required to obtain a solution because without viscous regularisation no dissipative part exists in the model. However, this is common in fracture mechanics, therefore, it can be concluded that implementation of the TSLs is fully correct.

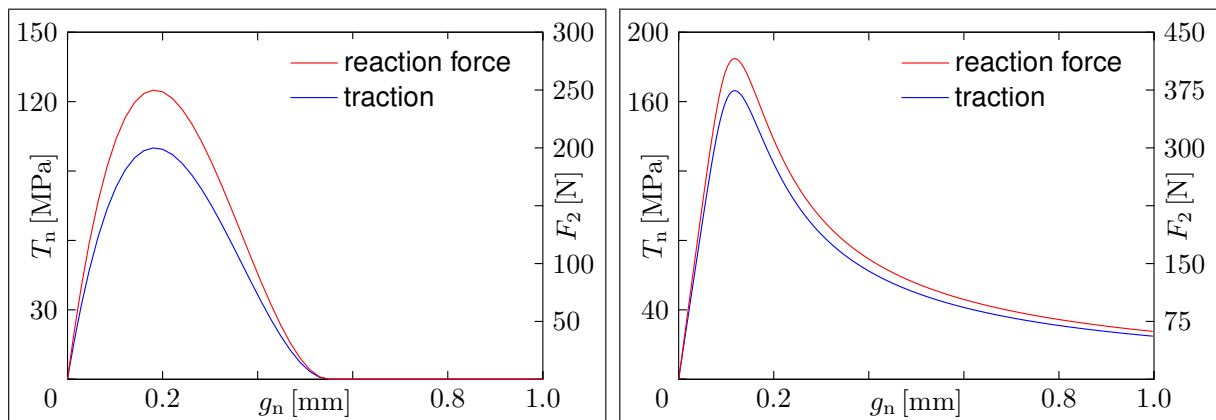


Figure 8.6: Results of Test-Setups for the interface for pure Mode I opening; NEEDLEMAN (left-hand side) and novel TSL (right-hand side)

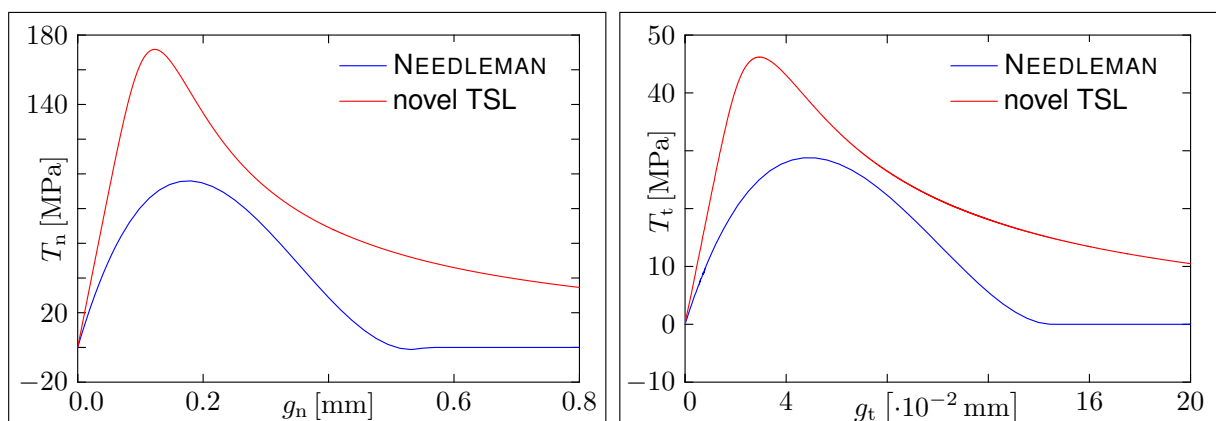


Figure 8.7: Results of Test-Setups for the interface for Mix Mode opening; T_n vs. g_n (left-hand side) and T_t vs. g_t (right-hand side)

8.3 Verification of UEL Subroutines

8.3.1 Bulk Constitutive Laws

As before, we start this section by verifying the UEL subroutine for the bulk material with the elastic contribution. Figure 8.8 presents the results of the two Test-Setups in e_2 -direction, which are presented in Sec. 8.1, on the left-hand side with one FE and on the right-hand side with four FEs. In both cases results a homogeneous stress state which is achieved after one iteration, therefore, we conclude that the implementation of the FE formulation of Chap. 6 into ABAQUS is correct. Up next, the implementation of the UEL with the inelastic material behaviour is verified, again with one FE and four FEs and for a constant applied displacement and a constant applied

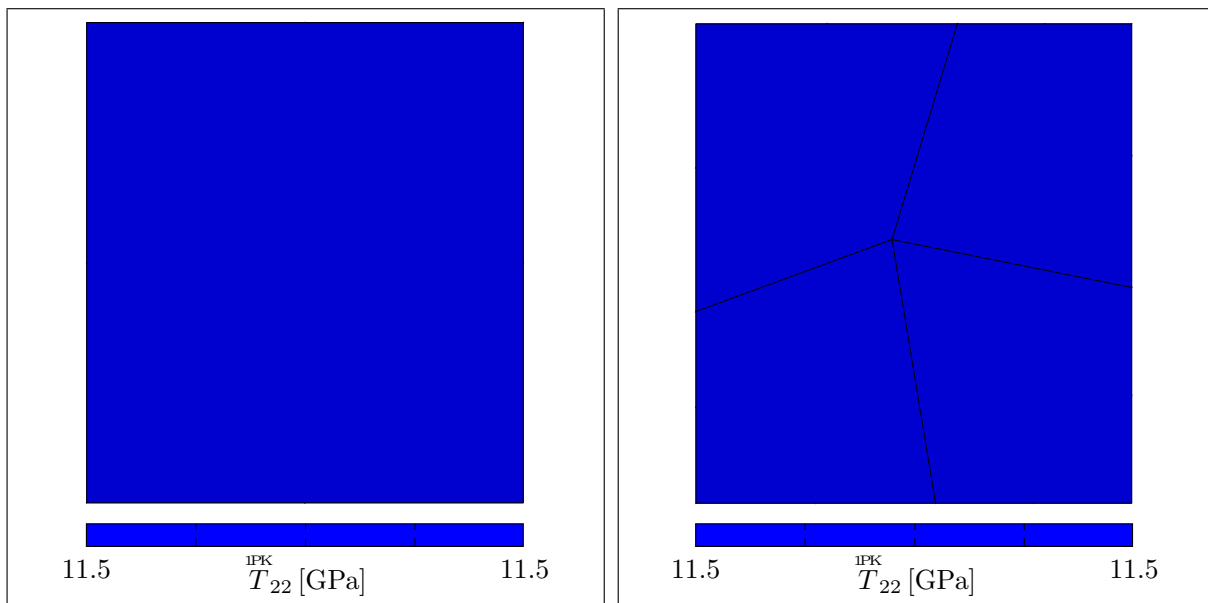


Figure 8.8: Results of Test-Setups for elastic UEL subroutine for the bulk material in e_2 -direction for one FE (left-hand side) and four FEs (right-hand side)

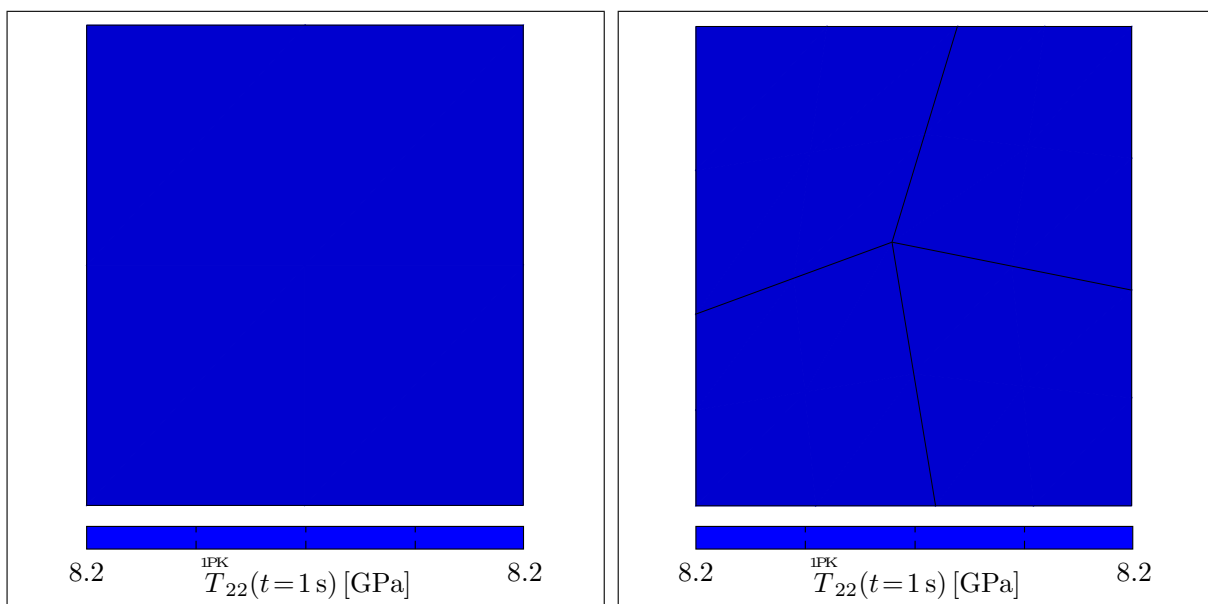


Figure 8.9: Results of Test-Setups for inelastic UEL subroutine for the bulk material in e_2 -direction for one FE (left-hand side) and four FEs (right-hand side)

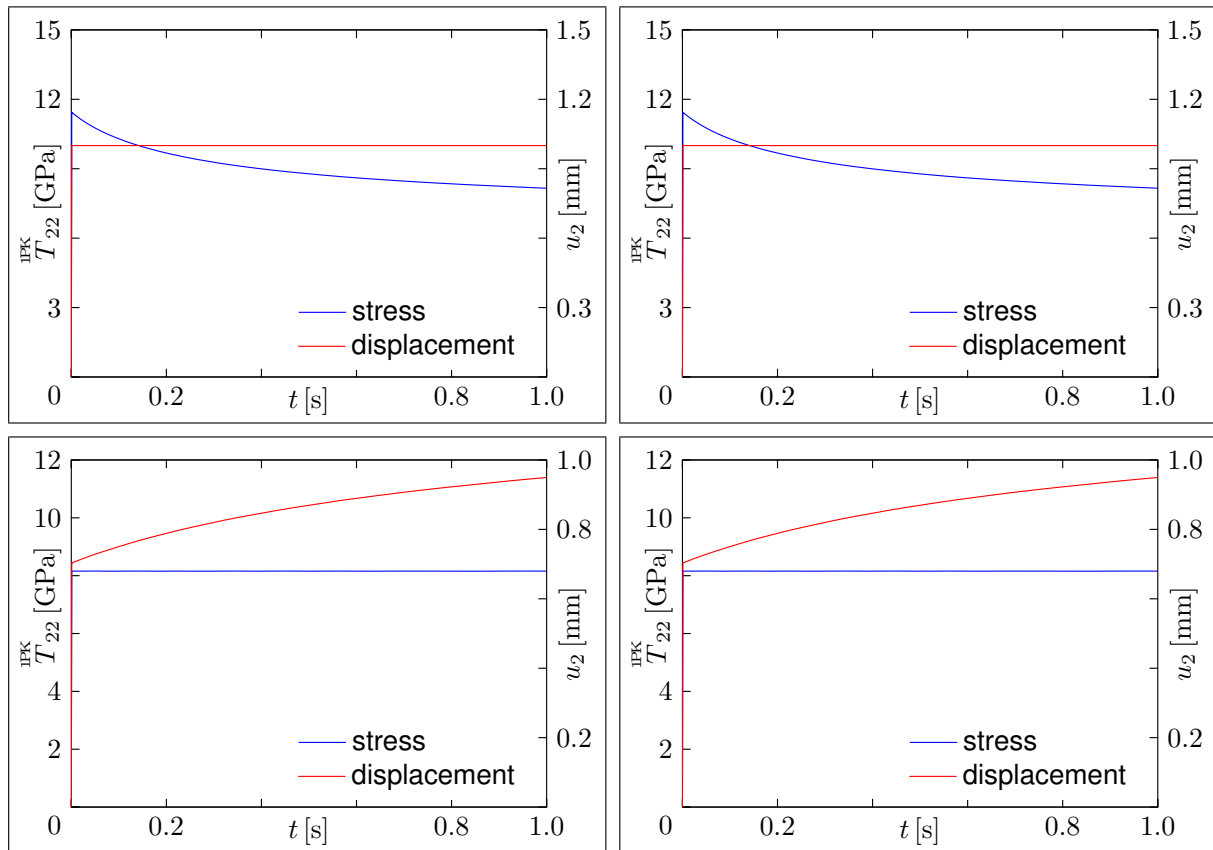


Figure 8.10: Creep results of inelastic UEL subroutine in e_2 -direction for one FE (left-hand side) and four FEs (right-hand side); on top placed diagrams show the stress relaxation under constant displacement and bottom placed diagrams show the linear increase of the displacement under constant stress

stress. In Fig. 8.9 the resulting, homogeneous stress state in e_2 -direction is presented. The left-hand side presents the result for one FE and the right-hand side for four FEs. In both pictures no discontinuities are present and the same stress is calculated. Further on, the same results are archived for all other stress components and the other tests. In the last step the implementation of the inelastic evolution equation is verified. Therefore, the test with one FE and four FEs are performed twice. Once with a constant applied displacement and then with a constant applied stress. The results are summarised in Figure 8.10: on the left-hand side the results with one FE and on the right-hand side the results calculated with four FEs are presented. The diagrams on top show the stress relaxation under a constant stress and the diagrams at the bottom show the linear increase of the displacement under a constant stress. The results of Figs. 8.9 and 8.10 lead to the conclusion that the implementation of the FE with an inelastic material behaviour of Chap. 6 into the software ABAQUS is correct.

8.3.2 Interface Constitutive Law

The last tests are performed with the TSL of Chap. 7, which is extended with the damage gradient. At first, a test with pure Mode I opening is performed. The calculation performed well without any errors or warnings. For verification purposes the reaction force and the normal traction are extracted from the result file and presented in Fig. 8.11 on the left-hand side. No oscillations or jumps are detectable from the plot, this is a good indication for a correct implementation. In the next step the Mix Mode behaviour is analysed and again reaction forces and tractions at one node are extracted and used for the verification. On the right-hand side

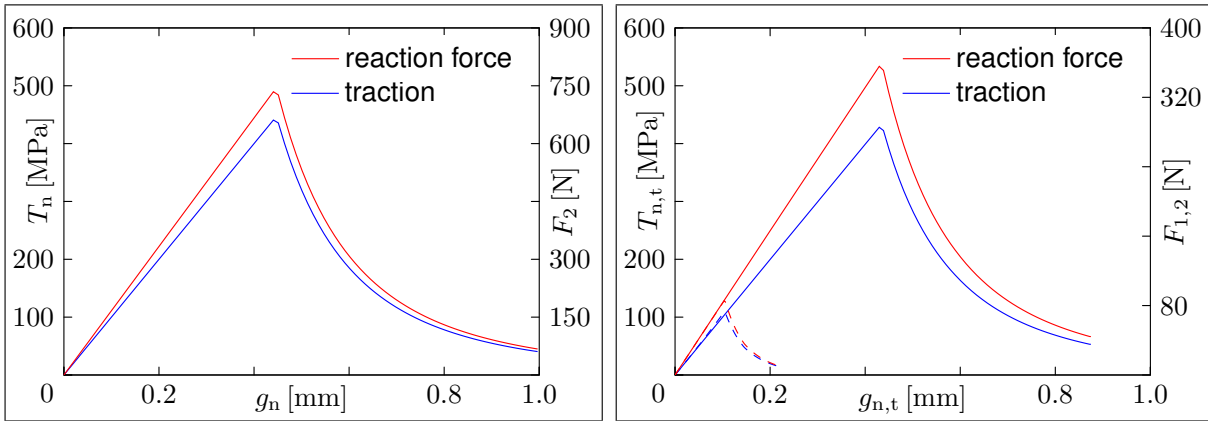


Figure 8.11: Results of Test-Setups for the interface UEL subroutine for pure Mode I opening (left-hand side) and Mix Mode opening (right-hand side); solid line represents normal and dashed line tangential opening

of Fig. 8.11 the results for one node are presented. The dashed lines stands for the results in the tangential direction and the solid lines represent the results in normal direction. Again, no oscillations or jumps are visible in the plot, nor where errors or warnings a problem during the execution. Hence, it is concluded that the implementation is correct.

8.4 Numerical Models

This section presents the FE models, that are used in this work. At first, a DCB test is presented which is followed by a 4PBT model. The DCB model is used to compare the different simulation procedures (static, dynamic) to each other and the 4PBT model is used to simulate the failure of the compound, which is presented in Chapter 2.

8.4.1 Double Cantilever Beam Test

The DCB test is used to compare the different simulations procedures, which are investigated in this work to each other. For these investigations the material parameters of Tab. 8.1 are used for the bulk and interface materials. The model has a length of $l = 100$ mm and a height of $h = 10$ mm. A plain strain state with a width of $b = 1$ mm is assumed. Due to symmetry considerations, only one half of beam is modelled. The bulk part is discretised with 160, 640

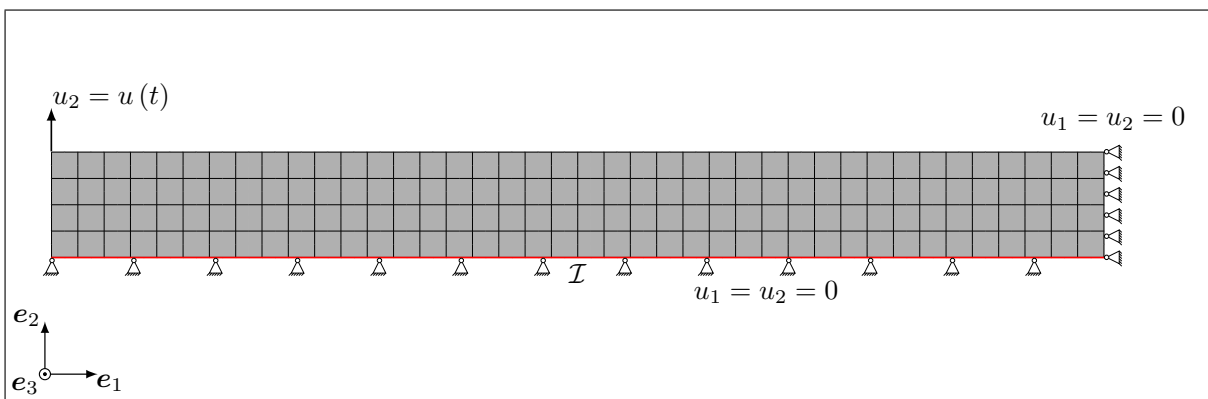


Figure 8.12: FE model of the DCB test with boundary conditions and interface area with 160 continuum and 40 interface elements

and 2560 continuum elements with a aspect ratio of 1 and the interface is discretised with 40, 80 and 160 zero-thickness, quadratic interface elements. On the right side the DCB is fixed in both direction and the lower part of the interface is fixed in both directions as well. This is necessary to guarantee that no rigid body motions can occur in the model. Due to the integration scheme of the cohesive element nodes placed on the same side of the element are decoupled and without fixing both DOF 's of the lower interface side rigid body motions are possible. The load of $u_2 = 2 \text{ mm}$ is applied in the top, left corner of the DCB in 1 s (cf. Fig. 8.12). The analysed time of $t = 1 \text{ s}$ is discretised in every simulation in the same way. The initial increment is 0.01 s, the minimum increment is $1 \cdot 10^{-10} \text{ s}$ and the maximum increment is 0.1 s. The time incrementation is controlled by the automatic time incrementation of ABAQUS [60]. This test is performed eighteen times: once as a static analysis with elastic and then with inelastic bulk material, after this as an implicit dynamic analysis with elastic and inelastic bulk material, and finally as a static analysis with a damage gradient extended constitutive law for the interface with an elastic and then with an inelastic bulk material. All simulations are performed for the three different discretisations. Results of every simulation are the required computational time t_{CPU} , and the number of increments N_{inc} and the shape of the reaction force 5 mm away from the bottom, left corner of the DCB. The computational time is the time which ABAQUS needs to solve the model, the time spend in the user subroutine is excluded. These results are presented in Sect. 10.1 in Figs. 10.1 and 10.2. The used data are summarised in Appendix B in Tabs. B.4, B.5 and B.6.

8.4.2 Four Point Bend Test

The 4PBT and the experimental setup is explained in Chap. 2 in detail, already. Here, we explain how the FE model is derived from the real experiment. In the experiment the loading is only applied in e_2 -direction, next to that the 4PBT is symmetric to the e_2 - e_3 -plane, thus, it is only necessary to model one half of the beam, we chose the right half of the beam. Further on, we are only interested in the stress state which arises in the middle of the beam, and since the deformation in e_3 -direction is symmetric the stress state is analysed by assuming a plane strain state. The geometric dimensions of the model are summarised in Tab. B.3 in Appendix B. The distance from the middle of the beam to the middle of the upper support is $l_1 = 10 \text{ mm}$ and to the middle of the lower support is $l_2 = 20 \text{ mm}$. Overall length of the model is 25 mm. For reasons of simplicity both supports are modelled as rigid bodies and the connection between the specimen model and the supports is realised by assuming hard contact without friction. The specimen is discretised with 2637 plane strain elements. The first interface \mathcal{I}_1 is discretised by 32 zero-thickness interface elements to simulate the cracking

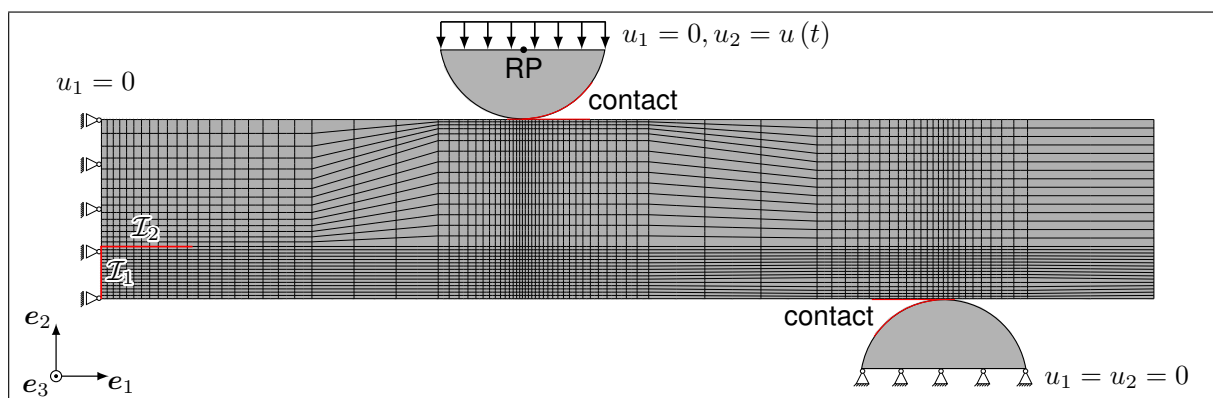


Figure 8.13: FE model of the 4PBT with rigid supports, applied boundary conditions, contact and interface areas

of the coating and the delamination is modelled with 11 zero-thickness interface elements. These numbers of interface elements lead to a length of interface elements in crack propagation direction of $38 \mu\text{m} < l_{\text{ele}} < 69 \mu\text{m}$, which is a suitable length of interface elements according to [42] ($50 \mu\text{m} < l_{\text{ele}} < 250 \mu\text{m}$ is recommended.). However, this is only a rule of thumb and we do not know if this is correct. However, in [144–146] it is shown that a too coarse mesh leads only to an adjustment of the cohesive parameters. We will see that later on. Besides, in [147] it is shown that less continuum elements as used in this model are able to approximate the stress state in a 4PBT, accurately. The increase in the number of continuum elements is only done to have a better approximation of the cracking and the delamination. Much more, the second interface is not defined between all continuum elements of the substrate and the coating, since we know from the experiment that this is not required. Whereas, it is more important that this would lead to strong numerical problems because coating and substrate are not sober connected, any more. As can be seen from Fig. 8.13 we try to use a high NE only in the regions where it is required and not overall to keep the model as small as possible because of the optimisation procedure. Boundary conditions are applied in the middle of the beam, at the lower support and the linear increasing displacement is applied on the upper support (cf. Fig. 8.13). The identification of the required material parameters is explained in Chapter 9. To compare the simulation with the experiment the reaction force calculated at the reference point (RP) is extracted after the simulation is finished (cf. Fig. 8.13). Since two interfaces are present in the model it is very unstable, and especially in the case of cracking and delamination. For stabilisation of the simulation the model is regularised with the viscous regularisation technique of ABAQUS, and the damping parameter is automatic adjusted based on the solution history. This is done to keep the influence onto the simulation as small as possible. The initial time increment is 0.01 s, the minimum increment is $1 \cdot 10^{-15}$ s and the maximum increment is 1.5 s. The very small minimum time increment is required to be able to resolve the cracking and delamination process, accurately. Next to this very small minimum time increment the allowed number of NEWTON iterations per time increment is increased from five to twenty. This is done to guarantee that the onset of cracking is found because the onset of cracking correlates with a strong reduction of the time increment, which is not possible with five allowable iterations in one increment.

9 Identification of Material Parameters

In this chapter we explain briefly the identification of all required material parameters. Whereby, these explanations are based on theories presented in [29, 30, 147]. However, in these works the identification of material parameters is limited to the isothermal case, whereas this thesis requires temperature dependent material parameters. Consequently, the extension of these theories to the non-isothermal case is performed and explained, here and much more this is the main concern of this chapter. In the end the identified values of material parameters are compared to values reported in the literature. This is done to verify the extended identification procedure. To keep this chapter as short as possible only necessary tables, diagrams, etc. are presented here. All further information are given in the Appendix B.

9.1 YOUNG'S Modulus

9.1.1 Substrate

The YOUNG's modulus of the substrate material under isothermal conditions is identified from the linear elastic range of 4PBT measurements trough linear regression, as it is shown in Fig. 9.1 for 400°C. For every temperature 4PBTs are performed at different test speeds, as well. The measurements of 4PBTs for 250°C and 300°C are presented in App. B in Figs. B.1 and B.2, respectively. For this analysis beams are used without coating. The basis is following equation

$$E_s = \frac{12M_{\text{exp}}}{bh_s^3\Gamma_{\text{exp}}}, \quad (9.1)$$

which is derived from the linear beam theory of BERNOULLI & EULER. Required cross section dimensions of the specimens are summarised in Tab. B.1 in App. B as well. Further on, this table presents the YOUNG's moduli determined through linear regression. The YOUNG's modulus ranges from 74.65 GPa at 20°C to 30.05 GPa at 400°C. Unfortunately, no comparable values for this specific alloy are found in the literature for this temperature range. However, it is realistic that a drastic reduction of the YOUNG's modulus occurs by increasing the temperature from 20°C to 400°C, because 400°C is approximately 68% of the melting temperature AISi10MgT6.

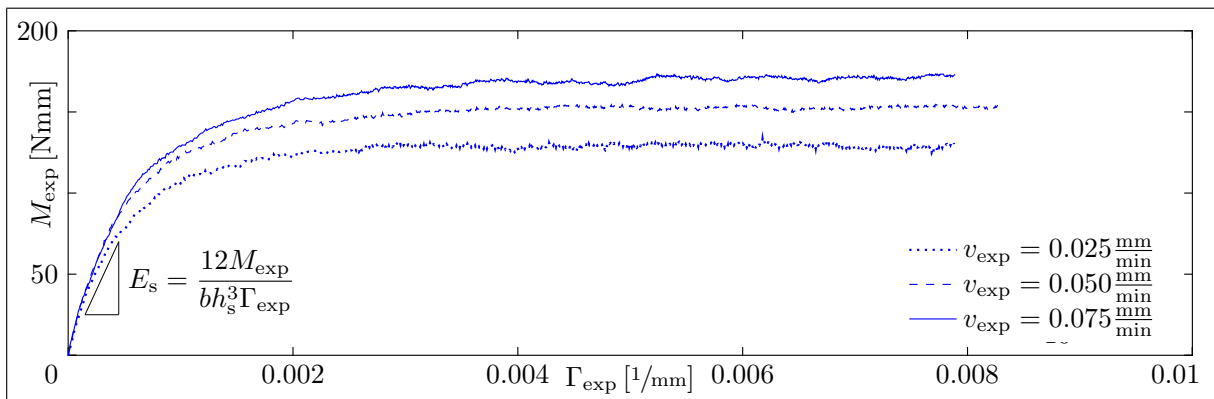


Figure 9.1: M_{exp} vs. Γ_{exp} curves of the substrate for 400°C and different test speeds

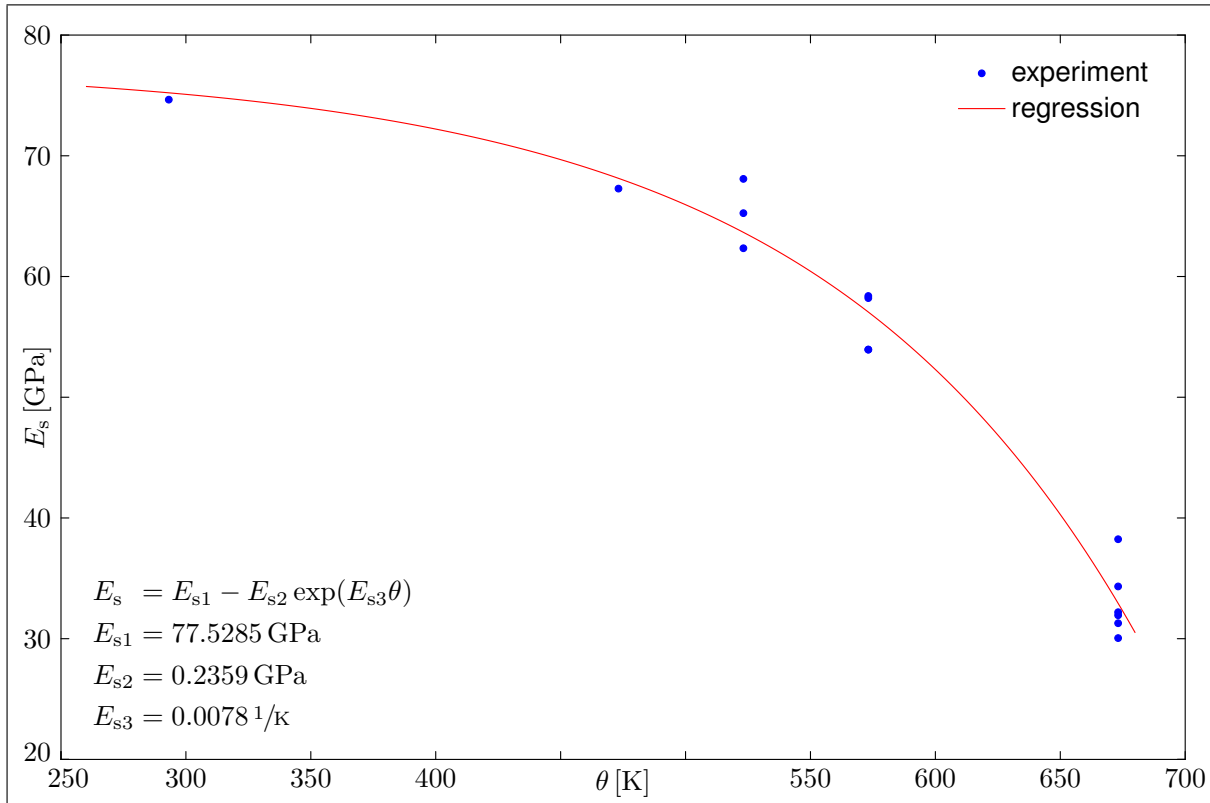


Figure 9.2: Temperature dependence of YOUNG’s modulus of the substrate

In [148], this is pointed out for a 6061 alloy with T6 heat treatment. For numerical simulations discrete points are not suitable, therefore, we calculate from the determined experimental YOUNG’s moduli values a smooth function, which describes the temperature dependence. We decided to use an exponential function because such a function is often used in physics to describe the temperature dependence of a quantity. The function is

$$E_s = E_{s1} - E_{s2} \exp(E_{s3}\theta) \tag{9.2}$$

with the three constants

$$E_{s1} = 77.5285 \text{ GPa}, \quad E_{s2} = 0.2359 \text{ GPa} \quad \text{and} \quad E_{s3} = 0.0078 \frac{1}{\text{K}},$$

that are calculated with the method of least squares. Figure 9.2 shows the temperature dependence of the YOUNG’s modulus of the substrate material with the experimental values and the determined function.

9.1.2 Coating

For the coating material the identification procedure is similar to the identification of the YOUNG’s modulus of the substrate material. Again, the foundation is the linear beam theory with the equation

$$E_c = \frac{12M_{\text{exp}}}{bh_c^3\Gamma_{\text{exp}}}. \tag{9.3}$$

However, the testing of a thin coating is very problematic, consequently, the number of successful 4PBTs is limited. Here we have four successful measurements. Two for 20°C and two for

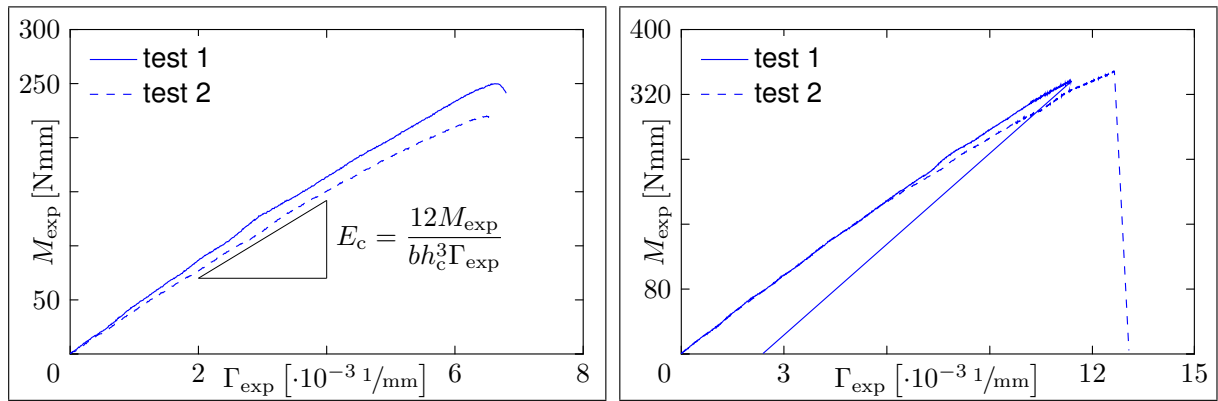


Figure 9.3: M_{exp} vs. Γ_{exp} curves of the coating for 20°C (left-hand side) and 400°C (right-hand side) and test speed $v_{\text{exp}} = 0.050 \frac{\text{mm}}{\text{min}}$

400°C. The results of these 4PBTs are presented in Fig. 9.3, on the left-hand side for 20°C and on the right-hand side for 400°C. All required cross section dimensions, next to the identified YOUNG's moduli, are presented in Tab. B.2 in Appendix B. The identification is done through linear regression. Compared to the literature the determined YOUNG's moduli are much lower than expected. This is due to the manufacturing process (HVOF sparying in this work), which produces a high porosity that leads to a YOUNG's modulus 2.5 times lower than expected (ca. 70 GPa compared to 170 GPa [36, 149]). For further information we refer to [29, 30, 147].

In the last step the temperature dependence needs to be determined. From the literature we know that the YOUNG's modulus of iron aluminide depends linear on it (cf. [36, 149]). Therefore, four measurements are enough. Figure 9.4 presents the temperature dependence of the

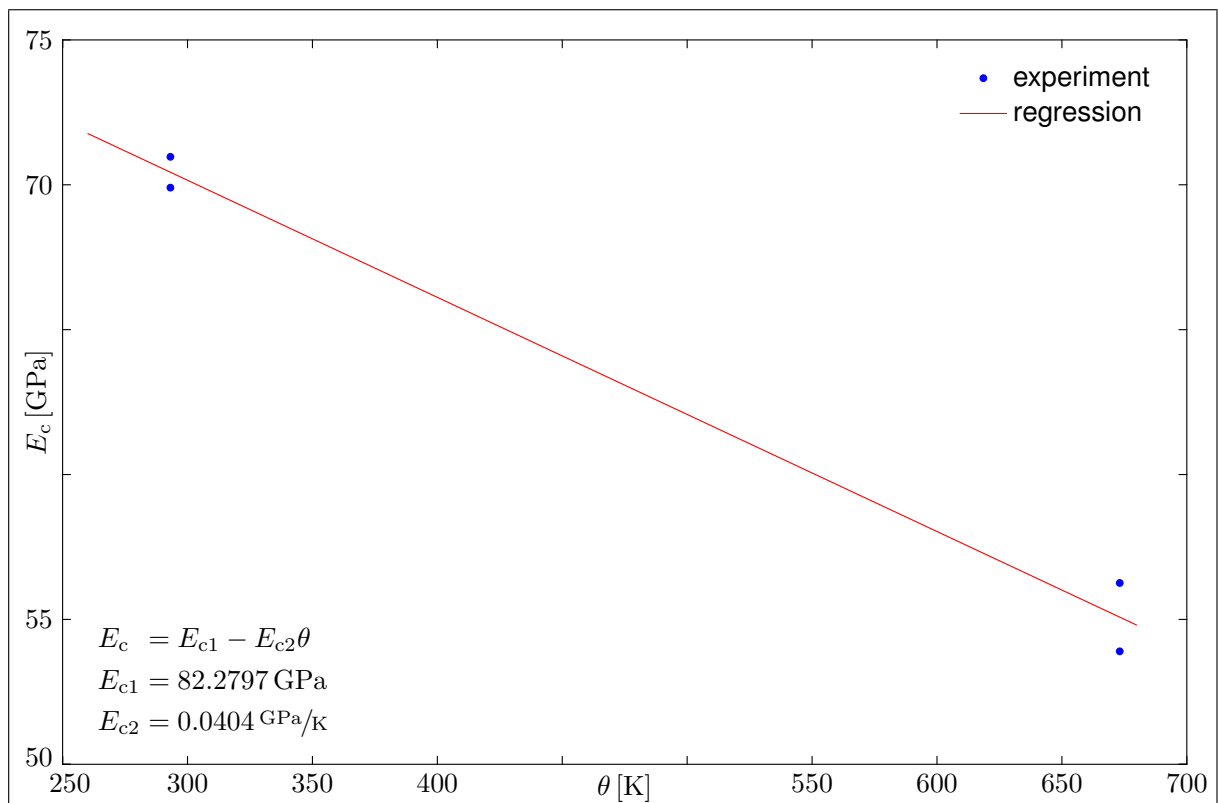


Figure 9.4: Temperature dependence of YOUNG's modulus of the coating

YOUNG's modulus of the coating material with the function

$$E_c = E_{c1} - E_{c2}\theta \quad (9.4)$$

and the two constants

$$E_{c1} = 82.2797 \text{ GPa} \quad \text{and} \quad E_{c2} = 0.0404 \frac{\text{GPa}}{\text{K}}.$$

9.2 Creep Parameters of the Substrate

This section explains in compact way the theory of identification of temperature dependent creep parameters from 4PBT measurements. As mentioned in Chap. 2 only secondary creep is considered, which can be described with power-law type functions (e.g. NORTON's law). Further on, we make the common assumption that the creep exponent is temperature independent and that the inelastic evolution equation is multiplicative decomposed into a mechanical and a temperature part [34, 35]. The temperature dependence is modelled with the ARRHENIUS function (cf. Eq. (5.14)). Usually, creep or tensile tests are performed to determine creep parameters [34, 35, 150]. Here, we assign this procedure to 4PBTs by using beam theory, again. As presented in [30], it is assumed that the stress rate is zero because of secondary creep, which leads to the statement that the moment rate is zero ($\dot{M} = 0$). From this the following equation is derived

$$M_{st} = K \left[\dot{\Gamma}_{st} \exp\left(\frac{Q}{R\theta}\right) \right]^{\frac{1}{N_s}} \quad \text{with} \quad K = \frac{2bN_s T_{s0}}{(1 + 2N_s)} a_s^{-\frac{1}{N_s}} \left(\frac{h_s}{2}\right)^{\frac{1+2N_s}{N_s}} \quad (9.5)$$

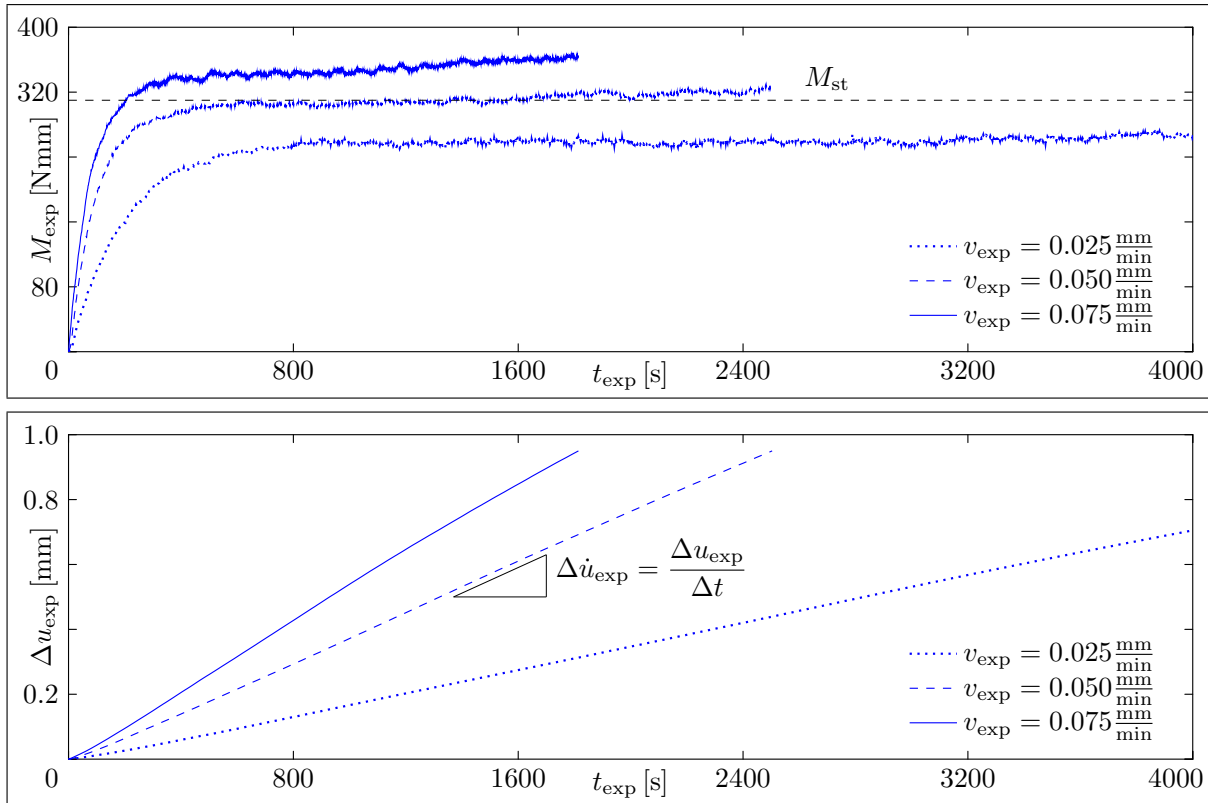


Figure 9.5: M_{exp} vs. t_{exp} (top) and Δu_{exp} vs. t_{exp} (bottom) curves of the substrate for 400°C and different test speeds

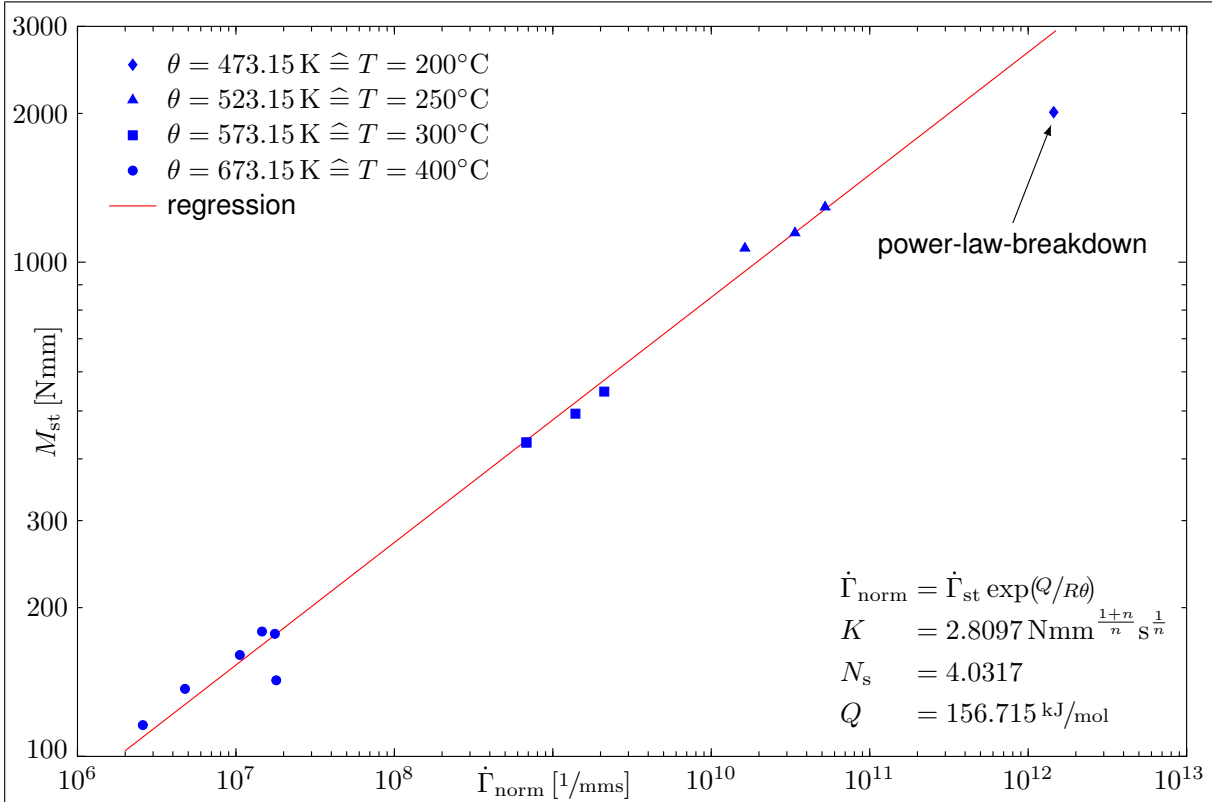


Figure 9.6: Creep master curve of the substrate for the temperature range $200^{\circ}\text{C} \leq T \leq 400^{\circ}\text{C}$

and $T_{s0} = 1 \text{ MPa}$. This parameter is only introduced to normalise the stress in the power-law. Further on, a so called normalised curvature is defined

$$\dot{\Gamma}_{\text{norm}} = \dot{\Gamma}_{\text{st}} \exp\left(\frac{Q}{R\theta}\right),$$

which is only required for the identification procedure and has no physical meaning. Equation (9.5) is highly non-linear, therefore, this equation is logarithmised and it results

$$\log(M_{\text{st}}) = \log(K) + \frac{1}{N_s} \log(\dot{\Gamma}_{\text{norm}}). \quad (9.6)$$

The required steady-state moments and curvatures are determined from the performed 4PBTs as it is presented in Fig. 9.5 for 400°C , on top for the steady-state moment and on the bottom for the steady-state curvature. The other measurements are presented in Appendix B. We search for the first time point where the moment curve starts to keep constant and then go to the measured difference displacement curve, determine at the same time point the difference displacement and from this the curvature according to Eq. (2.2), and finally the curvature velocity. This is done for all 4PBTs. The calculated values are presented in Tab. B.1 in Appendix B. Up next, the steady-state moments are plotted versus the normalised curvatures for all temperatures on a logarithmic scale (creep master curve) and then the activation energy Q is adjusted so that in the end all calculated points are placed on a line (cf. Fig. 9.6), approximately. The determined value of the activation energy is $Q = 156.715 \text{ kJ/mol}$, which fits to values other researchers determined for the activation energy of aluminium [151, 152]. In the next step a linear regression with Eq. (9.6) is performed to determine the creep exponent N_s and K . They have the values:

$$K = 2.8097 \text{ Nmm}^{\frac{1+N_b}{N_b}} \text{ s}^{\frac{1}{N_b}} \quad \text{and} \quad N_s = 4.0317.$$

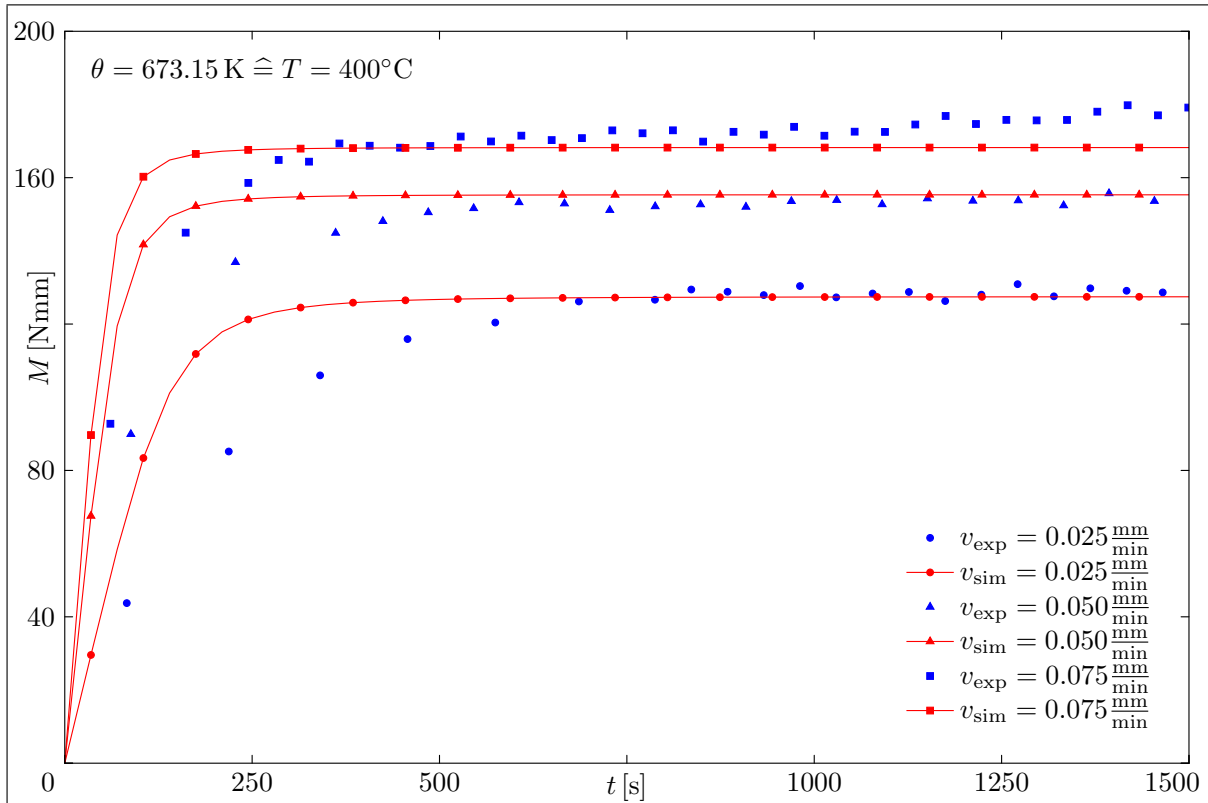


Figure 9.7: Verification of determined creep parameters at 400°C and for different test speeds

Subsequently, the creep factor can be calculated with the cross section dimensions of the specimen (cf. Tab. B.1) and the creep exponent from the constant K . It results a creep factor in the range of $1 \cdot 10^{-14} \text{ s}^{-1} \leq a_s \leq 1 \cdot 10^{-10} \text{ s}^{-1}$. This is a suitable size for the factor. Further on, the value of the creep exponent leads to the conclusion that dislocation creep is the dominating creep mechanism, which is reasonable as well. More details about this identification procedure can be found in [90]. It can be concluded from Fig. 9.6 that the temperature range of $250^\circ\text{C} \leq T \leq 400^\circ\text{C}$ can be described accurately with the determined parameters and the used power-law. However, it is not possible to describe temperatures below 250°C because the deviation between measurement and regression is too high. This is called power-law-breakdown. For further discussion we refer to [90, 101]. Up next, the identified parameters are verified. For this purpose, we use the theory presented in [29, 30]. Figure 9.7 shows the results of these simulations (red) compared to the experimental results (blue) for 400°C and three different test speeds. This comparison leads to the conclusion that power-law is able to describe the creep behaviour of the substrate material accurately, and that it is possible to identify creep parameters from 4PBTs. In App. B this verification is presented for 250°C in Fig. B.5 and for 300°C in Fig. B.6 as well. Only the beginning of the curve is not well described by the power-law because hardening phenomena are not considered. Nevertheless, for the analysis carried out in this work this approximation is sufficient.

9.3 Cohesive Parameters

The cohesive zone parameters are determined through numerical optimisation from 4PBTs. Therefore, the numerical model of Chap. 8 is used and then the test force, that is measured in the middle of the beam, is compared to the simulated force for every time step ($F-t$ curve). Another possibility would be to calculate the bending moment in the middle of the beam, however, this is too time-consuming. For the numerical optimisation the optimisation tool box of the

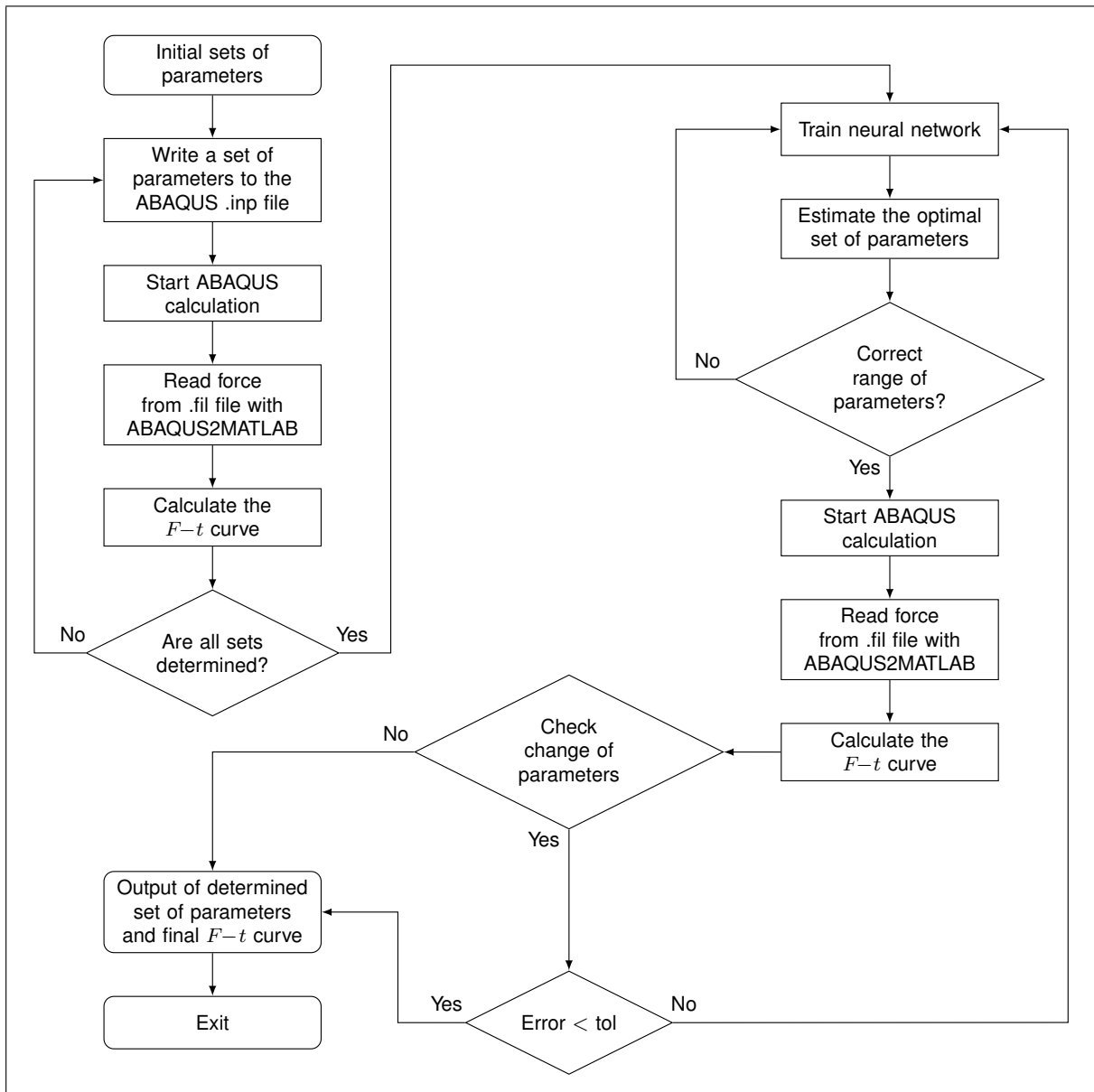


Figure 9.8: Flowchart of the optimisation algorithm

software MATLAB and for the FE simulations the software ABAQUS is used. Both programmes are connected with the tool ABAQUS2MATLAB [31], that allows us to use the benefits of both programmes. In the first step all cohesive zone parameters are determined under isothermal conditions and then after this step the temperature dependence is determined. Under isothermal conditions the optimisation algorithm of Fig. 9.8 is used. At the beginning it is necessary to define initial sets of cohesive zone parameters for which FE simulations are performed. After every simulation the $F-t$ curve is read from the result file (.fil) and saved in MATLAB. When all initial sets are evaluated and the $F-t$ curves are saved in MATLAB the neural network is trained with this data the first time to estimate a new set of parameters. Before the new simulation starts with these parameters, it is checked if the estimated set is in the expected range, and if every parameter is greater than zero. Otherwise, the set is forgotten and the training starts again. When the set of parameters fulfills all requirements the new FE simulation is performed and the $F-t$ curve is calculated. The training algorithm is repeated until the change in the parameters is less than 1% or the error of the $F-t$ curve is less than a user specified tolerance (here 0.25%). Finally, the algorithm gives as output the determined set of parameters and the

Table 9.1: Determined cohesive zone parameters under isothermal conditions for 250°C, 300°C and 400°C

T [°C]	\mathcal{I}_1			\mathcal{I}_2		
	T_{\max} [MPa]	g_{cr} [mm]	β [-]	g_{del} [mm]	S_{i0} [$\frac{mJ}{mm^2}$]	Y_{E0} [$\frac{mJ}{mm^2}$]
250	600.00	0.0050	0.95	1.00	$0.50 \cdot 10^{-3}$	0.05
300	425.00	0.0055	0.95	1.00	$0.56 \cdot 10^{-3}$	0.50
400	427.20	0.0055	0.97	1.00	$6.02 \cdot 10^{-3}$	1.30

belonging $F-t$ curve. This process is time-consuming, therefore, it is necessary to keep the model as simple as possible and use less FEs. The determined parameters are summed up in Tab. 9.1 and the final simulations are presented in Chapter 10.

At the beginning of the optimisation procedure a range for every parameter must be specified in which the parameter is expected. This is only simple for the maximum cohesive strength T_{\max} , that should be near the experimental determined strength of the coating (for 400°C it is $T_{\max} = 381$ MPa [30]). For the other parameters a higher range is necessary because no experimental data or other informations are available. The temperature dependence is presented in Appendix B.

9.4 Thermal Parameters of Substrate and Coating

Last required material parameters for numerical simulations are the heat capacity and conductivity, density and the coefficient of thermal expansion. We begin with the heat capacity c_s and conductivity κ_s for the substrate material AISi10MgT6. The temperature dependence of these parameters can be seen in Fig. 9.9, heat capacity is presented on the left-hand side and

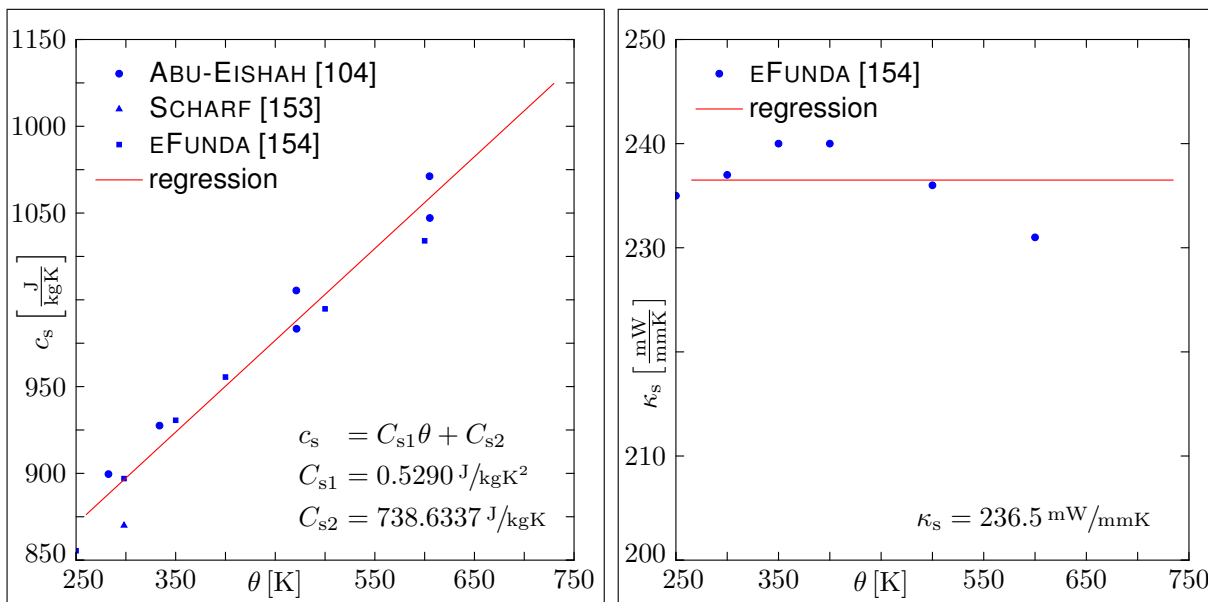


Figure 9.9: Temperature dependence of heat capacity (left-hand side) and heat conductivity (right-hand side) of the substrate

heat conductivity on the right-hand side. For the heat capacity the experimental data is taken from [104, 153, 154] and in the analysed temperature range it is possible to approximate heat capacity with the function

$$c_s = C_{s1}\theta + C_{s2}. \quad (9.7)$$

The two constants have the values

$$C_{s1} = 0.5290 \frac{\text{J}}{\text{kgK}^2} \quad \text{and} \quad C_{s2} = 738.6337 \frac{\text{J}}{\text{kgK}}.$$

Contrary to this the heat conductivity ranges only from 231 mW/mmK to 240 mW/mmK in the analysed temperature range and is approximated to be constant, therefore. Since, the error is only of 3.4%, which is a slight drawback compared to the great benefits. It results

$$\kappa_s = 236.5 \frac{\text{mW}}{\text{mmK}}. \quad (9.8)$$

Up next, heat capacity and conductivity for the coating material Fe24Al0.6Nb are determined. This is done with the experimental data of [36]. Now, both material parameters are linear functions of the temperature. The experimental data and the linear functions are presented in Fig. 9.10, on the left-hand side for heat capacity and on the right-hand side for heat conductivity. For heat capacity results the function

$$c_c = C_{c1}\theta + C_{c2} \quad (9.9)$$

with the two constants

$$C_{c1} = 0.2730 \frac{\text{J}}{\text{kgK}^2} \quad \text{and} \quad C_{c2} = 518.8479 \frac{\text{J}}{\text{kgK}},$$

and for heat conductivity the function

$$\kappa_c = K_{c1}\theta + K_{c2} \quad (9.10)$$

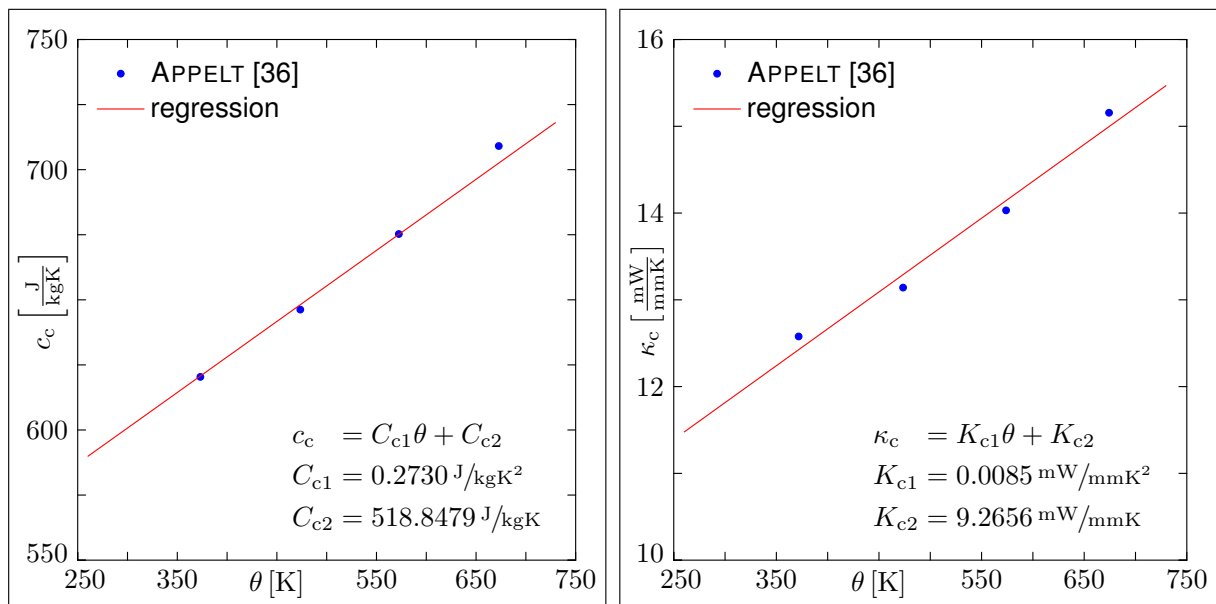


Figure 9.10: Temperature dependence of heat capacity (left-hand side) and heat conductivity (right-hand side) of the coating

Table 9.2: Temperature dependence of density of substrate and coating, values are taken from [153, 155] and [36]

material	$\rho_{25^\circ\text{C}}$ [$\frac{\text{g}}{\text{cm}^3}$]	$\rho_{500^\circ\text{C}}$ [$\frac{\text{g}}{\text{cm}^3}$]	ρ_{ave} [$\frac{\text{g}}{\text{cm}^3}$]	error [%]
AlSi10MgT6	2.65	2.56	2.61	3.4
Fe24Al0.6Nb	6.04	5.86	5.95	3.0

is determined with the two constants

$$K_{c1} = 0.0085 \frac{\text{mW}}{\text{mmK}^2} \quad \text{and} \quad K_{c2} = 9.2656 \frac{\text{mW}}{\text{mmK}} .$$

The two crucial thermal parameters are known for the substrate and coating material, now. Hence, the next material parameter is analysed. This is the density. From Tab. 9.2 it can be seen that only a slight temperature dependence of the density exists for both materials. For this reason we take the mean value of the density and assume that the density is constant in the considered temperature range. After this, the coefficient of thermal expansion is the last missing thermal parameter. According to [153] the coefficient of thermal expansion is constant between 20°C and 500°C and the value for AlSi10MgT6 is $25.31 \cdot 10^{-6} \text{ 1/K}$ and for Fe24Al0.6Nb it is $21.89 \cdot 10^{-6} \text{ 1/K}$. Due to the fact that the values are similar, no high thermal stresses arise, thus, thermal expansion is not considered in the analyses.

10 Simulation Results

In this chapter the results of all simulations are presented. We start with the comparison between the different simulation procedures, that are performed with the DCB test. The second section contains the results of the isothermal 4PBT simulations at 250°C, 300°C and 400°C. This chapter is closed with a non-isothermal simulation, which is presented in the last section.

10.1 Comparison Between Simulation Procedures

In this section the eighteen different DCB simulations are presented and compared to each other. Performed are a static simulation with viscous regularisation with elastic and inelastic material behaviour, an implicit dynamic simulation with damping (similar to viscous regularisation) and with elastic and inelastic material behaviour, and a static simulation with a damage gradient extended interface and continuum element (cf. Chap. 7). As well, for an elastic and an inelastic material behaviour. For the common static and dynamic simulation the TSL of Chap. 7 is used, whereby, the damage gradient extension is neglected. This investigation is done because, as mentioned earlier, it is well-known that the common quasi-static and dynamic, initial boundary value problem becomes ill-posed in the case of fracture, due to the change of the character of the system of PDEs. To solve this problem the model can be regularised with a

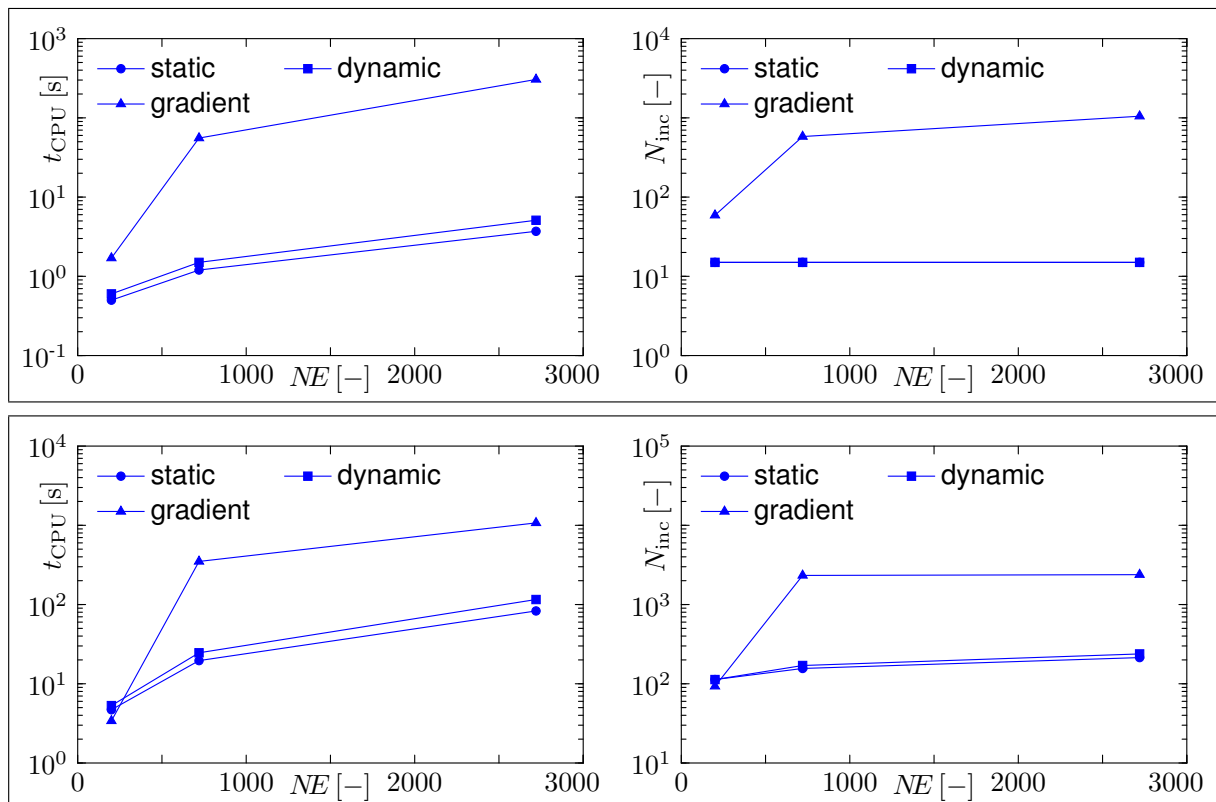


Figure 10.1: Computational time (left-hand side) and number of increments (right-hand side) to analyse a DCB test for different NE and different simulation procedures; with elastic (top) and inelastic material behaviour (bottom)

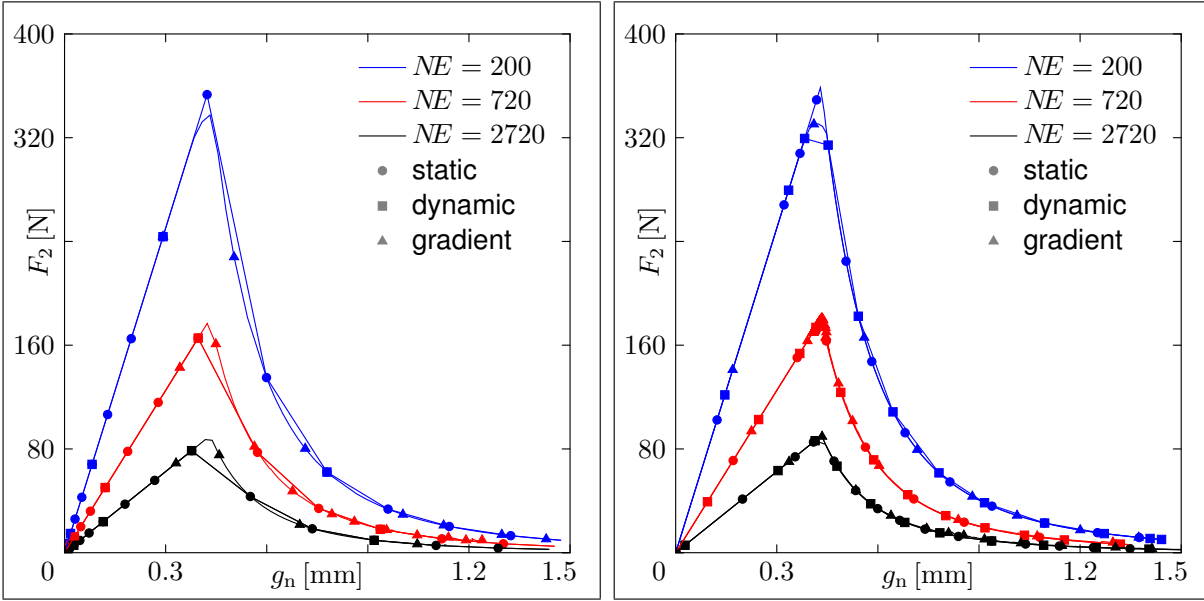


Figure 10.2: Reaction forces calculated at one node for a static, dynamic and a static simulation with damage gradient extension and for a pure elastic material behaviour (left-hand side) and an inelastic material behaviour (right-hand side)

gradient term or a viscosity is necessary [72, 156, 157]. However, which way is the most efficient is still unknown to the author. Therefore, this investigation is performed.

The main results of these simulations are presented in Figure 10.1. The required computational time t_{CPU} and number of increments N_{inc} for different NE are compared. Diagrams placed on top of Fig. 10.1 present the results for an elastic bulk material, and the diagrams placed at bottom show the results for an inelastic bulk material. On the left-hand side the required computational time and on the right-hand side the required number of increments is presented. It can be seen from these results that a static and a dynamic simulation have nearly the same numerical effort, if an elastic or inelastic material behaviour is used for the bulk. This holds true for all discretisations of the DCB test. Compared to these results the static simulation with damage gradient extension is drastically slower. For a coarse discretisation ($NE = 720$) the simulation is approximately ten times slower. This ratio increases to almost one hundred for a fine discretisation ($NE = 2720$). We relate this behaviour to the smaller required time step for a model with damage gradient extension (Otherwise the gradient term can not be resolved.) and to the higher number of $DOFs$. In the end we conclude that a simulation with damage gradient extension is not preferable and for reasons of efficiency, a static analysis with viscous regularisation or a dynamic analyses with damping should be performed. Whereby, a quasi-static simulation with viscous regularisations is the most efficient way. To verify the correctness of the solution the reaction forces versus the separation at one node are compared to each other (the reaction force has the same shape as the TSL). This comparison is presented in Fig. 10.2, on the left-hand side for an elastic and on the right-hand side for an inelastic bulk material. For every discretisation the same shape of reaction force versus separation curve (TSL) is calculated for all three simulation procedures. Due to a finer mesh the change of the curve is a result of the mesh dependence of the model, which is well-known [57, 72]. Further on, it is not possible to solve this mesh dependence by using a non-local TSL. In the end, we can conclude that all three simulation procedures yield the same results. Moreover, the determination is correct without the loss of elliptic or hyperbolic character of the governing equations since once the model is equipped with a viscosity and the other time with a gradient term [72]. However, it is recommended to use a quasi-static simulation with viscous regularisation.

10.2 Isothermal Simulations

In this section the results of the isothermal failure simulations of the 4PBT at 250°C, 300°C and 400°C are presented. The used material parameters for the bulk material are calculated from the functions determined in Chap. 9 of this work and are summarised in Table 10.1. The material parameters of the interfaces are summarised in Tab. 9.1 in Section 9.3 and required dimensions of the specimens are presented in Tab. B.3 in Appendix B. The applied load is adopted from the experimental data as well as the simulation time. Further on, all three simulations are performed with a velocity of $v_{\text{sim}} = 0.050 \frac{\text{mm}}{\text{min}}$ of the upper support. Because the performed simulations did not fit accurately (blue line with circles) to the experimental result, and because the creep factor a_s is the most inexact material parameter, due to the deviation of the activation energy, the creep factor is adjusted as well as the interface parameters. Table 10.2 presents the new, optimised material parameters, that are used for simulations as well. The results of both simulations are presented in the following for the temperatures 250°C, 300°C and 400°C.

Figure 10.3 presents the results of the isothermal 4PBT simulations at 250°C once with the material parameters of Chap. 9 and with optimised material parameters (blue line with triangles) as well. As can be seen, the simulation with the material parameters of Chap. 9 goes above the measurement, which indicates that the creep deformation is underestimated. This leads to the problem that it is not possible to determine the material parameters of the interfaces accurately in the end. Therefore, the creep factor is adjusted. The simulation with optimised creep factor and cohesive parameters is also presented in Fig. 10.3. The agreement with the experiment is much better, even though, the creep factor has only changed slightly. Adjusting the creep factor is based on the statement, that the identification of this parameter is the most inaccurate one because this parameter depends on the activation energy, which has usually a

Table 10.1: Material parameters of substrate and coating for 250°C, 300°C and 400°C

T [°C]	coating		substrate			
	E_c [GPa]	ν_c [-]	E_s [GPa]	ν_s [-]	a_s [s ⁻¹]	N_s [-]
250	61.14	0.30	63.66	0.33	$1.44 \cdot 10^{-14}$	4.0317
300	59.12	0.30	57.06	0.33	$2.61 \cdot 10^{-13}$	4.0317
400	55.08	0.30	32.93	0.33	$4.24 \cdot 10^{-11}$	4.0317

Table 10.2: Optimised material parameters under isothermal conditions for 250°C, 300°C and 400°C

T [°C]	substrate	\mathcal{I}_1			\mathcal{I}_2		
	a_s [s ⁻¹]	T_{max} [MPa]	g_{cr} [mm]	β [-]	g_{del} [mm]	S_{i0} [$\frac{\text{mJ}}{\text{mm}^2}$]	Y_{E0} [$\frac{\text{mJ}}{\text{mm}^2}$]
250	$4.00 \cdot 10^{-14}$	580.00	0.0050	0.95	1.00	$1.20 \cdot 10^{-2}$	1.00
300	$5.52 \cdot 10^{-13}$	445.64	0.0028	0.54	1.00	$8.45 \cdot 10^{-5}$	0.98
400	$2.30 \cdot 10^{-11}$	382.90	0.0093	1.03	1.00	$5.03 \cdot 10^{-3}$	0.54

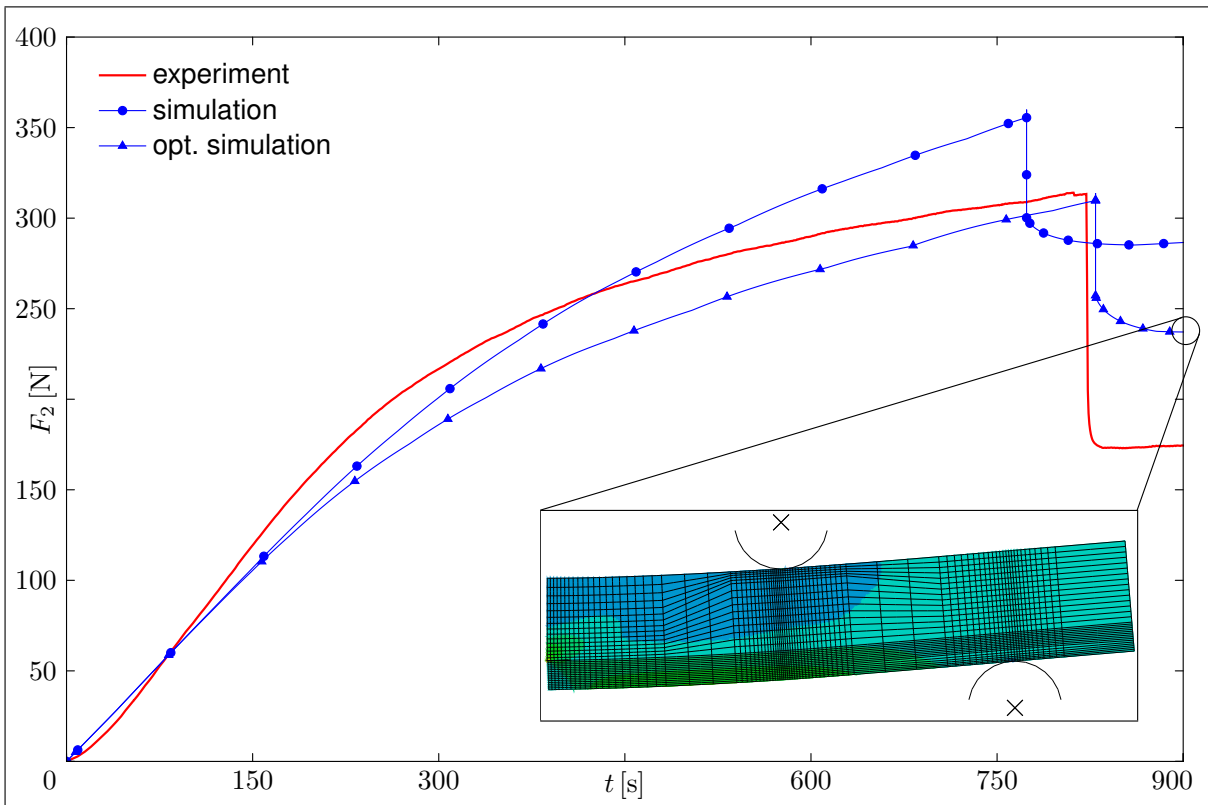


Figure 10.3: Comparison between experiment and simulation at 250°C; the FE pictures shows the stress distribution of T_{11}^K along the beam

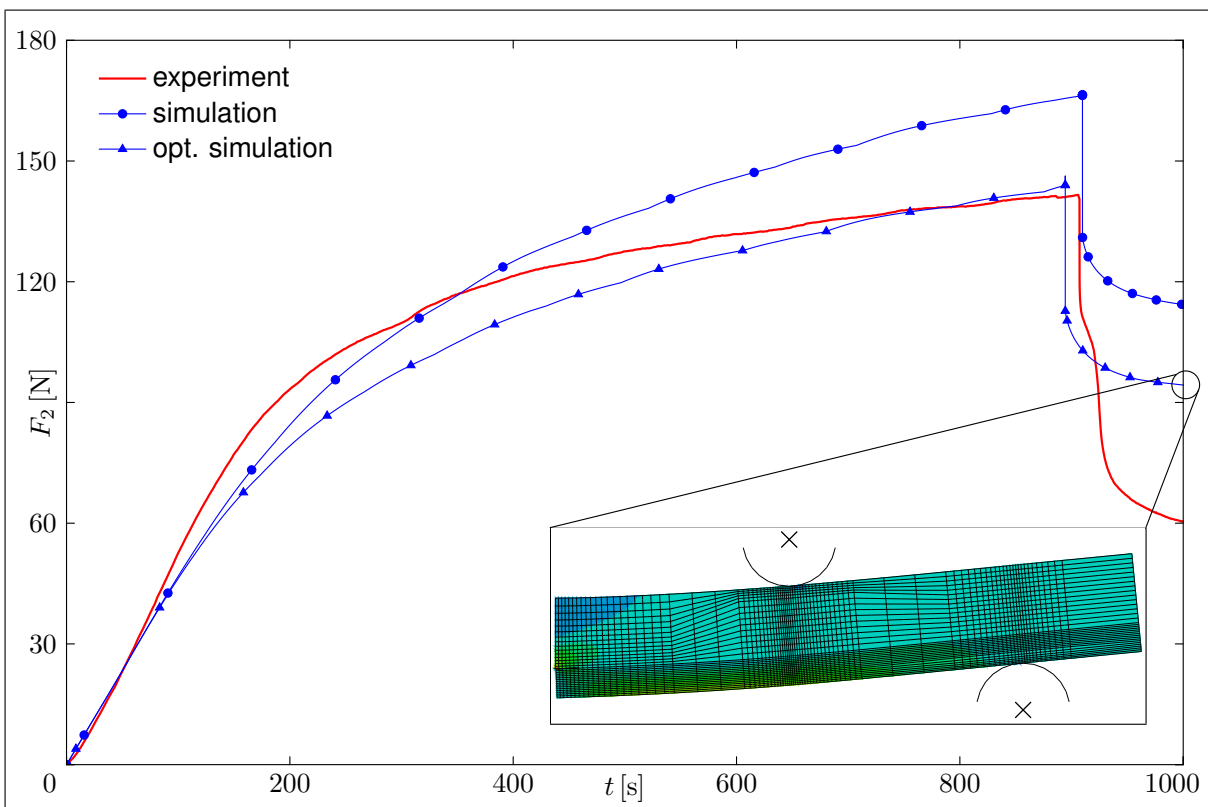


Figure 10.4: Comparison between experiment and simulation at 300°C; the FE pictures shows the stress distribution of T_{11}^K along the beam

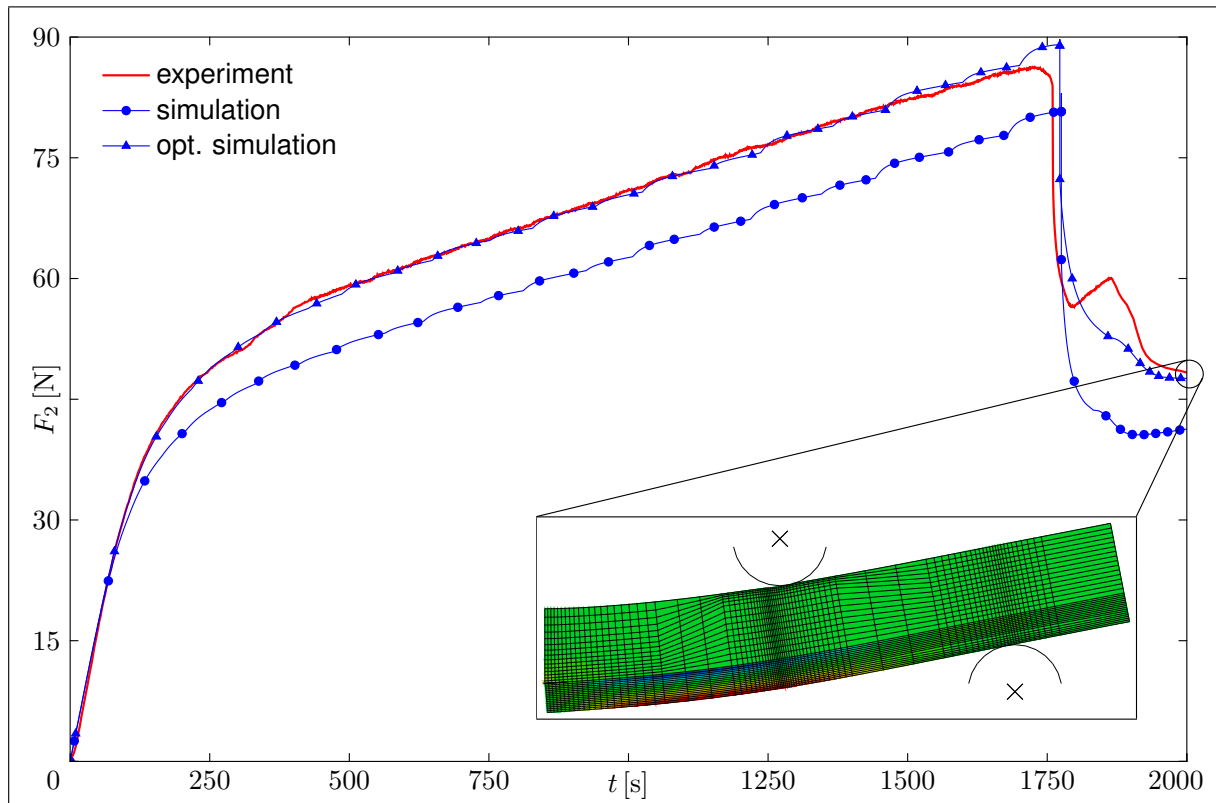


Figure 10.5: Comparison between experiment and simulation at 400°C; the FE pictures shows the stress distribution of T_{11}^K along the beam

deviation of 10 kJ/mol and they are related by an exponential function. Thus, deviation of activation energy has a huge influence. The new results fit better to the measurement. However, a deviation remains. Figure 10.4 presents similar results for a temperature of 300°C and Fig. 10.5 for 400°C. Again, the creep deformation is underestimated for 300°C and overestimated for 400°C but the onset of cracking is found in both cases. However, for a better approximation the creep factor is adjusted, which leads to a better approximation of the experiment in the end. Much more, the adjusting of the creep factor at all temperatures is a consequence of the assumption that the creep exponent N_s is temperature independent, which is a strong simplification and questionable, as mentioned in Chap. 9, but a crucial assumption for the used identification procedure. However, when more experimental data is available this assumption should be abandoned.

Further on, the discontinuities in the calculated curves (especially at 400°C) are a result of the viscous regularisation scheme and not, as someone could expect, a consequence of the contact conditions between beam and supports. At every discontinuity the used time step needs to be reduced because of arising destabilisations, that are a result of the used interface elements and also (slightly) by the inelastic deformation. However, the influence of these discontinuities is only large near the onset of cracking. Before and afterwards the influence is small. Finally, Fig. 10.6 presents the change of the stress distribution along the beam during the whole simulation at 400°C, and how the stress distribution changes due to the onset of cracking and crack propagation. Initially ($t = 0 \text{ s}$), the beam is stress-free, then, an usual stress distribution arises ($t = 300 \text{ s}$), whereby, in the coating a much higher stress is present as compared to the substrate. Due to further loading and creep deformation of the substrate, a reallocation of the stress takes place, which leads to the situation that the substrate is approximately stress-free and the coating carries the whole load ($t = 1000 \text{ s}$). This situation is enhanced with further loading and it results a stress concentration at the left, lower corner of the coating, that leads to the

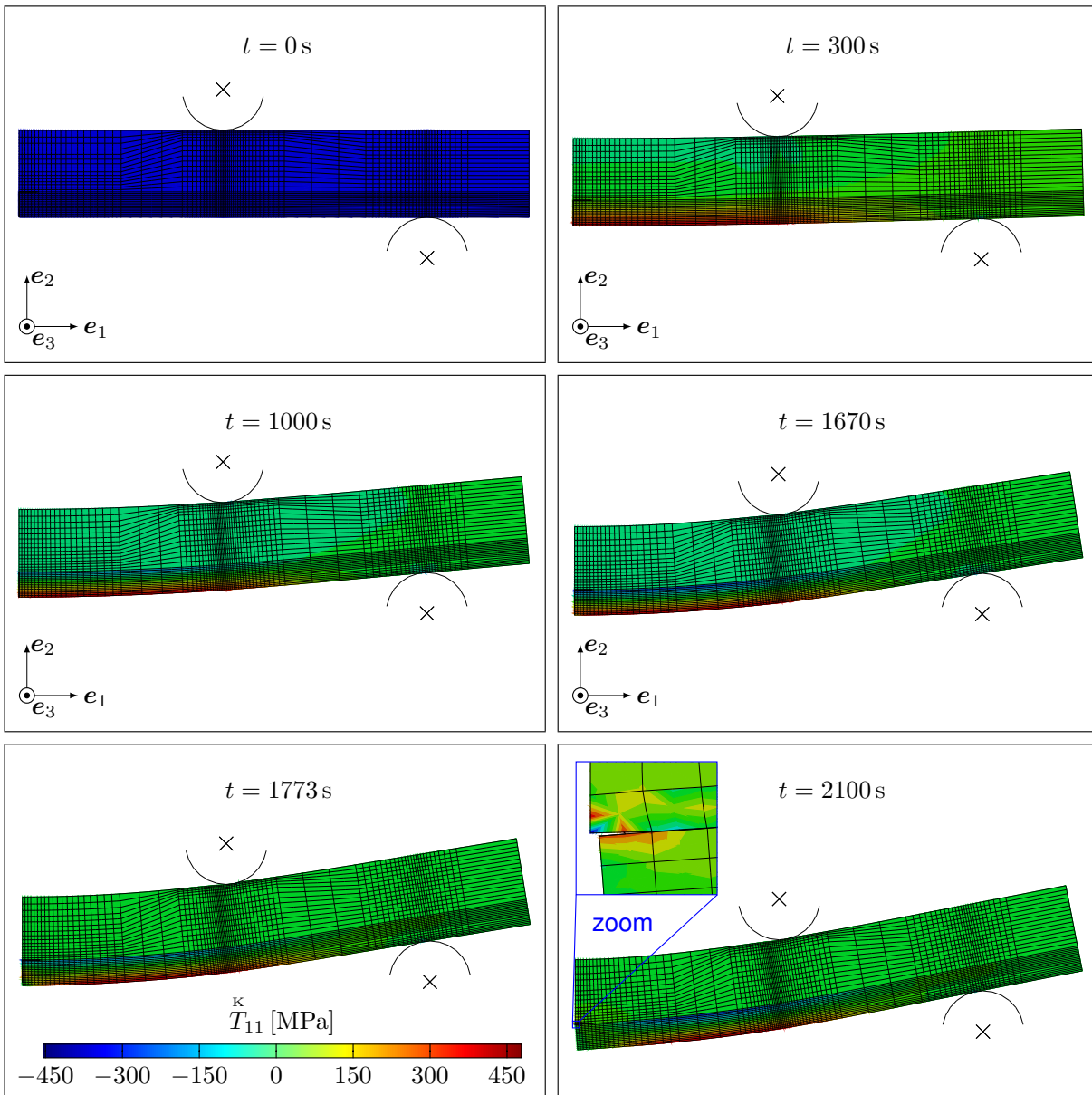


Figure 10.6: Change of the stress distribution of T_{11}^K in the beam during the simulation at 400°C

onset of cracking ($t = 1670$ s). With further loading the crack propagates through the coating, which leads to a rotation of this one and the remaining stress reallocates from the middle of the beam to the upper support ($t = 1773$ s). After failure of the whole coating a new stress concentration arises at the connection between coating and substrate. Although, because a high inelastic deformation (creep) is present and the stress reallocates, the delamination process of the coating starts not directly. There is a small break between these two processes. However, this process is not exactly reproducible with the model, as can be seen in Fig. 10.5. Finally, it results a delamination of a few μm ($t = 2100$ s). However, for such complicated simulations the achieved results and agreements with the experiments are good.

10.3 Non-Isothermal Simulation

This chapter presents the capabilities of the coupled thermo-mechanical problem, that is formulated in this work and solved with the FEM. The solution procedure is briefly explained in

Section 6.6.1. Even though, the arising numerical problems are outstanding and finding a solution without the viscous regularisation technique is impossible for large, non-linear models. Here, the biggest problem is that the time step has a strong contrary behaviour. This is represented by the equation

$$\Delta t_{\min} > \frac{\rho_b c_b}{6 \kappa_b} l_{\text{ele}}^2, \quad (10.1)$$

which describes a temperature and element size dependence of the minimal time step, that can be used in the thermo-mechanical analysis before the heat conduction equation starts oscillating [60]. However, the minimal usable time step resulting from this inequality is too large compared to the required minimal time step, which is necessary in the onset of cracking. This time step is in the range of $10^{-15}\text{s} < t_{\min} < 10^{-10}\text{s}$. The dependence of the time step on the material parameters is approximately constant. Also, this is confirmed by Fig. 10.7, which represents the temperature dependence of the minimal time step for the coating (left-hand side) and substrate material (right-hand side) for the smallest and largest used element sizes. Hence, reduction of the element size is the only possibility to decrease the minimal usable time step. However, by adjusting the element size another problem occurs. The element size is chosen in relation to the length scale of the cohesive zone, that is in general unknown and chosen after rules of thumb [42]. This is the case here too. Further on, the cohesive zone parameters depend on the length scale as well. Hence, a change of the element length changes the length scale and finally the cohesive zone parameters. It results an infinite loop, which can only be exited by performing a very costly and time-consuming optimisation procedure with a complex problem (of a high calculation time itself) or fixing one quantity (element length, length scale, etc.). This is the economical way and is done in this work. All identified parameters depend on this fixed element size, and therefore the time step is limited by Eq. (10.1).

For this reason oscillations and a destabilisation of the NEWTON-RAPHSON procedure are expected and the viscous regularisation scheme is used to stabilise the solution procedure, similar, as it is done for the isothermal case. However, with justifiable effort (less than a month) it is not possible to determine a suitable set of viscous regularisation parameters to start the simulation of the 4PBT under non-isothermal conditions. Whereby, this guarantees not that the simulation will complete successfully, and the problem is already decoupled. Therefore, a simpler problem is presented for which a suitable set of tolerances is found, and the simulation is successfully completed. This procedure allows at least to present the capabilities of the derived thermo-mechanical model.

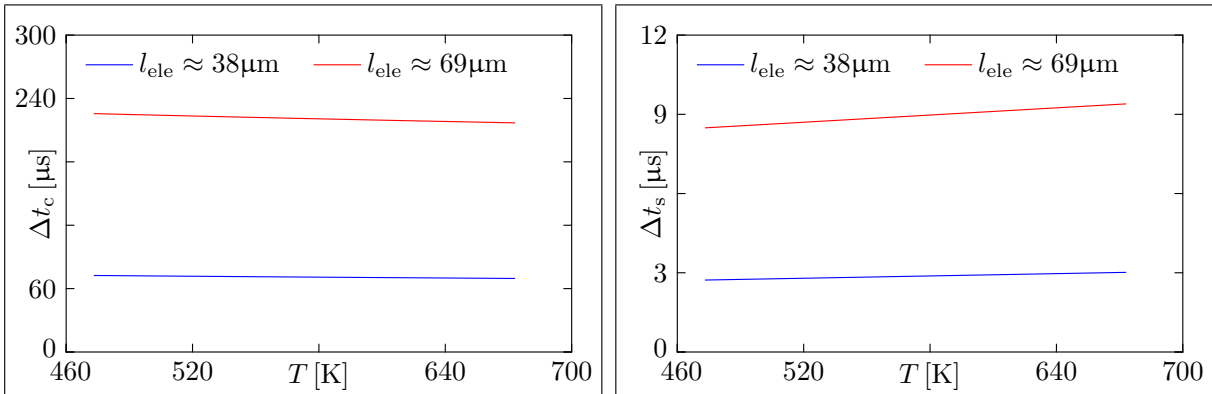


Figure 10.7: Temperature dependence of the minimal time step for the smallest and largest element length used in the 4PBT simulation on the left-hand side for the coating and on the right-hand side for the substrate material

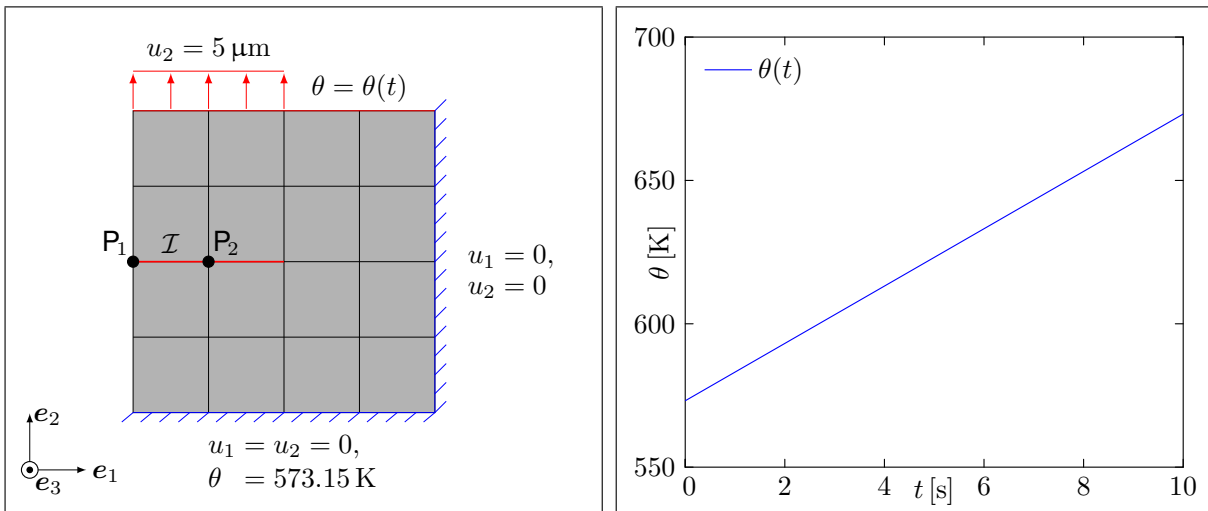


Figure 10.8: Analyzed thermo-mechanical problem (left-hand side) and temperature function (right-hand side)

The analysed model is presented in Fig. 10.8 on the left-hand side. It is a square with a length of 0.2 mm , that is discretised with sixteen plane continuum elements of linear material behaviour. Additionally, the square consists of a zero-thickness interface, which is discretised by four interface elements. To solve the mechanical problem DIRICHLET boundary conditions are applied at the edges at bottom, on the right side and on top of the square. For the thermal problem temperature boundary conditions are applied at the edges at bottom and on top of the problem. Initially, the temperature in the solution area is everywhere 573.15 K . At top the temperature increases from 573.15 K to 673.15 K in 10 s . This is shown in Fig. 10.8 on the right-hand side. Hence, a temperature gradient of 100 K exists in the model. The results of this simulation are presented in Figs. 10.9 and 10.10. Figure 10.9 shows the temperature change calculated at points P_1 (left-hand side) and P_2 (right-hand side) versus time. The red curve represents the temperature at top and the blue line at bottom of the interface. From these diagrams it can be seen that the temperature is on both sides of the interface the same up to $t \approx 5 \text{ s}$. Then, due to the onset of cracking, the heat conduction of the interface changes and the bottom of the interface cools down and the top keeps getting warmer. Next to that, Fig. 10.9 shows the influence of the factor a_d , which is the heat production due to cracking. An increase of this factor from zero to a specific value changes only the slope of the temperature curves. Whereby, a too high value of a_d leads to oscillations in the temperature because the integration algorithm fails. Figure 10.10 confirms these statements and shows next to that the temperature distribution in

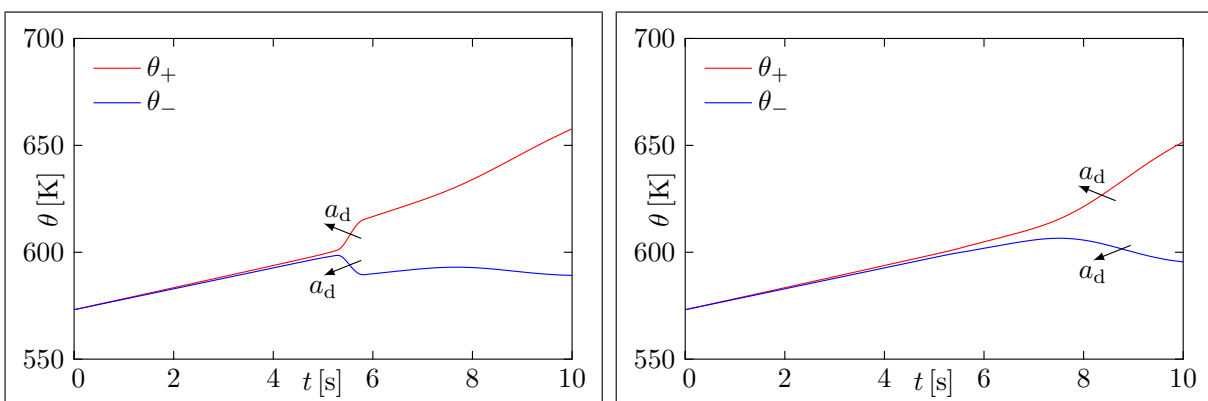


Figure 10.9: Temperature change at point P_1 (left-hand side) and P_2 (right-hand side) over time; a_d changes the sloop of the curve in the transition area

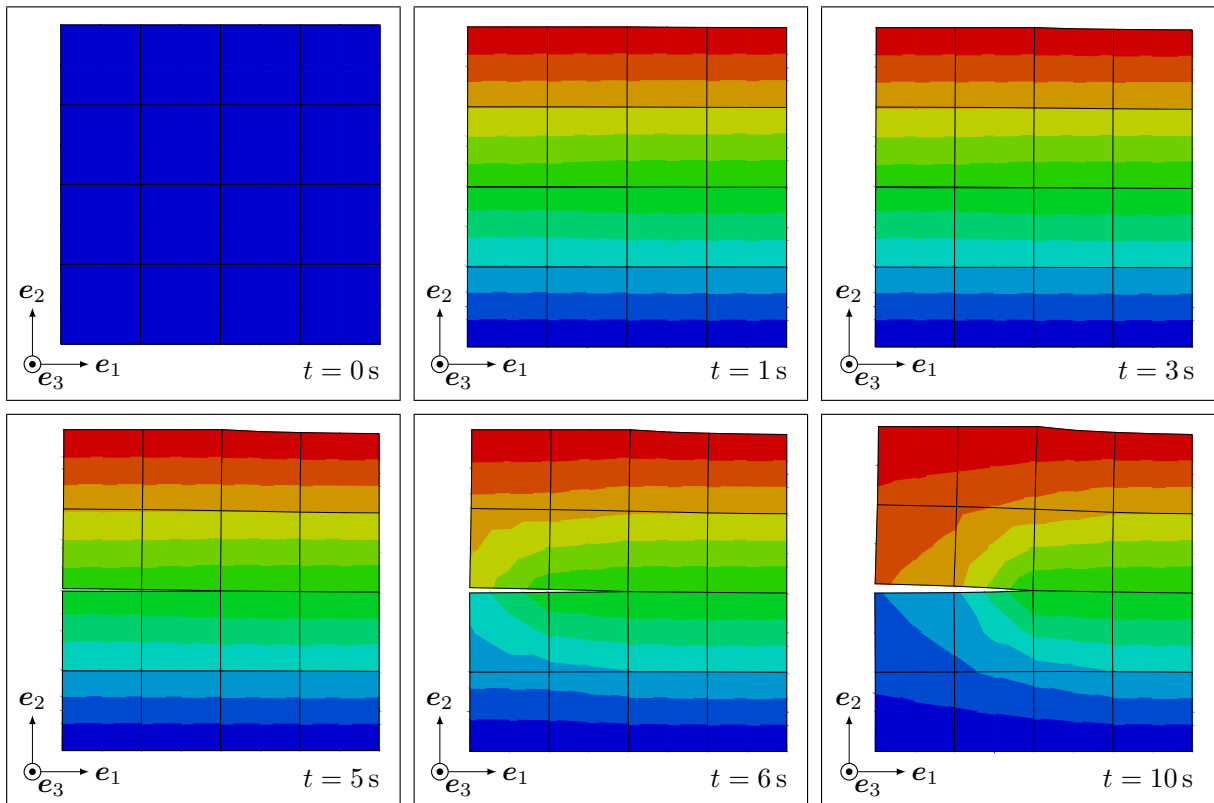


Figure 10.10: Temperature distribution in the model at different time points; red - high temperature, blue - low temperature

the whole solution area at different time points. Initially ($t = 0$ s), the interface has no influence on the temperature distribution and in the whole model results a temperature of $\theta = 573.15$ K. From $t = 1$ s to $t = 5$ s the temperature is approximately linear distributed from top to bottom, however, a slight influence of the interface onto the temperature distribution exists due to the length scale. Then the crack starts to propagate through the interface ($t = 6$ s), what leads to a strong change of the temperature distribution. The top side of the interface keeps getting warmer and in contrast to that the bottom side cools down. On the right side of the model (no interface) the temperature distribution is still approximately linear. The picture at $t = 10$ s shows the final temperature distribution in the model.

11 Summary, Conclusion and Outlook

This thesis deals with modelling the failure behaviour of a compound made of iron aluminide (Fe₂₄Al_{10.6}Nb) and aluminium (AlSi10MgT6) subjected to mechanical and thermal loads. Nowadays, fracture mechanics is a field of increasing interest due to the fact that the computational power increases from year to year. Without this increasing computational power it is not possible to solve the resulting mathematical problem. In the literature different possibilities exist to model the failure behaviour of a material. The CZM is used in this work. Therefore, this work begins with an introduction about the used materials and goes on with the basic principles of continuum mechanics and how the CZM is added to these principles. In the ongoing chapter constitutive laws are formulated and then it is explained how these laws are implemented into the FEM. For this work the software package ABAQUS is used. Next to this, the identification of all required, temperature dependent material parameters is explained in detail in this work. Further on, neural network optimisation is used to identify the cohesive zone parameters because not enough experimental data is available.

All fracture mechanical models have in common that they share the same basic problem and this is the change of the type of PDE in the case of damage evolution. Some call this phenomenon "loss of ellipticity" [75]. An identical problem occurs due to a strong inelastic material behaviour. To solve this problem it is necessary to regularise the model through the addition of a viscous term or use an explicit or implicit gradient theory or perform a dynamic analysis. The solution is always obtained by applying the full NEWTON-RAPHSON scheme to the system of PDEs. Due to the existence of all these different solution possibilities in this work three different procedures are compared: a quasi-static simulation with viscous regularisation, a dynamic simulation with damping and a quasi-static simulation, that is regularised with the damage gradient. This study is performed with a DCB example under mesh refinement and in the end the computation time and the required number of increments is compared to each other. This study is carried out to find the most efficient procedure for fracture mechanical analysis. This is important if someone once to analyse fracture processes in larger structures or constructions and to the author's knowledge this comparison does not exist in the literature. One result of this study is that it is far more efficient to perform a quasi-static simulation with viscous regularisation as a gradient regularised quasi-static simulation. The simulation with viscous regularisation is ten to one hundred times faster as the gradient regularised simulation. This is in agreement with results of other researchers (e.g. [158, 159]), which have high computation times due to a gradient regularised model as well. The dynamic simulation with damping is only slightly slower as a quasi-static simulation with viscous regularisation. High computation times due to many iterations in one time step which are necessary to resolve the gradient term in the constitutive law and many elements (many *DOF*s) are the main problems for the applicability of gradient regularised models, next to C_1 -continues elements, etc. Therefore, it is recommended to use viscous regularisation schemes in complex simulations because to the author's knowledge these problems are not solved, up to now. Further on, a gradient regularised CZM depends still on its length (or mesh size). For this reason the 4PBT simulations are performed under quasi-static conditions with viscous regularisation. Otherwise, the identification of cohesive zone parameters with neural network optimisation would be not possible because the overall computation time for one temperature (250°C, 300°C or 400°C) would have increased to months (three to four) instead of a few weeks (one to two). However, this holds only when the viscous regularisation tolerances are chosen correct.

Nevertheless, this procedure worked well for the 4PBT simulations under isothermal conditions, and the final simulations are in very good agreement with the experimental results (cf. Sect. 10.2). Also, this good agreement is a result of the proposed novel, rate dependent TSL which is formulated in this work and which suits well to the inelastic deformation processes taking place in the substrate material. However, for a 4PBT under non-isothermal conditions it was not possible to find a suitable set of viscous regularisation tolerances in an acceptable time range for performing a successful simulation. This is addressed to the contrary behaviour of heat conduction equation and balance of linear momentum in combination with fracture mechanical processes as discussed in detail in Section 10.3. For this reason an example simulation is performed in this section to present at least the capabilities of the model.

Coming to the end of this thesis, from the author's point of view the biggest challenge in the analysis of fracture mechanical processes through simulations is the time integration because time increments of a size are required that are unacceptable. This prevents the use of fracture mechanics for the analysis of real structures. Therefore, future work could be done in the following fields. The analysis of long time processes such as creep or low-cycle fatigue need large time steps for the time integration. However, the fracture process needs time steps in the size of μs , ns or even smaller. These are totally different requirements. Hence, it should be investigated if it is possible to use time scale methods to decouple both problems, integrate them independently and put them together in the end or decouple both problem in combination with a LAGRANGE multiplier to ensure the constraints. Maybe this leads to a faster integration. Another approach is to work directly on integration algorithms or improve viscous regularisation schemes (e.g. with more damping factors), so that these schemes could be used without applying a trial and error procedure to determine the required tolerances. In the authors opinion gradient theories should be avoided because more problems arise, besides the time integration. C_1 -continues elements are required, which is not straight forward for 2D and 3D continua, and material parameters arise, that cannot be interpreted. Next to that, it is expected that the simulation will still be slower as a simulation with viscous regularisation, thus, the applicability is not guaranteed. The last point is to use GREEN & NAGHDI type II or type III theory for the simulation of heat conduction since this PDE is of the same type as the balance of linear momentum (hyperbolic) [160]. Maybe, this is beneficial for the time integration of both equations, and the contrary behaviour of the allowable time increment can be avoided.

References

- [1] Altenbach, H. *Kontinuumsmechanik: Einführung in die materialunabhängigen und materialabhängigen Gleichungen*. 4. Auflage. Berlin · Heidelberg: Springer Vieweg, 2018. DOI: 10.1007/978-3-662-57504-8.
- [2] Lai, W., Rubin, D., and Krempl, E. *Introduction to Continuum Mechanics*. 4. Edition. Oxford: Butterworth-Heinemann, 2009.
- [3] Bertram, A. *Elasticity and Plasticity of Large Deformations: An Introduction*. 3. Edition. Berlin · Heidelberg: Springer, 2012. DOI: 10.1007/978-3-642-24615-9.
- [4] Bertram, A. and Glüge, R. *Solid Mechanics. Theory, Modeling, and Problems*. Springer, 2015. DOI: 10.1007/978-3-319-19566-7.
- [5] Lebedev, L. P., Cloud, M. J., and Eremeyev, V. A. *Tensor Analysis with Applications in Mechanics*. New Jersey · London · Singapore · Beijing · Shanghai · Hong Kong · Taipei · Chennai: World Scientific, 2010. DOI: 10.1142/9789814313995.
- [6] Itskov, M. *Tensor Algebra and Tensor Analysis for Engineers*. Springer International Publishing, 2015. DOI: 10.1007/978-3-319-16342-0.
- [7] Michelfeit, S. “Werkstoffgesetze einer AlSi-Gusslegierung unter Hochtemperaturbeanspruchung in Abhängigkeit des Werkstoffzustandes”. Dissertation. Technische Universität Darmstadt, 2012.
- [8] Schebek, L., Abele, E., Anderl, R., Sauer, A., and Zühlke, D. *Ressourceneffizienz durch Industrie 4.0—Potenziale für KMU des verarbeitenden Gewerbes*. Bertolt-Brecht-Platz 3, 10117 Berlin: VDI Zentrum Ressourceneffizienz GmbH (VDI ZRE), 2017.
- [9] Rauch, M. “Entwicklung eines Lebensdauerkonzeptes für Schaufel-Welle-Verbindungen stationärer Turbinen aus Nickelbasis- und 10 %-Chromlegierungen”. PhD thesis. Universität Stuttgart, 2006.
- [10] Goward, G. “Progress in coatings for gas turbine airfoils”. In: *Surface and Coatings Technology* 108-109, 1998, pp. 73–79. DOI: 10.1016/S0257-8972(98)00667-7.
- [11] Pint, B., DiStefano, J., and Wright, I. “Oxidation resistance: One barrier to moving beyond Ni-base superalloys”. In: *Materials Science and Engineering: A* 415(1-2), 2006, pp. 255–263. DOI: 10.1016/j.msea.2005.09.091.
- [12] Rajendran, R. “Gas turbine coatings – An overview”. In: *Engineering Failure Analysis* 26, 2012, pp. 355–369. DOI: 10.1016/j.engfailanal.2012.07.007.
- [13] Langston, L. “Each Blade a Single Crystal”. In: *American Scientist* 103(1), 2015, p. 30. DOI: 10.1511/2015.112.30.
- [14] Krüger, M., Jain, P., Kumar, K., and Heilmaier, M. “Correlation between microstructure and properties of fine grained Mo–Mo₃Si–Mo₅SiB₂ alloys”. In: *Intermetallics* 48, 2014, pp. 10–18. DOI: 10.1016/j.intermet.2013.10.025.
- [15] Griffith, A. A. “The Phenomena of Rupture and Flow in Solids”. In: *Philosophical Transactions of the Royal Society A: Mathematical, Physical and Engineering Sciences* 221(5 82-593), 1921, pp. 163–198. DOI: 10.1098/rsta.1921.0006.
- [16] Barenblatt, G. “The formation of equilibrium cracks during brittle fracture. General ideas and hypotheses. Axially-symmetric cracks”. In: *Journal of Applied Mathematics and Mechanics* 23(3), 1959, pp. 622–636. DOI: 10.1016/0021-8928(59)90157-1.

- [17] Dugdale, D. "Yielding of steel sheets containing slits". In: *Journal of the Mechanics and Physics of Solids* 8(2), 1960, pp. 100–104. DOI: 10.1016/0022-5096(60)90013-2.
- [18] Lemaitre, J. and Chaboche, J.-L. *Mechanics of Solid Materials*. Cambridge University Press, 1990. DOI: 10.1017/cbo9781139167970.
- [19] Lemaitre, J. and Desmorat, R. *Engineering Damage Mechanics*. Berlin · Heidelberg: Springer-Verlag, 2005. DOI: 10.1007/b138882.
- [20] Kuhn, C. "Numerical and Analytical Investigation of a Phase Field Model for Fracture". PhD thesis. Technische Universität Kaiserslautern, 2013.
- [21] Silling, S. *Reformulation of Elasticity Theory for Discontinuities and Long-Range Forces*. Tech. rep. 1998. DOI: 10.2172/1895.
- [22] Leuschner, M. "Numerically efficient computational homogenization: Fourier-accelerated nodal solvers and reduced basis model order reduction". PhD thesis. Universität Stuttgart, 2018. ISBN: 978-3-937399-50-8.
- [23] Kumar Goyal, V. "Analytical modeling of the mechanics of nucleation and growth of cracks". PhD thesis. Virginia Polytechnic Institute and State University, 2002.
- [24] Sermage, J. P., Lemaitre, J., and Desmorat, R. "Multiaxial Creep Fatigue under Anisothermal Conditions". In: *IUTAM Symposium on Creep in Structures*. Springer Netherlands, 2001, pp. 125–130. DOI: 10.1007/978-94-015-9628-2_13.
- [25] Gurtin, M. E. "Generalized Ginzburg-Landau and Cahn-Hilliard equations based on a microforce balance". In: *Physica D: Nonlinear Phenomena* 92(3-4), 1996, pp. 178–192. DOI: 10.1016/0167-2789(95)00173-5.
- [26] Miehe, C., Hofacker, M., and Welschinger, F. "A phase field model for rate-independent crack propagation: Robust algorithmic implementation based on operator splits". In: *Computer Methods in Applied Mechanics and Engineering* 199(45-48), 2010, pp. 2765–2778. DOI: 10.1016/j.cma.2010.04.011.
- [27] Bouvard, J., Chaboche, J.-L., Feyel, F., and Gallerneau, F. "A cohesive zone model for fatigue and creep-fatigue crack growth in single crystal superalloys". In: *International Journal of Fatigue* 31(5), 2009, pp. 868–879. DOI: 10.1016/j.ijfatigue.2008.11.002.
- [28] Chandra, N., Li, H., Shet, C., and Ghonem, H. "Some issues in the application of cohesive zone models for metal-ceramic interfaces". In: *International Journal of Solids and Structures* 39(10), 2002, pp. 2827–2855. DOI: 10.1016/s0020-7683(02)00149-x.
- [29] Nordmann, J. "Mechanische Eigenschaften von FeAl- AlSi Verbunden". Master Thesis. Otto-von-Guericke-Universität Magdeburg, 2017.
- [30] Nordmann, J., Thiem, P., Cinca, N., Naumenko, K., and Krüger, M. "Analysis of iron aluminide coated beams under creep conditions in high-temperature four-point bending tests". In: *The Journal of Strain Analysis for Engineering Design* 53(4), 2018, pp. 255–265. DOI: 10.1177/0309324718761305.
- [31] Papazafeiropoulos, G., Muñoz-Calvente, M., and Martínez-Pañeda, E. "Abaqus2Matlab: A suitable tool for finite element post-processing". In: *Advances in Engineering Software* 105, 2017, pp. 9–16. DOI: 10.1016/j.advengsoft.2017.01.006.
- [32] Kozhar, S. "Festigkeitsverhalten der Al-Si-Gusslegierung AlSi12CuNiMg bei erhöhten Temperaturen". Dissertation. Otto-von-Guericke Universität Magdeburg, 2010.
- [33] Nordmann, J., Aßmus, M., and Altenbach, H. "Visualising elastic anisotropy: theoretical background and computational implementation". In: *Continuum Mechanics and Thermodynamics* 30(4), 2018, pp. 689–708. DOI: 10.1007/s00161-018-0635-9.
- [34] Odqvist, F. K. G. and Hult, J. *Kriechfestigkeit metallischer Werkstoffe*. Springer Berlin Heidelberg, 1962. DOI: 10.1007/978-3-642-52432-5.

- [35] Naumenko, K. and Altenbach, H. *Modeling High Temperature Materials Behavior for Structural Analysis*. Springer International Publishing, 2016. DOI: 10.1007/978-3-319-31629-1.
- [36] Appelt, M. "Eisen-Aluminium-Legierungen für thermomechanisch belastete Komponenten im Abgasstrang". Dissertation. Karlsruher Institut für Technologie, 2013.
- [37] Böhlke, T. and Brüggemann, C. "Graphical representation of the generalized Hooke's law". In: *Technische Mechanik* 21(2), 2001, pp. 145–158. DOI: 10.5445/IR/1000013749.
- [38] Stoloff, N. "Iron aluminides: present status and future prospects". In: *Materials Science and Engineering: A* 258(1-2), 1998, pp. 1–14. DOI: 10.1016/s0921-5093(98)00909-5.
- [39] Fauchais, P. L., Heberlein, J. V., and Boulos, M. I. *Thermal Spray Fundamentals*. Springer US, 2014. DOI: 10.1007/978-0-387-68991-3.
- [40] Metco, S. *Einführung Thermisches Spritzen*. Tech. rep. Kelsterbach: Sulzer Metco, 2012.
- [41] Bach, F.-W., Laarmann, A., Möhwald, K., and Wenz, T., eds. *Moderne Beschichtungsverfahren*. Wiley, 2004. DOI: 10.1002/3527604278.
- [42] Schwalbe, K.-H., Scheider, I., and Cornec, A. *Guidelines for Applying Cohesive Models to the Damage Behaviour of Engineering Materials and Structures*. Springer Berlin Heidelberg, 2013. DOI: 10.1007/978-3-642-29494-5.
- [43] Barenblatt, G. "The Mathematical Theory of Equilibrium Cracks in Brittle Fracture". In: *Advances in Applied Mechanics*. Vol. 7. Elsevier, 1962, pp. 55–129. DOI: 10.1016/s0065-2156(08)70121-2.
- [44] Hillerborg, A., Modéer, M., and Petersson, P.-E. "Analysis of crack formation and crack growth in concrete by means of fracture mechanics and finite elements". In: *Cement and concrete research* 6(6), 1976, pp. 773–781.
- [45] Needleman, A. "An analysis of tensile decohesion along an interface". In: *Journal of the Mechanics and Physics of Solids* 38(3), 1990, pp. 289–324.
- [46] Needleman, A. "An analysis of decohesion along an imperfect interface". In: *Non-Linear Fracture*. Ed. by Knauss W.G., R. A. Springer Netherlands, 1990, pp. 21–40. DOI: 10.1007/978-94-017-2444-9_2.
- [47] Tvergaard, V. and Hutchinson, J. W. "The relation between crack growth resistance and fracture process parameters in elastic-plastic solids". In: *Journal of the Mechanics and Physics of Solids* 40(6), 1992, pp. 1377–1397. DOI: 10.1016/0022-5096(92)90020-3.
- [48] Ortiz, M and Suresh, S. "Statistical properties of residual stresses and intergranular fracture in ceramic materials". In: *Journal of Applied Mechanics* 60(1), 1993, pp. 77–84.
- [49] Xu, X.-P. and Needleman, A. "Void nucleation by inclusion debonding in a crystal matrix". In: *Modelling and Simulation in Materials Science and Engineering* 1(2), 1993, pp. 111–132. DOI: 10.1088/0965-0393/1/2/001.
- [50] Rice, J. R. and Wang, J.-S. "Embrittlement of interfaces by solute segregation". In: *Materials Science and Engineering: A* 107, 1989, pp. 23–40.
- [51] Camacho, G. and Ortiz, M. "Computational modelling of impact damage in brittle materials". In: *International Journal of Solids and Structures* 33(20-22), 1996, pp. 2899–2938. DOI: 10.1016/0020-7683(95)00255-3.
- [52] Nian, G., Li, Q., Xu, Q., and Qu, S. "A cohesive zone model incorporating a Coulomb friction law for fiber-reinforced composites". In: *Composites Science and Technology* 157, 2018, pp. 195–201. DOI: 10.1016/j.compscitech.2018.01.037.
- [53] Hattiangadi, A. and Siegmund, T. "An analysis of the delamination of an environmental protection coating under cyclic heat loads". In: *European Journal of Mechanics - A/Solids* 24(3), 2005, pp. 361–370. DOI: 10.1016/j.euromechsol.2005.01.003.

- [54] Han, T.-S., Ural, A., Chen, C.-S., Zehnder, A. T., Ingraffea, A. R., and Billington, S. L. “Delamination buckling and propagation analysis of honeycomb panels using a cohesive element approach”. In: *International Journal of Fracture* 115(2), 2002, pp. 101–123. DOI: 10.1023/a:1016333709040.
- [55] Rahulkumar, P., Jagota, A., Bennison, S., and Saigal, S. “Cohesive element modeling of viscoelastic fracture: application to peel testing of polymers”. In: *International Journal of Solids and Structures* 37(13), 2000, pp. 1873–1897. DOI: 10.1016/s0020-7683(98)00339-4.
- [56] Rezaei, S., Wulfinghoff, S., and Reese, S. “Prediction of fracture and damage in micro/nano coating systems using cohesive zone elements”. In: *International Journal of Solids and Structures* 121, 2017, pp. 62–74. DOI: 10.1016/j.ijsolstr.2017.05.016.
- [57] Needleman, A. “Some issues in cohesive surface modeling”. In: *Procedia IUTAM* 10, 2014, pp. 221–246. DOI: 10.1016/j.piutam.2014.01.020.
- [58] Bažant, Z. P. “Concrete fracture models: testing and practice”. In: *Engineering Fracture Mechanics* 69(2), 2002, pp. 165–205. DOI: 10.1016/s0013-7944(01)00084-4.
- [59] Scheider, I. and Brocks, W. “Simulation of cup–cone fracture using the cohesive model”. In: *Engineering Fracture Mechanics* 70(14), 2003, pp. 1943–1961. DOI: 10.1016/s0013-7944(03)00133-4.
- [60] *ABAQUS version 2017 documentation*. Dassault Systèmes, SIMULIA Corp. 2017.
- [61] Song, S. H. “Fracture of asphalt concrete: A cohesive zone modeling approach considering viscoelastic effects”. PhD thesis. University of Illinois, 2006. URL: <http://hdl.handle.net/2142/83307>.
- [62] Musto, M. and Alfano, G. “A novel rate-dependent cohesive-zone model combining damage and visco-elasticity”. In: *Computers & Structures* 118, 2013, pp. 126–133. DOI: 10.1016/j.compstruc.2012.12.020.
- [63] Allix, O. and Corigliano, A. “Geometrical and interfacial non-linearities in the analysis of delamination in composites”. In: *International Journal of Solids and Structures* 36(15), 1999, pp. 2189–2216. DOI: 10.1016/s0020-7683(98)00079-1.
- [64] Camanho, P. P. and Dávila, C. G. “Mixed-Mode Decohesion Finite Elements for the Simulation of Delamination in Composite Materials”. In: *Technical Memorandum*. TM-2002-211737. NASA. NASA, 2002, pp. 1–42.
- [65] Camanho, P. P., Davila, C. G., and Moura, M. F. de. “Numerical Simulation of Mixed-Mode Progressive Delamination in Composite Materials”. In: *Journal of Composite Materials* 37(16), 2003, pp. 1415–1438. DOI: 10.1177/0021998303034505.
- [66] Gurtin, M. E. “Thermodynamics and the cohesive zone in fracture”. In: *Journal of Applied Mathematics and Physics (ZAMP)* 30(6), 1979, pp. 991–1003. DOI: 10.1007/BF01590496.
- [67] Needleman, A. “A Continuum Model for Void Nucleation by Inclusion Debonding”. In: *Journal of Applied Mechanics* 54(3), 1987, p. 525. DOI: 10.1115/1.3173064.
- [68] Park, K. and Paulino, G. H. “Computational implementation of the PPR potential-based cohesive model in ABAQUS: Educational perspective”. In: *Engineering Fracture Mechanics* 93, 2012, pp. 239–262. DOI: 10.1016/j.engfracmech.2012.02.007.
- [69] Nase, M., Rennert, M., Naumenko, K., and Eremeyev, V. A. “Identifying traction–separation behavior of self-adhesive polymeric films from in situ digital images under T-peeling”. In: *Journal of the Mechanics and Physics of Solids* 91, 2016, pp. 40–55. DOI: 10.1016/j.jmps.2016.03.001.

- [70] Katona, M. G. "A simple contact-friction interface element with applications to buried culverts". In: *International Journal for Numerical and Analytical Methods in Geomechanics* 7(3), 1983, pp. 371–384. DOI: 10.1002/nag.1610070308.
- [71] Serpieri, R., Sacco, E., and Alfano, G. "A thermodynamically consistent derivation of a frictional-damage cohesive-zone model with different mode I and mode II fracture energies". In: *European Journal of Mechanics - A/Solids* 49, 2015, pp. 13–25. DOI: 10.1016/j.euromechsol.2014.06.006.
- [72] Borst, R. de. "Some recent issues in computational failure mechanics". In: *International Journal for Numerical Methods in Engineering* 52(12), 2001, pp. 63–95. DOI: 10.1002/nme.272.
- [73] Hill, R. "A general theory of uniqueness and stability in elastic-plastic solids". In: *Journal of the Mechanics and Physics of Solids* 6(3), 1958, pp. 236–249. DOI: 10.1016/0022-5096(58)90029-2.
- [74] Maier, G. and Hueckel, T. "Nonassociated and coupled flow rules of elastoplasticity for rock-like materials". In: *International Journal of Rock Mechanics and Mining Sciences & Geomechanics Abstracts* 16(2), 1979, pp. 77–92. DOI: 10.1016/0148-9062(79)91445-1.
- [75] Borst, R. de, Sluys, L., Muhlhaus, H.-B., and Pamin, J. "Fundamental issues in Finite Element analysis of localization of deformation". In: *Engineering Computations* 10(2), 1993, pp. 99–121. DOI: 10.1108/eb023897.
- [76] Gao, Y. F. and Bower, A. F. "A simple technique for avoiding convergence problems in finite element simulations of crack nucleation and growth on cohesive interfaces". In: *Modelling and Simulation in Materials Science and Engineering* 12(3), 2004, pp. 453–463. DOI: 10.1088/0965-0393/12/3/007.
- [77] Yu, H., Olsen, J. S., Olden, V., Alvaro, A., He, J., and Zhang, Z. "Viscous regularization for cohesive zone modeling under constant displacement: An application to hydrogen embrittlement simulation". In: *Engineering Fracture Mechanics* 166, 2016, pp. 23–42. DOI: 10.1016/j.engfracmech.2016.08.019.
- [78] Gens, A., Carol, I., and Alonso, E. "An interface element formulation for the analysis of soil-reinforcement interaction". In: *Computers and Geotechnics* 7(1-2), 1989, pp. 133–151. DOI: 10.1016/0266-352x(89)90011-6.
- [79] Schellekens, J. C. J. and Borst, R. de. "On the numerical integration of interface elements". In: *International Journal for Numerical Methods in Engineering* 36(1), 1993, pp. 43–66. DOI: 10.1002/nme.1620360104.
- [80] Svenning, E. "A weak penalty formulation remedying traction oscillations in interface elements". In: *Computer Methods in Applied Mechanics and Engineering* 310, 2016, pp. 460–474. DOI: 10.1016/j.cma.2016.07.031.
- [81] Vignollet, J., May, S., and Borst, R. de. "On the numerical integration of isogeometric interface elements". In: *International Journal for Numerical Methods in Engineering* 102(11), 2015, pp. 1733–1749. DOI: 10.1002/nme.4867.
- [82] Ghosh, G., Duddu, R., and Annavarapu, C. "A stabilized finite element method for enforcing stiff anisotropic cohesive laws using interface elements". In: *Computer Methods in Applied Mechanics and Engineering* 348, 2019, pp. 1013–1038. DOI: 10.1016/j.cma.2019.02.007.
- [83] Holzapfel, G. A. *Nonlinear Solid Mechanics*. Wiley John + Sons, 2000. ISBN: 047182319-8.

- [84] Fagerström, M. and Larsson, R. “A thermo-mechanical cohesive zone formulation for ductile fracture”. In: *Journal of the Mechanics and Physics of Solids* 56(10), 2008, pp. 3037–3058. DOI: 10.1016/j.jmps.2008.06.002.
- [85] Clausius, R. *The Mechanical Theory of Heat*. Macmillan, 1879.
- [86] Duhem, P. “On Some Recent Extensions of Statics and Dynamics”. In: *Mixture and Chemical Combination*. Springer Netherlands, 1901 [2002], pp. 291–309. DOI: 10.1007/978-94-017-2292-6_22.
- [87] Gullett, P. M., Horstemeyer, M. F., Baskes, M. I., and Fang, H. “A deformation gradient tensor and strain tensors for atomistic simulations”. In: *Modelling and Simulation in Materials Science and Engineering* 16(1), 2007. DOI: 10.1088/0965-0393/16/1/015001.
- [88] dell'Isola, F., Sciarra, G., and Vidoli, S. “Generalized Hooke's law for isotropic second gradient materials”. In: *Proceedings of the Royal Society A: Mathematical, Physical and Engineering Sciences* 465(2107), 2009, pp. 2177–2196. DOI: 10.1098/rspa.2008.0530.
- [89] Lee, E. H. “Elastic-plastic deformation at finite strains”. In: *Journal of Applied Mechanics* 36(1), 1969, pp. 1–6. DOI: 10.1115/1.3564580.
- [90] Eisenträger, J. “A framework for modeling the mechanical behavior of tempered martensitic steels at high temperatures”. PhD thesis. Otto von Guericke University Magdeburg, 2018. DOI: 10.25673/12268.
- [91] Helmholtz, H. “On the Thermodynamics of Chemical Processes”. In: *Physical Memoirs Selected and Translated from Foreign Sources*. Vol. 1. Physical Society of London, Taylor & Francis, 1882 [1888], pp. 43–97.
- [92] Truesdell, C. “The mechanical foundations of elasticity and fluid dynamics”. In: *Journal of Rational Mechanics and Analysis* 1, 1952, pp. 125–300.
- [93] Coleman, B. D. “Memories of Clifford Truesdell”. In: *The Rational Spirit in Modern Continuum Mechanics*. Kluwer Academic Publishers, 2003, pp. 1–13. DOI: 10.1007/1-4020-2308-1_1.
- [94] Musto, M. “On the formulation of hereditary cohesive-zone models”. PhD thesis. Brunel University School of Engineering and Design, 2014.
- [95] Needleman, A. “Material rate dependence and mesh sensitivity in localization problems”. In: *Computer Methods in Applied Mechanics and Engineering* 67(1), 1988, pp. 69–85. DOI: 10.1016/0045-7825(88)90069-2.
- [96] Coleman, B. D. and Gurtin, M. E. “Thermodynamics with internal state variables”. In: *The Journal of Chemical Physics* 47(2), 1967, pp. 597–613. DOI: 10.1063/1.1711937.
- [97] Truesdell, C. and Noll, W. *The Non-Linear Field Theories of Mechanics*. Springer Berlin Heidelberg, 2004. DOI: 10.1007/978-3-662-10388-3.
- [98] Ciarlet, P. G. *Three-Dimensional Elasticity*. Vol. 20. North Holland, 1994. ISBN: 9780444817761.
- [99] Glüge, R. and Kalisch, J. “Graphical Representations of the Regions of Rank-One-Convexity of some Strain Energies”. In: *Technische Mechanik* 32(2-5), 2012, pp. 227–237.
- [100] Mesures (BIPM), B. I. des Poids et. *The International System of Units (SI)*. Ed. by Mesures (BIPM), B. I. des Poids et. 9th ed. Pavillon de Breteuil F-92312 Sèvres Cedex France: Bureau International des Poids et Mesures (BIPM), 2019. ISBN: 978-92-822-2272-0.
- [101] Chaboche, J. “A review of some plasticity and viscoplasticity constitutive theories”. In: *International Journal of Plasticity* 24(10), 2008, pp. 1642–1693. DOI: 10.1016/j.ijplas.2008.03.009.

- [102] Bertram, A. and Krawietz, A. "On the introduction of thermoplasticity". In: *Acta Mechanica* 223(10), 2012, pp. 2257–2268. DOI: 10.1007/s00707-012-0700-6.
- [103] Fourier, J. B. J. *Théorie Analytique de la Chaleur*. Cambridge University Press, 2009. DOI: 10.1017/cbo9780511693229.
- [104] Abu-Eishah, S., Haddad, Y., Solieman, A, and Bajbouj, A. "A new correlation for the specific heat of metals, metal oxides and metal fluorides as a function of temperature". In: *Latin American applied research* 34(4), 2004, pp. 257–265.
- [105] Narender, K., Rao, A. S. M., Rao, K. G. K., and Krishna, N. G. "Temperature dependence of density and thermal expansion of wrought aluminum alloys 7041, 7075 and 7095 by gamma ray attenuation method". In: *Journal of Modern Physics* 04(03), 2013, pp. 331–336. DOI: 10.4236/jmp.2013.43045.
- [106] Hattiangadi, A. and Siegmund, T. "A numerical study on interface crack growth under heat flux loading". In: *International Journal of Solids and Structures* 42(24-25), 2005, pp. 6335–6355. DOI: 10.1016/j.ijsolstr.2005.05.050.
- [107] Iziumova, A., Bannikov, M., Plekhov, O, and V. Plekhova, E. "Infrared thermography study of the fatigue crack propagation". In: *Fracture and Structural Integrity* 21, 2012, pp. 46–53. DOI: 10.3221/IGF-ESIS.21.06.
- [108] Scheider, I. "Cohesive model for crack propagation analyses of structures with elastic-plastic material behavior Foundations and implementation". In: *GKSS research center, Geesthacht, 2001*.
- [109] Lorenz, A. "Untersuchung zum Rissverhalten einer FeAl Beschichtung unter Verwendung verschiedener Traction-Separation-Laws". Master Thesis. Otto-von-Guericke-Universität Magdeburg, 2019.
- [110] Kachanov, L. M. *Introduction to Continuum Damage Mechanics*. Springer Netherlands, 1986. DOI: 10.1007/978-94-017-1957-5.
- [111] Leckie, F. and Hayhurst, D. "Constitutive equations for creep rupture". In: *Acta Metallurgica* 25(9), 1977, pp. 1059–1070. DOI: 10.1016/0001-6160(77)90135-3.
- [112] Cocks, A. and Ashby, M. "On creep fracture by void growth". In: *Progress in Materials Science* 27(3-4), 1982, pp. 189–244. DOI: 10.1016/0079-6425(82)90001-9.
- [113] Airy, G. B. "IV. On the Strains in the Interior of Beams". In: *Philosophical Transactions of the Royal Society of London* 153, 1863, pp. 49–79. DOI: 10.1098/rstl.1863.0004.
- [114] Teodorescu, P. P. "One hundred years of investigations in the plane problem of the theory of elasticity". In: *Applied Mechanics Reviews* 17(3), 1964, pp. 175–186.
- [115] Maxwell, J. C. "I.—On Reciprocal Figures, Frames, and Diagrams of Forces". In: *Transactions of the Royal Society of Edinburgh* 26(1), 1870, pp. 1–40. DOI: 10.1017/s0080456-800-026351.
- [116] Levy, M. "Sur l'équilibre élastique d'une plaque rectangulaire". In: *Comptes Rendus Acad. Sci. Paris* 129, 1899, pp. 535–539.
- [117] Flamant, A. "Sur la répartition des pressions dans un solide rectangulaire chargé transversalement". In: *CR Acad. Sci. Paris* 114, 1892, pp. 1465–1468.
- [118] Golovin, K. S. "One problem in statics of an elastic body (in Russian)". In: *Izvestiya St. Peterburg Prakt. Tekhnol. Inst* 3, 1881, pp. 373–410.
- [119] Michell, J. H. "On the direct determination of stress in an elastic solid, with application to the theory of plates". In:
- [120] Carothers, S. D. "XXVI.—Plane strain in a wedge, with applications to masonry dams". In: *Proceedings of the Royal Society of Edinburgh* 33, 1914, pp. 292–306. DOI: 10.1017/s0370164600031448.

- [121] Love, A. E. H. *A Treatise on the Mathematical Theory of Elasticity*. Vol. 2. Cambridge University Press Warehouse, 1944.
- [122] Nordmann, J., Aßmus, M., Glüge, R., and Altenbach, H. “A Derivation of Hooke’s Law for Plane State Conditions”. In: *Archives of Mechanics*, 2020. under review.
- [123] Wriggers, P. *Nonlinear Finite Element Methods*. Springer Berlin Heidelberg, 2008. DOI: 10.1007/978-3-540-71001-1.
- [124] Dhondt, G. *The Finite Element Method for Three-Dimensional Thermomechanical Applications*. Wiley-Blackwell, 2004.
- [125] Szabó, B. and Babuška, I. *Introduction to Finite Element Analysis*. John Wiley & Sons, Ltd, 2011. DOI: 10.1002/9781119993834.
- [126] Verhegghe, B. and Powell, G. H. “Control of zero-energy modes in 9-node plane element”. In: *International Journal for Numerical Methods in Engineering* 23(5), 1986, pp. 863–869. DOI: 10.1002/nme.1620230508.
- [127] Zienkiewicz, O. C., Taylor, R. L., and Too, J. M. “Reduced integration technique in general analysis of plates and shells”. In: *International Journal for Numerical Methods in Engineering* 3(2), 1971, pp. 275–290. DOI: 10.1002/nme.1620030211.
- [128] Long, C. S. and Groenwold, A. A. “Reduced modified quadratures for quadratic membrane finite elements”. In: *International Journal for Numerical Methods in Engineering* 61(6), 2004, pp. 837–855. DOI: 10.1002/nme.1090.
- [129] Gauss, C. F. *Methodus nova integralium valores per approximationem inveniendi : auctore Carolo Friderico Gauss*. Ed. by Dieterich, H. Gottingae, 1815.
- [130] Reinoso, J. and Paggi, M. “A consistent interface element formulation for geometrical and material nonlinearities”. In: *Computational Mechanics* 54(6), 2014, pp. 1569–1581. DOI: 10.1007/s00466-014-1077-2.
- [131] Hilber, H. M., Hughes, T. J. R., and Taylor, R. L. “Improved numerical dissipation for time integration algorithms in structural dynamics”. In: *Earthquake Engineering & Structural Dynamics* 5(3), 1977, pp. 283–292. DOI: 10.1002/eqe.4290050306.
- [132] Cauchy, A.-L. “Analyse Mathématique. – Méthode générale pour la résolution des systèmes d’équations simultanées”. In: *Oeuvres complètes*. Cambridge University Press, 1897, pp. 399–402. DOI: 10.1017/cbo9780511702396.063.
- [133] Borst, R. de, Crisfield, M. A., Remmers, J. J. C., and Verhoosel, C. V. *Non-Linear Finite Element Analysis of Solids and Structures*. John Wiley & Sons, Ltd, 2012. DOI: 10.1002/9781118375938.
- [134] Rayleigh, J. W. S. *The Theory of Sound, Volume Two*. Dover Publications Incorporated, 1945. ISBN: 0486602931.
- [135] Caughey, T. K. and O’Kelly, M. E. J. “Classical Normal Modes in Damped Linear Dynamic Systems”. In: *Journal of Applied Mechanics* 32(3), 1965. DOI: 10.1115/1.3627262.
- [136] Hamitouche, L., Tarfaoui, M., and Vautrin, A. “An interface debonding law subject to viscous regularization for avoiding instability: Application to the delamination problems”. In: *Engineering Fracture Mechanics* 75(10), 2008, pp. 3084–3100. DOI: 10.1016/j.engfracmech.2007.12.014.
- [137] Brannon, R. *Rotation Reflection and Frame Changes Orthogonal tensors in computational engineering mechanics*. IOP Publishing, 2018. DOI: 10.1088/978-0-7503-1454-1.

- [138] Tuynman, G. M. “The derivation of the exponential map of matrices”. In: *The American Mathematical Monthly* 102(9), 1995, pp. 818–820. DOI: 10.1080/00029890.1995.12004668.
- [139] Simo, J. and Hughes, T. *Computational Inelasticity*. Springer-Verlag, 1998. DOI: 10.1007/b98904.
- [140] Song, S. H., Paulino, G. H., and Buttlar, W. G. “A bilinear cohesive zone model tailored for fracture of asphalt concrete considering viscoelastic bulk material”. In: *Engineering Fracture Mechanics* 73(18), 2006, pp. 2829–2848. DOI: 10.1016/j.engfracmech.2006.04.030.
- [141] Miehe, C., Hofacker, M., Schänzel, L.-M., and Aldakheel, F. “Phase field modeling of fracture in multi-physics problems. Part IIa. Coupled brittle-to-ductile failure criteria and crack propagation in thermo-elastic-plastic solids”. In: *Computer Methods in Applied Mechanics and Engineering* 294, 2015, pp. 486–522. DOI: 10.1016/j.cma.2014.11.017.
- [142] Miehe, C., Welschinger, F., and Hofacker, M. “Thermodynamically consistent phase-field models of fracture: Variational principles and multi-field FE implementations”. In: *International Journal for Numerical Methods in Engineering* 83(10), 2010, pp. 1273–1311. DOI: 10.1002/nme.2861.
- [143] Bathe, K.-J. *Finite Element Procedures*. Ed. by Bathe, K.-J. 2nd ed. 2014. ISBN: 978-0-9790049-5-7.
- [144] Alfano, G. and Crisfield, M. A. “Finite element interface models for the delamination analysis of laminated composites: mechanical and computational issues”. In: *International Journal for Numerical Methods in Engineering* 50(7), 2001, pp. 1701–1736. DOI: 10.1002/nme.93.
- [145] Turon, A., Dávila, C., Camanho, P., and Costa, J. “An engineering solution for mesh size effects in the simulation of delamination using cohesive zone models”. In: *Engineering Fracture Mechanics* 74(10), 2007, pp. 1665–1682. DOI: 10.1016/j.engfracmech.2006.08.025.
- [146] Ersoy, N., Ahmadvashaghbash, S., Engül, M., and Öz, F. E. “A Comparative Numerical Study Aiming to Reduce Computation Cost for Mode-I Delamination Simulations”. In: *European Conference on Composite Materials*. 2018.
- [147] Nordmann, J., Naumenko, K., and Altenbach, H. “Cohesive Zone Models—Theory, Numerics and Usage in High-Temperature Applications to Describe Cracking and Delamination”. In: *Advances in Mechanics of High-Temperature Materials*. Ed. by Naumenko, K. and Krüger, M. Vol. 117. Advanced Structured Materials. Springer International Publishing, 2019, pp. 131–168. DOI: 10.1007/978-3-030-23869-8_7.
- [148] Maissonette, D., Bardel, D., Robin, V., Nelias, D., and Suery, M. “Mechanical behaviour at high temperature as induced during welding of a 6xxx series aluminium alloy”. In: *International Journal of Pressure Vessels and Piping* 149, 2017, pp. 55–65. DOI: 10.1016/j.ijpvp.2016.12.004.
- [149] Köster, W. and Gödecke, T. *Physikalische Messungen an Eisen-Aluminium-Legierungen mit 10 bis 50 At.-% Al*. Forschungsbericht. Max-Planck-Institut für Metallforschung Stuttgart, 2009.
- [150] Hult, J. A. H. *Creep in Engineering Structures*. Waltham, Massachusetts: Blaisdell Pub. Co., 1966.

- [151] Uzan, N. E., Shneck, R., Yeheskel, O., and Frage, N. "High-temperature mechanical properties of AlSi10Mg specimens fabricated by additive manufacturing using selective laser melting technologies (AM-SLM)". In: *Additive Manufacturing* 24, 2018, pp. 257–263.
- [152] González-Doncel, G. and Sherby, O. "High temperature creep behavior of metal matrix Aluminum-SiC composites". In: *Acta Metallurgica et Materialia* 41(10), 1993, pp. 2797–2805. DOI: 10.1016/0956-7151(93)90094-9.
- [153] Scharf, S., Riedel, E., Stein, N., and Baehr, R. "Fe–Al/AlSi compound casting based on a targeted oxide removal". In: *Journal of Materials Processing Technology* 248, 2017, pp. 31–38. DOI: 10.1016/j.jmatprotec.2017.05.004.
- [154] eFunda, I. *Heat capacity and conductivity of aluminium*. 2019. URL: <http://efunda.com> (visited on 02/13/2020).
- [155] Pei, W., Zhengying, W., Zhen, C., Junfeng, L., Shuzhe, Z., and Jun, D. "Numerical simulation and parametric analysis of selective laser melting process of AlSi10Mg powder". In: *Applied Physics A* 123(8), 2017. DOI: 10.1007/s00339-017-1143-7.
- [156] Carstensen, C. "Ten remarks on nonconvex minimisation for phase transition simulations". In: *Computer Methods in Applied Mechanics and Engineering* 194(2-5), 2005, pp. 169–193. DOI: 10.1016/j.cma.2004.05.012.
- [157] Zimmer, J. "Jog my shape memory: dynamics as a challenge in mathematical materials science". In: *Philosophical Transactions of the Royal Society A: Mathematical, Physical and Engineering Sciences* 364(1849), 2006, pp. 3285–3300. DOI: 10.1098/rsta.2006.1898.
- [158] Basoglu, M. F., Zerín, Z., Kefal, A., and Oterkus, E. "A computational model of peridynamic theory for deflecting behavior of crack propagation with micro-cracks". In: *Computational Materials Science* 162, 2019, pp. 33–46. DOI: 10.1016/j.commatsci.2019.02.032.
- [159] Mandal, T. K., Nguyen, V. P., and Wu, J.-Y. "Length scale and mesh bias sensitivity of phase-field models for brittle and cohesive fracture". In: *Engineering Fracture Mechanics* 217, 2019, p. 106532. DOI: 10.1016/j.engfracmech.2019.106532.
- [160] Bargmann, S. "Remarks on the Green–Naghdi theory of heat conduction". In: *Journal of Non-Equilibrium Thermodynamics* 38(2), 2013. DOI: 10.1515/jnetdy-2012-0015.

Appendix A

Chapter 4: Continuum Mechanics

In this section Eq. (4.59) of Chap. 3 is derived in detail. The starting point is Equation (4.50).

$$\mathbf{T} : \mathbf{L} - \rho \dot{\psi}_b - \rho \eta_b \dot{\theta} - \frac{1}{\theta} \mathbf{q}_b \cdot (\nabla \theta) \geq 0$$

The velocity gradient is replaced by Eq. (4.7), the multiplicative split is inserted (Eq. (4.8)) and Eq. (4.56). It follows

$$\begin{aligned} & \mathbf{T} : \left(\dot{\mathbf{F}}_{el} \cdot \mathbf{F}_{el}^{-1} + \mathbf{F}_{el} \cdot \dot{\mathbf{F}}_{in} \cdot \mathbf{F}_{in}^{-1} \cdot \mathbf{F}_{el}^{-1} \right) - \rho \frac{\partial \psi_b}{\partial \mathbf{F}_{el}} : \dot{\mathbf{F}}_{el} - \rho \frac{\partial \psi_b}{\partial \theta} \dot{\theta} \\ & - \rho \eta_b \dot{\theta} - \frac{1}{\theta} \mathbf{q}_b \cdot (\nabla \theta) \geq 0 \end{aligned}$$

which is rearranged as follows

$$\begin{aligned} & \left[\mathbf{T} \cdot \mathbf{F}_{el}^{-\top} - \rho \frac{\partial \psi_b}{\partial \mathbf{F}_{el}} \right] : \dot{\mathbf{F}}_{el} - \rho \left[\eta_b + \frac{\partial \psi_b}{\partial \theta} \right] \dot{\theta} \\ & + \mathbf{F}_{el}^{\top} \cdot \mathbf{T} \cdot \mathbf{F}_{el}^{-\top} : \mathbf{L}_{in} - \frac{1}{\theta} \mathbf{q}_b \cdot (\nabla \theta) \geq 0, \quad \text{with } \mathbf{L}_{in} = \dot{\mathbf{F}}_{in} \cdot \mathbf{F}_{in}^{-1} \end{aligned}$$

The required manipulations are presented below in index notation. At first, the transformation of the elastic portion of the stress power is proven.

$$\mathbf{T} : \dot{\mathbf{F}}_{el} \cdot \mathbf{F}_{el}^{-1} = \mathbf{T} \cdot \mathbf{F}_{el}^{-\top} : \dot{\mathbf{F}}_{el}$$

Proof:

$$\begin{aligned} & \mathbf{T} : \dot{\mathbf{F}}_{el} \cdot \mathbf{F}_{el}^{-1} \\ & = T_{ij} \dot{F}_{el,kl} F_{el,mn}^{-1} \mathbf{e}_i \otimes \mathbf{e}_j : \mathbf{e}_k \otimes \mathbf{e}_l \cdot \mathbf{e}_m \otimes \mathbf{e}_n \\ & = T_{ij} \dot{F}_{el,kl} F_{el,mn}^{-1} \delta_{lm} \delta_{jn} \delta_{ik} \\ & = T_{ij} \dot{F}_{el,im} F_{el,mj}^{-1} \\ & \quad \mathbf{T} \cdot \mathbf{F}_{el}^{-\top} : \dot{\mathbf{F}}_{el} \\ & = T_{ij} F_{el,kl}^{-1} \dot{F}_{el,mn} \mathbf{e}_i \otimes \mathbf{e}_j \cdot \mathbf{e}_l \otimes \mathbf{e}_k : \mathbf{e}_m \otimes \mathbf{e}_n \\ & = T_{ij} F_{el,kl}^{-1} \dot{F}_{el,mn} \delta_{jl} \delta_{im} \delta_{kn} \\ & = T_{ij} F_{el,nj}^{-1} \dot{F}_{el,in} \end{aligned}$$

Then follows the transformation of the inelastic portion of the stress power.

$$\mathbf{T} : \mathbf{F}_{el} \cdot \dot{\mathbf{F}}_{in} \cdot \mathbf{F}_{in}^{-1} \cdot \mathbf{F}_{el}^{-1} = \mathbf{F}_{el}^{\top} \cdot \mathbf{T} \cdot \mathbf{F}_{el}^{-\top} : \dot{\mathbf{F}}_{in} \cdot \mathbf{F}_{in}^{-1}$$

Proof:

$$\begin{aligned}
 & \mathbf{T} : \mathbf{F}_{\text{el}} \cdot \dot{\mathbf{F}}_{\text{in}} \cdot \mathbf{F}_{\text{in}}^{-1} \cdot \mathbf{F}_{\text{el}}^{-1} \\
 &= T_{ij} F_{\text{el},kl} \dot{F}_{\text{in},mn} F_{\text{in},op}^{-1} F_{\text{el},qr}^{-1} \mathbf{e}_i \otimes \mathbf{e}_j : \mathbf{e}_k \otimes \mathbf{e}_l \cdot \mathbf{e}_m \otimes \mathbf{e}_n \cdot \mathbf{e}_o \otimes \mathbf{e}_p \cdot \mathbf{e}_q \otimes \mathbf{e}_r \\
 &= T_{ij} F_{\text{el},kl} \dot{F}_{\text{in},mn} F_{\text{in},op}^{-1} F_{\text{el},qr}^{-1} \delta_{ik} \delta_{jr} \delta_{lm} \delta_{no} \delta_{pq} \\
 &= T_{ij} F_{\text{el},im} \dot{F}_{\text{in},mo} F_{\text{in},oq}^{-1} F_{\text{el},qj}^{-1} \\
 & \quad \mathbf{F}_{\text{el}}^\top \cdot \mathbf{T} \cdot \mathbf{F}_{\text{el}}^{-\top} : \dot{\mathbf{F}}_{\text{in}} \cdot \mathbf{F}_{\text{in}}^{-1} \\
 &= F_{\text{el},ij} T_{kl} F_{\text{el},mn}^{-1} \dot{F}_{\text{in},op} F_{\text{in},qr}^{-1} \mathbf{e}_j \otimes \mathbf{e}_i \cdot \mathbf{e}_k \otimes \mathbf{e}_l \cdot \mathbf{e}_n \otimes \mathbf{e}_m : \mathbf{e}_o \otimes \mathbf{e}_p \cdot \mathbf{e}_q \otimes \mathbf{e}_r \\
 &= F_{\text{el},ij} T_{kl} F_{\text{el},mn}^{-1} \dot{F}_{\text{in},op} F_{\text{in},qr}^{-1} \delta_{ik} \delta_{ln} \delta_{pq} \delta_{jo} \delta_{mr} \\
 &= F_{\text{el},ij} T_{in} F_{\text{el},mn}^{-1} \dot{F}_{\text{in},jp} F_{\text{in},pm}^{-1}
 \end{aligned}$$

Through the introduction of the dissipative stress

$$\mathbf{T}_d = \mathbf{F}_{\text{el}}^\top \cdot \mathbf{T} \cdot \mathbf{F}_{\text{el}}^{-\top}$$

the final form is derived (Eq. (4.59)).

$$\left[\mathbf{T} \cdot \mathbf{F}_{\text{el}}^{-\top} - \rho \frac{\partial \psi_b}{\partial \mathbf{F}_{\text{el}}} \right] : \dot{\mathbf{F}}_{\text{el}} - \rho \left[\eta_b + \frac{\partial \psi_b}{\partial \theta} \right] \dot{\theta} + \mathbf{T}_d : \mathbf{L}_{\text{in}} - \frac{1}{\theta} \mathbf{q}_b \cdot (\nabla \theta) \geq 0$$

Chapter 5: Constitutive Laws

Derivation of the CAUCHY stress tensor

$$\mathbf{T} = \frac{1}{J} \frac{\partial \rho_0 \psi_b}{\partial \mathbf{B}_{\text{el}}} : \frac{\partial \mathbf{B}_{\text{el}}}{\partial \mathbf{F}_{\text{el}}} \cdot \mathbf{F}_{\text{el}}^\top$$

The first derivative yields

$$\begin{aligned}
 \frac{\partial \rho_0 \psi_b}{\partial \mathbf{B}_{\text{el}}} &= \frac{\partial \rho_0 \psi_b}{\partial I_{\mathbf{B}_{\text{el}}}} \frac{\partial I_{\mathbf{B}_{\text{el}}}}{\partial \mathbf{B}_{\text{el}}} + \frac{\partial \rho_0 \psi_b}{\partial III_{\mathbf{B}_{\text{el}}}} \frac{\partial III_{\mathbf{B}_{\text{el}}}}{\partial \mathbf{B}_{\text{el}}} \\
 &= \frac{\mu}{2} \mathbf{1} + \left[\frac{\lambda}{4} \left[1 - \frac{1}{III_{\mathbf{B}_{\text{el}}}} \right] - \frac{\mu}{2 III_{\mathbf{B}_{\text{el}}}} \right] III_{\mathbf{B}_{\text{el}}} \mathbf{B}_{\text{el}}^{-\top} \\
 &= \frac{\lambda}{4} (III_{\mathbf{B}_{\text{el}}} - 1) \mathbf{B}_{\text{el}}^{-\top} + \frac{\mu}{2} (\mathbf{1} - \mathbf{B}_{\text{el}}^{-\top}) \\
 &= \frac{\lambda}{4} (J^2 - 1) \mathbf{B}_{\text{el}}^{-\top} + \frac{\mu}{2} (\mathbf{1} - \mathbf{B}_{\text{el}}^{-\top})
 \end{aligned}$$

With the definition of the invariants of the left CAUCHY-GREEN tensor

$$I_{\mathbf{B}_{\text{el}}} = \text{tr}(\mathbf{B}_{\text{el}}) \qquad III_{\mathbf{B}_{\text{el}}} = \det(\mathbf{B}_{\text{el}})$$

the derivatives of them

$$\frac{\partial I_{\mathbf{B}_{\text{el}}}}{\partial \mathbf{B}_{\text{el}}} = \mathbf{1} \qquad \frac{\partial III_{\mathbf{B}_{\text{el}}}}{\partial \mathbf{B}_{\text{el}}} = III_{\mathbf{B}_{\text{el}}} \mathbf{B}_{\text{el}}^{-\top}$$

the relation between the determinant of the deformation gradient and the third invariant

$$\sqrt{III_{\mathbf{B}_{\text{el}}}} = \det(\mathbf{F}_{\text{el}}) = \det(\mathbf{F}) = J \qquad \iff \qquad III_{\mathbf{B}_{\text{el}}} = J^2$$

and the LAMÉ constants λ and μ . The second derivative follows to

$$\begin{aligned}\frac{\partial \mathbf{B}_{\text{el}}}{\partial \mathbf{F}_{\text{el}}} &= \frac{\partial \mathbf{F}_{\text{el}}}{\partial \mathbf{F}_{\text{el}}} \cdot \mathbf{F}_{\text{el}}^\top + \mathbf{F}_{\text{el}} \cdot \frac{\partial \mathbf{F}_{\text{el}}^\top}{\partial \mathbf{F}_{\text{el}}} \\ &= \mathbf{I} \cdot \mathbf{F}_{\text{el}}^\top + \mathbf{F}_{\text{el}} \cdot \mathbf{I} \\ &= \mathbf{F}_{\text{el}} \cdot \mathbf{I} + \mathbf{F}_{\text{el}} \cdot \mathbf{I} \\ &= 2\mathbf{F}_{\text{el}} \cdot \mathbf{I}\end{aligned}$$

Now, we concatenate everything in index notation to show that Eq. (5.4) is the result.

$$\begin{aligned}\mathbf{T} &= \frac{1}{J} \frac{\partial \rho_0 \psi_b}{\partial \mathbf{B}_{\text{el}}} : \frac{\partial \mathbf{B}_{\text{el}}}{\partial \mathbf{F}_{\text{el}}} \cdot \mathbf{F}_{\text{el}}^\top = \frac{1}{J} \mathbf{A} : \frac{\partial \mathbf{B}_{\text{el}}}{\partial \mathbf{F}_{\text{el}}} \cdot \mathbf{F}_{\text{el}}^\top \\ &= \frac{2}{J} A_{ij} F_{\text{el},kl} F_{\text{el},op} \left(\mathbf{e}_i \otimes \mathbf{e}_j : \mathbf{e}_k \otimes \mathbf{e}_l \cdot \mathbf{e}_n \otimes \mathbf{e}_m \otimes \mathbf{e}_m \otimes \mathbf{e}_n \cdot \mathbf{e}_p \otimes \mathbf{e}_o \right) \\ &= \frac{2}{J} A_{ij} F_{\text{el},kl} F_{\text{el},op} \delta_{nl} \delta_{np} \delta_{ik} \delta_{jm} \mathbf{e}_m \otimes \mathbf{e}_o \\ &= \frac{2}{J} A_{ij} F_{\text{el},in} F_{\text{el},on} \mathbf{e}_j \otimes \mathbf{e}_o \\ &= \frac{2}{J} \mathbf{A}^\top \cdot \mathbf{F}_{\text{el}} \cdot \mathbf{F}_{\text{el}}^\top \\ &= \frac{2}{J} \mathbf{A}^\top \cdot \mathbf{B}_{\text{el}} \\ &= \frac{2}{J} \mathbf{A} \cdot \mathbf{B}_{\text{el}} \\ &= \frac{2}{J} \frac{\partial \rho_0 \psi_b}{\partial \mathbf{B}_{\text{el}}} \cdot \mathbf{B}_{\text{el}}\end{aligned}$$

This holds true because the left CAUCHY-GREEN tensor is symmetric and, hence, the tensor $\mathbf{A} = \frac{\partial \rho_0 \psi_b}{\partial \mathbf{B}_{\text{el}}}$ is symmetric, too.

Up next, the product of left CAUCHY-GREEN tensor and deformation gradient is derived.

$$\mathbf{B}_{\text{el}} \cdot \mathbf{F}^{-\top} = \mathbf{F}_{\text{el}} \cdot \mathbf{F}_{\text{el}}^\top \cdot \mathbf{F}_{\text{el}}^{-\top} \cdot \mathbf{F}_{\text{in}}^{-\top} = \mathbf{F}_{\text{el}} \cdot \mathbf{F}_{\text{in}}^{-\top} = \mathbf{F} \cdot \mathbf{C}_{\text{in}}^{-1}$$

Chapter 6: FEM

Manipulation of the internal work of Eq. (6.6)

$$\delta \mathbf{H} : \overset{\text{IPK}}{\mathbf{T}} \cdot \mathbf{F}^\top = \delta \mathbf{H} \cdot \mathbf{F} : \overset{\text{IPK}}{\mathbf{T}}$$

Proof:

$$\begin{aligned}\delta \mathbf{H} : \overset{\text{IPK}}{\mathbf{T}} \cdot \mathbf{F}^\top &= \delta H_{ij} \overset{\text{IPK}}{T_{kl}} F_{mn} \mathbf{e}_i \otimes \mathbf{e}_j : \mathbf{e}_k \otimes \mathbf{e}_l \cdot \mathbf{e}_n \otimes \mathbf{e}_m \\ &= \delta H_{ij} \overset{\text{IPK}}{T_{kl}} F_{mn} \delta_{ln} \delta_{jm} \delta_{ik} \\ &= \delta H_{ij} \overset{\text{IPK}}{T_{in}} F_{jn}\end{aligned}$$

$$\begin{aligned}
 & \delta \mathbf{H} \cdot \mathbf{F} : \mathbf{T} \\
 &= \delta H_{ij} F_{kl} T_{mn} \mathbf{e}_i \otimes \mathbf{e}_j \cdot \mathbf{e}_k \otimes \mathbf{e}_l : \mathbf{e}_m \otimes \mathbf{e}_n \\
 &= \delta H_{ij} F_{kl} T_{mn} \delta_{ln} \delta_{im} \delta_{jk} \\
 &= \delta H_{ij} F_{jn} T_{in}
 \end{aligned}$$

Arranging of displacement, position, damage and temperature vector for a 2D cohesive element

$$\begin{aligned}
 \mathbf{u}^e &= [u_{1x} \quad u_{1y} \quad u_{2x} \quad \cdots \quad u_{ny}]^\top, \quad n = NN \\
 \mathbf{x}^e &= [x_{1x} \quad x_{1y} \quad x_{2x} \quad \cdots \quad x_{ny}]^\top, \quad n = NN \\
 \mathbf{d}^e &= [d_1 \quad d_2 \quad \cdots \quad d_n]^\top, \quad n = NN \\
 \boldsymbol{\theta}^e &= [\theta_1 \quad \theta_2 \quad \cdots \quad \theta_n]^\top, \quad n = NN
 \end{aligned}$$

Arranging of the displacement, damage and temperature mean value matrix for a linear and a quadratic element

$$\begin{aligned}
 \mathbf{M}_u^{\text{lin}} &= \begin{bmatrix} 1 & 0 & 0 & 0 & 0 & 0 & 1 & 0 \\ 0 & 1 & 0 & 0 & 0 & 0 & 0 & 1 \\ 0 & 0 & 1 & 0 & 1 & 0 & 0 & 0 \\ 0 & 0 & 0 & 1 & 0 & 1 & 0 & 0 \end{bmatrix} \\
 \mathbf{M}_d^{\text{lin}} &= \begin{bmatrix} 1 & 0 & 0 & 1 \\ 0 & 1 & 1 & 0 \end{bmatrix} \\
 \mathbf{M}_\theta^{\text{lin}} &= \begin{bmatrix} 1 & 0 & 0 & 1 \\ 0 & 1 & 1 & 0 \end{bmatrix} \\
 \mathbf{M}_u^{\text{quad}} &= \begin{bmatrix} 1 & 0 & 0 & 0 & 0 & 0 & 1 & 0 & 0 & 0 & 0 & 0 \\ 0 & 1 & 0 & 0 & 0 & 0 & 0 & 1 & 0 & 0 & 0 & 0 \\ 0 & 0 & 1 & 0 & 1 & 0 & 0 & 0 & 0 & 0 & 0 & 0 \\ 0 & 0 & 0 & 1 & 0 & 1 & 0 & 0 & 0 & 0 & 0 & 0 \\ 0 & 0 & 0 & 0 & 0 & 0 & 0 & 0 & 1 & 0 & 1 & 0 \\ 0 & 0 & 0 & 0 & 0 & 0 & 0 & 0 & 0 & 1 & 0 & 1 \end{bmatrix} \\
 \mathbf{M}_d^{\text{quad}} &= \begin{bmatrix} 1 & 0 & 0 & 1 & 0 & 0 \\ 0 & 1 & 1 & 0 & 0 & 0 \\ 0 & 0 & 0 & 0 & 1 & 1 \end{bmatrix} \\
 \mathbf{M}_\theta^{\text{quad}} &= \begin{bmatrix} 1 & 0 & 0 & 1 & 0 & 0 \\ 0 & 1 & 1 & 0 & 0 & 0 \\ 0 & 0 & 0 & 0 & 1 & 1 \end{bmatrix}
 \end{aligned}$$

Arranging of the displacement and temperature separation relation matrix. The ordering depends on the node numbering scheme of the element.

$$\begin{aligned}
 \mathbf{L}_u^{\text{lin}} &= \begin{bmatrix} -1 & 0 & 0 & 0 & 0 & 0 & 1 & 0 \\ 0 & -1 & 0 & 0 & 0 & 0 & 0 & 1 \\ 0 & 0 & -1 & 0 & 1 & 0 & 0 & 0 \\ 0 & 0 & 0 & -1 & 0 & 1 & 0 & 0 \end{bmatrix} \\
 \mathbf{L}_\theta^{\text{lin}} &= \begin{bmatrix} -1 & 0 & 0 & 1 \\ 0 & -1 & 1 & 0 \end{bmatrix}
 \end{aligned}$$

$$\mathbf{L}_u^{\text{quad}} = \begin{bmatrix} -1 & 0 & 0 & 0 & 0 & 0 & 1 & 0 & 0 & 0 & 0 & 0 \\ 0 & -1 & 0 & 0 & 0 & 0 & 0 & 1 & 0 & 0 & 0 & 0 \\ 0 & 0 & -1 & 0 & 1 & 0 & 0 & 0 & 0 & 0 & 0 & 0 \\ 0 & 0 & 0 & -1 & 0 & 1 & 0 & 0 & 0 & 0 & 0 & 0 \\ 0 & 0 & 0 & 0 & 0 & 0 & 0 & 0 & -1 & 0 & 1 & 0 \\ 0 & 0 & 0 & 0 & 0 & 0 & 0 & 0 & 0 & -1 & 0 & 1 \end{bmatrix}$$

$$\mathbf{L}_\theta^{\text{quad}} = \begin{bmatrix} -1 & 0 & 0 & 1 & 0 & 0 \\ 0 & -1 & 1 & 0 & 0 & 0 \\ 0 & 0 & 0 & 0 & -1 & 1 \end{bmatrix}$$

Arranging of the elasticity matrix

$$\mathbf{C}_i = \begin{bmatrix} E_n & 0 \\ 0 & E_t \end{bmatrix}$$

Deriving the material tangent matrix \mathfrak{A} for the bulk material

$$\begin{aligned} \mathfrak{A} &= \frac{\partial \mathbf{T}_{\text{IPK}}}{\partial \mathbf{F}} = \frac{\partial}{\partial \mathbf{F}} \left[\frac{\lambda}{2} (J^2 - 1) \mathbf{F}^{-\top} + \mu (\mathbf{F} \cdot \mathbf{C}_{\text{in}}^{-1} - \mathbf{F}^{-\top}) \right] \\ &= \lambda J \frac{\partial J}{\partial F_{mn}} F_{ji}^{-1} + \left[\frac{\lambda}{2} (J^2 - 1) - \mu \right] \frac{\partial F_{ji}^{-1}}{\partial F_{mn}} + \mu \left[\frac{\partial F_{ik}}{\partial F_{mn}} C_{\text{in},kj}^{-1} + F_{ik} \frac{\partial C_{\text{in},kj}^{-1}}{\partial F_{mn}} \right] \\ \frac{\partial J}{\partial F_{mn}} &= J F_{nm}^{-1} \quad \frac{\partial F_{ik}}{\partial F_{mn}} = \delta_{im} \delta_{kn} \end{aligned}$$

The derivative of an inverse transposed matrix is derived through the relation $\mathbf{A}^\top \cdot \mathbf{A} = \mathbf{1}$.

$$\begin{aligned} \frac{\partial \delta_{il}}{\partial F_{mn}} &= \frac{\partial}{\partial F_{mn}} \left[F_{ji} F_{lj}^{-1} \right]_{ilmn} \\ 0_{ilmn} &= \left[\delta_{jm} \delta_{in} F_{lj}^{-1} \right]_{ilmn} + \left[F_{ji} \frac{\partial F_{lj}^{-1}}{\partial F_{mn}} \right]_{ilmn} \\ \left[F_{ji} \frac{\partial F_{lj}^{-1}}{\partial F_{mn}} \right]_{ilmn} &= - \left[\delta_{jm} \delta_{in} F_{lj}^{-1} \right]_{ilmn} \\ \left[\delta_{jo} \frac{\partial F_{lj}^{-1}}{\partial F_{mn}} \right]_{olmn} &= - \left[F_{io}^{-1} \delta_{in} F_{lm}^{-1} \right]_{olmn} \\ \left[\frac{\partial F_{lo}^{-1}}{\partial F_{mn}} \right]_{olmn} &= - \left[F_{no}^{-1} F_{lm}^{-1} \right]_{olmn} \\ \left[\frac{\partial F_{ji}^{-1}}{\partial F_{mn}} \right]_{ijmn} &= - \left[F_{ni}^{-1} F_{jm}^{-1} \right]_{ijmn} \end{aligned}$$

This leads to the final formulation of the material tangent matrix.

$$A_{ijmn} = \lambda J^2 F_{nm}^{-1} F_{ji}^{-1} - \left[\frac{\lambda}{2} (J^2 - 1) - \mu \right] F_{ni}^{-1} F_{jm}^{-1} + \mu \left[\delta_{im} \delta_{kn} C_{\text{in},kj}^{-1} + F_{ik} \frac{\partial C_{\text{in},kj}^{-1}}{\partial F_{mn}} \right]$$

Inelastic velocity matrix for a PE

$$\mathbf{L}_{\text{in}} = \begin{bmatrix} \mathbf{L}_{\text{in}}^{\text{PE}} & 0 \\ \mathbf{0}^\top & L_{\text{in},33} \end{bmatrix} \quad \text{with} \quad \mathbf{L}_{\text{in}}^{\text{PE}} = \begin{bmatrix} L_{\text{in},11} & L_{\text{in},12} \\ L_{\text{in},12} & L_{\text{in},22} \end{bmatrix}$$

Eigenvalues of the inelastic velocity matrix

$$\alpha_1 = \frac{\text{tr}(\mathbf{L}_{\text{in}}^{\text{PE}})}{2} - \sqrt{\frac{\text{tr}(\mathbf{L}_{\text{in}}^{\text{PE}})^2}{4} - \det(\mathbf{L}_{\text{in}}^{\text{PE}})}$$

$$\alpha_2 = \frac{\text{tr}(\mathbf{L}_{\text{in}}^{\text{PE}})}{2} + \sqrt{\frac{\text{tr}(\mathbf{L}_{\text{in}}^{\text{PE}})^2}{4} - \det(\mathbf{L}_{\text{in}}^{\text{PE}})}$$

$$\alpha_2 = L_{\text{in},33}$$

Eigenvectors of the inelastic velocity matrix

$$\mathbf{v}_1 = \begin{bmatrix} -\frac{(\alpha_2 - L_{\text{in},11})}{2L_{\text{in},12}} \\ 1 \\ 0 \end{bmatrix} \quad \mathbf{v}_2 = \begin{bmatrix} -\frac{(\alpha_1 - L_{\text{in},11})}{2L_{\text{in},12}} \\ 1 \\ 0 \end{bmatrix} \quad \mathbf{v}_3 = \begin{bmatrix} 0 \\ 0 \\ 1 \end{bmatrix}$$

These formulations of eigenvalues and eigenvectors is valid if following statement holds.

$$L_{\text{in},12} \neq 0 \quad \text{and} \quad L_{\text{in},11} \neq L_{\text{in},22} \neq L_{\text{in},33}$$

For the other cases the relations are not presented, but they are derived straight forward. Spectral decomposition of inelastic velocity matrix

$$\mathbf{L}_{\text{in}} = \sum_{i=1}^3 \frac{\alpha_i}{\|\mathbf{v}_i\|^2} \mathbf{v}_i \cdot \mathbf{v}_i^{\top}$$

VOIGT scheme of a symmetric second-order tensor \mathbf{A} and a symmetric fourth-order tensor \mathcal{A} with $i, j = 1, 2$ (plane stress state). At first, the new "base vectors" are introduced.

$$\mathbf{E}_{V1} = \mathbf{e}_1 \otimes \mathbf{e}_1 \quad \mathbf{E}_{V2} = \mathbf{e}_2 \otimes \mathbf{e}_2 \quad \mathbf{E}_{V3} = \frac{1}{\sqrt{2}} (\mathbf{e}_1 \otimes \mathbf{e}_2 + \mathbf{e}_2 \otimes \mathbf{e}_1)$$

This leads to following vector-matrix representation of the afore mentioned tensors.

$$\mathbf{a} = \begin{bmatrix} A_{11} \\ A_{22} \\ \sqrt{2}A_{12} \end{bmatrix} \quad \mathbf{A} = \begin{bmatrix} A_{1111} & A_{1122} & \sqrt{2}A_{1112} \\ A_{1122} & A_{2222} & \sqrt{2}A_{2212} \\ \sqrt{2}A_{1112} & \sqrt{2}A_{2212} & 2A_{1212} \end{bmatrix}$$

Appendix B

Identification of Creep Parameters and YOUNG's Modulus of the Substrate

Table B.1: Cross section dimensions of all specimens made out of AlSi10MgT6, determined YOUNG's moduli, steady-state moments and curvatures for calculation of creep parameters

specimen	T [°C]	v_{exp} [$\frac{\text{mm}}{\text{min}}$]	b [mm]	h_s [mm]	E_s [GPa]	M_{st} [Nmm]	$\dot{\Gamma}_{\text{st}}$ [$\cdot 10^{-6} \frac{1}{\text{mms}}$]
1	20	0.050	3.59	2.995	74.65	–	–
2	200	0.050	3.59	3.01	67.28	2011.27	7.26
3	250	0.025	3.51	3.01	65.25	1067.03	3.67
4		0.050	3.53	3.01	62.34	1145.99	7.61
5		0.075	3.54	3.01	68.09	1292.61	11.79
6	300	0.025	3.50	2.99	53.95	431.70	3.56
7			3.50	2.99	53.95	431.70	3.56
8		0.050	3.60	3.00	58.21	493.72	7.26
9		0.075	3.54	2.99	58.39	547.24	11.03
10	400	0.0125	3.51	2.98	38.24	115.72	1.79
11		0.025	3.53	2.98	30.05	136.98	3.30
12		0.050	3.60	3.00	31.94	160.38	7.32
13		0.075	3.55	2.99	32.19	178.94	10.10
14		0.0875	3.50	3.00	34.33	177.01	12.17
15		31.28	3.54	2.89	31.28	142.58	12.42

Identification of YOUNG's Modulus of the Coating

Table B.2: Cross section dimensions of all specimens made out of Fe24Al0.6Nb and determined YOUNG's moduli

specimen	T [°C]	v_{exp} [$\frac{\text{mm}}{\text{min}}$]	b [mm]	h_c [mm]	E_c [GPa]
1	20	0.050	3.58	1.25	70.97
2			3.56	1.22	69.90
3	400	0.050	3.56	1.22	56.26
4			3.57	1.22	53.90

Cross Section Dimensions of the Compound Specimens

Table B.3: Cross section dimensions of all compound specimens

specimen	T [°C]	v_{exp} [$\frac{\text{mm}}{\text{min}}$]	b [mm]	h_c [mm]	h_s [mm]	h [mm]
1	250	0.050	3.435	1.240	3.480	4.720
2	300	0.050	3.450	1.240	2.960	4.200
3	400	0.050	3.485	1.240	3.015	4.255

Measurements to Determine YOUNG’S Modulus

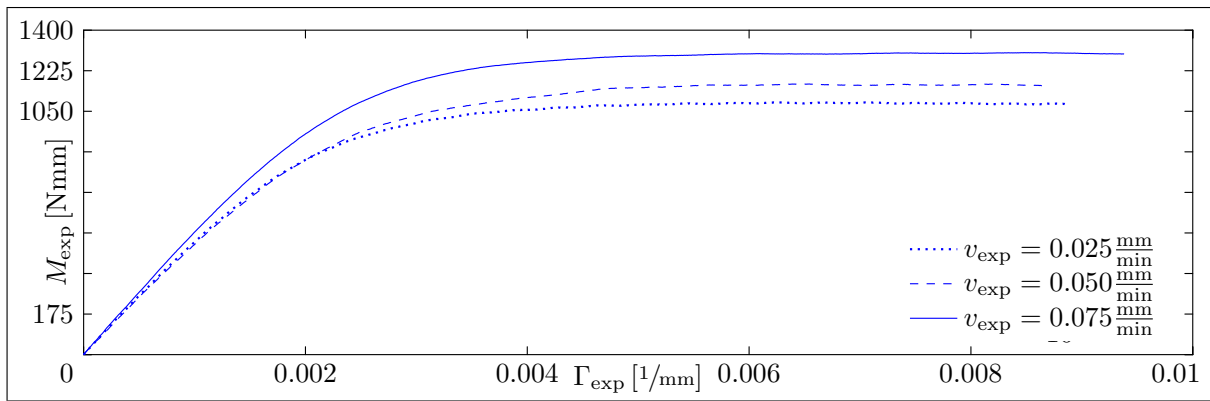


Figure B.1: M_{exp} vs. Γ_{exp} curves of the substrate for 250°C and different test speeds

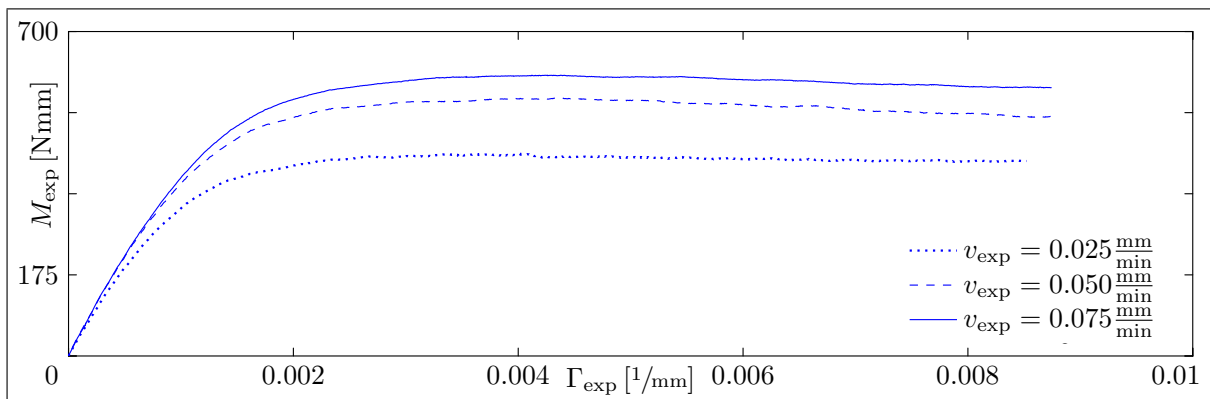


Figure B.2: M_{exp} vs. Γ_{exp} curves of the substrate for 300°C and different test speeds

Measurements to Determine Creep Parameters

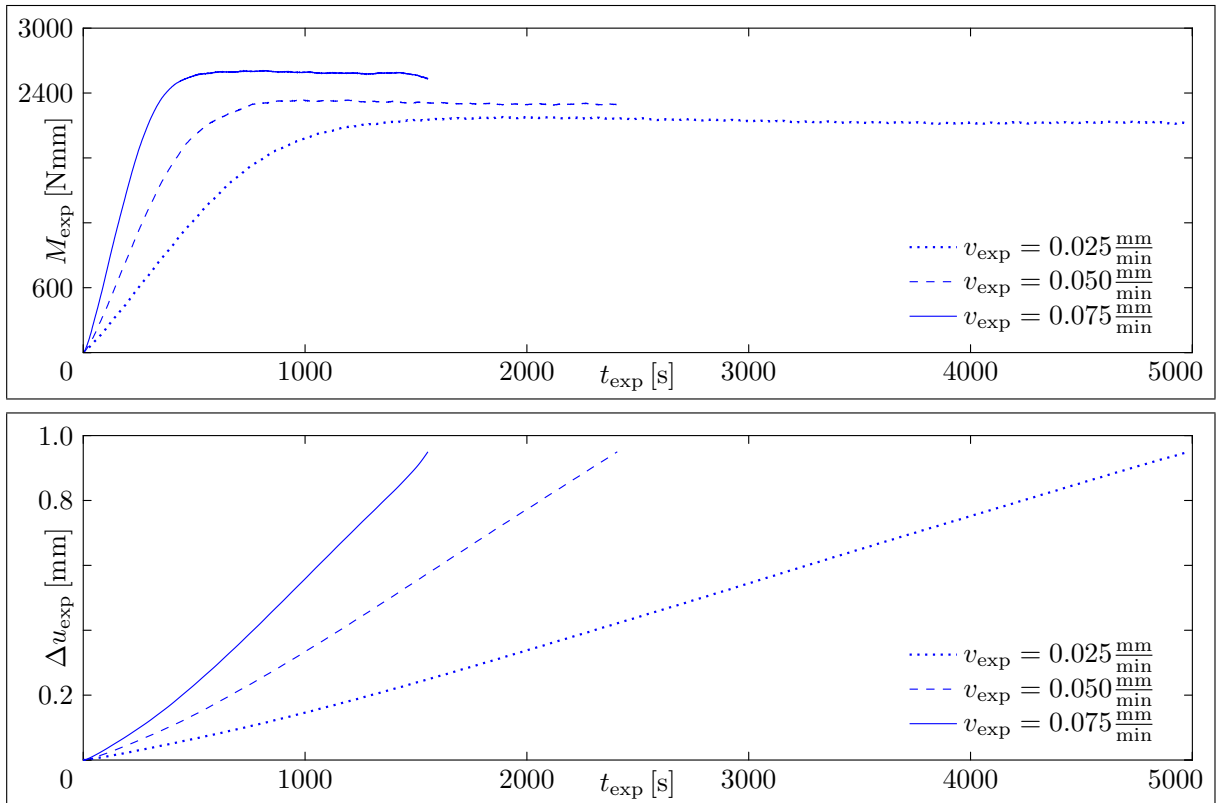


Figure B.3: M_{exp} (top) and Δu_{exp} (bottom) vs. t_{exp} of the substrate for 250°C

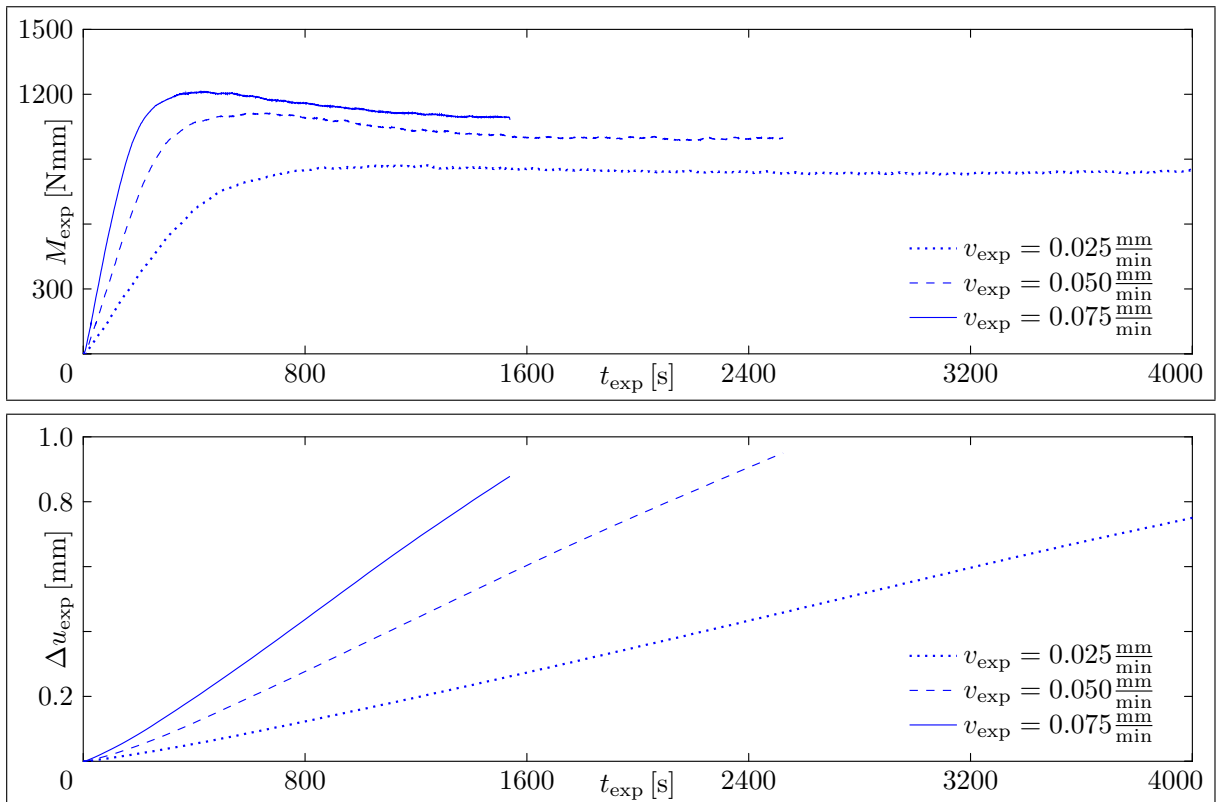


Figure B.4: M_{exp} (top) and Δu_{exp} (bottom) vs. t_{exp} of the substrate for 300°C

Verification of Creep Parameters

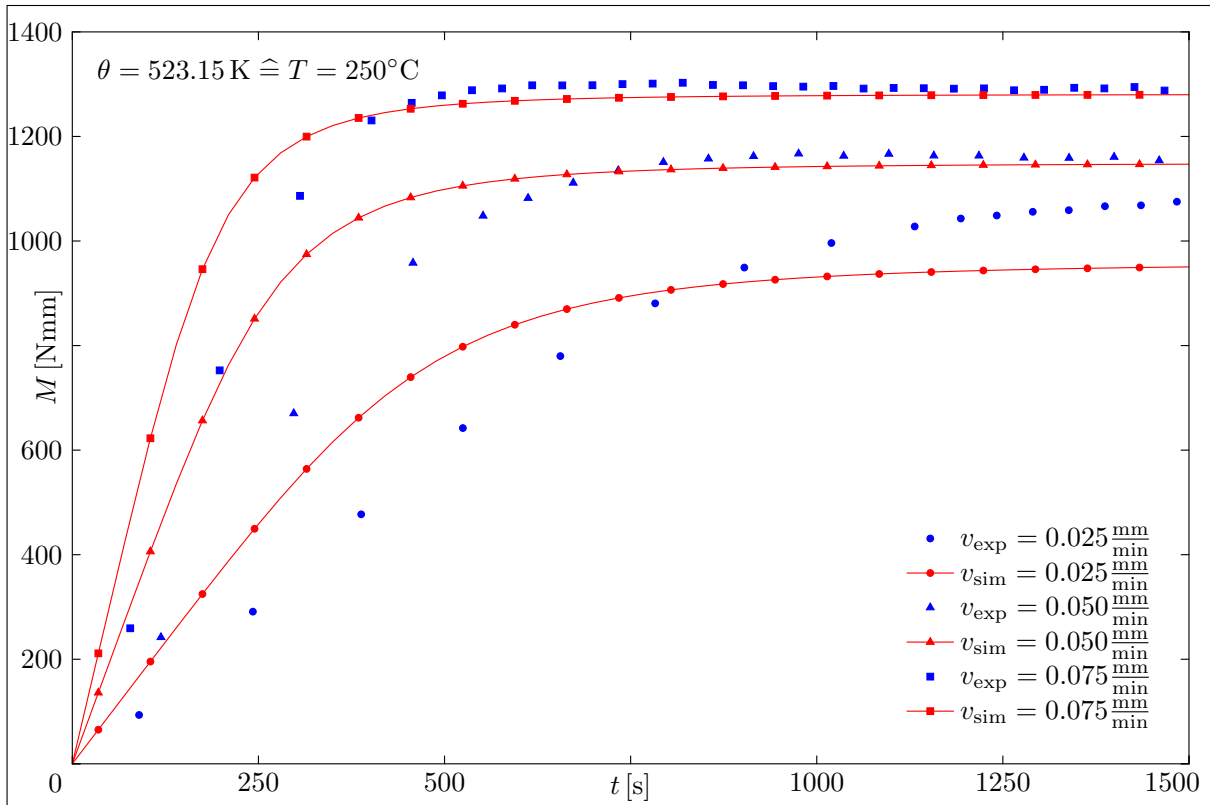


Figure B.5: Verification of determined creep parameters at 250°C and for different test speeds

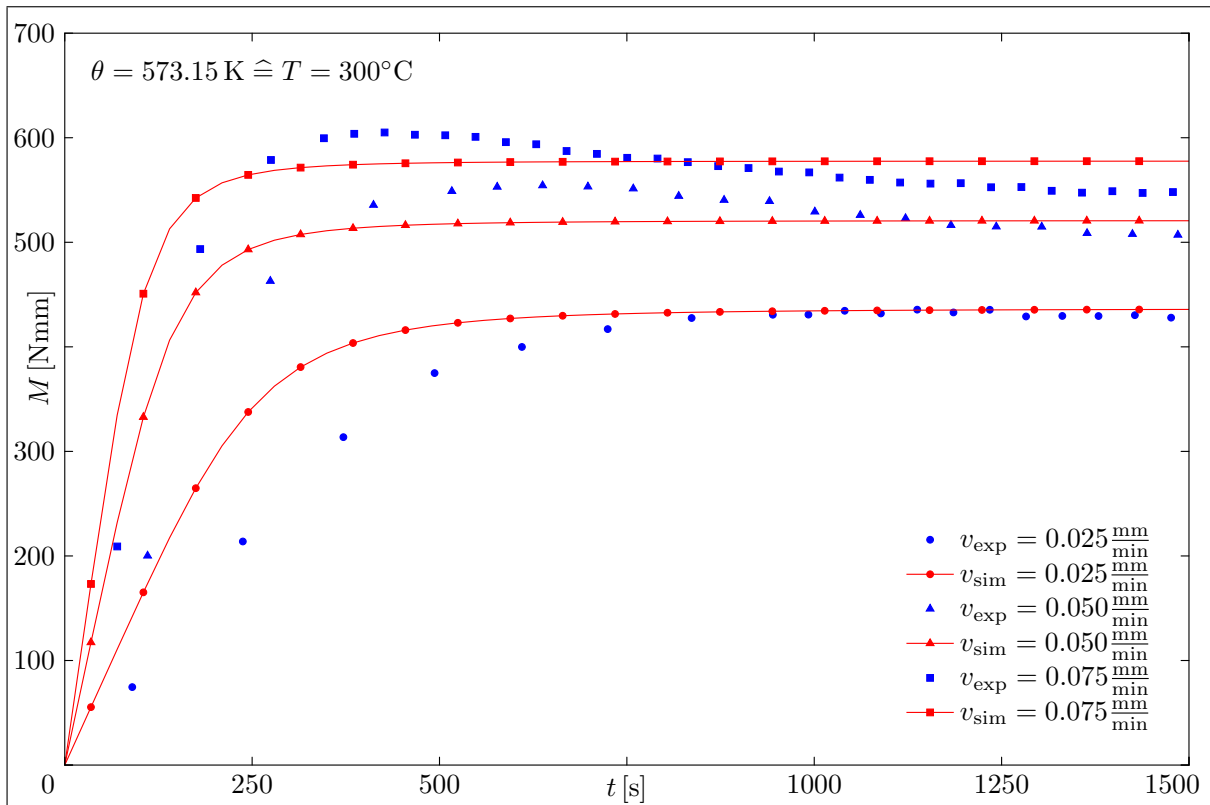


Figure B.6: Verification of determined creep parameters at 300°C and for different test speeds

Simulation Procedures

Table B.4: Computational time t_{CPU} and number of increments N_{Inc} for different simulation procedures and elastic and inelastic material behaviour of a DCB test with $NE = 200$

		material behaviour			
		elastic		inelastic	
		t_{CPU} [s]	N_{inc} [–]	t_{CPU} [s]	N_{inc} [–]
procedure	static	0.5	15	4.7	113
	dynamic	0.6	15	5.3	113
	gradient	1.7	59	3.4	93

Table B.5: Computational time t_{CPU} and number of increments N_{Inc} for different simulation procedures and elastic and inelastic material behaviour of a DCB test with $NE = 720$

		material behaviour			
		elastic		inelastic	
		t_{CPU} [s]	N_{inc} [–]	t_{CPU} [s]	N_{inc} [–]
procedure	static	1.2	15	19.6	156
	dynamic	1.5	15	24.6	170
	gradient	55.6	581	349.9	2330

Table B.6: Computational time t_{CPU} and number of increments N_{Inc} for different simulation procedures and elastic and inelastic material behaviour of a DCB test with $NE = 2720$

		material behaviour			
		elastic		inelastic	
		t_{CPU} [s]	N_{inc} [–]	t_{CPU} [s]	N_{inc} [–]
procedure	static	3.7	15	83.0	214
	dynamic	5.1	15	115.7	238
	gradient	305.4	1049	1072.6	2383

Temperature Dependence of Cohesive Zone Parameters

The cohesive zone parameters are all interpolated by the quadratic function

$$\square = q_1\theta^2 + q_2\theta + q_3 \quad (\text{B.1})$$

This is done, thus, for an isothermal simulation the same parameters result which are calculated with the numerical optimisation.

Table B.7: Temperature dependence of cohesive zone parameters and creep factor

\square	q_1	q_2	q_3
a_s	$1.4283 \cdot 10^{-15} \frac{\text{s}^{-1}}{\text{K}^2}$	$-1.5556 \cdot 10^{-12} \frac{\text{s}^{-1}}{\text{K}}$	$4.2294 \cdot 10^{-10} \text{s}^{-1}$
T_{\max}	$0.01373 \frac{\text{MPa}}{\text{K}^2}$	$-17.7416 \frac{\text{MPa}}{\text{K}}$	6103.2629MPa
g_{cr}	$7.2667 \cdot 10^{-7} \frac{\text{mm}}{\text{K}^2}$	$-8.4064 \cdot 10^{-4} \frac{\text{mm}}{\text{K}}$	0.2459mm
β	$8.7333 \cdot 10^{-5} \frac{1}{\text{K}^2}$	$-0.1039 \frac{1}{\text{K}}$	31.4262
S_{i0}	$1.9184 \cdot 10^{-6} \frac{\text{mJ}}{\text{mm}^2\text{K}^2}$	$-0.0023 \frac{\text{mJ}}{\text{mm}^2\text{K}}$	$0.7119 \frac{\text{mJ}}{\text{mm}^2}$
Y_{E0}	$-2.6667 \cdot 10^{-5} \frac{\text{mJ}}{\text{mm}^2\text{K}^2}$	$0.0288 \frac{\text{mJ}}{\text{mm}^2\text{K}}$	$-6.7866 \frac{\text{mJ}}{\text{mm}^2}$